Titre: Title:	Integrated Communication and Radar Scheme for Future Intelligent Transportation Systems
Auteur: Author:	Liang Han
Date:	2011
Type:	Mémoire ou thèse / Dissertation or Thesis
Référence: Citation:	Han, L. (2011). Integrated Communication and Radar Scheme for Future Intelligent Transportation Systems [Thèse de doctorat, École Polytechnique de Montréal]. PolyPublie. https://publications.polymtl.ca/592/

URL de PolyPublie: PolyPublie URL:	https://publications.polymtl.ca/592/
Directeurs de recherche: Advisors:	Ke Wu
Programme: Program:	génie électrique

UNIVERSITÉ DE MONTRÉAL

INTEGRATED COMMUNICATION AND RADAR SCHEME FOR FUTURE INTELLIGENT TRANSPORTATION SYSTEMS

LIANG HAN

DÉPARTEMENT DE GÉNIE ÉLECTRIQUE

ÉCOLE POLYTECHNIQUE DE MONTRÉAL

THÈSE PRÉSENTÉE EN VUE DE L'OBTENTION

DU DIPLÔME DE PHILOSOPHIAE DOCTOR (Ph.D.)

(GÉNIE ÉLECTRIQUE)

Juin 2011

UNIVERSITÉ DE MONTRÉAL

ÉCOLE POLYTECHNIQUE DE MONTRÉAL

Cette thèse intitulée:

INTEGRATED COMMUNICATION AND RADAR SCHEME FOR FUTURE INTELLIGENT TRANSPORTATION SYSTEMS

présentée par : HAN Liang

en vue de l'obtention du diplôme de : Philosophiae Doctor

a été dûment acceptée par le jury d'examen constitué de :

M. BOSISIO Renato, M.Sc.A., président

M. WU Ke, Ph.D., membre et directeur de recherche

M. NERGUIZIAN Chahé, Ph.D., membre

M. AFFES Sofiène, Ph.D., membre externe

DEDICATION

To my family

ACKNOWLEDGEMENT

First of all, I would like to express my sincere gratitude to my thesis supervisor, Dr. Ke Wu, who offered me an opportunity to pursue the PhD studies at the École Polytechnique de Montréal. This PhD project cannot be accomplished without his continuous support, his consistent encouragement, his inspiring guidance and his extraordinary foresight.

I am also very grateful to all the personnel at the Poly-Grames Research Center, especially all the technicians including Mr. Jules Gauthier, Mr. Traian Antonescu, Mr. Steve Dubé and Mr. Maxime Thibault. My gratitude extends to Mrs. Ginette Desparois for her assistance with all the administrative works and also to Mr. Jean-Sébastien Décarie for his technical support for solving all the IT problems.

My special thanks goes to the members of the examination jury for reading my thesis and providing their invaluable comments.

I would like to thank all the colleagues in the Poly-Grames Research Center, in particular Dr. Xiao-Ping Chen, Dr. Simone Winkler, Wen-Rui Li, Dr. Fanfan He, Dr. Lin Li and Dr. Ning Yang as well as all my friends in Canada and in China.

Last but not least, I would like to dedicate this thesis to my parents who gave me birth and brought me up. Additionally, I am very much indebted to my wife Mrs. Hongyan Zhou, who is always by my side.

RÉSUMÉ

Grâce à son impact social et économique, la journée mondiale de la santé 2004 a été dédiée à la sécurité routière. Le thème suivant : « La sécurité routière n’est pas accidentelle» a été abordé. Suite à cette rencontre, une attention toute particulière a été donnée à la problématique des accidents de la route. Afin d’augmenter la sécurité sur les routes et diminuer le nombre d’accidents, des systèmes intelligents de transport (ITS) ont été proposés. Ces systèmes utilisent les technologies avancées de communication et de détection. La structure ITS associe les fonctionnalités des Radars et des communications sans fils, permettant de rendre les futurs véhicules intelligents autonomes et collaboratifs. Ces deux fonctions peuvent être réalisées en utilisant deux systèmes radiofréquences individuels et indépendants. Toutefois, une meilleure solution consiste à intégrer, dans un seul dispositif, le système de communication et le radar. Ceci permet d’apporter de nombreux avantages comme par exemple la simplification et la miniaturisation du système, sa reconfigurabilité, l’augmentation de son efficacité, et enfin cela permettrait de réduire fortement ses coûts de développement et de réalisation, élément clé pour réussir la commercialisation du véhicule intelligent.

Intrinsèquement, le fonctionnement des communications sans fils et des Radar ne sont pas compatibles. En effet, ils requièrent des techniques de conception et d’implémentations différentes, ce qui les rend difficilement intégrables en un seul système. Afin de répondre aux grands défis technologiques présentés par cette intégration fonctionnelle, cette thèse de doctorat présente un développement compréhensif des systèmes intégrés de communication sans-fil et radar (iCars), placés dans un seul dispositif émetteur-récepteur et destinés aux futurs systèmes intelligents de transport.

Premièrement, après une recherche bibliographique approfondie, une nouvelle technique de modulation est proposée. Dans cette technique, les signaux radar et les signaux de communication sont arrangés en créneaux temporels séquentiels pendant un cycle d’opération, minimisant ainsi leurs interférences mutuelles. Cette technique permet d’obtenir une agilité temporelle et/ou une reconfigurabilité fonctionnelle, par l’ajustement adaptatif ou cognitif de toutes les durées de modulation de la forme d’onde, en accord avec les situations spécifiques de l’utilisation. De plus, une fusion fonctionnelle de deux modes d’opération devient possible en considérant les deux aspects suivants : le premier est que la portée et la vélocité obtenues en

mode radar peuvent être utilisées en mode communication afin de réduire la propagation par trajets multiples et afin de compenser l'étalement Doppler causé par la mobilité des unités intégrées. Le deuxième aspect se présente dans l'utilisation de la fonction de communication où différents émetteurs-récepteurs intégrés peuvent échanger des données pertinentes comme par exemple la distance et la vélocité d'une cible. Ceci peut mener au développement des réseaux de radar avec une portée et une précision améliorées. Enfin, d'un point de vue de réseautage, la modulation de la forme d'onde proposée est avantageuse puisqu'un créneau temporel spécifique peut alors être assigné à chaque unité dans la même cellule conformément à la méthode d'accès multiple par répartition temporelle, tandis que différentes cellules peuvent utiliser différentes fréquences dans la transmission des données conformément à la méthode d'accès multiple par répartition fréquentielle. Finalement, la technique de modulation proposée est avantageuse, d'un point de vu interconnexion. En effet, un point temporel spécifique peut être assigné à chaque unité d'une même cellule basé sur un multiplexage temporel (TDMA) tandis que différentes cellules peuvent utiliser différentes fréquences pour la transmission des données, cette fois-ci basé sur un multiplexage fréquentiel (FDMA).

Afin de confirmer le concept du système proposé, un prototype est réalisé fonctionnant à 5.9 GHz, Aux États-Unis, cette bande de fréquence a été allouée, par le FCC (Federal Communication Commission), aux applications de communications à courtes portées (DSRC). Conformément aux règlements de la FCC et à la demande des applications automobiles, les spécifications du système sont déterminées. Ensuite, une analyse du bilan de liaison est effectuée pour le mode radar et le mode communication. Cette analyse permet de mieux connaître les aspects théoriques de la fonctionnalité du système, et permet de déterminer les considérations spécifiques pour la conception. Un émetteur-récepteur hétérodyne conventionnel est modifié pour mettre en forme le type de modulation proposé. Ensuite, le système entier est modélisé puis analysé dans un environnement commercial de simulation afin d'optimiser la performance du système. Suite à une analyse poussée du système et une simulation méticuleuse, un prototype est réalisé utilisant des composants commerciaux. Des expérimentations sont également entreprise afin d'évaluer la performance du système en fonction des modes radar et de communication. Le taux d'erreur (BER) mesuré est en très bonne accord avec les valeurs théoriques. Les distances et vélocités détectées présentent une très petite erreur comparativement aux valeurs prédéfinies dans l'émulateur du canal.

Afin d'améliorer le débit de transfert des données dans le mode de communication et la résolution de portée dans le mode radar, un deuxième prototype est réalisé fonctionnant dans la bande ISM, c'est-à-dire autour de 24 GHz. Ce système est conçu à l'aide d'une technologie de guides d'onde intégrés sur substrat, qui présente plusieurs avantages comme par exemple son faible coût et sa compatibilité avec la technologie des circuits imprimés. Dans ce système, différents composants passifs issus de la technologie des guides d'ondes intégrés sur substrat, tels que des coupleurs larges bandes, des déphaseurs larges bandes et des filtres à haute sélectivité sont proposés. Ces circuits sont réalisés à partir d'une nouvelle méthode de conception utilisant des techniques de calibration numérique. En particulier, une méthode efficace et précise pour la synthèse des coupleurs interdigitaux (Lange) est proposée. En outre, une stratégie de modélisation est présentée pour la caractérisation et l'extraction des modèles équivalents de circuit du couplage mutuel d'ordre arbitraire. Cette technique est ensuite appliquée à la conception d'une paire de réseaux micro-ruban 8x8 fonctionnant à 24 GHz. Finalement, en intégrant les composants passifs en technologie guide d'onde intégrés sur substrat et les composants commerciaux, le système final fonctionnant à 24 GHz intégrant à la fois le système de communication haute vitesse et le système de détection de cibles haute précision, est réalisé.

Le système présenté dans cette thèse, intégrant des fonctionnabilités radar et de communication, a été démontré comme étant un système faible coût et apparait comme une solution avantageuse pour les fonctions requises des futures IVs. Ce produit peut aussi être très bénéfique pour l'industrie automobile du fait de sa simplicité d'architecture et de ses possibilités de reconfiguration.

ABSTRACT

Due to its growing social and economic impact, the world health day of 2004 was dedicated to road safety with its theme as “Road safety is no accident”. Thereafter, road traffic accidents have received unprecedented attention. In order to improve road safety, intelligent transportation systems (ITSs) have been proposed and deployed by making use of advanced information and communication technologies. Within the framework of ITSs, both wireless communication and radar sensing functions are indispensable for autonomous and cooperative operations of future intelligent vehicles (IVs). These two functions can definitely be achieved by using two individual and independent wireless systems. However, an attractive solution would be to integrate both communication and radar functions within a single transceiver platform, which could bring a lot of benefits such as system simplification and miniaturization, functional reconfiguration and fusion (mutual penetration and rapid processing/control of information), and especially efficiency enhancement and cost reduction that are the keys to the successful development and marketing of IVs.

Intrinsically, wireless communication and radar systems have incompatible operation principles, which require different design considerations and system implementations with respect to modulation techniques, required bandwidth, signal propagation and detection. To respond to these unprecedented design and technological challenges posed by the functional integration, this PhD thesis presents comprehensive study and development of **i**ntegrated **c**ommunication **a**nd **r**adar **s**ystems (iCars) based on a single transceiver platform for future ITSs.

Following a broad and in-depth literature review, first of all, a novel modulation scheme is proposed in this work, in which radar and communication signals are arranged in sequential time slots of one operation cycle and therefore, their interference is minimized. Also, time-agility or flexible functional reconfiguration can be easily achieved by adaptively or cognitively adjusting all software-programmable time durations in the modulation waveform according to usage situations. Moreover, functional fusion between two operation modes can be made possible from the following two aspects. One is that targets’ ranges and velocities obtained through the radar mode can be used in the communication mode to mitigate multipath fading and compensate the Doppler spreading effect caused by the mobility of onboard units. The other is that by making use of the communication features, different onboard transceivers can exchange data such as

targets' range and velocities, which in fact forms a radar network with range increment and accuracy enhancement of target finding. Finally, the proposed modulation waveform is advantageous from a networking perspective since a specific time slot can be assigned to each unit in the same service cell on the basis of a time division multiple access (TDMA) while different service cells can use different frequencies for data transmission based on the frequency division multiple access (FDMA).

In order to prove our proposed system concept, a low-frequency system demonstrator has been built in the 5.9-GHz band assigned by the U.S. federal communications commission's (FCC's) for dedicated short range communication (DSRC) applications. Based on the FCC's rules and practical requirements of automotive applications, system specifications are defined and then link budget analysis is performed for both radar and communication modes in order to provide theoretical insight into system functionality and understand special design considerations. Conventional heterodyne transceiver architecture is modified to adapt our proposed modulation waveform. Subsequently, the entire system is modeled and analyzed in a commercial simulation package in order to find out achievable system performance as well as perform system optimization. On the basis of careful system analysis and simulation, the proposed low-frequency system prototype is built with commercial off-the-shelf components, and experiments are carried out to evaluate system performance for both radar and communication modes. Measured bit-error-rate (BER) in the communication mode agrees very well with theoretical values, and measured detection ranges and velocities in the radar mode exhibit very small error compared to the predefined values in the channel emulator.

For enhancing data rate in the communication mode and range resolution in the radar mode, another high-frequency system has been designed and prototyped in the 24-GHz industrial, scientific and medical (ISM)-band with the help of the emerging substrate integrated waveguide (SIW) technology, which has presented multiple advantages such as low cost, high quality-factor (high-Q) and versatile compatibility with standard printed circuit board (PCB) process. In this 24-GHz system, a number of innovative SIW passive components including wideband couplers, broadband phase shifters and highly-selective filters have been proposed together with novel design and synthesis method by virtue of numerical calibration techniques. In particular, an accurate and efficient method has been proposed to synthesize four-line interdigitated (Lange) coupler. Moreover, a fundamental modeling strategy has also been proposed to characterize and establish equivalent circuit models of mutual coupling of any orders and this modeling technique is then applied in the design of a pair of 8×8 microstrip array at 24 GHz. Finally, by integrating our developed SIW passive components with commercial off-the-shelf active devices, the entire 24-GHz system is designed and prototyped onto a single substrate. Experimental results show very promising system performance for both high speed data communication and high accuracy target detection.

The integrated communication and radar scheme proposed in this thesis has been demonstrated as a cost-effective and advantageous solution for the functional requirements of future IVs. It will eventually benefit the automotive industry due to its low cost, simple system architecture, high efficiency and reconfigurable functionality.

TABLE OF CONTENTS

LIST OF TABLES

LIST OF FIGURES

LIST OF ACRONYMS AND ABBREVIATIONS

1-D	One-Dimensional
2-D	Two-Dimensional
3-D	Three-Dimensional
ADC	Analog-to-Digital Converter
AGC	Automatic Gain Control
AHSRA	Advanced Cruise-Assist Highway Systems Research Association
ALC	Automatic Level Control
AM	Amplitude-Modulated
APK	Amplitude-Phase Keying
ARIB	Association of Radio Industries and Businesses
ARM	Advanced RISC Machine
ASK	Amplitude Shift Keying
BFSK	Binary FSK
BPSK	Binary PSK
C2C	Car-to-Car
C2I	Car-to-Infrastructure
CAD	Computer-Aided-Design
CMOS	Complementary Metal-Oxide-Semiconductor
CPW	Coplanar Waveguide
CW	Continuous Wave
DC	Direct Current
DDS	Direct Digital Synthesizer
DOA	Direction of Arrival

DSP	Digital Signal Processing
DSRC	Dedicated Short Range Communication
DUT	Device-Under-Test
EBG	Electromagnetic Bandgap
EIRP	Effective Isotropic Radiated Power
EM	Electromagnetic
EMC	Electromagnetic Compatibility
EMI	Electromagnetic Interference
EVM	Error Vector Magnitude
FCC	Federal Communications Commission
FDD	Frequency Division Duplex
FDMA	Frequency Division Multiple Access
FEM	Finite Element Method
FFT	Fast Fourier Transform
FMCW	Frequency-Modulated Continuous Wave
FSK	Frequency Shift Keying
GPS	Global Positioning System
High-*Q*	High Quality-Factor
I	In-Phase
iCars	Integrated Communication and Radar System
IF	Intermediate Frequency
IR	Infra-Red
ISM	Industrial, Scientific and Medical
ITS	Intelligent Transportation System

IV	Intelligent Vehicle
LPF	Low-Pass Filter
LRR	Long Range Radar
MHMICs	Miniature Hybrid Microwave Integrated Circuits
MIMO	Multiple Input and Multiple Output
MMICs	Monolithic Microwave Integrated Circuits
MoM	Method-of-Moments
MPIE	Mixed Potential Integral Equation
NF	Noise Figure
OFDM	Orthogonal Frequency Division Multiplexing
OOK	On-Off Keying
PCB	Printed Circuit Board
PLL	Phase-Locked Loop
PN	Pseudo-Noise
PRBS	Pseudo-Random Bit Sequence
Q	Quadrature-Phase
QAM	Quadrature Amplitude Modulation
QPSK	Quadrature PSK
RCS	Radar Cross Section
RF	Radio Frequency
RISC	Reduced Instruction Set Computing
RSSI	Received Signal Strength Indicator
RTTT	Road Transport and Traffic Telematic
SEM	Scanning Electron Microscope

SIC	Substrate Integrated Circuit
SIIG	Substrate Integrated Image Waveguide
SINRD	Substrate Integrated Nonradiative Waveguide
SIW	Substrate Integrated (Rectangular) Waveguide
SMA	Subminiature Version A
SNR	Signal-to-Noise Ratio
SoC	System-on-Chip
SOC	Short-Open Calibration
SOLT	Short-Open-Load-Thru
SoS	System on Substrate
SRR	Short Range Radar
TDD	Time Division Duplex
TDMA	Time Division Multiple Access
TEM	Transverse Electromagnetic Mode
TOI	Third Order Intercept
TRL	Thru-Reflect-Line
UHF	Ultra-High-Frequency
USB	Universal Serial Bus
VHF	Very-High-Frequency
VNA	Vector Network Analyzer
VSWR	Voltage Standing Wave Ratio

INTRODUCTION

1. Motivation

According to the statistics of the world health organization [1], more than 1.2 million people were killed in road traffic crashes in 2004, which were 2.2 % of all global morality and the 9th leading cause of death. In addition to fatalities, between 20 and 50 million non-fatal injuries are estimated to occur annually around the world. It is anticipated that road traffic fatalities will be increased by 67 % by the year 2020 if appropriate actions are not taken. By the year 2030, it will rise to the 5th leading cause of death, resulting in an estimated 2.4 million fatalities per year. When it comes to Canada, one person dies every three hours on Canada's roads [2].

Road traffic injuries have both social and economic costs. On one hand, road crash survivors, their families, friends and other caregivers often suffer adverse social, physical and psychological effects. On the other hand, in terms of economics, the cost of road crash injuries is estimated at roughly 1% of gross national product in low-income countries, 1.5% in middle-income countries and 2% in high-income countries. Globally, the economic cost of road traffic injuries is about 518 billion dollars with low-income and middle-income countries accounting for 65 billion dollars.

In order to improve road safety, increase traffic mobility and sustain the environment, transportation professionals decided to apply affordable information, computing, and sensor technologies to traffic and road management around 1990, which gave birth to the concept of intelligent transportation systems (ITSs) that have been developed and deployed very quickly around the world. ITSs are dedicated to such application areas as convenience systems, safety systems, productivity systems and traffic-assist systems [3]. Typical ITS applications include parking assistance, adaptive cruise control, lane-keeping assistance, crash prevention, traffic jam dissipation, vehicle flow management and cooperative adaptive cruise control as well as platooning.

Within the framework of the ITS, intelligent vehicles (IVs) have to work in two manners [3]. On one hand, IVs should operate in an autonomous manner to sense the driving environment with the help of onboard sensors. Sensing technologies available today can be classified into the following categories: radar (**ra**dio **d**etection **a**nd **r**anging), lidar (**li**ght **d**etection **a**nd **r**anging), ultrasonic and machine vision. According to the effective working distance, radar can be further subdivided into short range radar (SRR) and long range radar (LRR). Machine vision mainly utilizes video camera, 3D-camera and far infra-red (IR) camera. A comparison of performance and cost of the available sensing technologies is made in Table 1 [4].

Table 1 Performance comparisons of available sensing technologies.

	SRR	LRR	Lidar	Ultrasonic Sensor	Video Camera	3D-Camera	Far IR Camera
Range Measurement (< 2m)	o	o	o	+ +	–	+ +	–
Range Measurement (2-30m)	+	+ +	+ +	–	–	o	–
Range Measurement (30-150m)	n.a.	+ +	+	– –	–	–	–
Angle Measurement (<10 deg)	+	+	+ +	–	+ +	+	++
Angle Measurement (>30 deg)	o	–	+ +	o	+ +	+	+ +
Angular Resolution	o	o	+ +	–	+ +	+	+ +
Direct Velocity Information	+ +	+ +	– –	o	– –	– –	– –
Operation in Rain	+ +	+	o	o	o	o	o
Operation in Fog or Snow	+ +	+ +	–	+	–	–	o
Operation if Dirt on Sensor	+ +	+ +	o	+ +	– –	– –	– –
Night Vision	n.a.	n.a.	n.a.	n.a.	–	o	+ +
Mounting and Exposure Trade-off	+ +	+ +	o	o	o	o	o
Cost	high	high	fair	low	low	low	low

++: Ideally suited; +: Good performance; o: Possible, but drawbacks to be expected; –: Only possible with large additional effort; —: Impossible; n.a.: Not applicable.

From the comparison in Table 1, we can have the following observations. Firstly, lidar is greatly restricted by the environmental conditions such as rain, fog or snow, and it cannot provide direct velocity information which is usually required by the ACC function, neither do machine vision-based sensors. Secondly, ultrasonic sensors are only able to detect a distance of several meters, which is only useful in very short-range applications. Thirdly, though machine vision-based sensors are good at angle measurement, their limitations lie in the capabilities of range and velocity measurement. On the basis of a comprehensive consideration, radar is the most promising and robust solution to vehicle sensing requirements in terms of environmental conditions, measurement capabilities, and installation. However, its practical applications are hindered by its high cost mostly attributed to the radio-frequency (RF) front-end circuit and system integration. Generally, the cost can be substantially reduced by employing highly-integrated and mass-producible design techniques which allow simultaneous size and cost reduction of radar sensors.

On the other hand, IVs should also operate in a cooperative manner to exchange information data and sensing parameters such as braking and acceleration between vehicles and also traffic, road and weather conditions between vehicles and roadside units or beacons [3]. In addition, other information transmission and data communications will be required for drivers and passengers such as broadband mobile internet. In such an integrated highway system as ITS, three types of communication protocols can be built up including command/response between service provider and end users, broadcast-to-listener and peer-to-peer.

In conclusion, both radar sensing and wireless communication functions are indispensable to the development of future IVs for ITS applications. In the meanwhile, such a functional fusion or convergence of radar and communication operations can also be found in other application scenarios such as wireless sensor network, in which each sensor has to generate a correct representation of the sensed quantity and then share it with other sensor nodes through wireless data links. Figure 1 shows these two application scenarios.

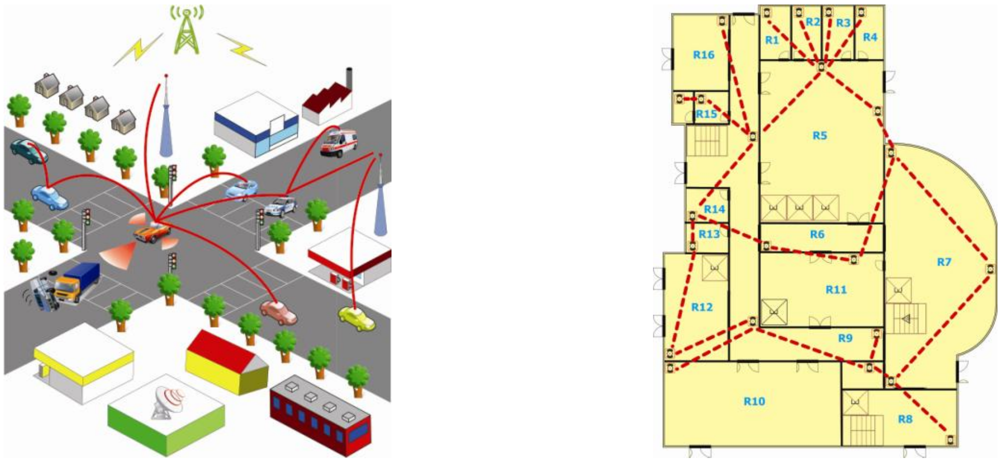

(a) Future ITS.

(b) Wireless sensor network.

Figure 1 Application scenarios of iCars.

In general, this functional fusion is certainly possible with two individual systems that are respectively dedicated to wireless communication and radar sensing functions. However, if these two functions can be integrated within a single transceiver platform, such an **i**ntegrated **c**ommunication **a**nd **r**adar **s**ystem (iCars) would definitely have a lot of advantages over two individual and independent systems, such as low cost, compact size, versatile functionality, low power consumption, low complexity, fast response, and high efficiency, as shown in Figure 2.

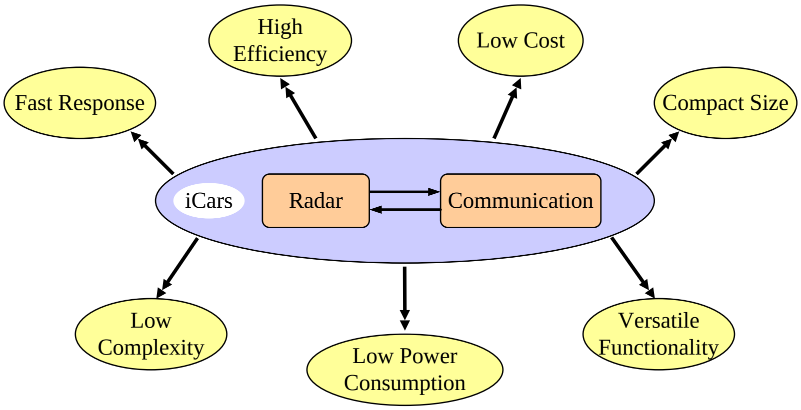

Figure 2 Benefits of functional integration.

Consequently, the present PhD thesis focuses on the study and development of iCars using a single transceiver for future ITS applications. Multi-functionality such as wireless communication and radar sensing will be integrated into a single radio transceiver for cost reduction with respect to system design. Furthermore, this multifunctional system will be designed using an innovative concept called substrate integrated waveguide (SIW) for further reducing cost with respect to system implementation. In this unique substrate integration platform, conventional passive high quality-factor (high-Q) waveguide structures and active devices can be integrated onto a single substrate in a monolithic manner. Therefore, the present PhD project is opportunely and strategically important for future development of ITSs.

2. Objectives

The overall objective of this thesis is to develop low-cost integrated multifunctional systems, in which two functions namely wireless communication and radar sensing are integrated into a single transceiver using the SIW technology. There are three detailed objectives progressively stemming from this overall objective.

1) To propose novel modulation scheme and transceiver architecture as well as to prove system concept through a low-frequency system demonstrator;

2) To model, design and characterize innovative passive components using substrate integration technology and arbitrary-order mutual coupling existing in coupled electromagnetic (EM) structures;

3) To prototype a high-frequency SIW-based system and validate system performance;

In a long-term, this project will lay a solid groundwork for developing a multifunctional SIW-based system-on-chip (SoC) or system-on-substrate (SoS) using advanced fabrication technique such as the inexpensive and mature complementary metal-oxide-semiconductor (CMOS) process. This multifunctional SoC or SoS will show its predominant advantages such as ultra low cost, miniaturized circuit size and greatly reduced power consumption.

3. Methodology

This project will make use of a top-down design approach, which starts from system concept to components development.

3.1 Proposition of modulation scheme and proof of system concept

The development of such an integrated transceiver platform presents a very interesting and challenging research topic. Recently, a number of systems have been demonstrated, which may be, in our opinions, described by and classified into the following categories.

1) Conventional frequency-modulated continuous wave (FMCW) radar waveforms can be amplitude-modulated (AM) with communication data [5] in order to achieve simultaneous functions of communication and radar. However, the proposed system in [5] only works in a master-slave manner, which means that the slave side (the AM data receiver in [5]) is not able to autonomously transfer data. Moreover, the frequency of the data signal carrier must be carefully chosen in order to reduce mutual interference between the radar and the enabled duplex communication.

2) Radar and communication signals can be separated in the frequency domain. In [6], pulse radar with communication capability was realized by specially allocating the communication channel over the first null of the spectrum of the pulse radar signal. In spite of the fact that measurements have demonstrated a good suppression of the radar signal in the communication receiver under the condition of a low data rate, this spectrum-overlapping scheme is not suitable for high data rate communications.

3) Radar and communication functions can also be integrated together using spread spectrum technique, which possesses the advantages of secure and robust (anti-fading) communication, strong resistance to interference and jamming, low probability of intercept, and multiple access capability. Typical forms of the spread spectrum technique are direct-sequence spread spectrum [7]-[11], code-hopping spread spectrum [12], time-hopping spread spectrum [13], and chirp spread spectrum [14]. By making use of the orthogonality of pseudo-noise (PN) codes [7]-[13] or the quasi-orthogonality of upchirp and downchirp waveforms [14], the radar and communication functions should ideally be able to operate

simultaneously without interference. However, the system design and implementation associated with time/frequency synchronization is very complex and thus of high cost. Moreover, the spectrum utilization is inefficient, which makes this technique attractive only for millimetre-wave applications where a large amount of frequency resource is available.

4) Multi-carrier, especially orthogonal frequency division multiplexing (OFDM) technique that is well-known in wireless communication has also been introduced into the design of radar waveforms. This is because it has no range-Doppler coupling issue and therefore, independent and unambiguous range and Doppler processing are possible [15]-[17]. In addition, it also allows for the simultaneous operation of radar and communication functions [18]-[24]. The OFDM technique has a higher spectral efficiency than the spread spectrum technique, less complex receiver architecture due to the avoidance of inter-symbol and inter-channel interferences, and more flexible spectrum adaptation and sub-carrier modulation. However, OFDM systems are more sensitive to Doppler spreads than single-carrier modulated systems, and therefore the frequency synchronization should be very accurate, which results in complex signal processing and high cost. In addition, due to the cyclic prefix/guard interval required in system design, the transmission efficiency is degraded. Moreover, a high peak-to-average-power ratio requires a highly-linearized transmitter, which generally suffers from low power added efficiency.

5) Probably the best way to minimize the interference between radar and communication signals is to arrange them sequentially in time domain, which means simultaneous radar sensing and radio communication are no longer possible in this case. Conventional FMCW radar systems integrated with amplitude shift keying (ASK) [25] and frequency shift keying (FSK) [26] as well as direct-sequence spread spectrum technique [27] have been demonstrated.

In order to reduce system cost and design complexity, and also minimize interference between communication and radar signals as well as increase system flexibility and reliability, we have proposed a novel kind of time-agile modulation scheme [28]. In the proposed periodic modulation waveform shown in Figure 3, each operation cycle is composed of one radar cycle and one radio (communication) cycle. The radar cycle is composed of an upchirp, a constant-frequency period, and a downchirp. Following the radar cycle, the radio cycle is another constant-frequency period that can be used for any digital bandpass modulation techniques such as amplitude shift keying (ASK), frequency shift keying (FSK), phase shift keying (PSK) and even some combinations among them like quadrature amplitude modulation (QAM). Through rigorous theoretical analysis, the condition for phase continuity has been found in order to minimize out-of-band spectrum growth.

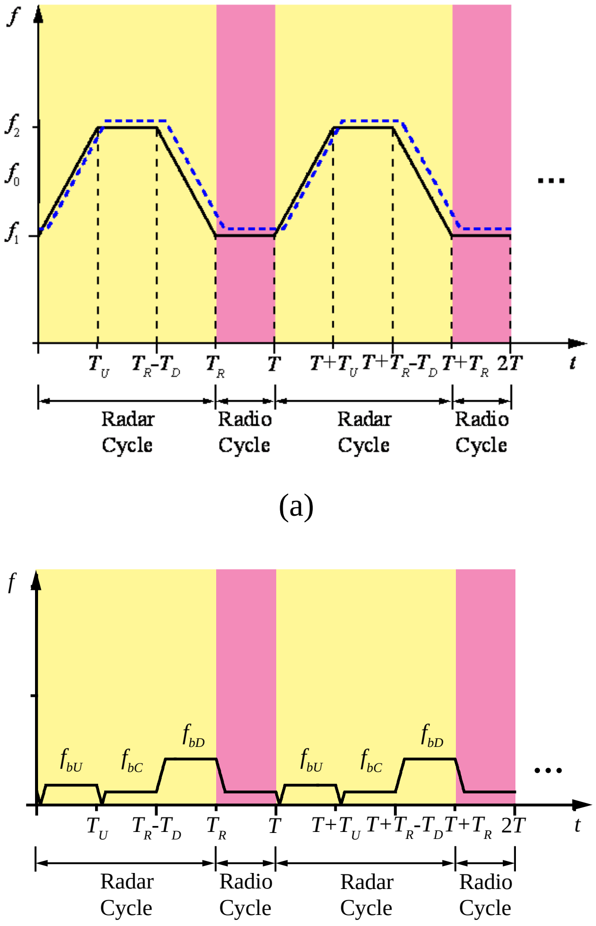

(a)

(b)

Figure 3 (a) Proposed time-agile modulation waveform and (b) beat frequencies at the output of the receiving front-end.

Our proposed modulation waveform has a number of attractive and distinct features as follows.

1) The radar and communication operations are separated in the time domain so that mutual interference is minimized.

2) In a multi-user environment, each onboard unit can be assigned with a specific time slot based on the time division multiple access (TDMA).

3) Either constant-frequency period in one operation cycle can be used for communication mode since the proposed modulation waveform is symmetrical. As a result, the network capacity can be increased by specifying different constant frequencies in different service cells on the basis of frequency division multiple access (FDMA).

4) Our proposed modulation scheme is implemented with the help of a software-defined platform, in which a direct digital synthesizer (DDS) is used to generate the modulated waveform since the amplitude, frequency and phase of the DDS output signal can be easily and accurately controlled through software programming. Moreover, since communication and radar modes in the proposed modulation scheme are arranged in sequential time slots, time-agility or a flexible functional reconfiguration can be easily achieved by adaptively or cognitively adjusting all software-programmable time duration in the modulation waveform according to usage situations.

5) Since radar and communication modes are staggered, there is possibility of joint operation or data fusion between them. For example, targets' velocities and ranges that are obtained in the radar mode can be used in the communication mode to resist multipath fading and compensate the Doppler spread caused by the mobility of the on-board units. On the other hand, by making use of the communication capability, different onboard transceivers can exchange such data as targets' velocities and ranges, and thus, a radar network is formed. The benefits of such data fusion platform are its range increment and accuracy enhancement of the target finding.

A low-frequency system demonstrator has been designed and prototyped over 5.9 GHz band for the U.S. federal communications commission (FCC)'s dedicated short range communication (DSRC) applications. DSRC is a short-to-medium range wireless protocol in the application scenarios of roadside-to-vehicle and vehicle-to-vehicle communications, and this term has also been identified with dedicated ITS spectrum allocations in various regions of the world. For example, this spectrum allocation is in the 5.9-GHz band in the United States and in the 5.8-GHz frequency range in Europe, Japan, and China. On Dec. 17, 2003, the U.S. FCC licensed the 5850-5925 MHz band as an exclusive 75 MHz radio spectrum for DSRC devoted to ITS safety applications [29]. In Europe, on Mar. 15, 2002, the frequency bands of 5795-5805 MHz (two European channels) and 5805-5815 MHz (two "national" channels) were designated for the road transport and traffic telematic (RTTT) systems [30]. In Japan, within the program of Advanced Cruise-Assist Highway Systems Research Association (AHSRA), electronic toll collection has been successfully transitioned to DSRC because of the high reliability, large data transfer, and rapid messaging (to accommodate vehicles at highway speeds) that the protocol supports. In September 2001, ARIB established the standard for DSRC [31]. China released the national standard "Electronic Toll Collection−Dedicated Short Range Communication" in 2007 [32] and it has been deploying a nationwide network.

On the basis of the proposed system specifications derived from FCC's rules and practical requirements of ITS applications, system functionality has been verified through link budget analysis of both radar and radio (communication) mode. Our analysis reveals that there are three major difference between them including signal attenuation, channel bandwidth and output signal-to-noise ratio (energy per bit to noise spectrum density ratio in the radio mode), which are then taken into considerations for designing our transceiver. In the meantime, conventional radio transceiver architectures has been studied and adapted to the proposed modulation waveform.

As two of the most critical building part in the transceiver, upconverter and downconverter are firstly analyzed and optimized using harmonic balance simulation in a commercial simulation package. Then, the entire system is modeled in the same package but with another simulator (Ptolemy) that is able to cosimulate both baseband signal processing circuits and radio-frequency (RF) front-ends. System simulations have been carried out to predict and optimize achievable system performance for both radar and communication functions. Our simulation has shown very good results regarding both radio communication and radar sensing.

This 5.9-GHz system demonstrator is then prototyped with commercial off-the-shelf components that can be easily purchased without any difficulty. After each building blocks of the transceiver was designed, prototyped and validated through experiments, the entire transmitter and receiver are respectively integrated and encased into two housings for electromagnetic compatibility (EMC) and electromagnetic interference (EMI) considerations. A number of experiments are made to evaluate system performance. For the radio mode, measured constellations of binary PSK (BPSK), 8PSK and 16QAM signals present very good system performance for data reception and in the case of 10-Mbps BPSK signals, measured BER has excellent agreement with simulated ones. Moreover, the radar performance is evaluated by configuring a channel emulator with a set of delays from 1500 ns to 5000 ns and a set of velocities from 10 m/s to 80 m/s. Measured values agree very well with predefined values in the channel emulator, which demonstrates excellent capability of target finding of our proposed multifunctional system.

3.2 Development of innovative passive components and modeling of arbitrary-order mutual-coupling

Since both the maximum rate of data communication and the range resolution of radar detection can be enhanced by using a wider frequency range or band, another high-frequency system prototype has been developed in the 24-GHz ISM-band with a bandwidth up to 250 MHz. Conventional RF front-ends at 24 GHz may be designed with metallic waveguide technology which is bulky, heavy and expensive due to high precision machining. With the rapid development of semiconductor process, monolithic microwave integrated circuits (MMICs) have gradually replaced waveguide technology in certain applications due to their compact size, easy integration and low cost. However, the applications of MMICs are still limited since the intrinsic high-*Q* of the waveguide structures are of great demand for such components as filters, duplexers, and couplers. Therefore, a hybrid and monolithic integration of planar MMICs and non-planar waveguide structures presents the best solution for obtaining optimum system performance.

As an response to this design challenge, a possibly revolutionary concept of high-frequency ICs called substrate integrated circuits (SICs) was proposed and has been intensively studied for various kinds of components and front-end subsystems [33]-[56]. In this unique circuit platform of ICs design, the non-planar structures such as classical rectangular waveguides, coaxial lines and various dielectric waveguides can be “synthesized” or “transformed” into planar form so that conventional planar and non-planar structures can be made within single substrate using the same processing technique such as the standard printed circuit board (PCB) process. Such a synthesis or transformation is achieved by using discrete metallic vias and/or air hole arrays to simulate equivalent electrical wall or low/high dielectric index contrast. The synthesized non-planar structures of the SICs typically include substrate integrated (rectangular) waveguide (SIW), substrate integrated non-radiative dielectric (SINRD) guide, and substrate integrated image guide (SIIG), as shown in Figure 4. Generally, the equivalent non-planar structures in planar form are able to preserve a great deal of guided-wave properties of the original counterparts. In addition, electrical, mechanical and thermal properties of both planar and non-planar structures can be made compatible over a very wide frequency range.

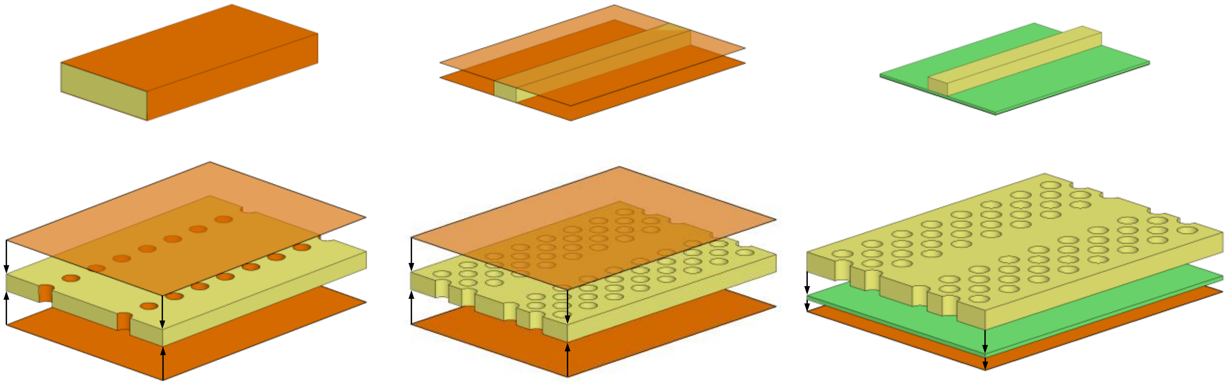

(a) SIW: substrate integrated (rectangular) waveguide

(b) SINRD: substrate integrated nonradiative waveguide

(c) SIIG: substrate integrated image waveguide

Figure 4 Three typical family members of SICs.

The SIW technology presents the optimum solution for our system design and implementation at 24 GHz judging from integration capability and circuit performance in connection with conductor, dielectric and radiation losses. Based on the SIW technology, our high-frequency system was designed and prototyped onto a single substrate by integrating active circuits such as amplifiers, mixers and passive SIW components such as filters and couplers.

In a similar manner, after the proposition of system specifications and analysis of link budget, our transceiver architecture for 24-GHz system is presented and the entire system is subjected to simulation and optimization. A number of innovative SIW structures, especially wideband couplers, broadband phase shifters and highly-selective filters have been synthesized and designed with the help of field-theory-based computer-aided-design (CAD) technique. In addition, an accurate synthesis method has been proposed for four-line interdigitated (Lange) coupler through both theoretical derivation and experimental verification. Based on the proposed method, a composite microstrip-to-CPW interdigitated coupler is developed, which is used as the intermediate frequency (IF) coupler in the 24-GHz system.

Mutual coupling, as a very fundamental and important issue in system development is also investigated during the course of this PhD project. Previous research mainly focuses on the modeling of low-order mutual coupling (adjacent coupling) since it is very difficult to characterize high-order mutual coupling (crosstalk coupling). In order to accurately model mutual coupling of arbitrary order, we have proposed a fundamental strategy, which starts from the modeling of the first-order mutual coupling. The proposed method consists of two main steps. First of all, an equivalent circuit model describing low-order mutual coupling is characterized and established, of which each parametric value is accurately extracted by making use of a numerical calibration technique. Then, the circuit model for high-order mutual coupling is generated from the low-order models, and it can further be used for the modeling of mutual coupling of any higher-orders. The accuracy and efficiency of the proposed method are demonstrated by three different kinds of EM structures including linear and planar array antennas, finite periodic electromagnetic structures and low-pass filters. Our proposed method has proven to be effective and helpful for the analysis and iterative design of microwave circuits and array antennas. By means of this proposed modeling technique, we have designed a pair of 8×8 microstrip array antenna on a thin layer substrate for our 24-GHz system prototype.

3.3 Prototyping and measurement of 24-GHz system

Finally, the entire 24-GHz system has been synthesized onto a single substrate by integrating our designed SIW passive components together with active devices. The fabricated transmitter and receiver prototypes are assembled into two separate housings. A number of comprehensive experiments have been conducted to validate our system performance. In the first place, measured constellations of 50-Mbps BPSK and quadrature PSK (QPSK) signals show very good performance in the case of an input power of −60 dBm. Furthermore, measured results both in the laboratory and in a more practical environment (indoor garage) manifest very good system performance with respect to radar function.

4. Original Contributions

In this thesis, the complete development of iCars for future ITSs is presented in a systematic and top-down manner. Principle scientific contributions lie in not only the novelty of proposed modulation scheme and system concept, but also the design and prototyping of a 5.9-GHz system demonstrator and more importantly a 24-GHz system prototype using the SIW technology. In the development of the 24-GHz system prototype, a number of innovative passive SIW components have been proposed together with detailed synthesis and analysis method. An original idea is put forward for synthesizing four-line interdigitated couplers and it has been proved to be more accurate and flexible than conventional methods. Another important contribution of this thesis is the modeling of arbitrary-order mutual coupling that is ubiquitous in coupled electromagnetic structures and antenna arrays. This modeling technique is based on successive extraction and establishment of equivalent circuit models of mutual coupling from low orders to high orders. Its accuracy and efficiency have been demonstrated by three different kinds of electromagnetic structures including linear and planar array antennas, finite periodic structures and low-pass filters. All in all, this thesis is concerned with almost all design aspects from system-level analysis to component-level design, from electronic circuits to electromagnetic structures, from CAD simulation to experimental verification and from original idea to final prototyping.

5. Thesis Organization

This thesis is organized as follows. In Chapter 1, following a brief introduction of radio communication and radar sensing technologies, some design considerations associated with our multifunctional system will be discussed and our proposed system concept will be presented with rigorous theoretical analysis. Then, in Chapter 2 and Chapter 3, the development of a 5.9-GHz system demonstrator will be given in detail from system design and simulation to system prototyping and measurement. Chapter 4 covers the analysis and simulation for the 24-GHz system prototype while the development of various passive components is given in Chapter 5 including wideband SIW coupler, broadband SIW phase shifter and highly-selective SIW bandpass filters as well as interdigitated couplers. In Chapter 6, our proposed method for modeling arbitrary-order of mutual coupling will be described and the design of a 24-GHz microstrip array antenna will be showcased as one of its application examples. Chapter 7 deals with the prototyping and experiment of the 24-GHz system. Finally, this thesis will be summarized with a concise conclusion and some future perspectives.

CHAPTER 1 DESIGN CONSIDERATIONS AND SYSTEM CONCEPT

In order to make this thesis self-complete and self-contained, the first chapter begins with a brief introduction of basic digital bandpass modulation techniques, and quadrature architecture with respect to signal demodulation is also introduced since it is widely implemented in our system. In addition, the basic operation principles of continuous wave (CW) radar including Doppler radar and FMCW radar will be described. Then, by comparing the similarity and difference of radio communication and radar systems, design considerations of iCars will be addressed with respect to channel models, modulation techniques and bandwidth requirements, duplex mode and digital signal processing (DSP). Our discussion leads to the proposed modulation scheme for time-agile and joint operation of radio communication and radar sensing modes. Following a rigorous theoretical analysis of the modulation scheme, the system concept will be presented at last.

1.1 Basic digital bandpass modulations and quadrature demodulation for radio communications

Radio communications are used for exchanging information through radio waves over a distance. In radio communication systems, a process called digital modulation is very crucial since it transforms digital symbols into waveforms that are compatible with the characteristics of the channel, so that signal transmission becomes more efficient [57]. Digital modulation includes baseband modulation and bandpass modulation. In the baseband modulation, these waveforms are a sequence of shaped pulses, which are made suitable for wired communications. On the other hand, in the bandpass modulation, shown in Figure 1.1, the shaped pulses further modulate a high-frequency sinusoidal signal, which is often called a carrier. The bandpass modulation is essentially shifting the low-frequency spectrum of the shaped pulses to a high carrier frequency. In this way, it brings up a number of advantages for wireless signal transmission. First, high-frequency signals can be radiated effectively by an antenna with reasonable size. Second, high-frequency signals from different sources can share a single channel through frequency-division multiplexing. Third, interference can be minimized through some modulation schemes. Finally, some system operations such as filtering and amplification can be easily performed by properly choosing a carrier frequency.

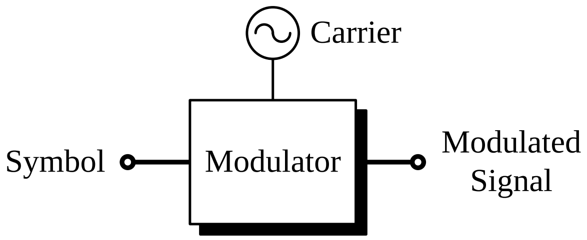

Figure 1.1 A digital bandpass modulator.

Let us denote a sinusoidal signal as,

$$s(t) = A\cos(\omega t + \theta) \tag{1.1}$$

where A, ω, θ are the amplitude, the radian frequency and the phase of the signal, respectively. By varying these three parameters individually, we can obtain three fundamental bandpass modulation techniques: ASK, FSK and PSK.

1.1.1 Amplitude shift keying

The general analytic expression of an ASK signal is

$$s_i(t) = A_i(t)\cos(\omega_c t + \theta_0) \quad i = 1, \ldots, N \tag{1.2}$$

where A_i will have N discrete values while ω_c and θ_0 are constant. Binary ASK is often called on-off keying (OOK), and Figure 1.2(a) shows the digital symbols and the corresponding modulated waveform of an OOK signal. Another common graphical illustration of the modulated waveform in the signal space is called constellation diagram, in which constellation points represent the possible symbols that may be selected by a given modulation scheme. The horizontal (real) and vertical (imaginary) axes represent the in-phase (I) and the quadrature-phase (Q) components of the complex envelope, respectively. An important feature of the constellation diagram is that the receiver can make use of the Euclidean distance between signal points to decide which signal was actually transmitted. Therefore, two signals with a smaller Euclidean distance are more difficult to be distinguished. Figure 1.2(b) gives the constellation diagram of a typical OOK signal having two possible amplitudes.

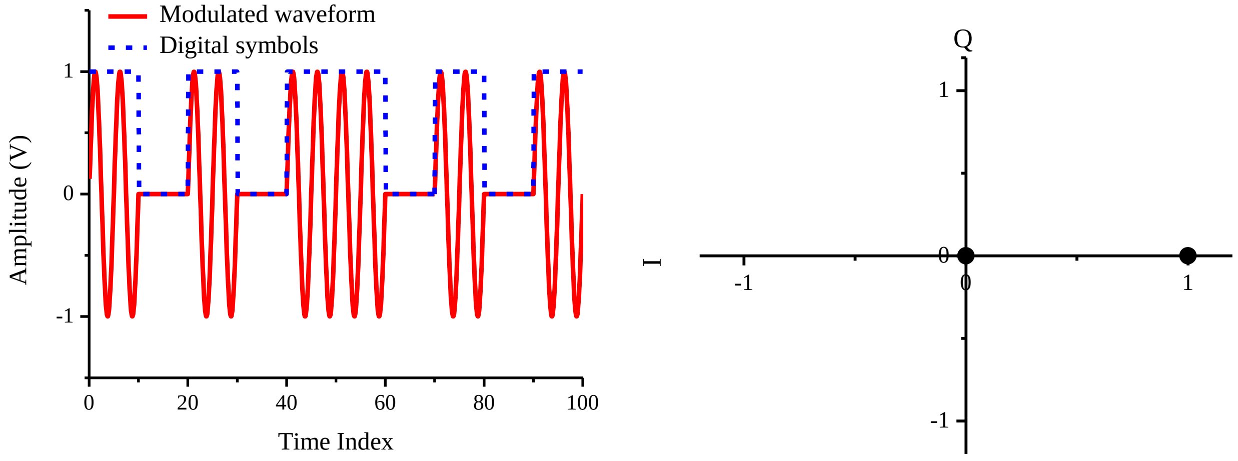

(a) (b)

Figure 1.2 (a) Waveform and (b) constellation diagram of OOK signal.

1.1.2 Frequency shift keying

The general analytic expression of an FSK signal is

$$s_i(t) = A_0 \cos\left(\omega_i(t)t + \theta_0\right) \quad i = 1, \ldots, N \qquad (1.3)$$

where ω_i will have N discrete values while A_0 and θ_0 are constant. Figure 1.3(a) shows the digital symbols and the corresponding modulated waveform of a binary FSK (BFSK) signal. We can see that in the modulated waveform, two different frequencies are selected according to the value of digital symbols. The constellation diagram of BFSK signals is depicted in Figure 1.3(b). In Figure 1.3(b), two constellation points of BFSK signals are located on the real and imaginary axes, respectively, and they are orthogonal to each other, and the Euclidean distance between two BFSK signal points are obviously larger than the OOK signal, which means a low detection error can be achieved under the same condition of signal-to-noise ratio (SNR).

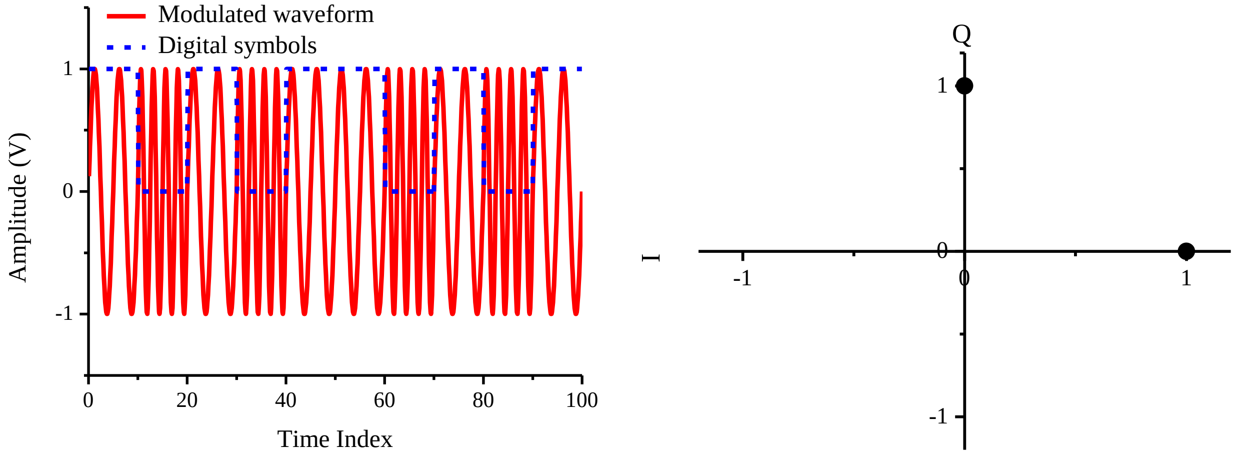

(a) (b)

Figure 1.3 (a) Waveform and (b) constellation diagram of BFSK signal.

1.1.3 Phase shift keying

The general analytic expression of a PSK signal is

$$s_i(t) = A_0 \cos(\omega_c t + \theta_i(t)) \quad i = 1, \ldots, N \tag{1.4}$$

where θ_i will have N discrete values while A_0 and ω_c are constant.

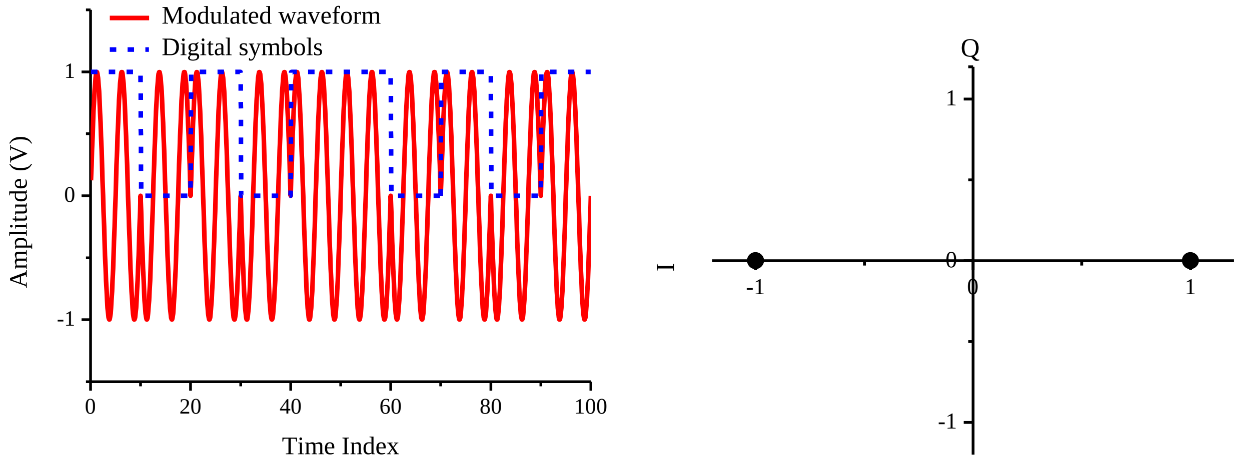

(a) (b)

Figure 1.4 (a) Waveform and (b) constellation diagram of BPSK signal.

Figure 1.4(a) shows the digital symbols and the corresponding modulated waveform of a binary PSK (BPSK) signal. We can see that the modulated waveform adopts two different phase conditions according to the value of digital symbols. From the corresponding constellation diagram shown in Figure 1.4(b), we can observe that the BPSK signal has the largest Euclidean distance for a given signal energy, and therefore, it should have the lowest detection error for a given SNR compared to OOK and BFSK signals.

1.1.4 Quadrature amplitude modulation

Based on the fundamental modulation techniques, high-order modulation schemes can be easily constructed. For example, the ASK and PSK modulations can be combined together to achieve a joint modulation called amplitude-phase keying (APK) by varying both amplitude and phase of a carrier. A subset of APK is quadrature amplitude modulation (QAM), which has a rectangular constellation diagram as shown in Figure 1.5. From another point of view, QAM is essentially a process in which two orthogonal carriers are amplitude modulated and combined together. It should be mentioned that PSK can be regarded as a special case of QAM, where the magnitude of the modulated signal is constant with only phase varying. In Figure 1.5(a), 4QAM is also regarded as quadrature PSK (QPSK). Due to its high transmission efficiency, QAM is extensively used in wireless communications.

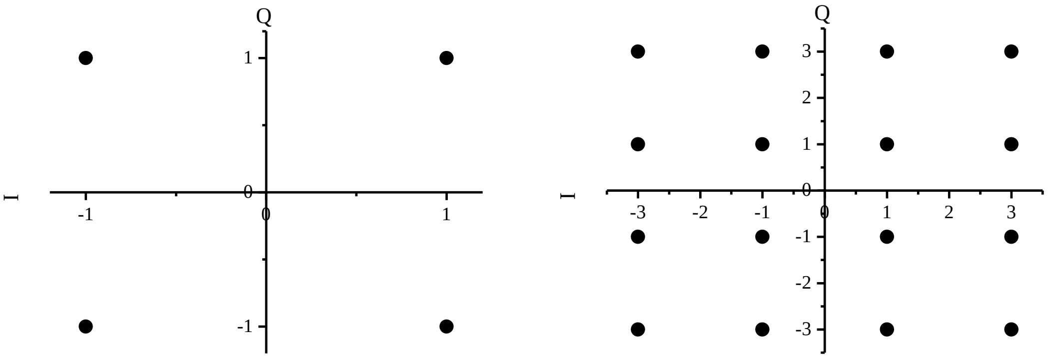

(a)

(b)

Figure 1.5 Constellation diagram of (a) 4QAM (QPSK) signal and (b) 16QAM signal.

1.1.5 Quadrature demodulation

A reverse process of modulation is called demodulation, through which the modulated waveform is transformed back to digital symbols. In the following paragraphs, quadrature demodulation will be briefly described.

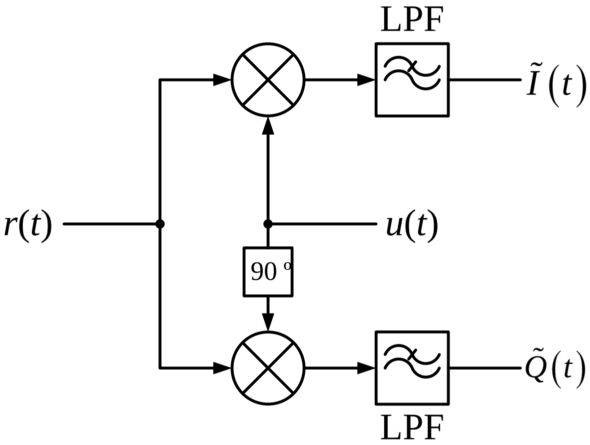

Figure 1.6 Block diagram of an ideal quadrature demodulator.

Suppose the received signal can be expressed as

$$r(t) = \tilde{I}(t)\cos(\omega_c t) + \tilde{Q}(t)\sin(\omega_c t) \tag{1.5}$$

where $\tilde{I}(t)$ and $\tilde{Q}(t)$ are the I and Q components of the received signal with noise. ω_c is the radian frequency of the carrier.

At the receiver, a reference signal $u(t)$ is used to demodulate the received signal and it can be simply denoted as

$$u(t) = \cos(\omega_c t) \tag{1.6}$$

From Figure 1.6, we can derive the complete process of quadrature demodulation for both I-channel (upper branch) and Q-channel (lower branch). In the I-channel, the received signal is mixed with a coherent reference signal, and then the mixing products are filtered by a low-pass filter (LPF), which gives the in-phase component of the received signal. This process can be mathematically represented as follows.

$$\begin{aligned} r(t)\cos(\omega_c t) &= \left[\tilde{I}(t)\cos(\omega_c t)+\tilde{Q}(t)\sin(\omega_c t)\right]\cos(\omega_c t) \\ &= \tilde{I}(t)\frac{1+\cos(2\omega_c t)}{2}+\tilde{Q}(t)\frac{\sin(2\omega_c t)}{2} \\ &\xrightarrow{\text{LPF}} \tilde{I}(t) \end{aligned} \tag{1.7}$$

Similarly, the quadrature component of the received signal can be obtained by mixing the received signal with a coherent reference signal having 90 °phase shift.

$$\begin{aligned} r(t)\sin(\omega_c t) &= \left[\tilde{I}(t)\cos(\omega_c t)+\tilde{Q}(t)\sin(\omega_c t)\right]\sin(\omega_c t) \\ &= \tilde{I}(t)\frac{\sin(2\omega_c t)}{2}+\tilde{Q}(t)\frac{1-\cos(2\omega_c t)}{2} \\ &\xrightarrow{\text{LPF}} \tilde{Q}(t) \end{aligned} \tag{1.8}$$

1.2 Brief introduction to continuous wave radar

Radar is an acronym for **ra**dio **d**etection **a**nd **r**anging. As its name suggests, it is an electronic system which emits electromagnetic energy into space, receives the echo signal from a reflecting object, and by comparing the received signal with the emitted signal, the location of the target can be determined together with other target-related information such as the moving speed and the direction [58]. Basically, radar systems can be categorized as pulse radars and CW radars. Compared to pulse radars, CW radars have a number of advantages such as lower probability of intercept, better detection of short range target[1] and looser requirements of peak power generation. Therefore, it is possible to use solid state devices to design CW radars, which definitely shrink the circuit size and facilitate the manufacture and system assembly. The disadvantages of CW radars are the leakage from the transmitter to the receiver that usually needs a pair of separate antennas and the linearity requirements with respect to the source generation, which can be alleviated by using digital technology such as DDS and phase-locked loop (PLL). Considering the application scenarios, performance requirements and cost considerations, we will focus on CW radars in this project.

---

[1] It should be noted that Doppler radar cannot detect target range, which will be described in the following section.

1.2.1 Doppler radar

Doppler radar is the simplest form of CW radars, and it makes use of the Doppler effect to detect the radial velocity of a target. It is well-known that when a wave is incident onto a moving target, its frequency would be shifted by an amount called Doppler frequency. Figure 1.7 illustrates the operation principle of Doppler radar and Figure 1.8 depicts an example of transmitted and received signals.

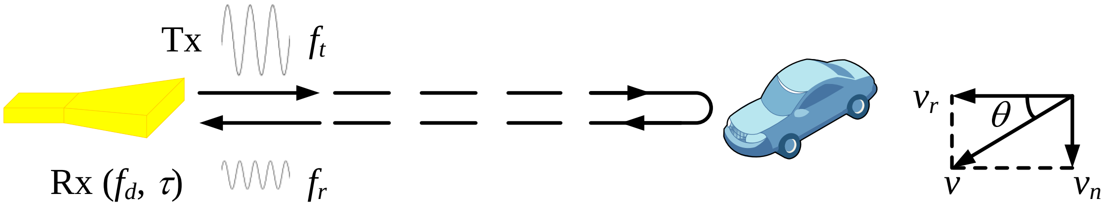

Figure 1.7 Operation principle of the Doppler radar.

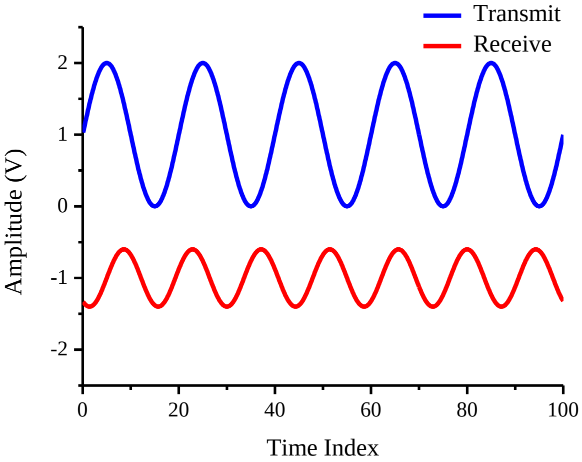

Figure 1.8 Transmitted and received waveforms of a Doppler radar.

Let us denote the transmitted continuous sinusoidal signal as

$$s(t) = A\cos(2\pi f_0 t + \theta_0) \tag{1.9}$$

where A is the amplitude and f_0 is the frequency of the signal. θ_0 is an arbitrary initial phase of the transmitted signal. The reflected signal received by the Doppler radar can be expressed as

$$r(t) = A'\cos(2\pi f_0 (t-\tau) + \theta_0) \tag{1.10}$$

where *A*’ is the attenuated amplitude and τ is the time delay that are determined by the distance *R*(*t*) between the radar and the target.

$$\tau = \frac{2R(t)}{c_0} \tag{1.11}$$

where c_0 is the speed of light. Suppose the target is moving towards the radar unit, the distance *R*(*t*) is related to the radial velocity of the target v_r by

$$R(t) = R_0 - v_r t \tag{1.12}$$

where R_0 is the initial target range at $t = 0$.

Therefore, by substituting (1.11) and (1.12) into (1.10), we can obtain that

$$r(t) = A^{'} \cos\left[2\pi f_0 \left(t - \frac{2(R_0 - v_r t)}{c_0}\right) + \theta_0\right] \tag{1.13}$$

After manipulation, the above expression can be simplified as,

$$r(t) = A^{'} \cos\left[2\pi\left(f_0 + \frac{2v_r}{c_0} f_0\right)t + \theta_0 - \frac{4\pi R_0 f_0}{c_0}\right] \tag{1.14}$$

At the receiver, the received signal is mixed with a reference signal (a duplicate of the transmitted signal). After filtering the high-frequency mixing products, a beat signal can be generated as

$$\begin{aligned} s(t)r(t) &= A\cos(2\pi f_0 t + \theta_0)\, A^{'} \cos\left[2\pi\left(f_0 + \frac{2v_r}{c_0} f_0\right)t + \theta_0 - \frac{4\pi R_0 f_0}{c_0}\right] \\ &\xrightarrow{\text{LPF}} \cos\left(2\pi \frac{2v_r}{c_0} f_0 t - \frac{4\pi R_0 f_0}{c_0}\right) \end{aligned} \tag{1.15}$$

After (1.15), in spite of a constant phase term, the frequency shift caused by the Doppler effect is contained in the beat frequency, and the Doppler frequency is related to the radial velocity of the target by

$$f_d = \frac{2v_r}{c_0} f_0 \tag{1.16}$$

Therefore, the radial velocity of the target can be easily calculated from the estimated Doppler frequency by

$$v_r = \frac{c_0 f_d}{2 f_0} = \frac{\lambda_0 f_d}{2} \tag{1.17}$$

where λ_0 is the wavelength of the transmitted signal.

The resolution of the velocity detection of Doppler radar can be derived in the following way. The velocity resolution is directly determined by the estimation accuracy of the Doppler frequency, which is inversely proportional to the duration of observation time *T*.

$$v_{r,res} = \frac{\lambda_0 f_{d,res}}{2} = \frac{\lambda_0}{2T} \tag{1.18}$$

Therefore, given the frequency of the transmitted signal, the detection resolution of the target velocity is inversely proportional to the duration of the observation time *T*. A longer observation time is helpful to generate velocity detection with a higher resolution.

1.2.2 Discrimination of the sign of the beat frequency

The quadrature demodulator shown in Figure 1.6 can also be used for discriminating the sign of the beat frequency [59]. Let us designate the received signal as

$$r(t) = \cos\left[(\omega_0 \pm \omega_d)t\right]$$

where ω_0 is the radian frequency of the transmitted signal and ω_d is the radian Doppler frequency. A plus sign of ω_d indicates an incoming target while a minus sign indicates a target moving away from the radar unit. Without loss of generality, the amplitude in the above expression is considered as unity and the initial phase is zero. The reference signal in this case is taken as

$$u(t) = \cos(\omega_0 t)$$

As a result, the output of the I-channel of the demodulator is

$$\begin{aligned} r(t)\cos(\omega t) &= \cos\left[(\omega \pm \omega_d)t\right]\cos(\omega t) \\ &= \frac{\cos\left[(2\omega \pm \omega_d)t\right] + \cos(\pm\omega_d t)}{2} \\ &\xrightarrow{\text{LPF}} \cos(\pm\omega_d t) \end{aligned} \tag{1.19}$$

In a similar fashion, the output of the Q-channel of the demodulator is

$$\begin{aligned} r(t)\sin(\omega t) &= \cos\left[(\omega \pm \omega_d)t\right]\sin(\omega t) \\ &= \frac{\sin\left[(2\omega \pm \omega_d)t\right] - \sin(\pm\omega_d t)}{2} \\ &\xrightarrow{\text{LPF}} -\sin(\pm\omega_d t) \\ &= \cos(\pm\omega_d t + \pi/2) \end{aligned} \tag{1.20}$$

Therefore, the sign of the beat frequency can be determined as follows. If $\omega_d > 0$ (an incoming target), the phase of the output at the I-channel lags that of the output of the Q-channel. However, if $\omega_d < 0$ (an outgoing target), the phase of the output at the I-channel leads that of the output of the Q-channel.

1.2.3 Frequency-modulated continuous wave radar

From our previous discussion, we can conclude that Doppler radar can only detect the target velocity since the time delay of radio wave propagation is not known. Nevertheless, if the round-trip time delay is available, the target range can be also detected. FMCW radars overcome this problem by applying frequency modulation onto a continuous wave, which can be used as a timing mark.

Figure 1.9 shows two periods of transmitted and received waveforms of triangular FMCW signal. In one operation cycle, the frequency of the transmitted signal is linearly increased from f_1 to f_2 (upchirp) for the first half of the operation cycle and then linearly swept from f_2 to f_1 (downchirp) for the second half. The corresponding modulation diagram is depicted in Figure 1.10(a).

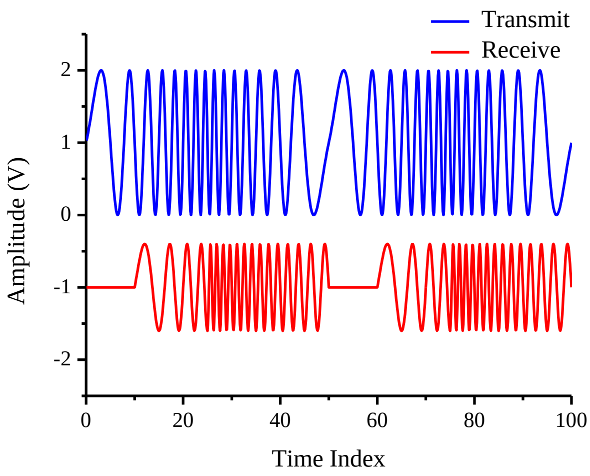

Figure 1.9 Transmitted and received waveforms of triangular FMCW signal.

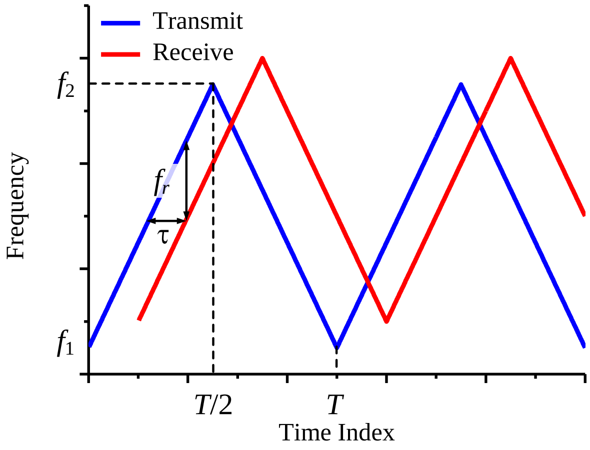

(a)

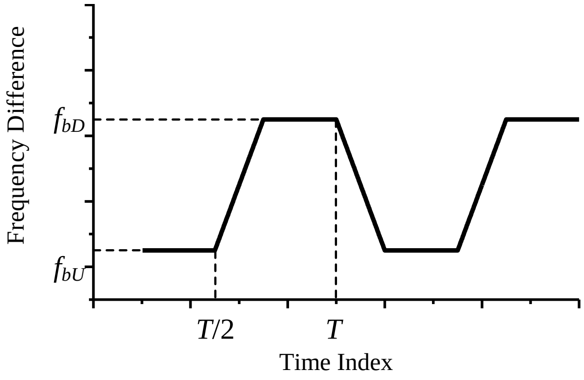

(b)

Figure 1.10 (a) Triangular FMCW signal and (b) the beat frequency.

In Figure 1.10(a), we can find that time delay τ between the transmitted and received signals corresponds to a frequency difference of f_r.

$$f_r = \frac{\Delta B}{T/2}\tau \tag{1.21}$$

where ΔB is the frequency sweeping bandwidth, which equals to $f_2 - f_1$.

From (1.21), we can see that if we can estimate frequency difference f_r from the beat signal, the time delay of radio wave propagation can be obtained by

$$\tau = \frac{f_r}{\Delta B}T/2 \tag{1.22}$$

Consequently, the target distance can be calculated by

$$R = c_0\frac{\tau}{2} = c_0\frac{f_r}{\Delta B}T/4 \tag{1.23}$$

Moreover, the range resolution can be formulated as

$$R_{res} = c_0\frac{f_{r,res}}{\Delta B}T/4 \tag{1.24}$$

Since the resolution of the estimation of beat frequency $f_{r,res}$ is inversely proportional to the duration of observation cycle ($T/2$ in this case), by substituting this relationship into (1.24), we can conclude that the range resolution is independent of the duration of operation cycle, and it is only determined by the sweeping bandwidth ΔB as shown in (1.25).

$$R_{res} = \frac{c_0}{2\Delta B} \tag{1.25}$$

In the case of a moving target, the beat frequency is the combination of range frequency f_r and Doppler frequency f_d. In the upchirp, we can obtain one beat frequency f_{bU} while in the downchirp, we can obtain another beat frequency f_{bD}. These two beat frequencies can be expressed by

$$f_{bU} = f_r - f_d \tag{1.26}$$

$$f_{bD} = f_r + f_d \tag{1.27}$$

Therefore, f_r can be obtained from the average of two beat frequencies and f_d can be found from their difference.

1.3 Design considerations

After a brief introduction of some fundamental modulation techniques used in radio communication and radar systems, some design considerations related to system operations will be discussed in order to reveal the intrinsic differences between these two sorts of radio systems.

1.3.1 Channel model

Channel is the medium over which electromagnetic (radio) wave propagates, and it essentially plays a very crucial role in designing radio communications and radar sensing systems.

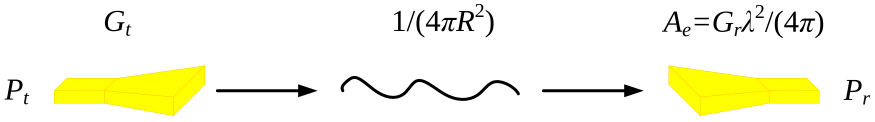

Figure 1.11 Wave propagation for radio communications.

Figure 1.11 describes the wave propagation in the free space for radio communications. The relationship between the transmitted power and the received power is governed by the Friis equation, which in the simplest form can be expressed as

$$P_r = \frac{P_t G_t}{4\pi R^2}\frac{G_r \lambda^2}{4\pi} \tag{1.28}$$

where P_t is the output power of the radio transmitter, P_r is the received power, λ is the wavelength of the carrier, R is the communication range, G_t and G_r are the gains of the transmitting and receiving antennas, respectively. Therefore, the attenuation of the radio wave A_{radio} over a distance of R can be found as

$$A_{radio} = \sqrt{\frac{P_r}{P_t}} = \sqrt{G_t G_r}\,\frac{\lambda}{4\pi R} \tag{1.29}$$

Under the condition of an additive white Gaussian noise (AWGN) channel, the channel impulse response for the radio signal is simply a Dirac's delta function, of which only two parameters namely attenuation and delay are derived by the communication range. Let us suppose the complex envelope of the transmitted signal is $s(t)e^{j2\pi fct}$, the received radio signal can be represented by

$$r_{radio}(t) = \mathrm{Re}\left\{A_{radio}s\left(t-\tau_{radio}\right)e^{j2\pi f_c\left(t-\tau_{radio}\right)}\right\} + n(t) \tag{1.30}$$

where A_{radio} is the amplitude attenuation defined by (1.29) and τ_{radio} is the time delay of the radio channel response. $n(t)$ is the noise process introduced by the radio channel.

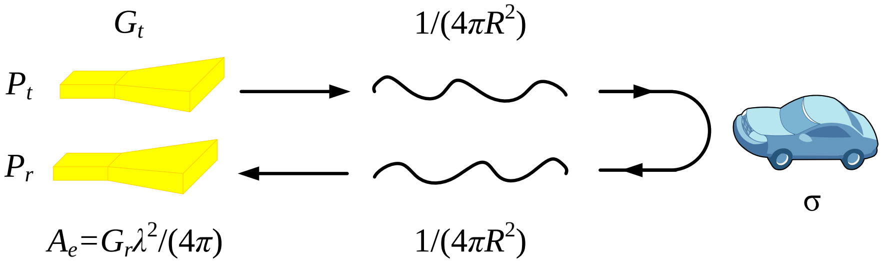

Figure 1.12 Wave propagation for radar sensing.

When it comes to the radar operation shown in Figure 1.12, the radio wave experiences a round-trip propagation. In this case, the relationship between the transmitted signal and the received signal can be described by the radar equation given below.

$$P_r = \frac{P_t G_t}{4\pi R^2}\frac{\sigma}{4\pi R^2}\frac{G_r\lambda^2}{4\pi} \tag{1.31}$$

where P_t is the output power of the radar transmitter, P_r is the received power, λ is the wavelength of the carrier, R is the detecting range, σ is the radar cross section (RCS) of the target, G_t and G_r are the gains of the transmitting and receiving antennas, respectively. The resulting attenuation ratio A_{radar} can be obtained as

$$A_{radar}=\sqrt{\frac{P_r}{P_t}}=\sqrt{G_tG_r}\,\frac{\lambda}{4\pi R}\sqrt{\frac{\sigma}{4\pi R^2}} \tag{1.32}$$

Compared with (1.29), the attenuation of radar signals shown in (1.32) is much higher in spite of a RCS gain. Furthermore, the complex envelope of the radar signals can be described by the following expression,

$$r_{radar}\left(t\right)=\mathrm{Re}\left\{A_{radar}e^{-j2\pi f_d t}s\left(t-\tau_{radar}\right)e^{j2\pi f_c\left(t-\tau_{radar}\right)}\right\}+n\left(t\right) \tag{1.33}$$

where A_{radar} is the amplitude attenuation and τ_{radar} is the time delay of the radar channel response. $n(t)$ is the noise process introduced by the radar channel. From (1.33), it can be found that in addition to an amplitude attenuation and a time delay, the frequency of the transmitted signal is shifted by f_d due to the Doppler effect involved in the process.

Based on (1.30) and (1.33), we can come to the following conclusion for system operation in free space: the major difference of channel models for radio communications and radar sensing is that radar signal has much higher attenuation than radio signal, and it has Doppler frequency shift in the case of a moving target.

1.3.2 Modulation scheme and bandwidth requirements

Numerous bandpass modulation schemes such as ASK, FSK, PSK and QAM are widely used in radio communications. Through bandpass modulation, the spectrum of baseband signals is shifted to the carrier frequency and the channel bandwidth of radio communications is determined by the required data rate and the adopted modulation scheme. Generally, high-order modulation techniques have high spectral efficiency that is defined by the maximum data rate over the given bandwidth, but high-order modulation also increases the complexity of design and implementation. Therefore, there is a trade-off between efficiency and complexity.

On the other hand, frequency modulation is used to enable CW radars to detect target range. The range resolution of FMCW radars is inversely proportional to the sweeping bandwidth. Therefore, in order to achieve high range resolution, a large bandwidth is required for frequency sweeping. However, the channel bandwidth of FMCW radars is determined by the beat frequency, which is much smaller than the sweeping bandwidth.

In conclusion, radio communication and radar sensing propose different requirements on the system bandwidth, which is also an important aspect for designing our hybrid system.

1.3.3 Duplex mode

Radio communications can operate in different modes, such as simplex, half-duplex and full-duplex. Full-duplex can be further subdivided into time-division duplex (TDD) and frequency-division duplex (FDD). In a strict sense, TDD emulates a full-duplex communication over a half-duplex communication link. On the other hand, in FMCW radar systems, the transmitted signal and the received signal are almost located in the same spectrum since the beat frequency is very small. Therefore, FDD communication is not feasible for radio transceivers with CW radar functions in the same platform and TDD mode has to be adopted for the communication mode in our system.

1.3.4 Digital signal processing

The demodulated baseband communication signals or beat frequencies in the radar are processed using different algorithms due to their different functional requirements. In FMCW radars, beat frequencies are usually estimated through fast Fourier transform (FFT) while in radio communication systems transmitted data are recovered using certain sorts of demodulation and detection methods corresponding to the adopted modulation technique. The functional reconfiguration between radio communications and radar sensing proposes the utility of a software-defined platform for implementing different DSP algorithm modules in our system.

1.4 Proposed modulation scheme

Based on our literature review, communication and radar signals can be separated in the frequency domain [6], code domain [7]-[14], or time domain [25]-[27] and the most practical and simplest way to minimize their interference is to allocate them sequentially in the time domain. Figure 1.13(a) shows two operation cycles of our proposed time-agile modulation scheme [58]. In Figure 1.13(a), black solid line represents the transmitted signal while blue dashed line stands for the received signal. The beat frequencies obtained at the output of the receiving front-end is depicted in Figure 1.13(b).

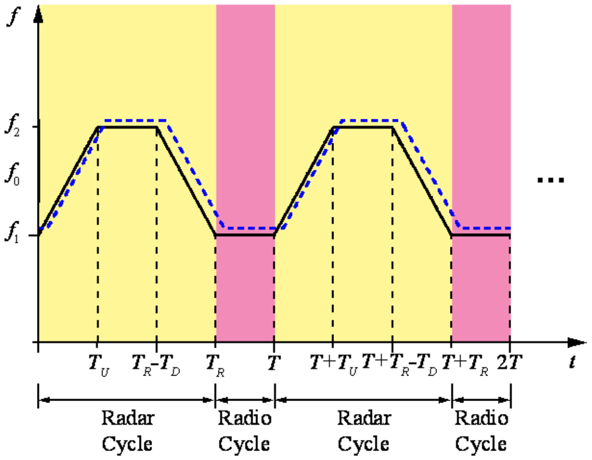

(a) Transmitted and received signals.

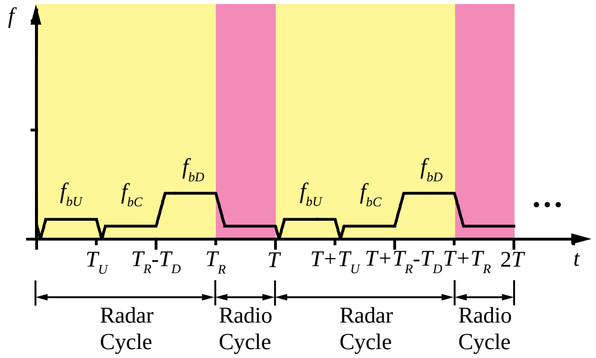

(b) beat frequencies.

Figure 1.13 Time-agile modulation waveform.

In Figure 1.13(a), each operation cycle of T is divided into two time slots which are dedicated to the radar mode (in canary) and the radio (or communication) mode (in magenta), respectively. The radar cycle has a time interval of totally T_R, including an upchirp of T_U, a constant-frequency period of $T_R - T_U - T_D$ and a downchirp of T_D. In the upchirp, the frequency is linearly swept from f_1 to f_2 while it is linearly decreased from f_2 to f_1 in the downchirp. Immediately following the radar cycle, the radio cycle is located in another constant-frequency period, whose duration T_c is equivalent to $T-T_R$. In fact, all possible time durations may be adaptively or cognitively deployed according to application scenarios.

As shown in Figure 1.13(b), in the radar mode, one beat frequency can be obtained in each period, which is further denoted respectively as f_{bU}, f_{bC}, and f_{bD}. A quadrature demodulator is implemented in our system to determine the sign of the beat frequencies [58] as described in Section 1.2.2.

1.4.1 Phase continuity condition

The frequency of the periodic modulated waveform can be expressed as

$$f(t)=\begin{cases} f_1+K_U\left(t-nT\right) & nT\le t\le nT+T_U \\ f_2 & nT+T_U\le t\le nT+T_R-T_D \\ f_2-K_D\left[\left(t-nT\right)-\left(T_R-T_D\right)\right]=f_1+K_D\left[T_R-\left(t-nT\right)\right] & nT+T_R-T_D\le t\le nT+T_R \\ f_1 & nT+T_R\le t\le nT+T \end{cases} \tag{1.34}$$

where f_1 and f_2 are the start and the stop frequencies of the sweeping, and K_U and K_D are the chirp rates of the upchirp and downchirp, respectively. n is an integer for considering the periodicity of the waveform.

By integrating the frequency over time, it is easy to find the phase of the modulated waveform as follows.

$$\varphi(t)=\begin{cases} 2\pi\left[f_1\left(t-nT\right)+K_U\left(t-nT\right)^2/2\right]+\varphi_0 & nT\le t\le nT+T_U \\ 2\pi f_2\left(t-nT-T_U\right)+\varphi_1 & nT+T_U\le t\le nT+T_R-T_D \\ 2\pi\left[f_2\left(t-nT-\left(T_R-T_D\right)\right)-K_D\left(t-nT-\left(T_R-T_D\right)\right)^2/2\right]+\varphi_2 & nT+T_R-T_D\le t\le nT+T_R \\ 2\pi f_1\left(t-nT-T_R\right)+\varphi_3 & nT+T_R\le t\le nT+T \end{cases} \tag{1.35}$$

where φ_0 is the initial phase and is set to zero for simplicity, φ_1 and φ_2 are the phase difference at the transition between different time periods (such as $t = nT+T_U$, $t = nT+T_R-T_D$, and $t = nT+T_R$) in order to keep the phase constant for minimizing the occupied spectrum. Their expressions are given below,

$$\begin{cases} \varphi_1 = 2\pi\left(f_1 T_U + K_U T_U^2/2\right) \\ \varphi_2 = 2\pi f_2\left(T_R - T_D - T_U\right) + \varphi_1 = 2\pi\left[-K_U T_U^2/2 + f_2\left(T_R - T_D\right)\right] \\ \varphi_3 = 2\pi\left[f_2 T_D - K_D T_D^2/2\right] + \varphi_2 = 2\pi\left(f_2 T_R - K_U T_U^2/2 - K_D T_D^2/2\right) \end{cases} \tag{1.36}$$

In addition, since the modulated waveform is periodic, it is necessary to also consider phase discontinuity (suppose no modulation) at such instant time as $t = nT$.

$$2\pi\left[f_1 T + K_U T^2/2\right] = 2\pi f_1\left(T - T_R\right) + \varphi_3 + 2m\pi + \varphi_4 \tag{1.37}$$

where φ_4 is the phase difference at $t = nT$ and m is an arbitrary integer.

After manipulation, φ_4 is found as,

$$\varphi_4 = 2\pi\left[\Delta B\left(T^2/2T_U - T_R + T_U/2 + T_D/2\right) - m\right] \tag{1.38}$$

Let us consider a simple case. If the upchirp, the constant-frequency period and the downchirp have the same time intervals ($T_U = T_D = T_R/3 = T/4 = T_s$), the phase continuity at $t = nT$ requires that,

$$m = 6\Delta B T_S \tag{1.39}$$

(1.39) imposes a restriction that the product of the sweeping bandwidth ΔB and the time duration T_S must be an integer in order to make the phase of the modulated signal continuous in consecutive operation cycles. Figure 1.14 compares the spectrum of modulated waveform for different conditions of phase continuity. It is obvious that the spectrum of a modulated waveform with continuous phase has the smallest bandwidth while a large phase discontinuity increases the occupied bandwidth.

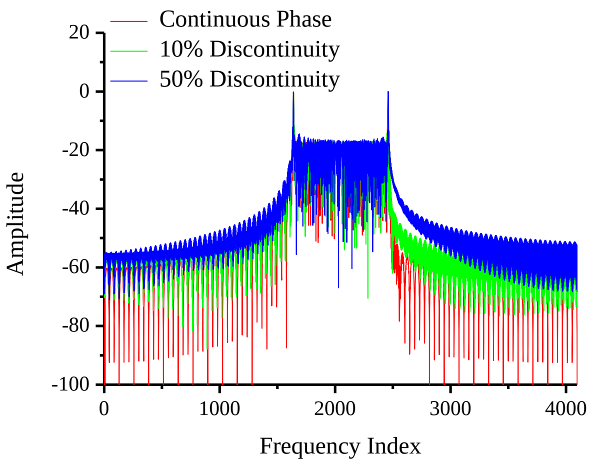

Figure 1.14 Spectrum of modulated waveform for different conditions of phase continuity.

1.4.2 Operation of the radar mode

Assume the transmitted signal $s(t)$ can be represented by a simple expression.

$$s(t) = \cos(\varphi(t)) \tag{1.40}$$

then the reflected signal from the target $r(t)$ is

$$r(t) = A\cos(\varphi(t-\tau)) \tag{1.41}$$

where A represents the amplitude attenuation of the transmitted signal and τ is the time delay. Since A is only a multiplicative term in the following derivation, we will omit it for simplicity. For the same reason, the phase jump due to the reflection at the target is set to zero. A duplicate of the transmitted signal is used as a reference signal, which mixes with the reflected signal in the quadrature demodulator. Let us consider the beat signal in the I-channel after removing the high-order mixing products by the LPF.

$$b_I(t) = \cos(\varphi(t) - \varphi(t-\tau)) \tag{1.42}$$

The expression of the beat signal will be derived for each period of the radar cycle.

1) Upchirp ($t \in [nT, nT + T_U]$)

The phase difference $\Delta\varphi$ between the transmitted and the received signals can be found as

$$\begin{aligned}\Delta\varphi(t) &= \varphi(t) - \varphi(t-\tau) \\ &= 2\pi\left[f_1\tau + K_U\left(t - nT\right)\tau - K_U\tau^2/2\right]\end{aligned} \tag{1.43}$$

In the case of an outgoing target, τ is related to t as,

$$\tau = \frac{2\left(R_0 + vt\right)}{c_0} \tag{1.44}$$

where R_0 is the initial distance between the transmitter and the target, and c_0 is the speed of light.

We substitute τ into (1.43), and after manipulation, we can obtain the following expression.

$$\Delta\varphi(t) = 2\pi\left[f_1\frac{2\left(R_0 + vt\right)}{c_0} + K_U\left(t - nT\right)\frac{2\left(R_0 + vt\right)}{c_0} - K_U\left(\frac{2\left(R_0 + vt\right)}{c_0}\right)^2 \Big/ 2\right] \tag{1.45}$$

Bear in mind that our observation time slot is between [0, T_U], we have to change the variable from t to t' in the above expression, where t' varies in the range of [0, T_U]. After applying $t' = t - nT$, we can obtain,

$$\Delta\varphi\left(t' + nT\right) = 2\pi\left\{ f_1\tau_{nU} - \frac{K_U}{2}\tau_{nU}^2 + \left[f_1\frac{2v}{c_0} + K_U\tau_{nU}\left(1 - \frac{2v}{c_0}\right)\right]t' + K_U\left[\frac{2v}{c_0} - \frac{1}{2}\left(\frac{2v}{c_0}\right)^2\right]t'^2\right\} \tag{1.46}$$

where $R_{nU} = R_0 + vnT$ is the initial distance between the transmitter and the target at time $t = nT$, and $\tau_{nU} = 2R_{nU}/c_0$ is the time delay if the target is stationery.

From (1.46), we can find out that the beat signal is also a linear frequency modulated signal, of which the initial frequency is $f_{bU} = f_1 2v/c_0 + K_U\tau_{nU}(1-2v/c_0)$ and the chirp rate is $2K_U[2v/c_0 - (2v/c_0)^2/2]$. In addition, there is constant phase θ_0 equivalent to $\theta_0 = f_1\tau_{nU} - K_U\tau_{nU}^2/2$.

Since the target velocity is much smaller than the speed of light, f_{bU} can be approximated as,

$$f_{bU} = f_1 2v/c_0 + K_U\tau_{nU} = f_{vU} + f_{rU} \tag{1.47}$$

From (1.47), we can see that f_{bU} contains two components, one is related to the target velocity f_{vU}, and the other is related to the target range f_{rU}. However, it is not possible to differentiate between f_{vU} and f_{rU}, and this is the problem of velocity-range coupling in conventional linear FMCW radars.

2) Constant-frequency period ($t \in \left[nT + T_U, nT + T_R - T_D \right]$)

The phase difference $\Delta\varphi$ can be found as

$$\Delta\varphi(t) = 2\pi f_2 \frac{2(R_0 + vt)}{c_0} \tag{1.48}$$

Similarly, by applying transformation $t' = t - nT - T_U$, we can obtain that,

$$\Delta\varphi(t' + nT + T_U) = 2\pi f_2 \tau_{nC} + 2\pi f_2 \frac{2v}{c_0} t' \tag{1.49}$$

where R_{nC} is the initial target range at time $t = nT + T_U$, and it equals $R_{nC} = R_0 + v(nT_R + T_U)$, and $\tau_{nC} = 2R_{nC}/c_0$ is the time delay for a stationary target. The beat frequency in this time interval is $f_{bC} = f_2 2v/c_0$.

3) Downchirp ($t \in \left[nT + T_R - T_D, nT + T_R \right]$)

The phase difference $\Delta\varphi$ can be found as

$$\Delta\varphi(t) = 2\pi \left\{ f_2 \frac{2(R_0 + vt)}{c_0} - K_D \left(t - nT - (T_R - T_D) \right) \frac{2(R_0 + vt)}{c_0} + K_D \frac{2(R_0 + vt)^2}{c_0^2} \right\} \tag{1.50}$$

In the same manner, by applying transformation $t' = t - nT - (T_R - T_D)$, we can obtain that,

$$\Delta\varphi(t' + nT + T_R - T_D) = 2\pi \left[f_2 \tau_{nD} + K_D \frac{\tau_{nD}^2}{2} + \left(f_2 \frac{2v}{c_0} - K_D \tau_{nD} \left(1 - \frac{2v}{c_0} \right) \right) t' + K_D \left(-\frac{2v}{c_0} + \frac{1}{2} \left(\frac{2v}{c_0} \right)^2 \right) t'^2 \right] \tag{1.51}$$

where $R_{nD} = R_0 + v[nT + (T_R - T_D)]$ is the initial distance between the transmitter and the target at time $t = nT + (T_R - T_D)$, and $\tau_{nD} = 2R_{nD}/c_0$ is the time delay if the target is stationary.

Similar to the upchirp, the beat signal in the downchirp is also a linear frequency modulated signal, of which the initial frequency is $f_{bD} = f_2 2v/c_0 - K_D \tau_{nD}(1 - 2v/c_0)$, the chirp rate is $2K_D[-2v/c_0 + (2v/c_0)^2/2]$, and constant phase θ_0 which equals $\theta_0 = f_2 \tau_{nD} - K_D \tau_{nD}^2/2$.

Since the target velocity is much smaller than the speed of light, we can approximate f_{bD} to be,

$$f_{bD} = f_2\, 2v/c_0 - K_D \tau_{nD} = f_{vD} - f_{rD} \tag{1.52}$$

From the above expression, we can see that f_{bD} contains two components, one is related to target velocity f_{vD}, and the other is related to target range f_{rD}.

In summary, we have obtained one beat frequency in each period of the entire radar cycle for a single target,

$$\begin{cases} f_{bU} = f_{vU} + f_{rU} = f_1\, 2v/c_0 + K_U\, 2R_{nU}/c_0 \\ f_{bC} = f_{vC} = f_2\, 2v/c_0 \\ f_{bD} = f_{vD} - f_{rD} = f_2\, 2v/c_0 - K_D\, 2R_{nD}/c_0 \end{cases} \tag{1.53}$$

where f_{vi} ($i = U, C,$ and D) are the beat frequencies related to target velocity v while f_{rj} ($j = U$ and D) are the beat frequencies related to initial target range R_{nj} ($j = U$ and D) at the beginning of the upchirp and the downchirp, respectively. K_U and K_D are the upchirp rate and the downchirp rate, respectively.

Based on the assumption that the target velocity remains unchanged during the entire radar cycle, the calculation of target range and velocity can be summarized as follows.

(1) Estimate the beat frequency in the upchirp;

(2) Estimate the beat frequency in the constant-frequency period and calculate the target velocity v;

(3) Substitute the calculated target velocity into the estimated beat frequency in the upchirp, and calculate the initial target range R_{nU} at the beginning of the upchirp;

(4) Estimate the beat frequency in the downchirp and calculate the initial target range R_{nD} at the beginning of the downchirp with the calculated target velocity from the constant-frequency period.

In a multi-target environment, the total radar cycle can be used to determine the real targets and eliminate the ghost targets [60]. In order to enhance the resolving capability in a low-mobility environment, the chirp rate can also be made variable in a number of consecutive operation cycles [61].

1.4.3 Operation of the radio mode

In the radio mode, the output frequency of the modulated signal is kept constant over the entire radio cycle, and therefore the transmitted signal is actually a constant carrier which can be modulated by information data using modulation techniques such as ASK, FSK, PSK, or even a number of combinations among them.

1.4.4 System synchronization

The system clocks of different onboard transceivers in a network environment can be synchronized either by the timing information of global positioning system (GPS), or by other techniques such as network time protocol [62]. Detailed study and analysis is out of the scope of this thesis. Therefore, we assume that after the synchronization, these transceivers will have the same time reference. Note that in the proposed system, all the transceivers in the same service cell make use of the same carrier frequency for data communication, while either constant-frequency period can be used for data communication for different service cells.

In the radio cycle, each onboard unit works in a TDD mode, which means it cannot transmit and receive data simultaneously. Let us take now two onboard units for example. If unit 1 transmits data to unit 2, the instant output sweeping signal on unit 2 is unmodulated and it is then used as a reference signal for demodulating the received signal from unit 1. In a multi-user environment, time division multiple access (TDMA) can be applied by assigning a specific time slot to each onboard unit.

1.4.5 Summary

Based on our discussions, the proposed modulation scheme has the following attractive features.

1) The radar and communication operations are separated in the time domain so that mutual interference is minimized and the same spectrum can be reutilized.

2) The frequency is continuously swept between f_1 and f_2, and therefore, the spectrum of the modulated waveform is constrained with minimum out-of-band spectral growth. Phase

continuity can also be considered by a proper choice of sweeping bandwidth and time duration of an operation cycle.

3) Either constant-frequency period in one operation cycle can be used for communication mode since the proposed modulation waveform is symmetrical. As a result, the network capacity can be increased by specifying f_1 and f_2 in different service cells on the basis of frequency division multiple access (FDMA).

4) Time-agility or a flexible functional reconfiguration can be easily achieved by adaptively or cognitively adjusting all time duration in the modulation waveform through software programming according to usage situations.

5) Since radar and communication modes are staggered, there is possibility of joint operation or data fusion between them. For example, targets' velocities and ranges that are obtained in the radar mode can be used in the communication mode to resist multipath fading and compensate the Doppler spread caused by the mobility of the on-board units. On the other hand, by making use of the communication capability, different onboard transceivers can exchange such data as targets' velocities and ranges, and thus, a radar network is formed. The benefits of such data fusion platform are its range increment and accuracy enhancement of the target finding.

1.5 Conclusion

This chapter briefly introduces several basic digital bandpass modulation techniques and the operation principle of continuous wave radar. Following a comparison between the radio communication and radar systems, a novel kind of modulation scheme possessing a number of distinct features has been proposed together with our system concept.

CHAPTER 2 A LOW-FREQUENCY SYSTEM DEMONSTRATOR: DESIGN, SIMULATION AND VALIDATION

To prove the proposed modulation scheme and system concept, an experimental system prototype has been designed and demonstrated in the 5.9-GHz band that has been assigned for DSRC applications by the U.S. FCC. This chapter starts with a brief review of the FCC's DSRC standard, based on which together with practical requirements of ITS applications we propose our system specifications. In order to guarantee proper system functionality, a link budget analysis is performed for both radar and radio (communication) modes, and the analysis results prompt the proposition of our transceiver architecture. Then, our system performance is analyzed with the help of a commercial circuit simulation package and simulation results show very good system performance for both radio communication and radar sensing.

2.1 System analysis

2.1.1 Brief review of the FCC's DSRC protocol

On Dec. 17, 2003, FCC licensed a frequency range from 5.85 GHz to 5.925 GHz with an exclusive bandwidth of 75 MHz for DSRC-based ITS applications [29]. According to the FCC's DSRC ruling, the total 75-MHz spectrum is divided into eight channels, which are composed of one 5 MHz channel and seven 10 MHz channels including one control channel and six service channels. This channel allocation scheme is listed in Table 2.1.

Table 2.1 Channel allocation for DSRC.

		CH175			CH181		
Reserved	CH172	CH174	CH176	CH178	CH180	CH182	CH184
	Service (Vehicle-to-Vehicle)	Service	Service	Control	Service	Service	Service (High Power)
5 MHz	10 MHz	10 MHz	10 MHz	10 MHz	10 MHz	10 MHz	10 MHz

5850 5855 5865 5875 5885 5895 5905 5915 5925 MHz

In the DSRC band, the 5-MHz channel is reserved for harmonization with potential extension of unlicensed national information infrastructure band. The service channels CH172 is dedicated to public safety and private vehicle-to-vehicle communications while CH184 is dedicated for public safety and “high-power, long range” communications of up to 1000 meters and private uses when authorized by a frequency coordinator. However, private applications must not interfere with, and must accept interference from existing public safety applications when transmitting on CH184. Four 10-MHz service channels namely CH174/176 and CH180/182 can be aggregated to provide up to two 20-MHz service channels named CH175 and CH181, respectively, for increasing the possible maximum data rate. In addition, CH178 is dedicated for the control channel.

DSRC devices, which can be used for equipment-type certification for roadside units and onboard units, are categorized into four classes based on the maximum output power. Table 2.2 gives a summary of these four classes of devices.

Table 2.2 Four classes of DSRC devices.

Device Class	Maximum Output Power
A	0 dBm
B	10 dBm
C	20 dBm
D	28.8 dBm

Moreover, based on the effective isotropic radiated power (EIRP), four installation classes are defined, which are summarized in Table 2.3.

Table 2.3 Four installation classes.

Class	Maximum EIRP	Maximum Transmission Range
1	10 dBm	<15 meters
2	20 dBm	<100 meters
3	33 dBm	<400 meters
4	44.8 dBm	<1000 meters

2.1.2 System specifications and link budget analysis

Based on the FCC's rules and practical requirements of automotive detection, a series of system specifications listed in Table 2.4 is defined for our proposed multifunctional system.

In order to prove proper system functionality, a link budget analysis is carried out for both radar and radio functions, respectively. The analysis results are listed in Table 2.5 for reference. Note that in Table 2.5, certain system parameters such as transmitting power and gains of both transmitting and receiving antennas as well as noise figure of the receiver, are set to be the same for both radar and radio modes because the same transceiver is used.

From Table 2.5, the following observations can be obtained. First of all, despite the presence of a RCS gain of the target, the path loss of the radar mode is much larger than the radio mode due to the round-trip signal propagation. Therefore, the receiver should be able to compensate the amplitude fluctuation of the incoming signal with a wide range of gain control. Second, since the beat frequencies of the radar mode are much lower than the radio channel bandwidth, tunable low-pass filters are required for achieving optimal performance. Third, the required signal-to-noise ratio (energy per bit to noise spectrum density (E_b/N_0) ratio in the radio mode) is different for radar and radio functions. The total system link margin is 6.8 dB for the radar mode and 41.5 dB for the radio mode. These link margins include potential implementation loss and atmospheric loss as well as fading loss that is more pronounced in the case of a radio mode operation.

Table 2.4 Specifications of 5.9-GHz system demonstrator.

Mode	Specifications	Values
	Frequency Range	5850 to 5925 MHz
	Maximum Channel Bandwidth	20 MHz
Radar	Maximum Detectable Range	300 m
	Range Resolution	7.5 m
	Maximum Detectable Velocity	±250 km/h (64.44 m/s)
	Velocity Resolution	±10 km/h (2.78 m/s)
	Probability of False Alarm	1e-6
	Probability of Detection	0.9
Radio	Maximum Communication Range	1000 m
	Maximum Data Rate	10 Mbps
	Bit Error Rate for BPSK	1e-6

Table 2.5 Link budget analysis for 5.9-GHz system demonstrator.

Parameters	Radar Mode	Radio Mode
Function Range	300 m	1000 m
Total Cycle	60 ms	20 ms
Receiver Bandwidth	100 KHz	20 MHz
Transmitting Power	28.8 dBm	28.8 dBm
Transmitting Antenna Gain	16 dBi	16 dBi
Path Loss	194.8 dB	107.8 dB
Radar Cross Section Gain of a Car	36.8 dB	—
Receiving Antenna Gain	16 dBi	16 dBi
Signal Power at the Receiver Input	–97.2 dBm	–47.0 dBm
Noise Power at the Receiver Input	–124.0 dBm	–101.0 dBm
SNR at the Receiver Input	26.8 dB	54.0 dB
Receiver Noise Figure	5 dB	5 dB
SNR at the Receiver Output	21.8 dB	49.0 dB
Data Rate	—	10 Mbps
E_b/N_0	—	52.0 dB
Required SNR (E_b/N_0 for radio mode)	15 dB	10.5 dB
Link Margin	6.8 dB	41.5 dB

2.1.3 Transceiver architecture

Figure 2.1 shows the heterodyne transceiver architecture of the proposed radar-radio data fusion system. A pair of transmitting and receiving array antennas was designed on the basis of a microstrip technology in order to increase the isolation between the transmitting and receiving channels.

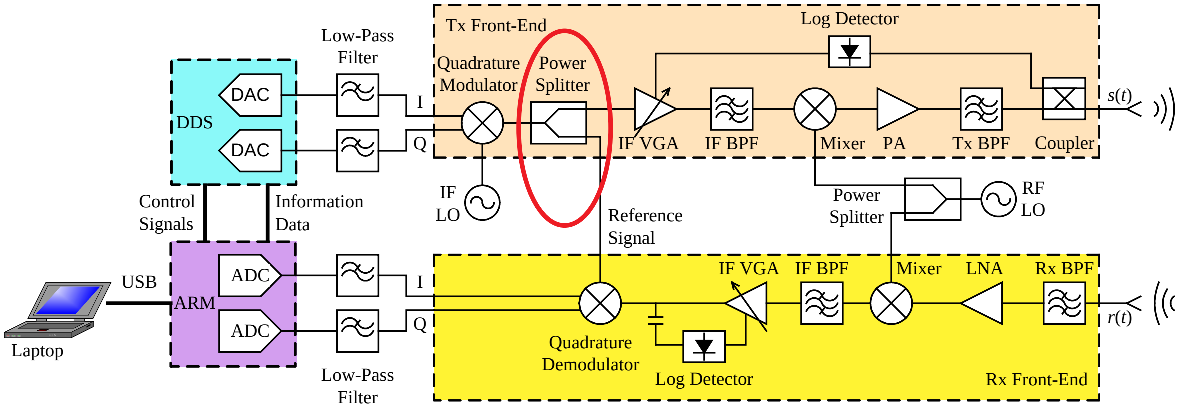

Figure 2.1 Transceiver architecture of 5.9-GHz system demonstrator.

Our proposed modulation waveform is generated by a DDS since it can control amplitude, frequency and phase of the output signal very easily and precisely through software programming. Moreover, it is also able to realize different modulation such as ASK, FSK, PSK, and a number of combinations among them.

In the transmitting channel, the control signals and the frequency-sweeping signals of the DDS as well as the information data are sent by an advanced RISC machine (ARM) board. Both I and Q components of the modulated signals generated by the DDS are filtered by two LPFs, respectively, and they are firstly upconverted to intermediate frequency (IF) through a quadrature modulator. Subsequently, the IF signal is divided into two portions, one of which is further upconverted to RF by a single sideband upconverter and radiated by the transmitting array antenna after amplification. An automatic level control (ALC) loop is introduced in order to provide power back-off capability.

For the receiving channel, in the radar cycle, the reflected wave from the target is firstly amplified and downconverted by an image reject mixer. Then the reflected signal is demodulated using a quadrature architecture with a reference signal (the other portion of the IF signal) from the transmitter. Three beat frequencies are obtained during the upchirp, the constant-frequency period and the downchirp, respectively. On the other hand, in the radio cycle, no modulation takes place in the transmitter, and thus the reference signal is a pure carrier with constant frequency. In this case, the information data from other transmitting units can be successfully recovered. Both I and Q components of the beat signal are digitized by two analog-to-digital converters (ADCs) embedded within the ARM board, which communicates with a laptop through the universal serial bus (USB) interface. An automatic gain control (AGC) circuit is implemented after the IF bandpass filter in order to compensate channel attenuation variations for both radio and radar signals.

2.2 System simulation

In order to predict and optimize system performance, our proposed system was analyzed in a commercial circuit simulation package [63]. The transmitter and the receiver are simulated respectively, which are then combined together with channel models for running system simulation and optimization.

2.2.1 Simulation of the upconverter

As shown in Figure 2.2, the transmitter is divided into four building blocks: a modulator, an active power divider, an upconverter and an ALC circuit. Since the upconverter is the most critical part in the transmitting signal chain, we will focus on the analysis and design of the upconverter in the following paragraphs. An iterative design routine including chip selection, performance evaluation, and budget analysis, is performed in order to satisfy our proposed design specifications in connection with the transmitter.

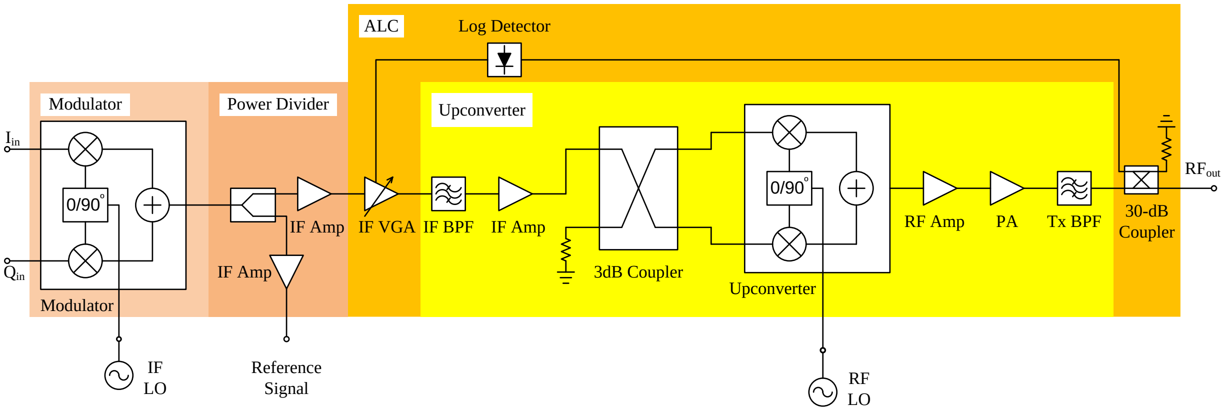

Figure 2.2 Block diagram of the transmitter.

2.2.1.1 Harmonic balance simulation

Depending on our system specifications, we select a proper chip for each functional block in Figure 2.2. Then, the performance of the upconverter was analyzed using the functional diagram in Figure 2.3 with the help of the specifications of each chip given in its datasheet. In Figure 2.3, the IF BPF (A400+) is a three-order Chebyshev filter, and the Tx BPF is a five-order elliptic filter, which will be replaced with an SIW BPF described in the next chapter.

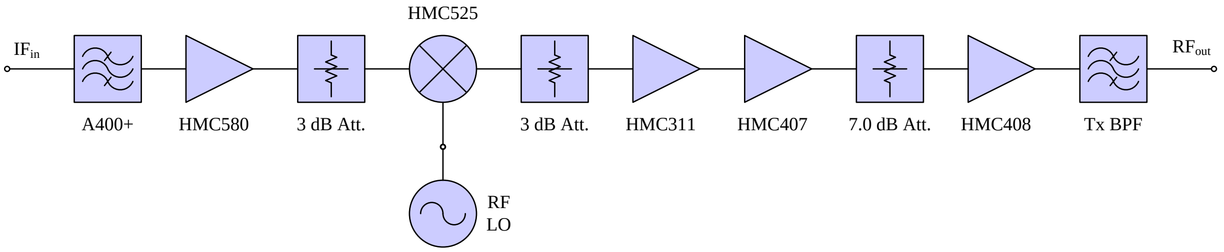

Figure 2.3 Simulation diagram of the upconverter.

In the beginning, the gain performance of the upconverter was evaluated. An IF input signal with a power of −10 dBm is injected into the upconverter, and the resulting RF output after the Tx BPF is plotted in Figure 2.4. We can see that the simulated output power of the upconverter is +29.59 dBm, which leaves a power margin of about 0.8 dB over our specified value of +28.8

dBm for considering the insertion loss of the connector between the transmitter and the transmitting antennas.

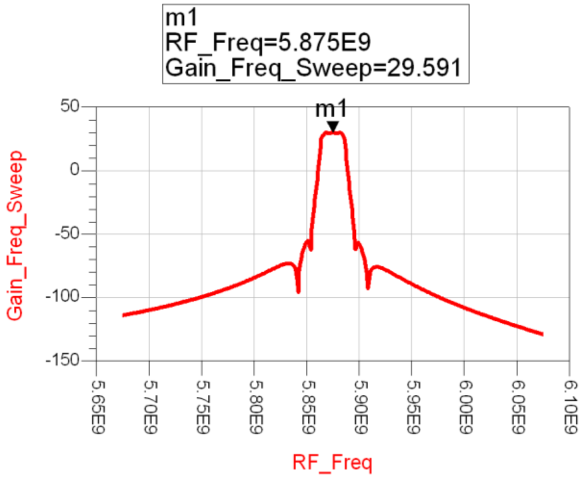

Figure 2.4 Simulated output gain of the upconverter.

Then, the power of the input IF signal is swept from −40 dBm to 10 dBm in order to find the 1-dB gain compression point of the upconverter. Simulation results are plotted in Figure 2.5. We can see that the maximum gain of the upconverter is 40.48 dB with the input P1dB of −9.5 dBm. Since the nominal value of the input power is −10 dBm, the transmitter is operating below 1-dB gain compression point.

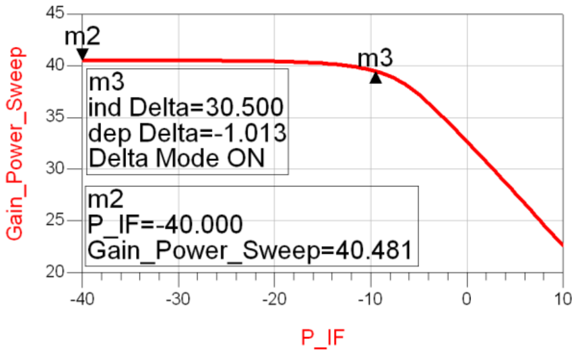

Figure 2.5 Simulated gain compression characteristics of the upconverter.

2.2.1.2 Chain budget analysis

In order to investigate the influence of each component on the overall performance of the upconverter, the chain budget of the upconverter at the center frequency is also analyzed in the case of a nominal input power of −10 dBm. Simulated results are given in Figure 2.6.

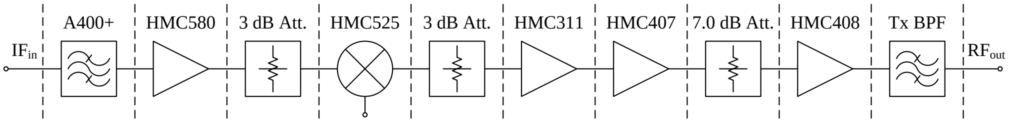

	A400+	HMC580	3 dB Att.	HMC525	3 dB Att.	HMC311	HMC407	7.0 dB Att.	HMC408	Tx BPF
Gain (dB) of Comp.	-3.0	20.0	-3.0	-8.0	-3.0	14.0	15.0	-7.0	20.0	-2.0
S_{11} (dB) of Comp.	-42.3	-28.0	-400.0	-5.0	-400.0	-10.0	-12.0	-400.0	-8.0	-64.3
S_{22} (dB) of Comp.	-42.3	-12.0	-400.0	-5.0	-400.0	-10.0	-15.0	-400.0	-10.0	-64.3
OutP1dB (dBm) of Comp.	1000.0	21.2	1000.0	6.4	1000.0	13.1	26.1	1000.0	33.3	1000.0
OutTOI (dBm) of Comp.	1000.0	37.0	1000.0	17.0	1000.0	24.0	41.0	1000.0	45.0	1000.0
NF (dB) of Comp.	3.0	2.8	3.0	11.1	3.0	4.8	5.7	7.0	6.6	2.0

Out_Gain (dB) in Chain		-3.2	16.0	11.7	4.0	0.2	14.2	29.2	21.5	41.7	39.7
Out_P1dB (dBm) in Chain		1000.0	20.1	15.8	4.2	0.4	10.6	23.8	16.1	32.1	30.1
Out_TOI (dBm) in Chain		1000.0	37.0	31.5	16.2	9.8	20.9	33.8	26.0	42.8	40.5
In_NF(dB) in Chain	3.0	5.8	5.8	8.7	8.9	9.5	9.5	9.5	9.5	9.5	
In_S_{11} (dB) in Chain	-20.5	-14.5	-11.0	-5.0	-12.7	-6.7	-11.7	-22.0	-8.0	-64.3	

Figure 2.6 Simulated chain budget of the upconverter.

In Figure 2.6, the first six rows list the specifications of each component including gain, S_{11}, S_{22}, output P1dB, output third-order intercept (TOI) and noise figure (NF). In addition, the following rows give the total value for such upconverter performances as gain, output P1dB, output TOI, S_{11} and NF. From Figure 2.6, we can see that our designed upconverter has very good input matching ($|S_{11}| = -20.5$ dB). In case that the input power is −10 dBm, the output power of the upconverter is 29.7 dBm. The output P1dB and output TOI of the upconverter are 30.1 dBm and 40.5 dBm, respectively. Furthermore, it should also be mentioned that though noise figure is characterized at the input of the upconverter, its value increases as the number of cascaded components in Figure 2.6 and therefore the rightmost value (9.5 dB) indicates the noise figure of the upconverter.

2.2.2 Simulation of the downconverter

The receiver shown in Figure 2.7 is segmented into three building blocks including a downconverter, an AGC circuit and a demodulator. Our attention will be paid to the analysis and optimization of downconverter due to its critical role in the receiver.

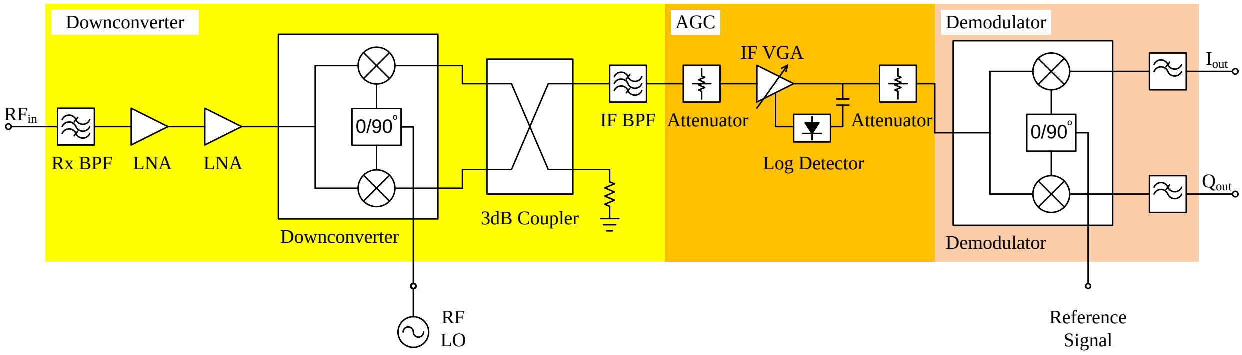

Figure 2.7 Block diagram of the receiver.

2.2.2.1 Harmonic balance simulation

The receiver is simulated with an input power of −90 dBm according to the diagram in Figure 2.8. Two stages of low noise amplifier are used for increasing the gain and reducing the noise figure of the receiver. The Rx BPF and IF BPF are the same as the Tx BPF and IF BPF in Figure 2.3.

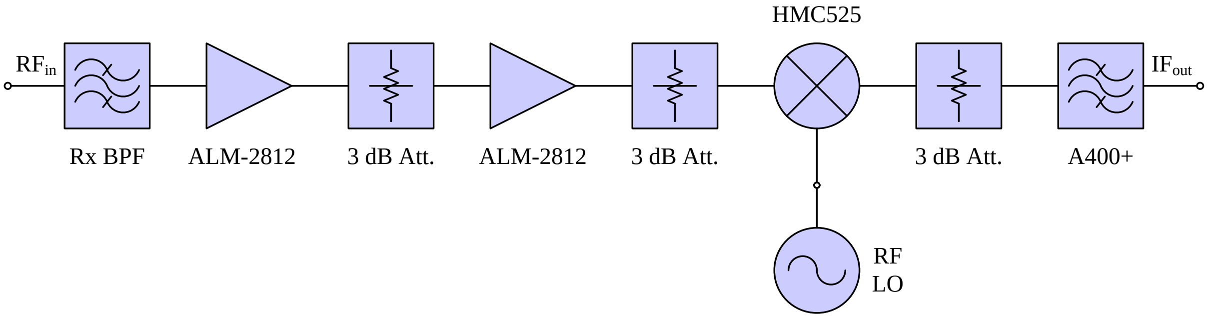

Figure 2.8 Simulation diagram of the downconverter.

Simulation results in Figure 2.9 show that the simulated gain of the downconverter is about 24.2 dB. Additionally, the gain compression performance of the downconverter presented in Figure 2.10 indicates that the input P1dB of the downconverter is around −31 dBm, which fully covers the input signal level that is under consideration in our system. Though high gain is required at the receiver for amplifying the received weak signals, the primary function of downconverter is to convert the received RF signal to IF signal with minimum distortion since high gain amplification can be easily achieved in the IF stage.

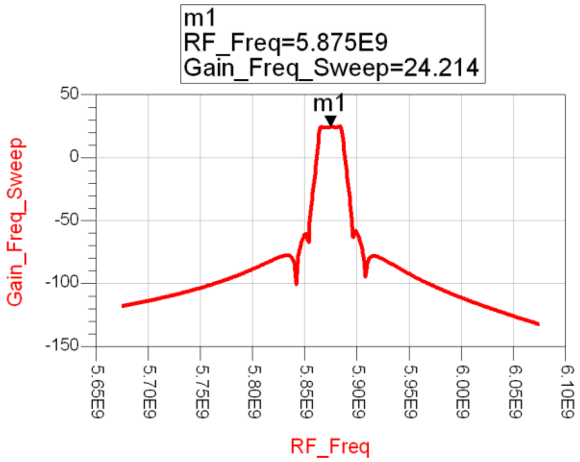

Figure 2.9 Simulated output gain of the downconverter.

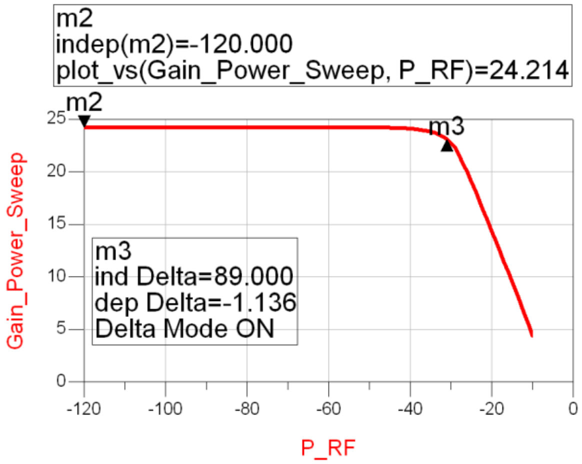

Figure 2.10 Simulated gain compression characteristics of the downconverter.

2.2.2.2 Chain budget analysis

Similar to the upconverter, a chain budget analysis was also performed for the downconverter. The first six rows of Figure 2.11 give the specifications of each component while the rest lists the analysis results. It can be seen that in addition to good input matching ($|S_{11}| = -14.7$ dB), the designed downconverter has a noise figure of 4.9 dB, which are mainly ascribed to the Rx BPF. The gain of the downconverter without compression is 24.2 dB, and the input P1dB and input TOI are respectively −31.5 dBm and −21.9 dBm, which differ from the output P1dB and output TOI by the compressed gain and small signal gain, respectively.

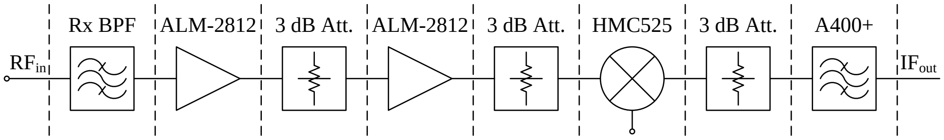

	Rx BPF	ALM-2812	3 dB Att.	ALM-2812	3 dB Att.	HMC525	3 dB Att.	A400+
Gain (dB) of Comp.	-2.0	22.9	-3.0	22.9	-3.0	-8.0	-3.0	-3.0
S_{11} (dB) of Comp.	-64.3	-10.1	-400.0	-10.1	-400.0	-5.0	-400.0	-43.3
S_{22} (dB) of Comp.	-64.3	-18.1	-400.0	-18.1	-400.0	-5.0	-400.0	-43.3
Out_P1dB (dBm) of Comp.	1000.0	8.7	1000.0	8.7	1000.0	4.4	1000.0	1000.0
Out_TOI (dBm) of Comp.	1000.0	20.7	1000.0	20.7	1000.0	15.0	1000.0	1000.0
NF (dB) of Comp.	2.0	1.6	3.0	1.6	3.0	11.1	3.0	3.0

	RF_{in}								IF_{out}
Out_Gain (dB) in Chain		-2.4	20.9	17.7	40.8	36.5	30.2	27.2	24.2
Out_P1dB (dBm) in Chain		1000.0	9.1	5.9	8.9	4.7	-2.3	-5.3	-8.3
Out_TOI (dBm) in Chain		1000.0	20.7	17.4	20.7	16.2	8.7	5.2	2.2
In_NF(dB) in Chain	2.0	3.5	3.5	3.5	3.5	4.9	4.9	4.9	
In_S_{11} (dB) in Chain	-14.7	-10.7	-17.2	-11.2	-11.0	-5.0	-49.3	-43.3	
In_P1dB (dBm) in Chain	-31.5	-33.9	-10.6	-13.8	16.0	11.7	1000.0	1000.0	
In_TOI (dBm) in Chain	-21.9	-23.9	-0.9	-4.0	24.2	21.1	1000.0	1000.0	

Figure 2.11 Simulated chain budget of the downconverter.

2.2.3 System-level simulation

2.2.3.1 System modeling

Our system performance is modeled and analyzed using the Ptolemy simulator platform in the same simulation package [63], which is based on a time synchronous flow and enables the co-simulation of the digital back-ends together with the RF front-ends. Block diagram of the system simulation is depicted in Figure 2.12.

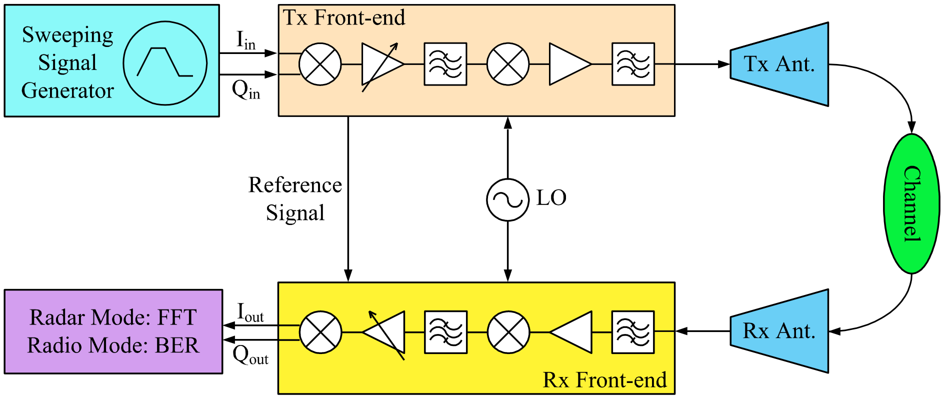

Figure 2.12 System simulation diagram.

In Figure 2.12, the whole system is divided into several functional blocks which are modeled individually. The modulated waveform is generated by a module called “Sweeping Signal Generator”. Typical modulated signals at the output of this module are plotted in Figure 2.13. The transmitter and the receiver front-end modules are designed based on the heterodyne architectures as respectively described in Figure 2.3 and Figure 2.8.

Our previous discussion concludes that the channel models are different between the radar mode and the radio mode. From (1.30), we can see that the impulse response of the radio channel is defined by two parameters, namely, amplitude attenuation and time delay. Therefore, the transmitted signal is attenuated and delayed according to the communication range. On the other hand, the expression given in (1.33) indicates that in addition to amplitude attenuation and time delay, the frequency of the transmitted signal is shifted by f_d due to the Doppler effect involved in the process. In our simulation, the transmitted signal is firstly attenuated and delayed corresponding to the target range, and then, the Doppler frequency shift which is associated with the target velocity is applied to the transmitted signal through a quadrature modulation.

Radar beat frequencies and radio baseband signals are processed in a software-defined manner. The radio baseband signals are coherently demodulated while the beat frequencies in the radar mode are estimated by the FFT with zero padding.

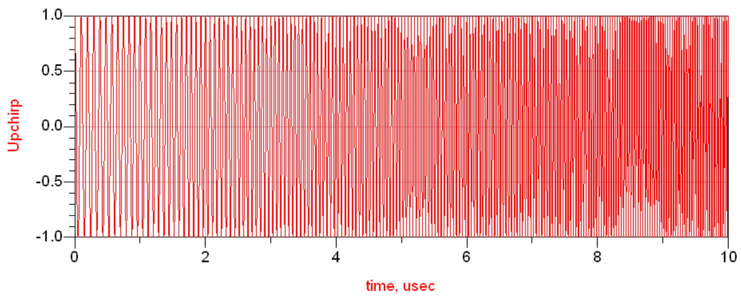

(a) Upchirp.

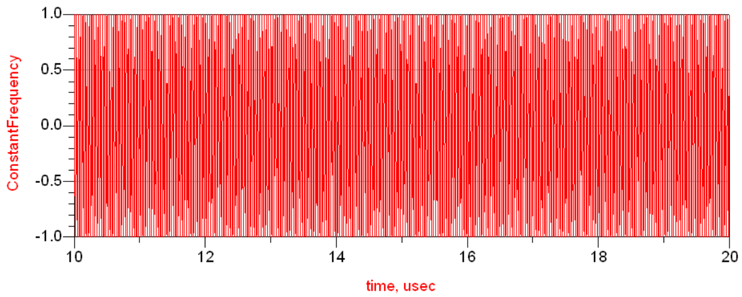

(b) Constant frequency.

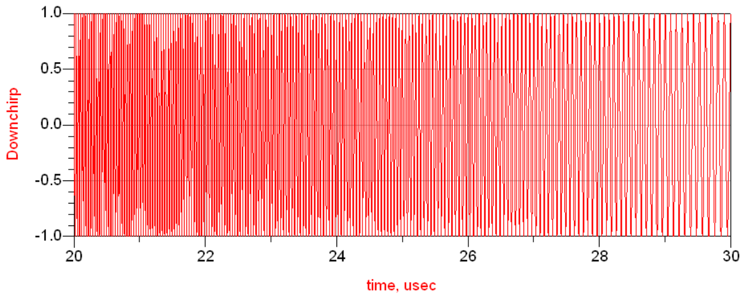

(c) Downchirp.

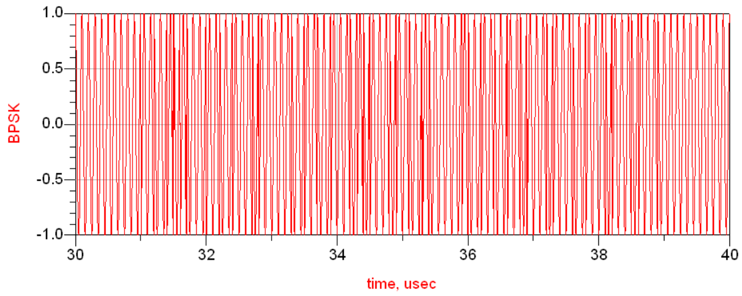

(d) BPSK.

Figure 2.13 Simulated modulated waveforms.

2.2.3.2 Simulation of radar mode

Simulation results of the radar mode are summarized in Table 2.6. To reduce the simulation time, the time duration T_s is set to 1 ms. Our simulation generates the same results as the predefined range and velocity, which has effectively demonstrated proper system functionality.

Table 2.6 Simulation results of the radar mode.

Simulation parameters		Simulation results	
T_S	1 ms	f_{bU}	37.5 KHz
ΔB	20 MHz	f_{bC}	2.5 KHz
f_{RF}	5875 MHz	f_{bD}	42.5 KHz
R	300 m	Calculated R	300 m
v	31.09 m/s	Calculated v	63.83 m/s

It should be mentioned that in the simulation, only the beat signals from $0.1T_S$ to $0.9T_S$ of each period is kept for frequency estimation. Therefore, our frequency estimation has a resolution of 1.25 KHz owing to this short time duration. Only those velocities that can generate a Doppler frequency multiple of this frequency resolution, can be accurately detected. However, in real applications, the time duration T_S is 20 ms, which guarantees a velocity resolution of 1.6 m/s.

2.2.3.3 Simulation of radio mode

The radio mode is simulated by applying a BPSK modulation with a data rate of 10 Mbps. Figure 2.14 compares the transmitted and the received radio baseband signals in the conditions of different E_b/N_0. It is obvious that the received signal is heavily contaminated by the noise in the case of a low SNR and a high SNR is definitely conducive to recover the transmitted signal.

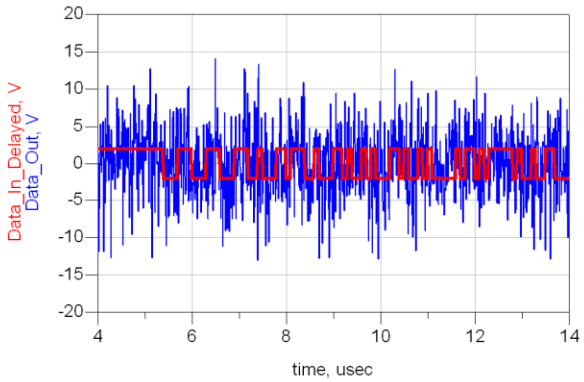

(a) E_b/N_0 = 0 dB.

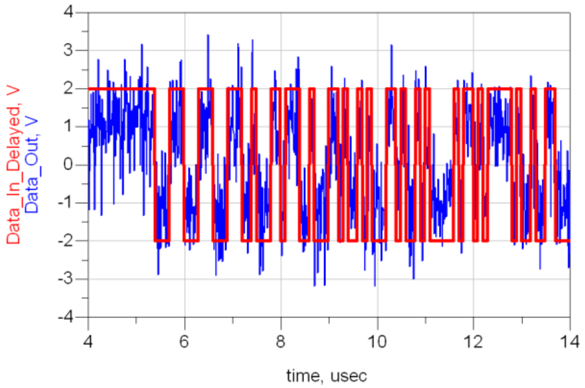

(b) E_b/N_0 = 10 dB.

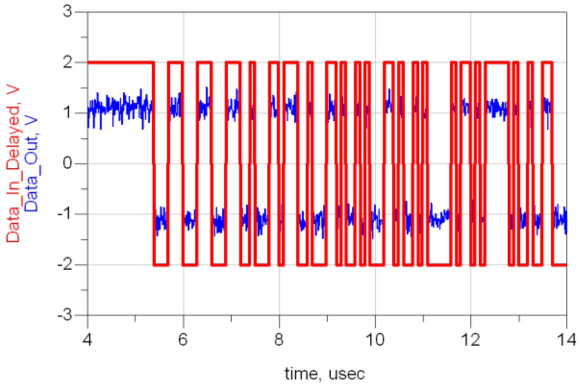

(b) E_b/N_0 = 20 dB.

Figure 2.14 Comparison between transmitted and received radio baseband signals.

The simulated bit-error-rate (BER) for the radio mode is compared with the well-known theoretical result [64] in Figure 2.15. It can be proved that under the condition of an AWGN channel, the system performance matches well with the theoretical results.

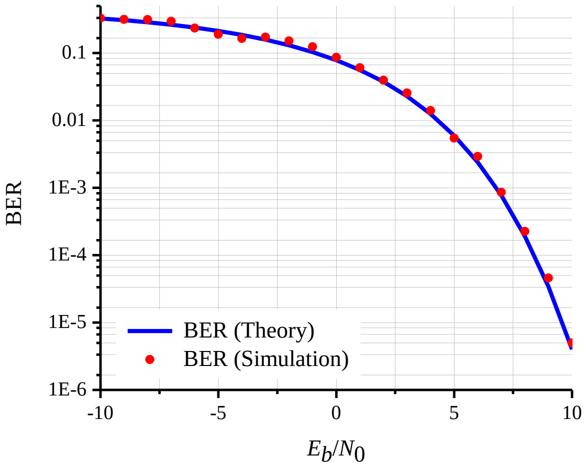

Figure 2.15 Simulated BER of the radio mode.

2.3 Conclusion

This chapter reviews key aspects of the FCC's DSRC rules, which together with practical requirements of ITS application define our system specifications. Subsequently, a link budget analysis is performed for both communication and radar modes in order to provide guidance to design our transceiver. The conventional heterodyne transceiver architecture has been modified to adapt our proposed modulation waveform. Our transceiver is then analyzed in a commercial simulation package, which is followed by a system-level simulation. Simulation results of the upconverter and downconverter as well as the entire system have proved our design and presented very good performance.

CHAPTER 3 A LOW-FREQUENCY SYSTEM DEMONSTRATOR: PROTOTYPING AND EXPERIMENT

After studying and proving the system functionality through circuit simulations, we have prototyped and measured each building block in our system in order to make sure of its functionality and performance through experiments. Following this procedure, the transmitter and the receiver are individually built by integrating its constituents and respectively encased in a metallic box for blocking spurious radiation and reception of electromagnetic fields. Then, the whole system is subjected to experimental verification for both communication and radar modes. In this chapter, prototyping and experiments of the 5.9-GHz system demonstrator will be presented.

3.1 Circuits design and system prototyping

3.1.1 Direct digital synthesizer

Our proposed modulation waveform is generated by means of a DDS (AD9854). It has five operation modes including single tone, FSK, ramped FSK, chirp and BPSK, which can be selected by a mode select signal. In addition, the mode select signal can also be duplexed to send information data that are then used to modulate the output signal of DDS. Figure 3.1 gives a photo of an evaluation board of the DDS used in this work.

Figure 3.1 Photo of the DDS evaluation board.

3.1.2 ALC and AGC circuits

From our link budget analysis, we have concluded that the receiver should be able to compensate the attenuation difference between the radar and the radio channels with the help of an AGC circuit. Moreover, the transmitter in our system is also equipped with an ALC circuit for providing the capability of power back-off in case of high-order modulation techniques.

In general, the ALC and AGC circuits share the same block diagram as shown in Figure 3.2, but essentially ALC circuit requires a constant input P1dB of the variable gain amplifier (VGA) while AGC circuit requires a constant output P1dB. In Figure 3.2, the input signal is firstly amplified by the VGA and possibly additional stages of amplifiers. Then, a portion of the amplified input signal is coupled before being sent to output. The coupled signal is detected by a logarithmic detector in our case, which generates a direct current (DC) voltage indicating its input power. Subsequently, this DC voltage is compared with a predefined setting voltage and their difference is a received signal strength indicator (RSSI), which is used to control the gain of the VGA in the loop.

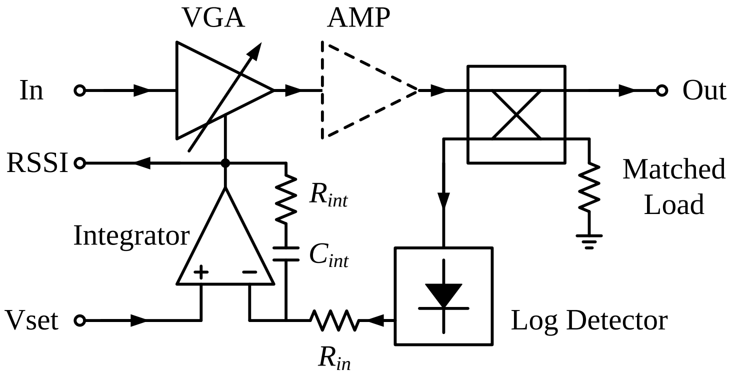

Figure 3.2 Block diagram of the ALC/AGC circuit.

3.1.3 SIW bandpass filters

In order to suppress the out-of-band spurious signals and reject the interference signal, a transmitting bandpass filter (Tx BPF) is deployed at the output of the PA while a receiving bandpass filter is adopted at the input of the LNA. These two BPFs are designed with cross-coupled resonators and implemented using the substrate integrated waveguide (SIW) technology, which has such advantages as low cost, low loss and high-*Q*, and seamless compatibility with standard PCB fabrication process as well as easy integration with active components. Furthermore, the out-of-band suppression of planar BPFs is normally very poor due to the space coupling brought by the open/semi-open field profile. However, the EM fields of SIW circuits are well confined within the substrate, and therefore it is easy to achieve high out-of-band attenuation since the input and output of SIW BPFs can be very easily isolated by assembling metallic septum on the housing cover. Both the Tx and Rx BPFs are designed on a substrate of RT/duroid® 6002 with a permittivity of 2.94 and a thickness of 0.5 mm.

3.1.3.1 Tx BPF

The specifications of the Tx BPF are listed in Table 3.1. It is centered at the center frequency of the DSRC band with a fractional bandwidth of 3.8%. Additionally, there is a transmission zero located at 6.26 GHz in order to suppress the feedthrough of the RF LO.

Table 3.1 Specifications of the Tx BPF.

Specifications	Value
Passband	From 5.775 to 6 GHz
In-band insertion loss	<1.5 dB
In-band return loss	>15 dB
Transmission zero	6.26 GHz
Out-of-band attenuation	>30 dB up to 7 GHz

According to the given specifications, a BPF with generalized Chebyshev filtering response is synthesized by using the method in [65], and the synthesized coupling matrix is given below.

$$M = \left[\begin{array}{cccccc} & S & 1 & 2 & 3 & L \\ S & 0 & 0.0414 & 0 & 0 & 0 \\ 1 & 0.0414 & 0.0032 & 0.0378 & 0.0129 & 0 \\ 2 & 0 & 0.0378 & -0.0125 & 0.0378 & 0 \\ 3 & 0 & 0.0129 & 0.0378 & 0.0032 & 0.0414 \\ L & 0 & 0 & 0 & 0.0414 & 0 \end{array}\right] \tag{3.1}$$

The Tx BPF is implemented with three TE_{101} SIW cavities with cross couplings through inductive windows as shown in Figure 3.3(a). From the synthesized coupling matrix, we can find that since the transmission zero is located above the passband, all the couplings between resonators have the same sign. An equivalent circuit topology is given in Figure 3.3(b).

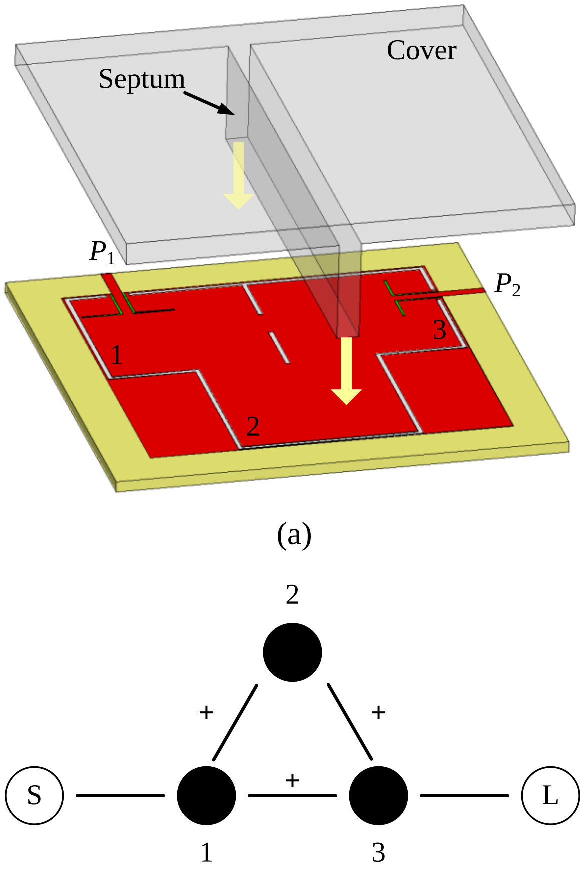

(a)

(b)

Figure 3.3 Sketch of the Tx BPF and its equivalent circuit topology.

Figure 3.4 compares the simulated results of the Tx BPF obtained in a commercial finite-element-method (FEM)-based full-wave simulator [66] with our synthesized results. We can see that the simulated results agree very well with the synthesized results with a certain deviation in the upper stopband due to spurious high-order modes of the SIW cavities. The simulated performance is summarized as follows. The insertion loss at the center frequency is 0.86 dB with a return loss better than 20 dB over the entire band. In addition, a transmission zero is clearly observed at 6.26 GHz and the out-of-band attenuation is higher than 34 dB up to 7 GHz. Finally, the variation of in-band group delay is less than 1.5 ns.

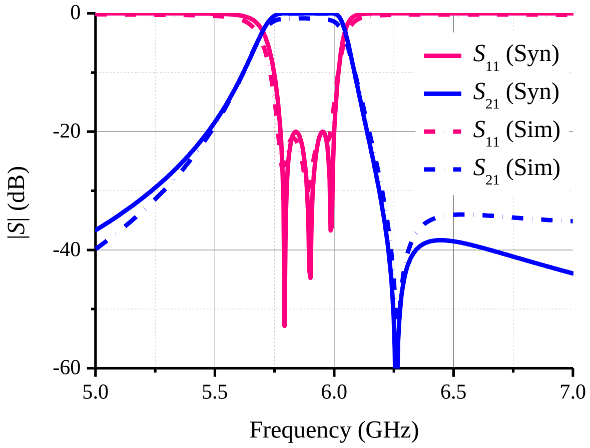

(a) *S* parameters.

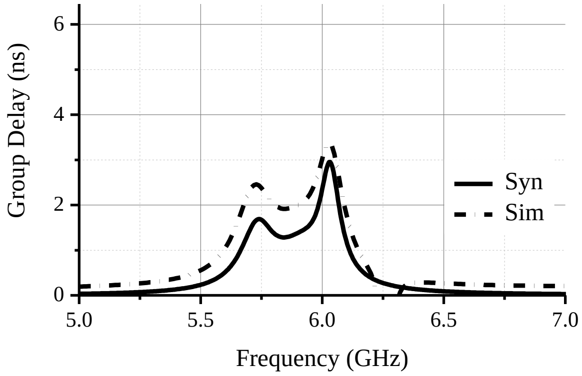

(b) Group delay.

Figure 3.4 Comparison between synthesized and simulated results of the Tx BPF.

3.1.3.2 Rx BPF

Table 3.2 gives the specifications of the Rx BPF. It has the same frequency range as the Tx BPF since our system operates in TDD mode. However, different from the Tx BPF, a transmission zero is located at 5.56 GHz in order to suppress the LO feedthrough of the channel emulator that is used in our measurement setup.

Table 3.2 Specifications of the Rx BPF.

Specifications	Value
Passband	From 5.775 to 6 GHz
In-band insertion loss	<1.5 dB
In-band return loss	>15 dB
Transmission zero	5.56 GHz
Out-of-band attenuation	>30 dB below the passband

By using the same synthesis method [65], we can obtain the coupling matrix given below.

$$M = \left[\begin{array}{cccccc} & S & 1 & 2 & 3 & L \\ S & 0 & 0.0414 & 0 & 0 & 0 \\ 1 & 0.0414 & -0.0035 & 0.0375 & -0.0140 & 0 \\ 2 & 0 & 0.0375 & 0.0136 & 0.0375 & 0 \\ 3 & 0 & -0.0140 & 0.0375 & -0.0035 & 0.0414 \\ L & 0 & 0 & 0 & 0.0414 & 0 \end{array}\right] \tag{3.2}$$

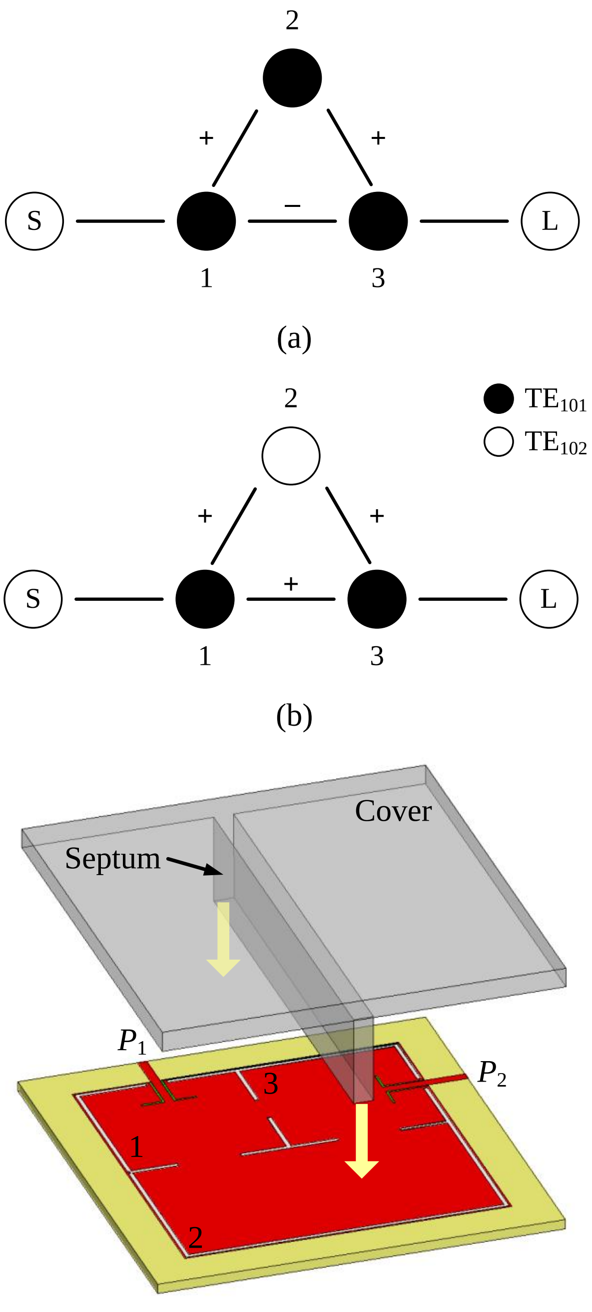

(a)

(b)

(c)

Figure 3.5 Sketch of the Rx BPF and its equivalent circuit topology.

From the coupling matrix, we can find that the coupling between resonators 1 and 2 and that between resonators 1 and 3 have opposite sign which means that they have different coupling polarity. The filter topology is shown in Figure 3.5(a). If the magnetic coupling is defined as the positive coupling, then the electric coupling will be the negative coupling. SIW BPF with electric coupling mechanism has been reported in [34] and the electric coupling was obtained by etching slots on both the top and the bottom metals of the SIW. However, this technique would fail if the filter is assembled on a base or packaged in a metallic housing. Therefore, another topology described in Figure 3.5(b) is adopted in this work. In Figure 3.5(b), the original resonator 2 was replaced by a resonator with reverse phase between the input and the output. A corresponding sketch of the Rx BPF based on SIW technology is depicted in Figure 3.5(c), and resonator 2 in Figure 3.5(b) is realized by a TE_{102} SIW cavity while others are designed by TE_{101} SIW cavities. In this case, the input/output coupling and the inter-resonator coupling are realized by the same technique as the Tx BPF.

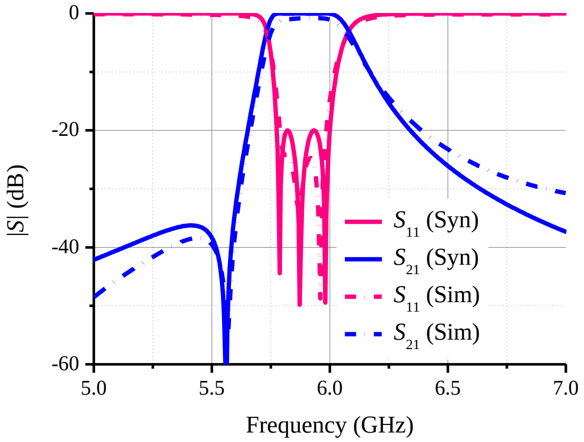

(a) *S* parameters.

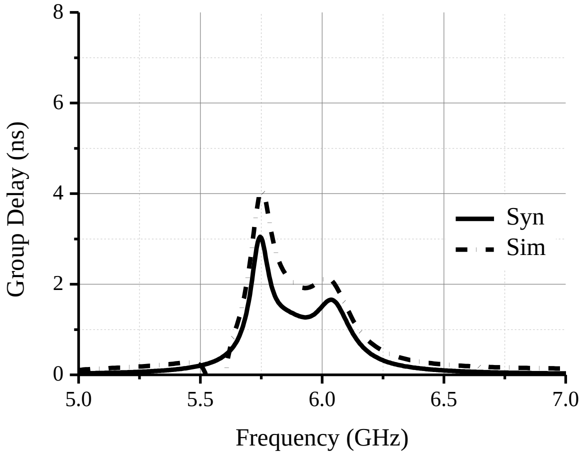

(b) Group delay.

Figure 3.6 Comparison between synthesized and simulated results of the Rx BPF.

The simulated results from a full-wave simulator [66] are compared with the synthesized results in Figure 3.6, and they have a good agreement. The insertion loss at the center frequency is 0.84 dB and the return loss is better than 20 dB within the specified band. In addition, a transmission zero is clearly observed at 5.56 GHz with an out-of-band attenuation higher than 38 dB below the passband. Finally, the variation of in-band group delay is less than 2.2 ns.

3.1.4 Microstrip array antenna

A pair of microstrip array antennas is designed in our system in order to increase the isolation between the transmitting and the receiving channels. In this array, the radiating element is a microstrip inset-fed patch antenna, which is sketched with dimensions in Figure 3.7.

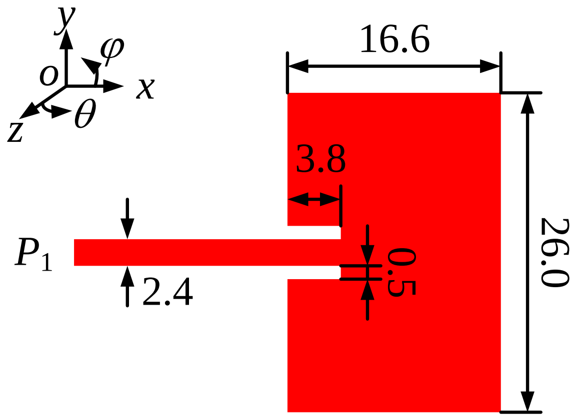

Figure 3.7 Sketch of an element in the array.

The substrate selected is RT/duroid® 5880 with a permittivity of 2.2 and a thickness of 0.5 mm. The simulated and measured return losses of the radiating element are compared in Figure 3.8, and it shows an excellent agreement between simulation and measurement. The frequency band for voltage standing wave ratio (VSWR) less than 2 is from 5.825 to 5.945 GHz, which fully covers the specified DSRC band.

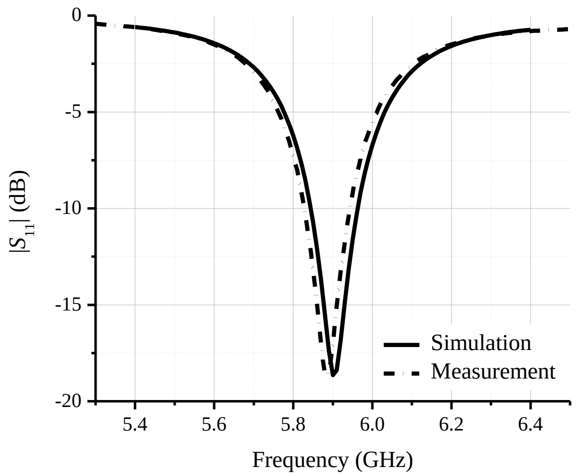

Figure 3.8 Comparison between simulated and measured return losses of the element.

The measured gain shown in Figure 3.9 is about 7 dBi with a variation of 1 dB. In addition, Figure 3.10 compares the simulated and measured radiation patterns at the center frequency. The measured *H*-plane pattern agrees well with the simulation result, but the measured *E*-plane is affected by the absorbing material close to the antenna.

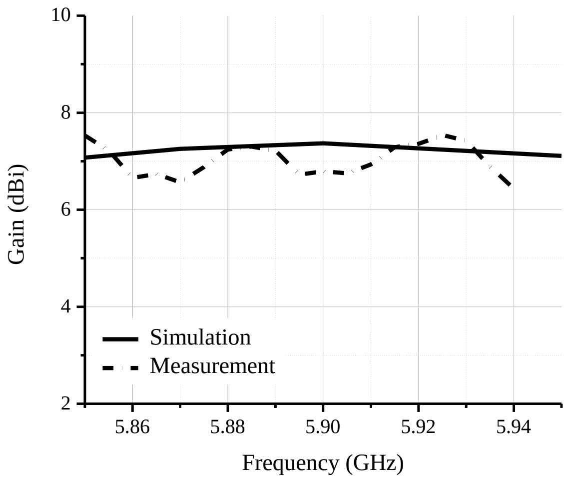

Figure 3.9 Comparison between simulated and measured gains of the element.

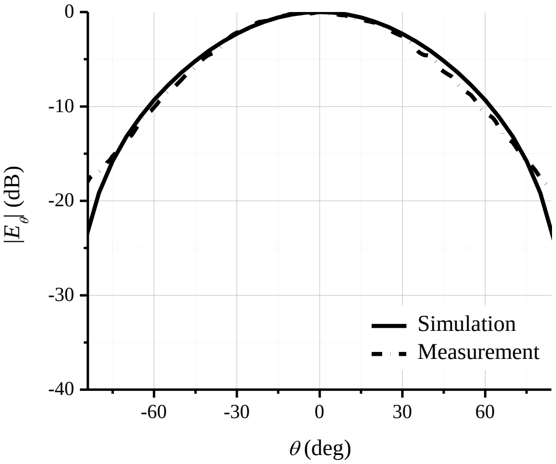

(a) *H*-plane.

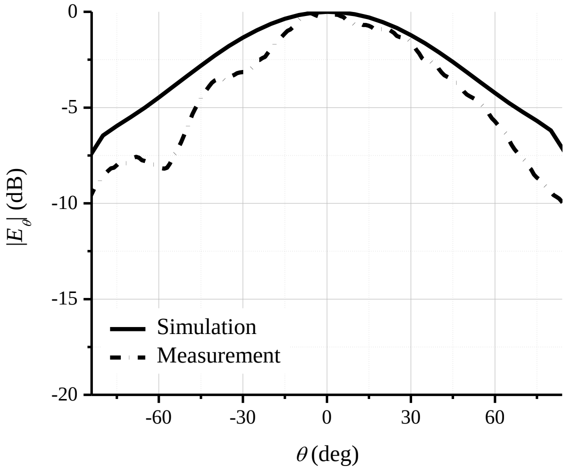

(b) *E*-plane.

Figure 3.10 Comparison between simulated and measured radiation patterns of the element.

On the basis of the radiating element, a 2 × 4 microstrip planar array is designed with uniform excitation. A sketch in Figure 3.11 shows that this planar array consists of eight radiating elements, which are fed by a corporate feeding network that is composed of a series of power dividers with equal splitting ratio.

Figure 3.11 Sketch of the planar array.

Simulated and measured return losses of the planar array are compared in Figure 3.12, and an excellent agreement can be found. The return loss is better than 10 dB from 5.815 to 5.935 GHz, which fully satisfies our design specifications. Measured radiation pattern at center frequency is compared with simulated ones in Figure 3.13. On one hand, measured *H*-plane pattern has a shift of three degrees owing to misalignment. On the other hand, measured *E*-plane pattern is distorted by the absorbing material close to the array under test and it is also not symmetrical with the central plane, which might be caused by the rotation error in the positioner.

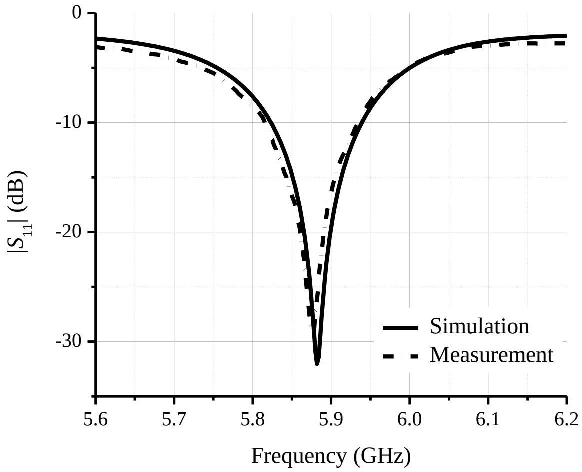

Figure 3.12 Comparison between simulated and measured return losses of the array.

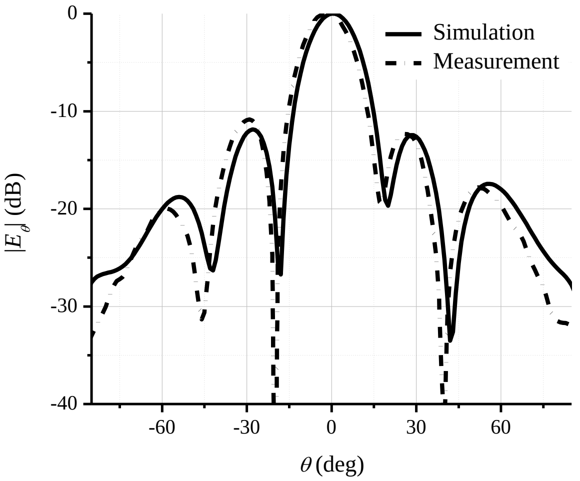

(a) *H*-plane.

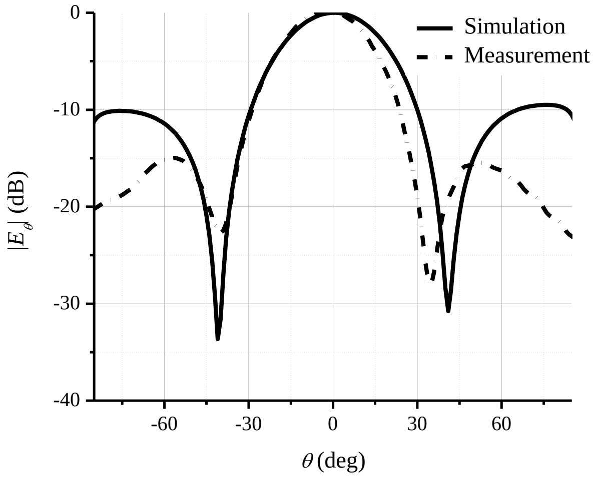

(b) *E*-plane.

Figure 3.13 Comparison between simulated and measured radiation patterns of the array.

Measured gain shown in Figure 3.14 is very close to the specified value of 16 dBi. Considering the measured error including the system error and the gain variation of the standard horn antenna, this planar array is satisfactory to be adopted in the system measurement.

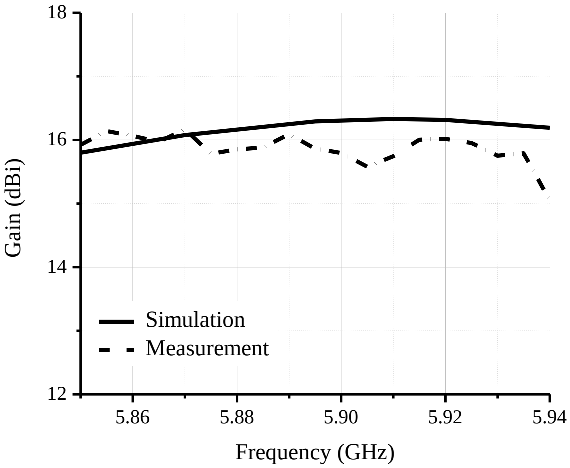

Figure 3.14 Comparison between simulated and measured gains of the array.

3.1.5 System prototyping and housing

The whole system is divided into several parts which are fabricated individually but on the same substrate (0.5 mm-thick RT/duroid® 6002). There are two reasons. One is the fabrication limit of in-house equipments and the other is that the performance of each part can be measured and validated before being integrated together.

Furthermore, in order to block the radiation from the circuits to the outside (EMC) and also prevent the radiation from outside (EMI), it is a common practice to enclose the entire system in a metallic housing. Therefore, our transmitter and receiver prototypes are integrated into two metallic housing respectively as shown in Figure 3.15. It should be mentioned that there are metallic septums on the housing covers, which are mounted onto the SIW BPFs for isolating their inputs and outputs.

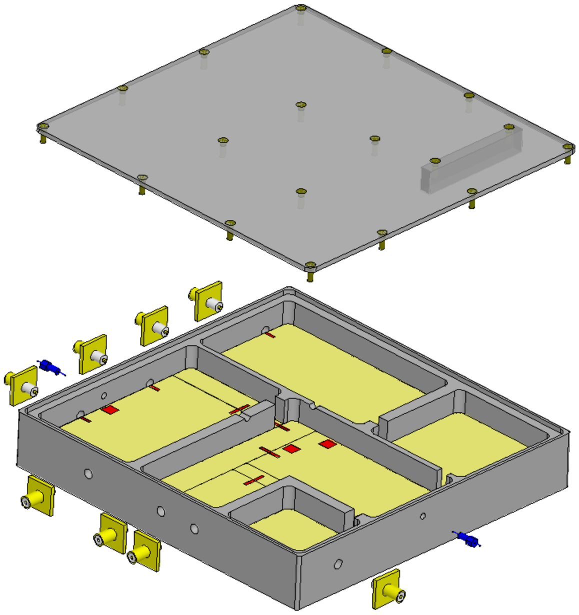

(a) Tx housing.

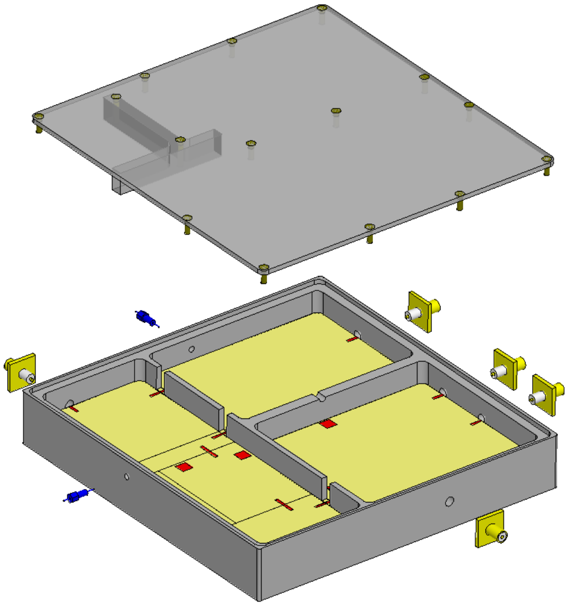

(b) Rx housing.

Figure 3.15 Illustration of Tx and Rx housings.

Photos of the fabricated transmitter and receiver prototypes are shown in Figure 3.16 and the the transmitter and receiver prototypes have the same size of 15×15 cm^2.

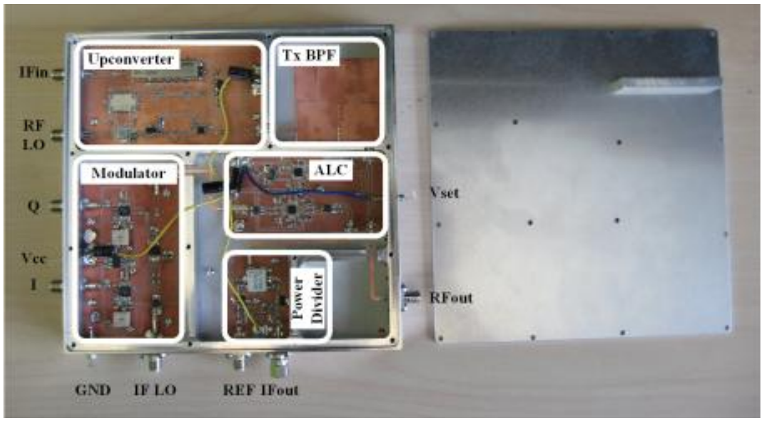

(a) Transmitter prototype.

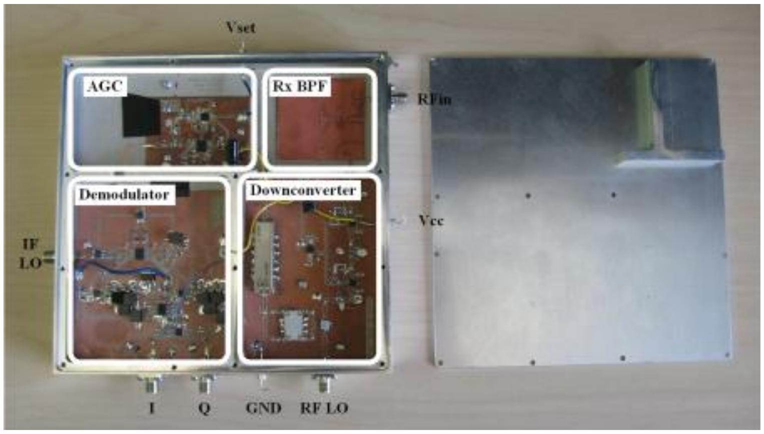

(b) Receiver prototype.

Figure 3.16 Photos of Tx and Rx prototypes.

3.2 Measurement of circuit prototypes

3.2.1 Modulator

A quadrature modulator (AD8345) is selected for modulating the baseband signal. One of the most critical parameter of the quadrature modulator is the sideband suppression, which is defined as the power ratio between the unwanted sideband and the expected sideband and it is determined by the amplitude and phase imbalances of the modulator. The sideband suppression of the modulator is measured by injecting a pair of quadrature signals and measuring the power difference given by a spectrum analyzer (Agilent E4440A) as shown in Figure 3.17. From Figure

3.17, we can find that the sideband suppression of the modulator is around −40 dBc, and also the modulator can suppress the carrier by 20 dB.

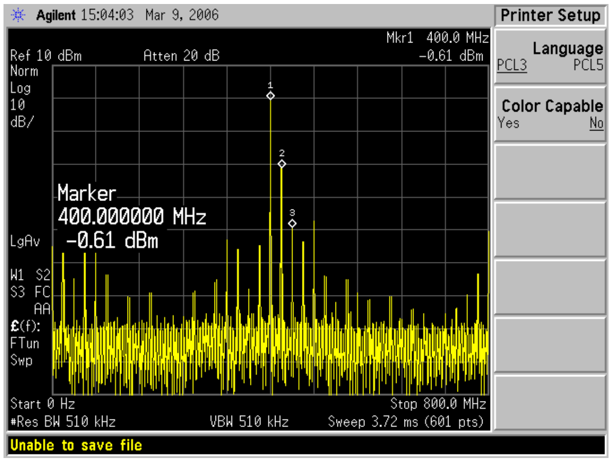

Agilent 15:04:03 Mar 9, 2006

Mkr1 400.0 MHz
-0.61 dBm

Ref 10 dBm Atten 20 dB
Norm
Log
10
dB/

Marker
400.000000 MHz
-0.61 dBm

Start 0 Hz Stop 800.0 MHz
#Res BW 510 kHz VBW 510 kHz Sweep 3.72 ms (601 pts)

Unable to save file

(a) Expected output.

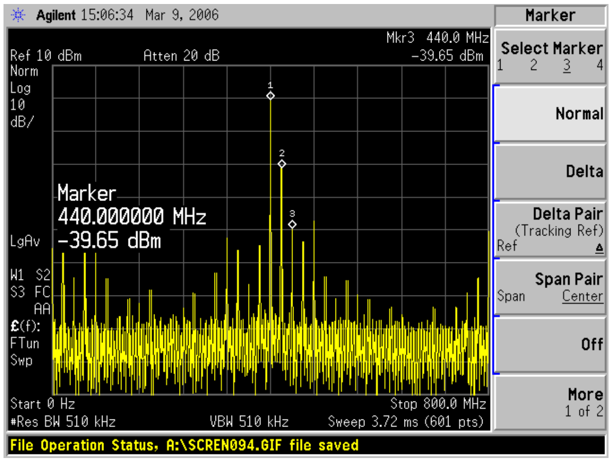

Agilent 15:06:34 Mar 9, 2006

Mkr3 440.0 MHz
-39.65 dBm

Ref 10 dBm Atten 20 dB
Norm
Log
10
dB/

Marker
440.000000 MHz
-39.65 dBm

Start 0 Hz Stop 800.0 MHz
#Res BW 510 kHz VBW 510 kHz Sweep 3.72 ms (601 pts)

File Operation Status, A:\SCREN094.GIF file saved

(b) Mirror output.

Figure 3.17 Measured sideband suppression of the modulator.

3.2.2 ALC circuit

According to the block diagram shown in Figure 3.2, an ALC circuit is built with a VGA (ADL5300) and a logarithmic detector (AD8318). It should be noted that there are additional amplifying stages between the VGA and the coupler, and the power of the output signal is coupled at the output of the power amplifier. The measured relationship between the output power and the setting voltage is shown in Figure 3.18. The measured gain control range is 51.5 dB with a slope of −0.04 dB/mV. Additionally, the measured curve presents a very high linearity, which indicates a very small error of gain adjustment of the prototyped ALC circuit.

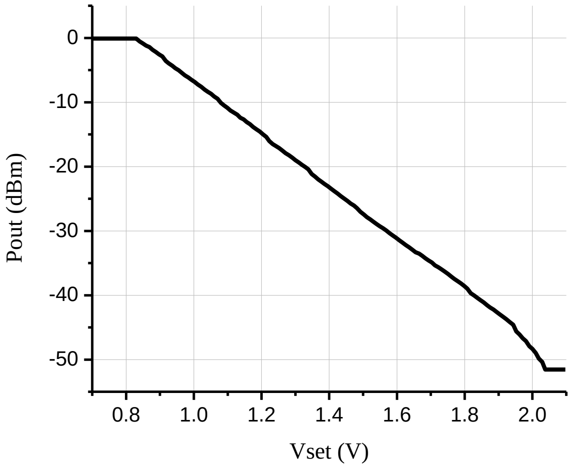

Figure 3.18 Measured ALC performance.

3.2.3 Upconverter

A series of comprehensive experiments are made to evaluate the performance of the prototyped upconverter without the Tx BPF. In the beginning, the intermodulation performance of the upconverter is approximately measured by injecting a two-tone signal and then the output third-order intermodulation product of the upconverter is measured. In the same time, the gain compression characteristics can also be approximately obtained. Our experiments are carried out with various frequency differences between two tones, from 50 kHz to 500 kHz. From the measured results shown in Figure 3.19, we can see that the upconverter prototype has an input P1dB of −10 dBm with a gain of 41.6 dB, and it is very close to our analysis result and satisfies our design specifications. Also, the measured TOI for these three different settings of frequency difference are consistent, and the measured output TOI is about 42 dBm.

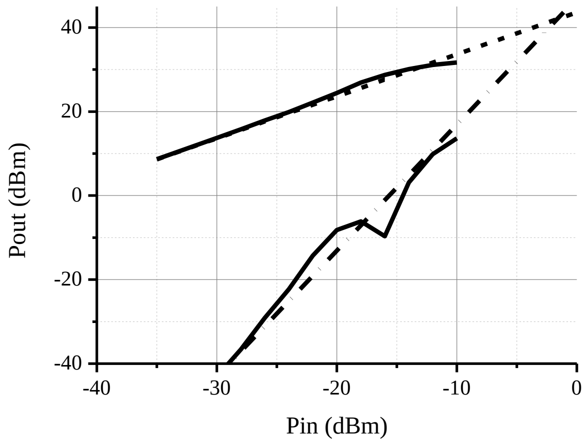

(a) 50 kHz.

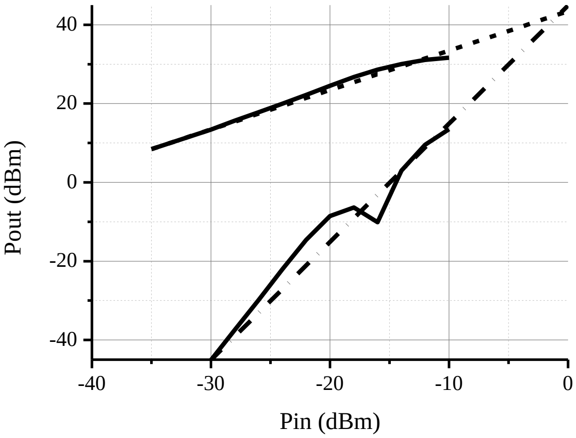

(b) 100 kHz.

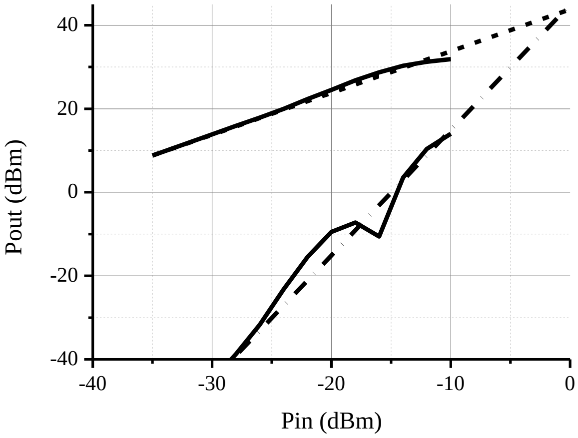

(c) 500 kHz.

Figure 3.19 Measured intermodulation performance of the upconverter.

Since a single sideband mixer is used in our upconverter, the sideband suppression performance of the upconverter is also measured, and the measured sideband suppression is −44.4 dBc and the measured carrier leakage is about −43 dBm.

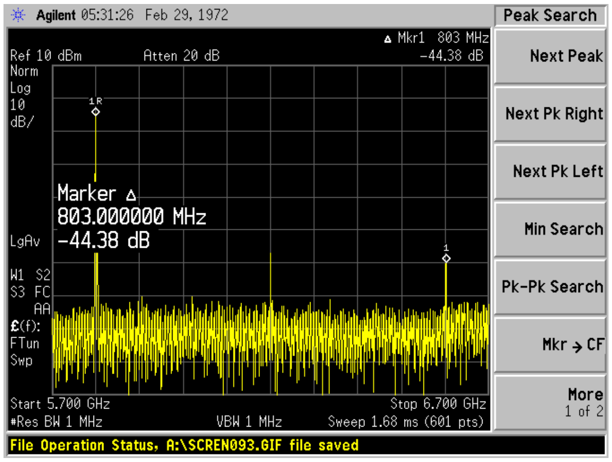

File Operation Status, A:\SCREN093.GIF file saved

Figure 3.20 Measured sideband suppression performance of the upconverter.

In order to evaluate the modulation accuracy of the upconverter, the error vector magnitude (EVM) is also measured with two input power levels using a vector signal analyzer (Rohde & Schwarz FSIQ40). Measurement results in the cases of three different modulation techniques are shown from Figure 3.21 to Figure 3.23. The following conclusions can be reached. In the first place, measured EVM is increased with the input power level. For example, in the case of BPSK modulation (Figure 3.21), measured EVM is increased from 1.5 % to 3 % if the input power is increased from −28 dBm to −18 dBm. Furthermore, for the same input power, measured EVM is increased from low- to high-order modulation schemes due to the reduction of Euclidean distance between constellation points as it can be seen from Figure 3.21(b) to Figure 3.23(b).

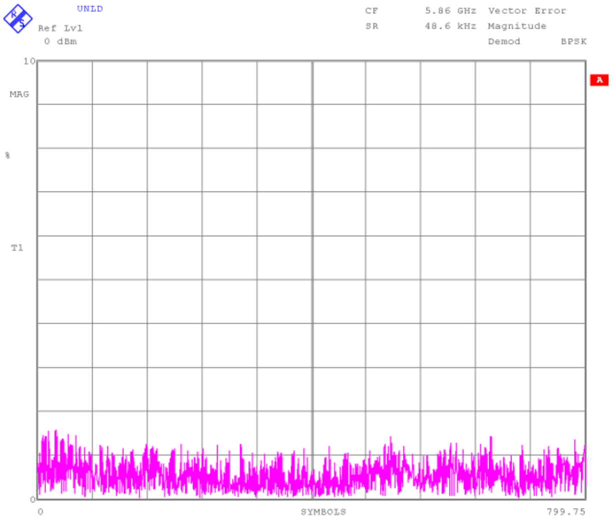

(a) $P_{in} = -28$ dBm.

(b) $P_{in} = -18$ dBm.

Figure 3.21 Measured EVM of BPSK signals.

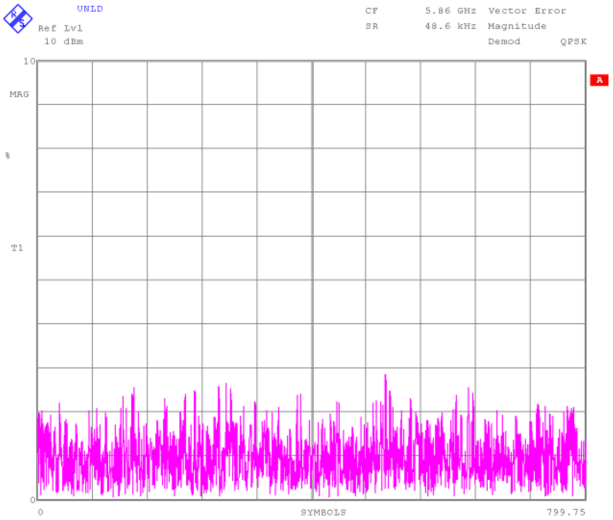

(a) $P_{in} = -28$ dBm.

(b) $P_{in} = -18$ dBm.

Figure 3.22 Measured EVM of QPSK signals.

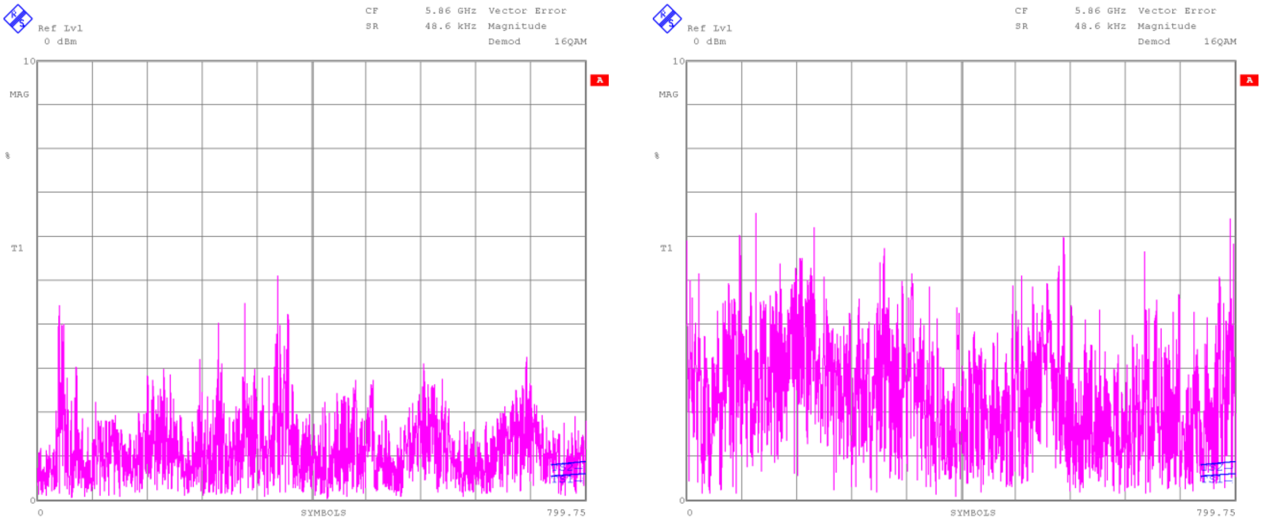

(a) $P_{in} = -28$ dBm.

(b) $P_{in} = -18$ dBm.

Figure 3.23 Measured EVM of 16QAM signals.

3.2.4 Active power divider

One distinct and key component in our proposed transceiver is the active power divider, which splits the modulated IF signal into two portions. The requirement for this device is good amplitude and phase balance as well as good impedance matching. Figure 3.24 shows the measured wideband performances of the active power divider. We can see that the measured impedance matching is better than 15 dB at the IF frequency and the output two channels have very good amplitude and excellent phase balance. When the amplifiers are switched off, this active power divider presents an isolation of more than 25 dB at the IF frequency of 400 MHz.

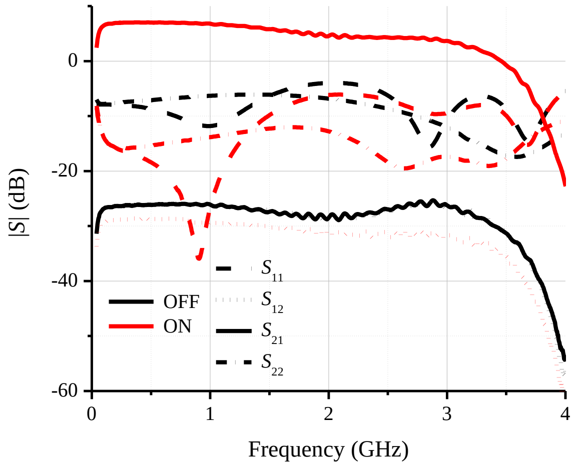

(a) $|S_{12}|$.

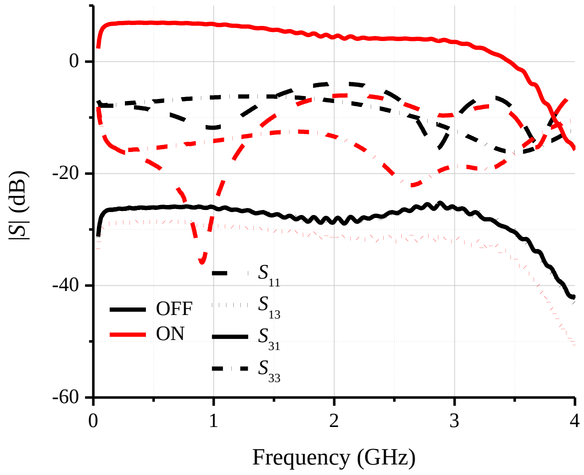

(b) $|S_{13}|$.

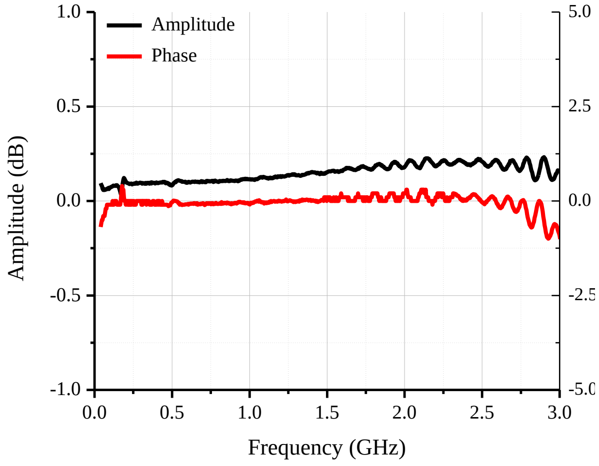

(c) Amplitude and phase balances.

Figure 3.24 Measured performances of the active power divider.

3.2.5 Downconverter

The gain and the noise figure of the downconverter without the Rx BPF are measured with a noise figure analyzer (Agilent N8975A) and the measurement results in Figure 3.25 show that the downconverter has a gain over 27 dB and a noise figure less than 1.5 dB for our interested frequency band. Considering the attenuation of the Rx BPF, the gain and the noise figure of the downconverter would be 25 dB and 3.5 dB.

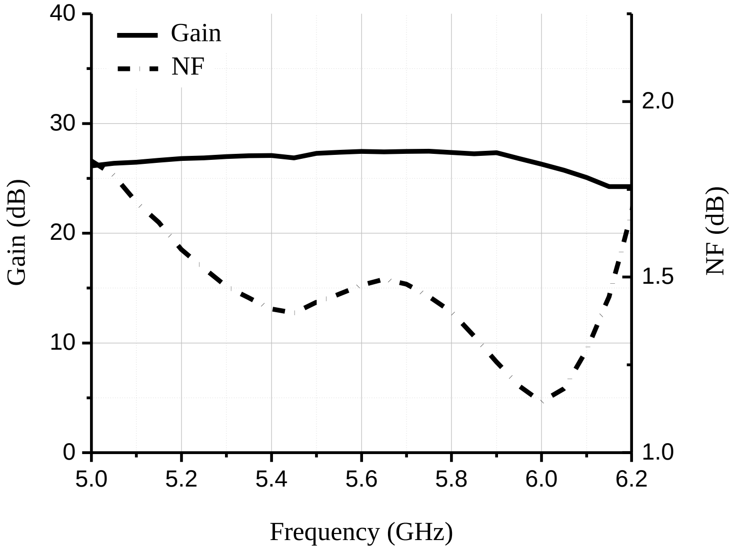

Figure 3.25 Measured gain and noise figure of the downconverter.

The gain compression and third-order intermodulation distortion of the downconverter is approximately measured under the conditions of different frequency differences between two injected sinusoidal signal tones. Measurement results in Figure 3.26 show that the downconverter has an input P1dB of −30 dBm and an input TOI of −15 dBm, which present a high linearity of our developed downconverter.

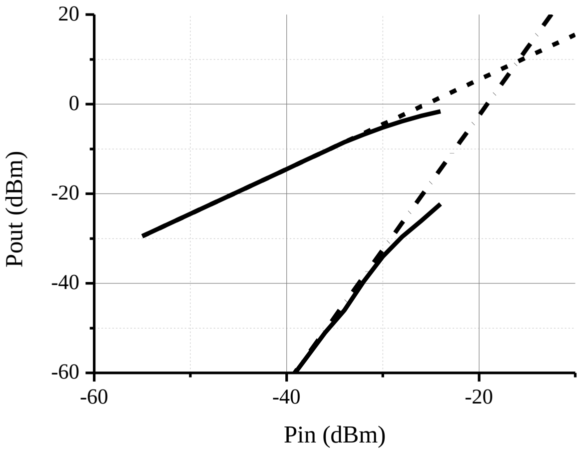

(a) 50 kHz.

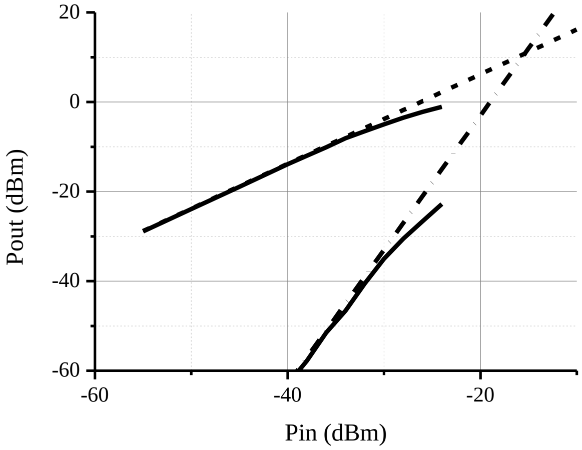

(b) 100 kHz.

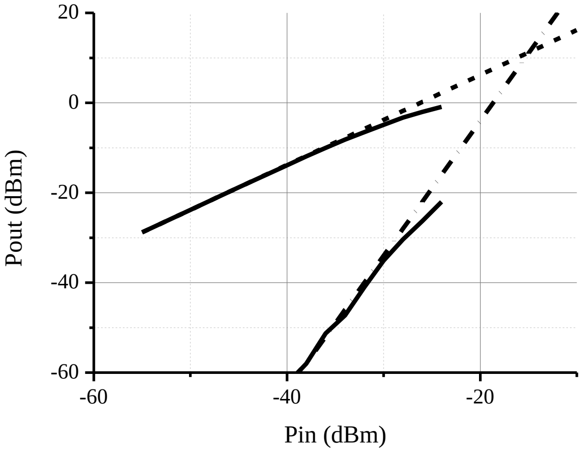

(c) 500 kHz.

Figure 3.26 Measured intermodulation performance of the downconverter.

Similar to that of the upconverter, the EVMs of the downconverter are measured for BPSK, QPSK and 16QAM signals with two input power levels and the results are given from Figure 3.27 to Figure 3.29. For a very low input signal level (−90 dBm), measured EVM of the downconverter is close to 10 % for all three modulation techniques. Nevertheless, if the input power is increased by 50 dB, measured EVMs are within 3 %, which suggests a great improvement of system performance.

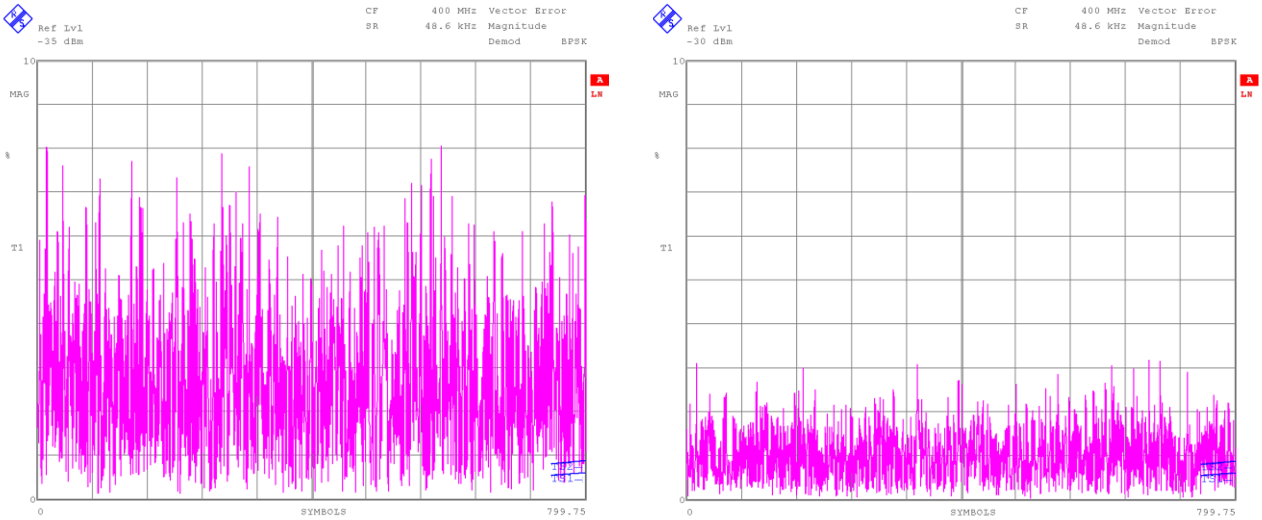

(a) P_{in} = −90 dBm.

(b) P_{in} = −40 dBm.

Figure 3.27 Measured EVM of BPSK signals.

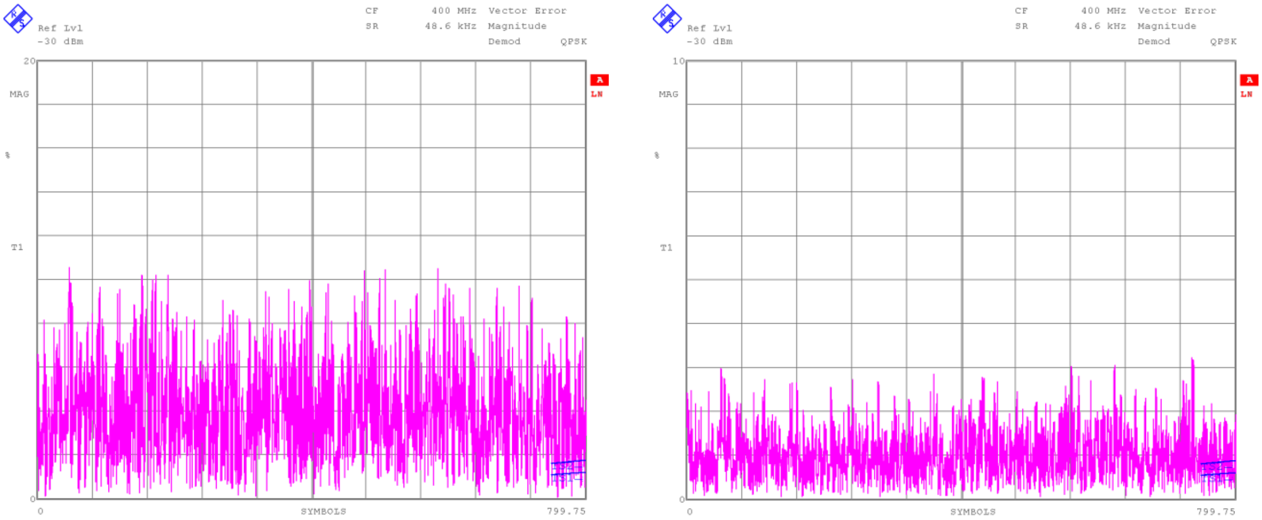

(a) P_{in} = −90 dBm.

(b) P_{in} = −40 dBm.

Figure 3.28 Measured EVM of QPSK signals.

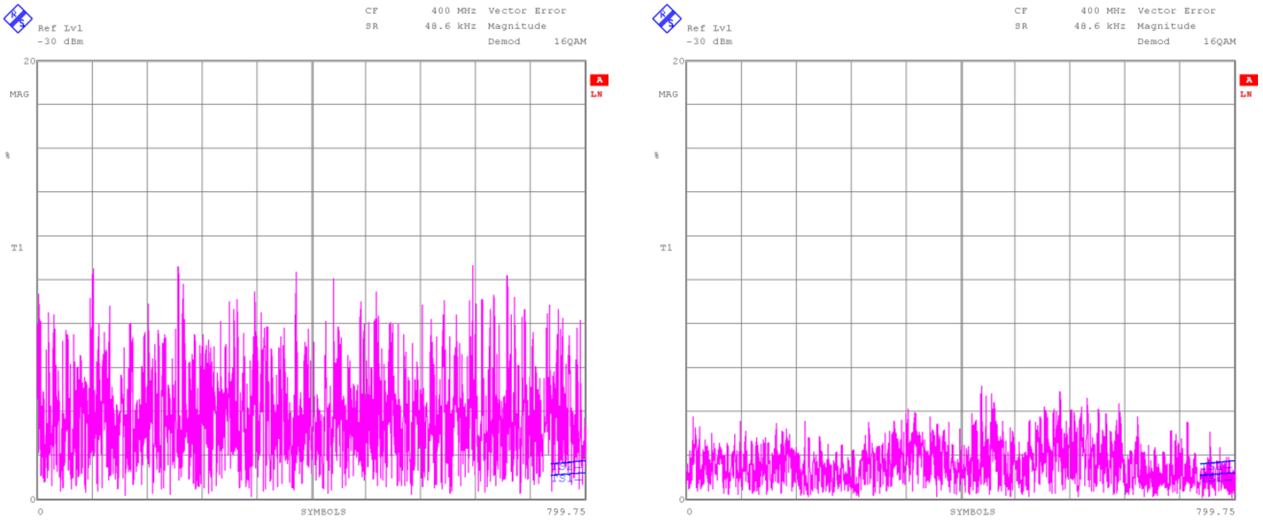

(a) $P_{in} = -90$ dBm.

(b) $P_{in} = -40$ dBm.

Figure 3.29 Measured EVM of 16QAM signals.

3.2.6 AGC circuit

Similar to the ALC circuit in the transmitter, an AGC circuit is designed in the receiver path on the basis of the block diagram in Figure 3.2. Measured performance of the AGC circuit is given in Figure 3.30. It presents that the prototyped AGC circuit has a gain control range of 40 dB with the same slope of −0.04 dB/mV that is defined by the logarithmic detector. A good linearity of gain control is also observed for the AGC circuit.

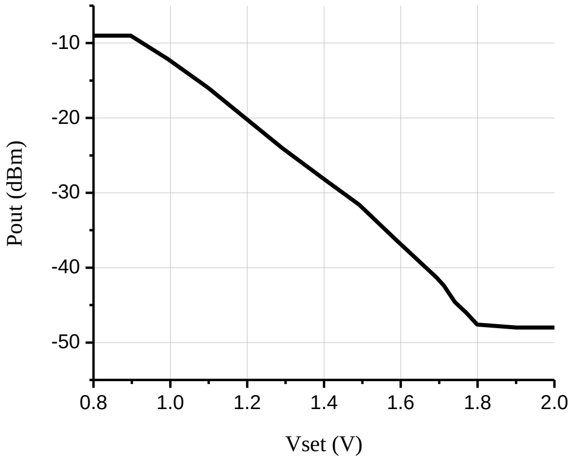

Figure 3.30 Measured AGC performance.

3.3 System measurement

After each building block being prototyped and measured, the transmitter and the receiver are separately encased into two boxes as shown in Figure 3.15. In this section, measurement of system performance will be presented in detail.

3.3.1 Measurement of the receiver prototype

In the beginning, the constellation of the received signal is measured using the setup sketched in Figure 3.31. The transmitted signal is generated with the help of a vector signal generator (Agilent E4438C), and then the transmitted signal is fed into a channel emulator (EB Propsim C8), which is able to simulate different channel conditions. In this case, the channel model in the channel emulator is set as AWGN. The channel emulator outputs the noisy signal to the receiver prototype, and finally both I and Q baseband signals are sent to a digital oscilloscope (Agilent DSO81204B) for observing the constellation of the demodulated signal. In Figure 3.31, two signal generators (Rohde & Schwarz SMR40 and Anritsu MG3694A) are used as the IF LO and RF LO, respectively.

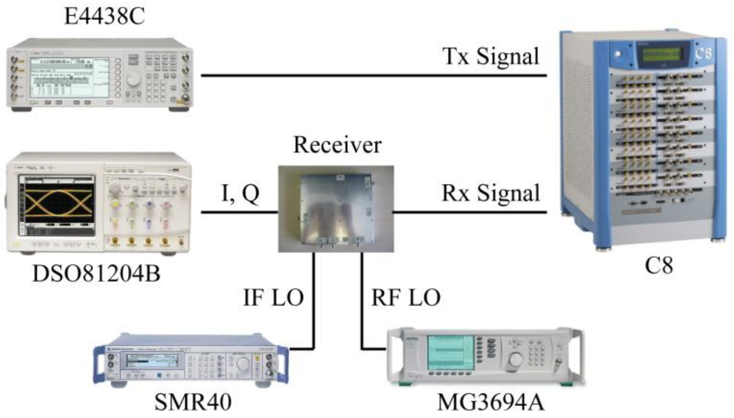

Figure 3.31 Experiment setup for measuring the constellation of demodulated signal.

Demodulated signals for three different modulation techniques including BPSK, 8PSK and 16 QAM are shown in Figure 3.32, Figure 3.33 and Figure 3.34, respectively. For the same modulation technique, the power level of the input signal is set at −100 dBm, and then it is increased by 10 dB in order to observe the improvement of the signal constellation. From Figure 3.32 to Figure 3.34, we can observe very good signal constellation when the input signal power level is −90 dBm. However, if the input signal level is 10 dB less, the receiver will fail to work properly for 8PSK and 16QAM as it can be seen from Figure 3.33(a) and Figure 3.34(a).

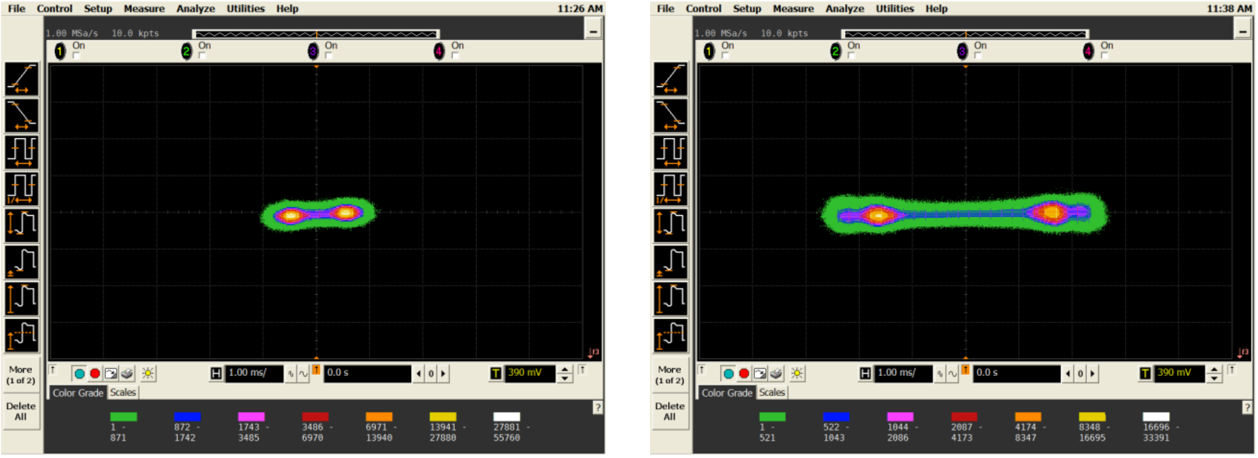

(a) $P_{in} = -100$ dBm. (b) $P_{in} = -90$ dBm.

1.55%	1.55%	3.1%	6.3%	12.5%	25.0%	50.0%

(c) Enlarged color bar.

Figure 3.32 Measured constellation of BPSK signals.

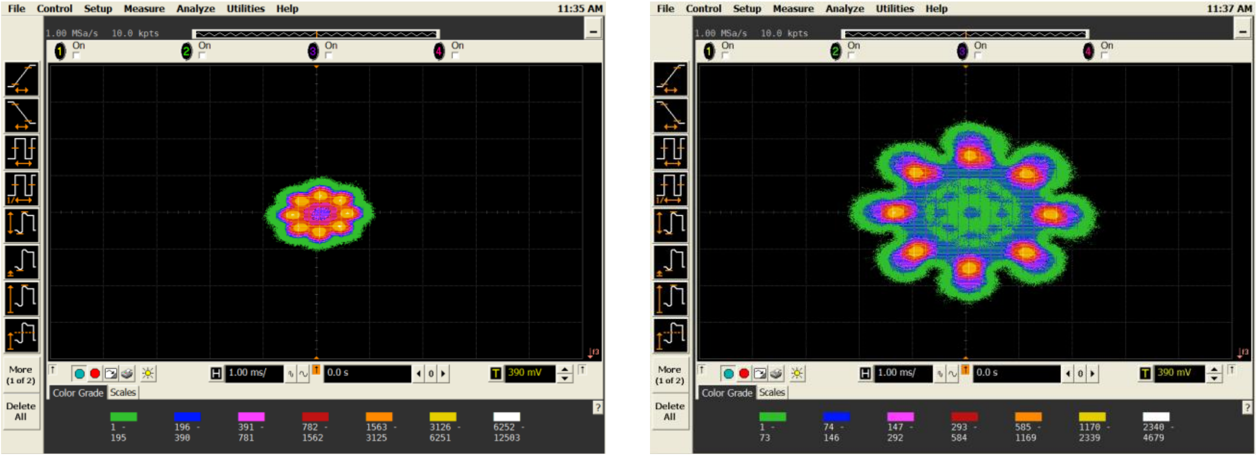

(a) $P_{in} = -100$ dBm. (b) $P_{in} = -90$ dBm.

1.55%	1.55%	3.1%	6.3%	12.5%	25.0%	50.0%

(c) Enlarged color bar.

Figure 3.33 Measured constellation of 8PSK signals.

(a) $P_{in} = -100$ dBm. (b) $P_{in} = -90$ dBm.

1.55%	1.55%	3.1%	6.3%	12.5%	25.0%	50.0%

(c) Enlarged color bar.

Figure 3.34 Measured constellation of 16QAM signals.

In the case of the same modulation technique, the signal constellation would become smeared if the input power of the signal remains the same but the data rate is increased. Theoretically, if the rate of data transmission is doubled, the required signal power should also be doubled (3 dB) in order to achieve the same system performance. In order to support our conclusion, the constellations of demodulated signal in three cases of data rates are measured for the same input signal power of −90 dBm and the results are given in Figure 3.35, Figure 3.36 and Figure 3.37. Note that from Figure 3.35 to Figure 3.37, each color in the enlarged color bar indicates the percentage of recorded data in the constellation diagram.

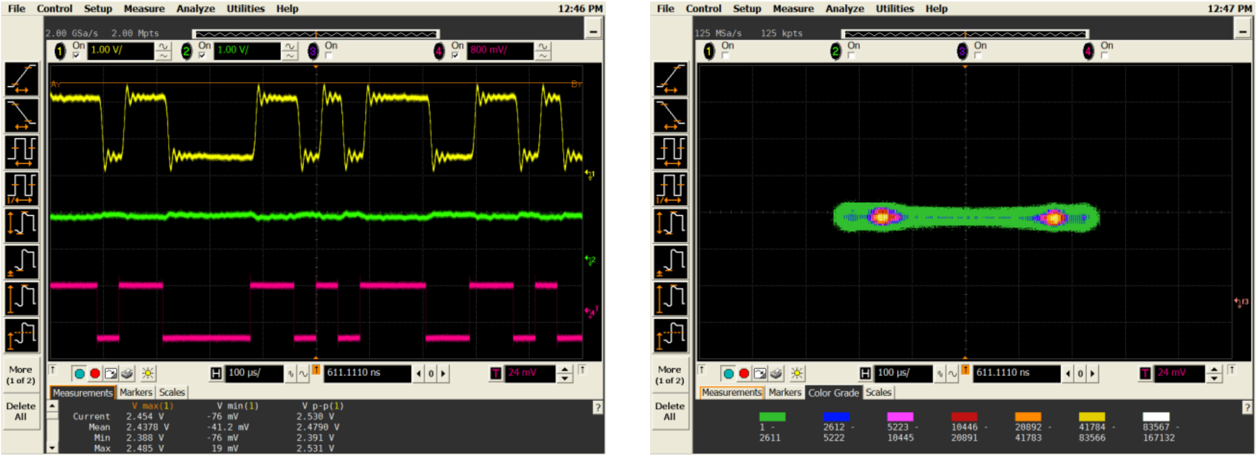

```
          V max(1)     V min(1)     V p-p(1)
Current   2.454 V      -76 mV       2.530 V
   Mean   2.4378 V     -41.2 mV     2.4790 V
    Min   2.388 V      -76 mV       2.391 V
    Max   2.485 V       19 mV       2.531 V
```

```
1 -     2612 -   5223 -   10446 -   20892 -   41784 -   83567 -
2611    5222     10445    20891     41783     83566     167132
```

(a) Waveform. (b) Constellation.

1.55%	1.55%	3.1%	6.3%	12.5%	25.0%	50.0%

(c) Enlarged color bar.

Figure 3.35 Measured results of BPSK signals for a data rate of 24.3 kbps.

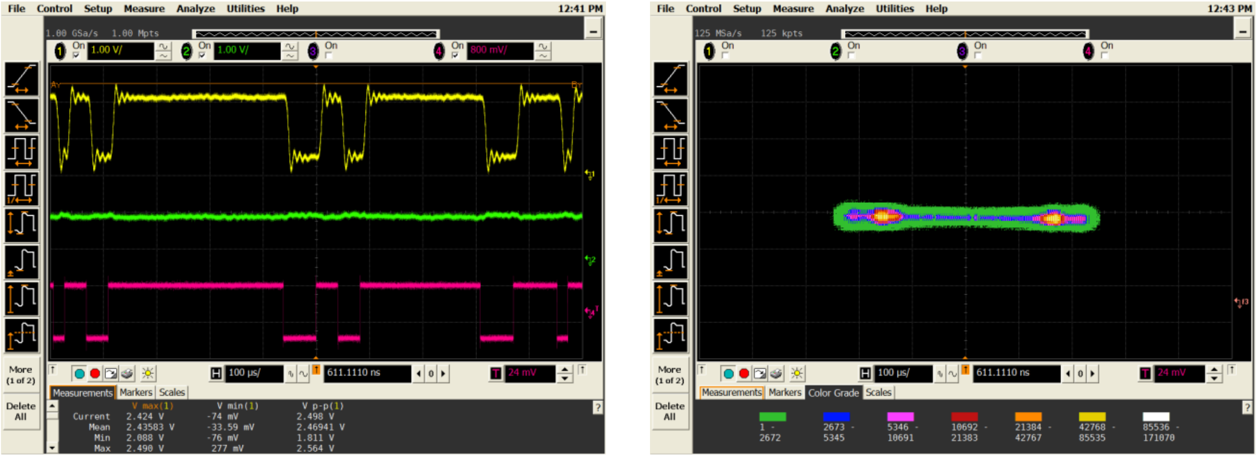

```
          V max(1)     V min(1)     V p-p(1)
Current   2.424 V      -74 mV       2.498 V
   Mean   2.43583 V    -33.59 mV    2.46941 V
    Min   2.088 V      -76 mV       1.811 V
    Max   2.490 V       277 mV      2.564 V
```

```
1 -     2673 -   5346 -   10692 -   21384 -   42768 -   85536 -
2672    5345     10691    21383     42767     85535     171070
```

(a) Waveform. (b) Constellation.

1.55%	1.55%	3.1%	6.3%	12.5%	25.0%	50.0%

(c) Enlarged color bar.

Figure 3.36 Measured results of BPSK signals for a data rate of 48.6 kbps.

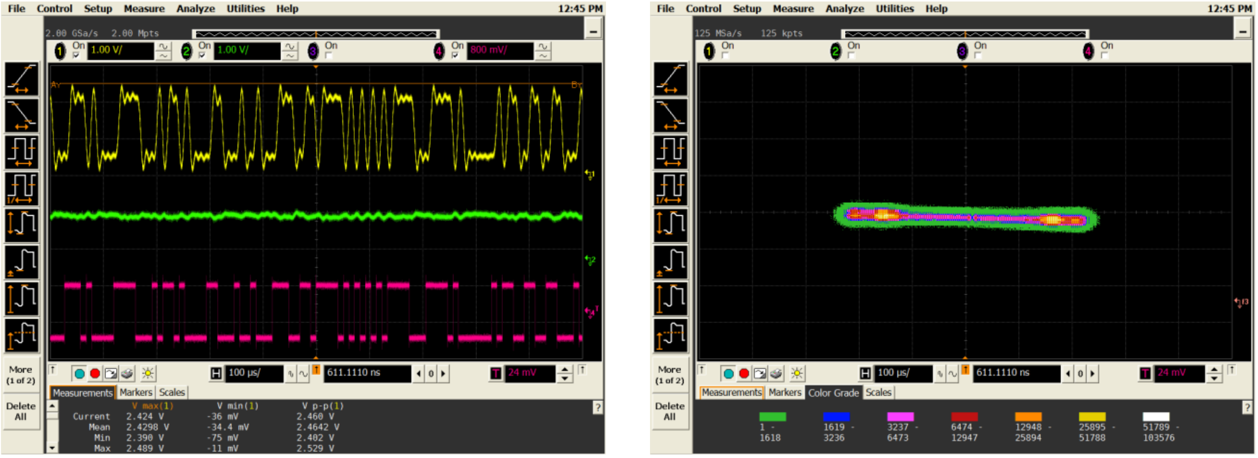

```
           V max(1)    V min(1)    V p-p(1)
Current    2.424 V     -36 mV      2.460 V
   Mean    2.4298 V    -34.4 mV    2.4642 V
    Min    2.390 V     -75 mV      2.402 V
    Max    2.489 V     -11 mV      2.529 V
```

(a) Waveform.

(b) Constellation.

(c) Enlarged color bar.

Figure 3.37 Measured results of BPSK signals for a data rate of 97.2 kbps.

3.3.2 Laboratory experiment

3.3.2.1 Radio mode

The BER measurement setup of the receiver is sketched in Figure 3.38. The BER tester (Anritsu MP1630B) generates a 10-Mbps pseudo-random bit sequence (PRBS) with a maximum length of 2^{23}-1, which is modulated by a vector signal generator (Agilent E4438C) and then fed into the channel emulator (EB Propsim C8) with the configuration of an AWGN channel. The output of the channel emulator is injected into the receiver, and then the demodulated signal is sent back to the BER tester which calculates the BER by comparing the transmitted data and the received data. In Figure 3.38, two signal generators (Anritsu MG3694A and Rohde & Schwarz SMR40) are used as the RF LO and IF LO, respectively.

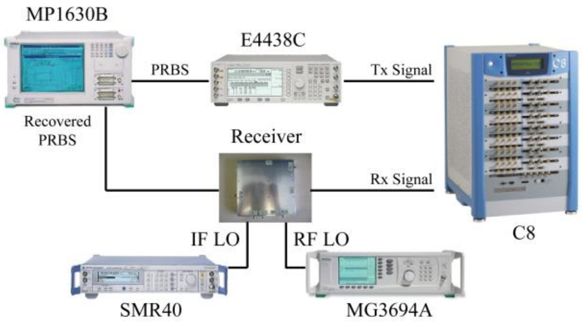

Figure 3.38 BER measurement setup.

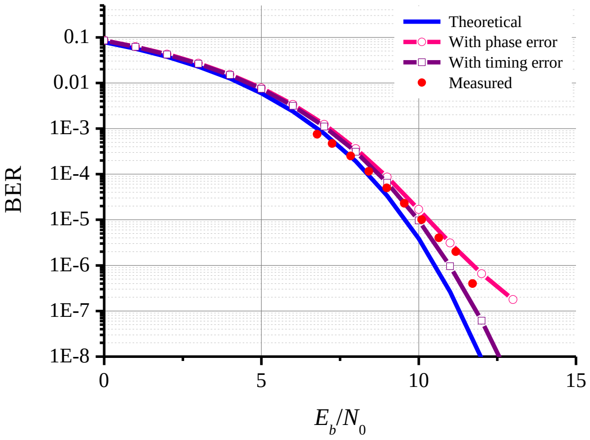

Figure 3.39 BER measurement results.

The measured BER is compared with the theoretical values in Figure 3.39. It can be observed that they agree pretty well except for a small deviation at high E_b/N_0 when the measured BER is too low and thus difficult to detect. Another reason is the theoretical BER is derived from the ideal system model, which is not obtainable in this practical implementation due to phase noise degradation and nonlinear distortion involved in the experiment. In order to evaluate these parasitic effects, two important aspects of system measurement are analyzed. One is the phase error with a mean of zero and a variance of 0.25 while the other is the timing error with a mean of zero and a variance of $0.15/\pi$. In order to simplify our analysis, they are separately considered. Simulation results shown in Figure 3.39 manifest that both the phase and timing errors that exist in our system measurement can easily degrade the measured BER, which is bounded by our simulated curves due to the fact that these two effects are actually not independent.

3.3.2.2 Radar mode

The system performance in the radar mode is measured using the test setup shown in Figure 3.40. This test setup is arranged in a way corresponding to Figure 2.12. The modulated signal generated by the DDS is sent to the transmitter, and then after being amplified and upconverted, the transmitted signal is fed into the channel emulator. The channel emulator is configured to have a set of time delays from 1500 ns to 5000 ns and a set of target velocities from 10 m/s to 80 m/s, which fully covers the requirements in practical applications. The transmitted signal is attenuated by the channel emulator and two additional external attenuators. The input signal level at the receiver is −100 dBm. The received signal is then downconverted and amplified, and sampled by ADCs in the ARM board. The digitized signal is sent to the laptop for signal processing through the USB interface. The FFT algorithm with zero padding is used to estimate the beat frequencies, from which the time delay and the velocity configured in the channel emulator are finally calculated.

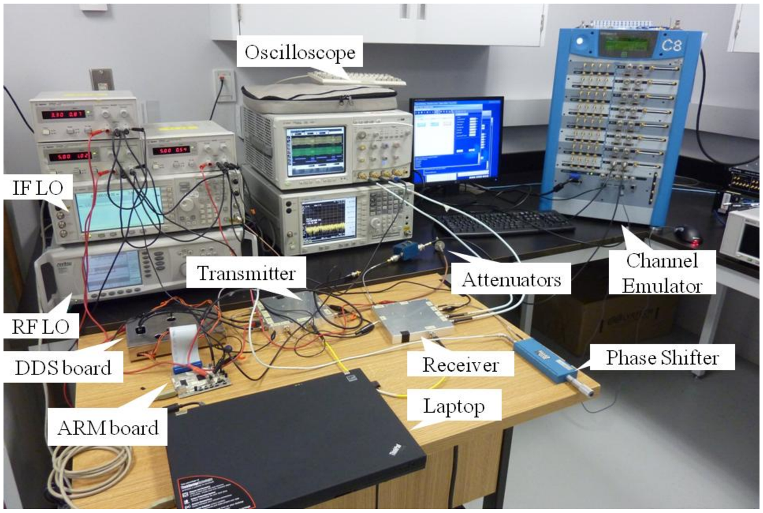

Figure 3.40 Measurement setup of the radar mode.

Table 3.3 Comparison between predefined values and measurement results.

Predefined values		Measured results	
Delays (ns)	Velocities (m/s)	Delays (ns)	Velocities (m/s)
1500	10	1500.95	10.00
1500	20	1503.92	19.84
1500	30	1497.99	29.99
1500	40	1497.99	39.99
1500	50	1495.02	49.99
1500	60	1497.99	59.83
1500	70	1500.95	69.83
1500	80	1497.99	79.83
2000	10	1996.33	10.15
2000	20	1996.33	19.99
2000	30	1996.33	29.99
2000	40	1996.33	39.99
2000	50	1996.33	49.83
2000	60	1996.33	59.83
2000	70	1996.33	69.83
2000	80	1996.33	79.67
3000	10	2995.97	10.00
3000	20	2995.97	19.99
3000	30	2993.00	29.99
3000	40	2993.00	39.99
3000	50	2993.00	49.99
3000	60	2993.00	59.83
3000	70	2998.94	69.83
3000	80	2993.00	79.97
4000	10	4001.55	9.85
4000	20	3995.62	19.99
4000	30	3995.62	29.99
4000	40	3989.69	40.14
4000	50	3992.65	49.99
4000	60	3995.62	59.83
4000	70	3995.62	69.83
4000	80	3995.62	79.67
5000	10	4992.30	10.00
5000	20	4992.30	19.99
5000	30	4989.33	29.99
5000	40	4989.33	39.99
5000	50	4992.30	49.83
5000	60	4992.30	59.83
5000	70	4989.33	69.83
5000	80	4989.33	79.98

Table 3.3 lists both the predefined and measured time delays and target velocities, which are also plotted in Figure 3.41 in order to provide a better visualization.

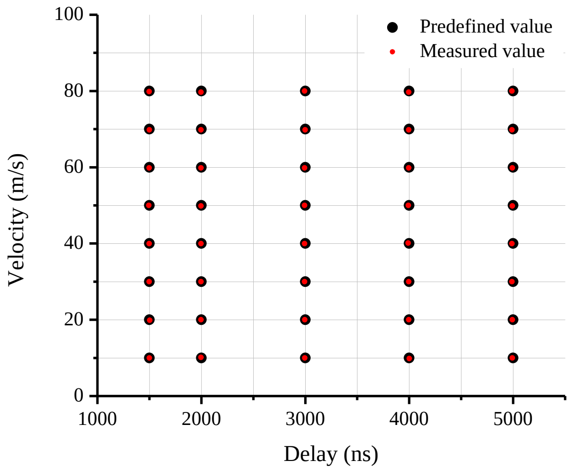

Figure 3.41 Measured results of the radar mode.

Based on our measurement results, mean and standard deviation of our delay and velocity measurement are respectively calculated and shown in Table 3.4 and Table 3.5. Very small error is observed, which fully demonstrates excellent target finding capability of our proposed multifunctional transceiver.

Table 3.4 Mean and standard deviation of delay measurement.

Delay (ns)	Mean (ns)	Standard deviation
1500	1499.10	2.72
2000	1996.33	0.00
3000	2994.50	2.25
4000	3995.20	3.34
5000	4990.80	1.59

Table 3.5 Mean and standard deviation of velocity measurement.

Velocity (m/s)	Mean (m/s)	Standard deviation
10	10.00	0.11
20	19.96	0.07
30	29.99	0.00
40	40.02	0.07
50	49.93	0.09
60	59.83	0.00
70	69.83	0.00
80	79.82	0.15

3.3.2.3 Joint mode

The same test setup in Figure 3.40 is also used to perform an overall evaluation of the system performance. Figure 3.42 shows a typical waveform of the received signal in the case of a static object. The yellow and green curves represent the output signals of the receiver front-end at both I and Q channels, respectively. The purple curve shows the mode select signal of the DDS and it is also duplexed to send information data in the radio mode.

In the radio mode, the ADCs are running at four times of the bit rate in our implementation. The Gardner synchronization algorithm is applied for three reasons [67]-[69]. The first is that the ADCs’ clock is not synchronized with the received data sequence. The second is the existence of the ADC time jitter. The third is that a timing recovery loop in the synchronization algorithm can provide the best timing for sampling the matched filter output at the peaks, where the signal-to-noise ratio is the highest and the signal detection will have the lowest error. The recovered data is compared together with the transmitted data and the received data in Figure 3.43, from which it can be seen that the transmitted data can be successfully recovered.

Acquisition is stopped.
50.0 MSa/s   10.0 Mpts

Source	Vertical Scale	Offset	Horizontal Scale	Position
channel 1	1.00 V/div	-1.169 V	20.0000 ms/div	0.0 s
channel 2	1.00 V/div	1.560 V	20.0000 ms/div	0.0 s
channel 3	200 mV/div	746 mV	20.0000 ms/div	0.0 s

Figure 3.42 A typical waveform of the received signal for a static object.

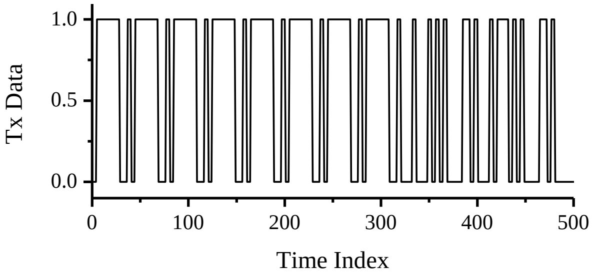

(a) Transmitted signal.

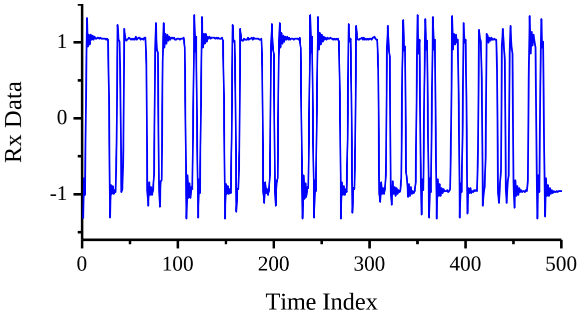

(b) Received signal.

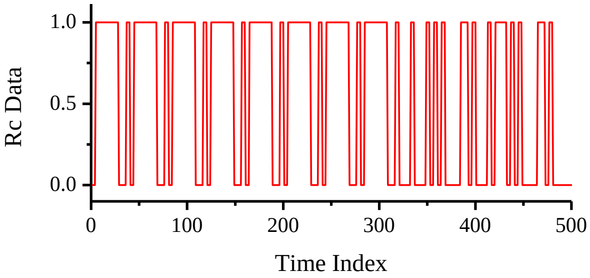

(c) Recovered signal.

Figure 3.43 Comparison between transmitted data, received data and recovered data.

3.3.3 Experiment on terrace

For proving the system performance in real-world applications, our system prototype was also used to measure the distance of the baluster on a terrace and the measurement setup is shown in Figure 3.44. Measurement results given in Figure 3.45 assert that our system has a high accuracy of range detection.

Figure 3.44 Experiment setup for measuring the distance of a baluster.

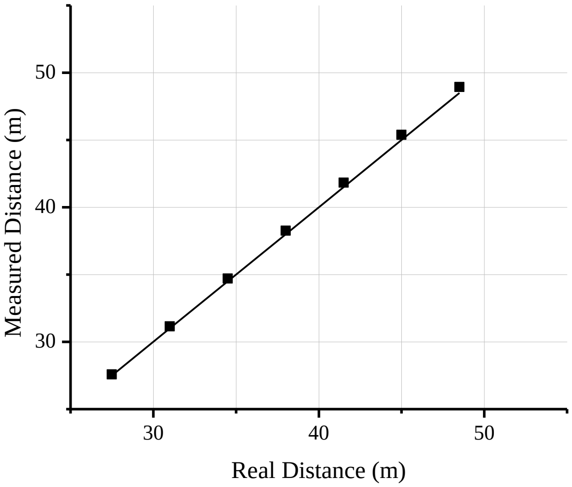

Figure 3.45 Measured results of the baluster.

3.4 Conclusion

This chapter describes the design of a number of circuits for our 5.9-GHz system demonstrator including the DDS, ALC and AGC circuits, SIW bandpass filters, and microstrip array antenna. In addition, measurement results of system building blocks such as modulator, downconverter, and active power divider are presented. The entire system is finally prototyped and measured for different operation modes both in the lab and on the terrace. Experimental results show very good system performance, which validates our proposed modulation waveform and system concept.

CHAPTER 4 A 24-GHZ SYSTEM PROTOTYPE: ANALYSIS AND SIMULATION

Both data rate for the communication mode and range resolution for the radar mode of our 5.9-GHz system demonstrator are limited by the available bandwidth of the DSRC rule that is defined by the U.S. FCC. Nevertheless, there is a bandwidth up to 250 MHz in the 24-GHz ISM-band that is also adopted for vehicular applications. Therefore, our proposed system concept will be prototyped at 24 GHz by using the SIW technology, which has been proven to be more cost-effective than conventional solutions [35]. In this chapter, we will present the analysis and simulation of our 24-GHz system prototype .

4.1 System analysis

4.1.1 System specifications and link budget analysis

Based on the FCC's rules and practical requirements for vehicular applications, we proposed the specifications listed in Table 4.1 for our 24-GHz system prototype. Note that in this proof-of-concept study, the sweeping bandwidth is 100 MHz, which is limited by our DDS evaluation board. However, compared to our low-frequency system demonstrator, both the range resolution and communication data rate can be increased by a factor of 5.

In the same way, link budget was analyzed for validating system functionality and the analysis results are listed in Table 4.2 for reference. Compared to our analysis results in Table 2.5, we can find that in addition to higher attenuation of the radio-wave at 24 GHz, the maximum transmitting power is limited to 10 dBm, and therefore, two array antennas with 22 dBi will be designed to guarantee the system operational range. For our 24-GHz system prototype, similar conclusions can be made from the comparison between radar and radio modes. First of all, the radar signal has higher attenuation in spite of the RCS gain, and therefore, the receiver will be equipped with an AGC circuit. In addition, the receiver bandwidth has to be reduced to 100 KHz for suppressing excessive noise in the radar mode. Furthermore, radar and radio modes have respectively 10.9 dB and 10.4 dB link margins, which include potential implementation loss and atmospheric loss as well as fading loss which is more pronounced in the radio mode for data communications.

Table 4.1 System specifications of 24-GHz system prototype.

Mode	Specifications	Values
	Frequency Range	24.075 to 24.175 GHz
Radar	Maximum Detectable Range	100 m
	Range Resolution	1.5 m
	Maximum Detectable Velocity	±260 km/h (69.44 m/s)
	Velocity Resolution	±1.8 km/h (0.5 m/s)
	Probability of False Alarm	1e-6
	Probability of Detection	0.9
Radio	Maximum Communication Range	500 m
	Maximum Data Rate	50 Mbps
	Bit Error Rate for BPSK	1e-6

Table 4.2 Link budget analysis for 24-GHz system prototype.

Parameters	Radar Mode	Radio Mode
Function Range	100 m	500 m
Total Cycle	37.5 ms	12.5 ms
Receiver Bandwidth	100 KHz	100 MHz
Transmitting Power	10 dBm	10 dBm
Transmitting Antenna Gain	22 dBi	22 dBi
Path Loss	200.2 dB	114.1 dB
Radar Cross Section Gain of a Car	49.1 dB	—
Receiving Antenna Gain	22 dBi	22 dBi
Signal Power at the Receiver Input	–97.1 dBm	–68.1 dBm
Noise Power at the Receiver Input	–131.0 dBm	–94.0 dBm
SNR at the Receiver Input	33.9 dB	25.9 dB
Receiver Noise Figure	8 dB	8 dB
SNR at the Receiver Output	25.9 dB	17.9 dB
Data Rate	—	50 Mbps
E_b/N_0	—	20.9 dB
Required SNR (E_b/N_0 for radio mode)	15 dB	10.5 dB
Link Margin	10.9 dB	10.4 dB

4.1.2 Transceiver architecture

The transceiver architecture of our 24-GHz system prototype is sketched in Figure 4.1. In our transceiver, our proposed modulation waveform is generated with the same DDS evaluation board and an ARM board is used to send the control signals and data signals into the DDS board. Since the operation principle of this transceiver is similar to that of the 5.9-GHz system demonstrator, we would not repeat it here. However, some differences between the present 24-GHz system prototype and 5.9-GHz system demonstrator will be described. First, the power back-off of the transmitted signal is controlled by the DDS instead of an additional ALC circuit. Second, the transmitted IF signal is split by an interdigitated coupler and its detailed design procedure will be presented in the next chapter. Third, the RF signal after the mixer is successively filtered by a RF BPF and a Tx BPF that are both implemented using the SIW technology. Fourth, in the receiving chain, the Rx BPF is the same as the Tx BPF since the system is operating in TDD mode. Finally, a portion of the received signal is coupled to indicate the received signal strength as well as to control the IF VGA for compensating the signal attenuation.

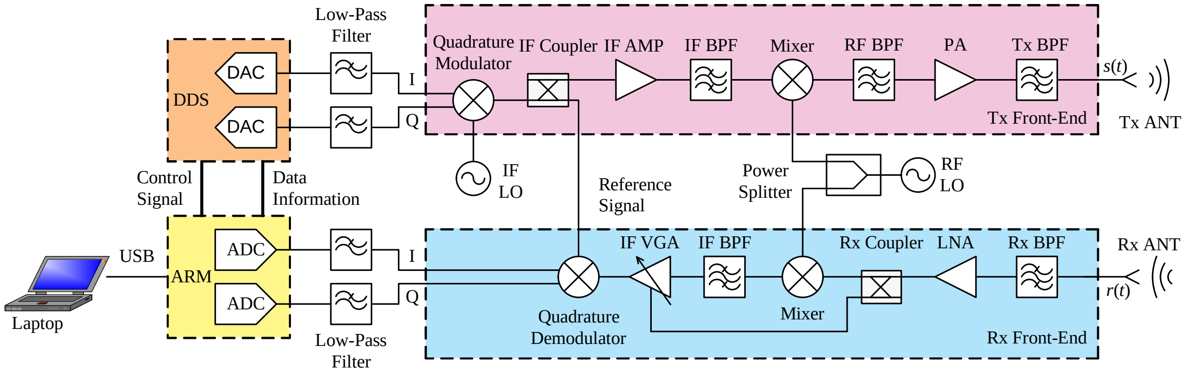

Figure 4.1 Transceiver architecture of 24-GHz system prototype.

4.2 System simulation

4.2.1 Chain budget simulation of the upconverter

In the design of the upconverter, two design aspects are considered. One is that the number of amplifiers is minimized, and the other is that amplifying stages are located at the IF frequency since low-frequency amplifiers are much cheaper than their high-frequency counterparts. Our designed upconverter is simulated using the block diagram in Figure 4.2. Since we have introduced the harmonic balance simulation in Section 2.2.1 and 2.2.2, we are going to present only the simulation results of the chain budget.

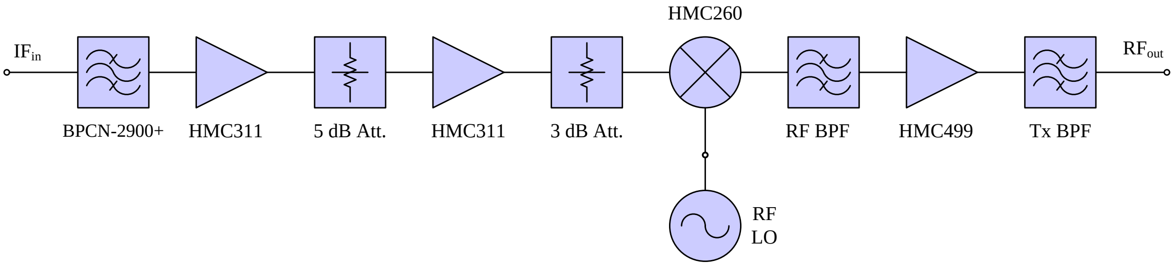

Figure 4.2 Simulation diagram of the upconverter.

Figure 4.3 gives the simulation results of chain budget of our upconverter in the case of a nominal input power of −10 dBm. From Figure 4.3, we can observe that the input return loss is 10.4 dB because of the poor matching of the first gain block (HMC311). In case that the input power is −10 dBm, the output power of the upconverter is 10.2 dBm. The output P1dB and output TOI of the upconverter are 10.5 dBm and 19.7 dBm, respectively. Finally, the noise figure of the upconverter is 13.5 dB.

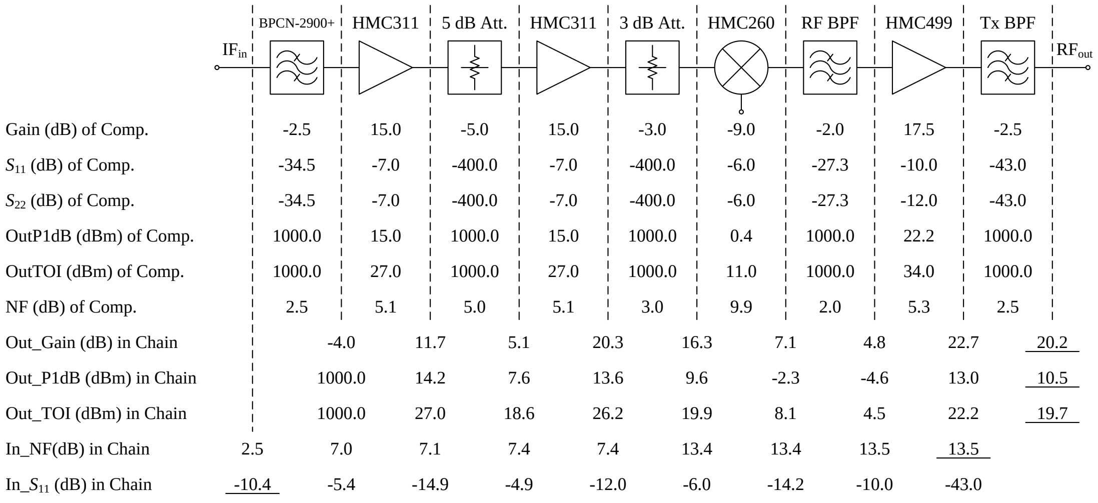

	IF$_{in}$	BPCN-2900+		HMC311		5 dB Att.		HMC311		3 dB Att.		HMC260		RF BPF		HMC499		Tx BPF	RF$_{out}$
Gain (dB) of Comp.		-2.5		15.0		-5.0		15.0		-3.0		-9.0		-2.0		17.5		-2.5	
S_{11} (dB) of Comp.		-34.5		-7.0		-400.0		-7.0		-400.0		-6.0		-27.3		-10.0		-43.0	
S_{22} (dB) of Comp.		-34.5		-7.0		-400.0		-7.0		-400.0		-6.0		-27.3		-12.0		-43.0	
OutP1dB (dBm) of Comp.		1000.0		15.0		1000.0		15.0		1000.0		0.4		1000.0		22.2		1000.0	
OutTOI (dBm) of Comp.		1000.0		27.0		1000.0		27.0		1000.0		11.0		1000.0		34.0		1000.0	
NF (dB) of Comp.		2.5		5.1		5.0		5.1		3.0		9.9		2.0		5.3		2.5	
Out_Gain (dB) in Chain			-4.0		11.7		5.1		20.3		16.3		7.1		4.8		22.7		20.2
Out_P1dB (dBm) in Chain			1000.0		14.2		7.6		13.6		9.6		-2.3		-4.6		13.0		10.5
Out_TOI (dBm) in Chain			1000.0		27.0		18.6		26.2		19.9		8.1		4.5		22.2		19.7
In_NF(dB) in Chain	2.5		7.0		7.1		7.4		7.4		13.4		13.4		13.5		13.5		
In_S_{11} (dB) in Chain	-10.4		-5.4		-14.9		-4.9		-12.0		-6.0		-14.2		-10.0		-43.0		

Figure 4.3 Simulated chain budget of the upconverter.

4.2.2 Chain budget simulation of the downconverter

The downconverter is simulated according to the block diagram in Figure 4.4. The Rx BPF is essentially the same as the Tx BPF in the upconverter, which will be outlined in the next chapter.

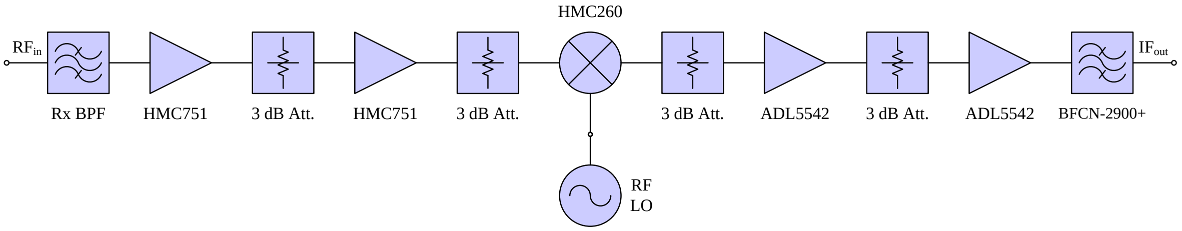

Figure 4.4 Simulation diagram of the downconverter.

The budget analysis results of the receiving chain given in Figure 4.5 presents very good input matching and low noise figure, which satisfy our design specifications. The downconverter has a small signal gain of about 60 dB, and it will be compressed by 1 dB when the input power is −46.5 dBm. Moreover, the input and output TOI are −29.6 dBm and 30.4 dBm, respectively.

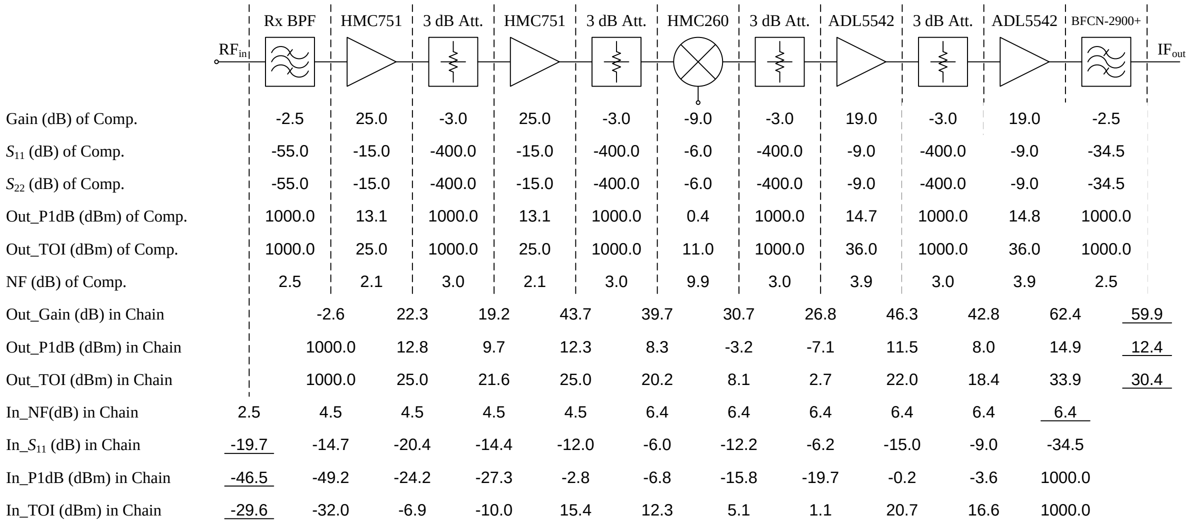

	RF$_{in}$	Rx BPF		HMC751		3 dB Att.		HMC751		3 dB Att.		HMC260		3 dB Att.		ADL5542		3 dB Att.		ADL5542		BFCN-2900+	IF$_{out}$
Gain (dB) of Comp.		-2.5		25.0		-3.0		25.0		-3.0		-9.0		-3.0		19.0		-3.0		19.0		-2.5	
S_{11} (dB) of Comp.		-55.0		-15.0		-400.0		-15.0		-400.0		-6.0		-400.0		-9.0		-400.0		-9.0		-34.5	
S_{22} (dB) of Comp.		-55.0		-15.0		-400.0		-15.0		-400.0		-6.0		-400.0		-9.0		-400.0		-9.0		-34.5	
Out_P1dB (dBm) of Comp.		1000.0		13.1		1000.0		13.1		1000.0		0.4		1000.0		14.7		1000.0		14.8		1000.0	
Out_TOI (dBm) of Comp.		1000.0		25.0		1000.0		25.0		1000.0		11.0		1000.0		36.0		1000.0		36.0		1000.0	
NF (dB) of Comp.		2.5		2.1		3.0		2.1		3.0		9.9		3.0		3.9		3.0		3.9		2.5	
Out_Gain (dB) in Chain			-2.6		22.3		19.2		43.7		39.7		30.7		26.8		46.3		42.8		62.4		59.9
Out_P1dB (dBm) in Chain			1000.0		12.8		9.7		12.3		8.3		-3.2		-7.1		11.5		8.0		14.9		12.4
Out_TOI (dBm) in Chain			1000.0		25.0		21.6		25.0		20.2		8.1		2.7		22.0		18.4		33.9		30.4
In_NF(dB) in Chain	2.5		4.5		4.5		4.5		4.5		6.4		6.4		6.4		6.4		6.4		6.4		
In_S_{11} (dB) in Chain	-19.7		-14.7		-20.4		-14.4		-12.0		-6.0		-12.2		-6.2		-15.0		-9.0		-34.5		
In_P1dB (dBm) in Chain	-46.5		-49.2		-24.2		-27.3		-2.8		-6.8		-15.8		-19.7		-0.2		-3.6		1000.0		
In_TOI (dBm) in Chain	-29.6		-32.0		-6.9		-10.0		15.4		12.3		5.1		1.1		20.7		16.6		1000.0		

Figure 4.5 Simulated chain budget of the downconverter.

4.2.3 System-level simulation

4.2.3.1 Simulation of radar mode

System performance in the radar mode is verified by comparing the predefined target range and velocity with simulation results. The comparison made in Table 4.3 shows that our system can obtain very accurate detection results.

Table 4.3 Simulation results of the radar mode.

Simulation parameters		Simulation results	
T_S	0.5 ms	f_{bU}	105 KHz
ΔB	100 MHz	f_{bC}	5 KHz
f_{RF}	24125 MHz	f_{bD}	95 KHz
R	75 m	Calculated R	75 m
v	31.09 m/s	Calculated v	31.09 m/s

It should be noted that in our system, a high IF LO and a low RF LO are selected and therefore, the frequency sweeping is reversed through the frequency upconverting, which results in the fact that beat frequency in the upchirp is higher than that in the downchirp for an incoming target.

4.2.3.2 Simulation of radio mode

In the case of the data transmission, Figure 4.6 compares the transmitted signal having a rate of 50 Mbps with the demodulated signal from our system under three different conditions of E_b/N_0. It is obvious that the demodulated signal is hardly contaminated by the noise for low E_b/N_0, however, it can still be recovered through matched filters. On the other hand, we can also conclude that a modulated signal with high E_b/N_0 can be accurately demodulated by our receiver with a very small distortion from Figure 4.6(c).

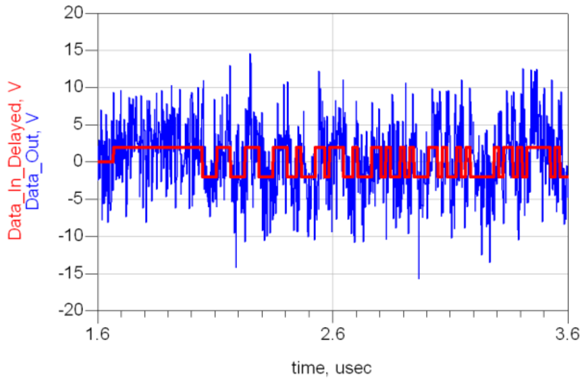

(a) E_b/N_0 = 0 dB.

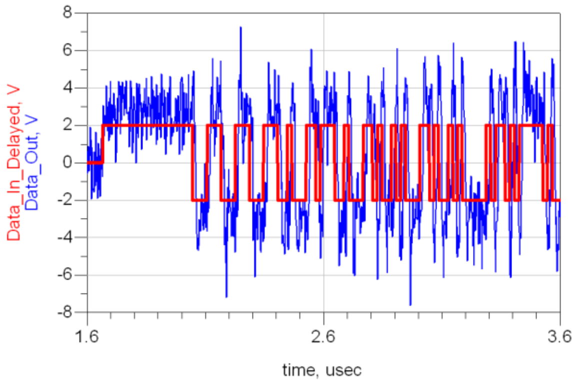

(b) E_b/N_0 = 10 dB.

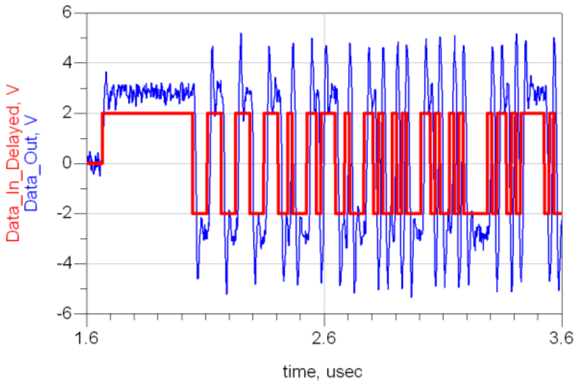

(b) E_b/N_0 = 20 dB.

Figure 4.6 Comparison between transmitted and received radio baseband signals.

4.3 Conclusion

This chapter is concerned with the design and simulation of our 24-GHz system. Following the system specifications and link budget analysis, the transceiver architecture is presented and analyzed. Then, simulation of the entire system is carried out for both radar and radio mode, which shows very good performance.

CHAPTER 5 DESIGN OF PASSIVE COMPONENTS FOR 24-GHZ SYSTEM PROTOTPYE

Our 24-GHz system prototype is designed by means of the SIW technology, and therefore, in this chapter, we will introduce synthesis and design methods of a number of innovative SIW structures including wideband SIW couplers, broadband SIW phase shifters, and highly-selective SIW filters. In addition, an accurate method for synthesizing four-line interdigitated couplers will presented and two design examples will be described including a conventional Lange coupler and a composite microstrip-CPW coupler that is used as the IF coupler in our systems.

5.1 Wideband 3-dB 90 ºSIW couplers

So far, conventional short-slot or Riblet hybrid has been directly implemented using SIW technology for developing mixers [36]-[37] and array antennas [38]-[40]. However, the original Riblet hybrid makes use of a capacitive dome or tuning screws to improve the field matching, which complicates the design procedure and the fabrication process [71]. Therefore, a simple Riblet hybrid was reported using multi-stepped coupling section in order to keep the bandwidth in connection with good coupler performances [72]. It eventually leads to arc-type tapering junction for facilitating the fabrication that is usually designed through iterative optimization [73].

As we know, SIW can be regarded as a specific dielectric-filled rectangular waveguide, of which the guided wavelength varies quickly with frequency, especially when the substrate has a high dielectric constant. Therefore, this strong dispersion effect renders it difficult to achieve a wide bandwidth judging from both amplitude and phase responses for directional couplers using the SIW technology.

In this section, a wideband SIW coupler is thoroughly studied, whose simplified geometry is shown in Figure 5.1. Through a smooth coupling slot tapering, good matching of EM fields and effective suppression of high-order modes can be expected over a wide frequency band. An accurate and efficient design procedure is proposed in order to facilitate the development of this kind of directional couplers [41].

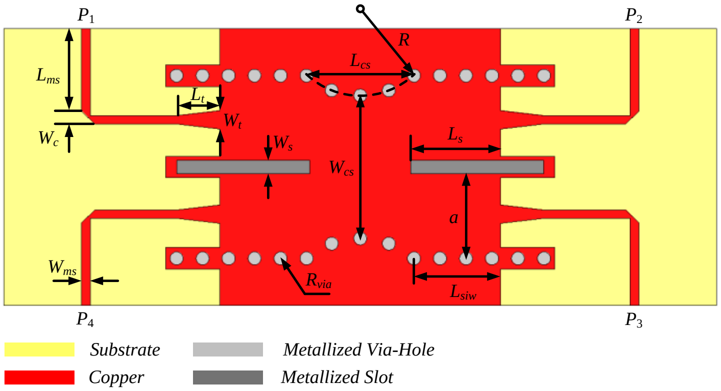

Figure 5.1 Simplified sketch of circularly-tapered SIW directional coupler.

5.1.1 Operation principle of Riblet hybrid

The coupling slot area of Riblet hybrid is a multi-mode region. If the bifurcation thickness of waveguide can be neglected, the operation principle of Riblet hybrid requires that the approximate slot length L_{cs} satisfy the following equation [74],

$$\left(\beta_e - \beta_o\right) L_{cs} = \frac{\pi}{4} \tag{5.1}$$

where $\beta_e = 2\pi/\lambda_{ge}$, and $\beta_o = 2\pi/\lambda_{go}$ are the propagation constants of the even and odd modes, respectively.

5.1.2 Extraction of the propagation constants of even and odd modes

From the above description, the key parameters to design such circularly-tapered couplers are the propagation constants of the even and odd modes. In this subsection, we will describe how to accurately extract the propagation constants of these two modes by making use of a numerical thru-reflect-line (TRL) calibration technique [42],[75] by using a commercial FEM-based software package [66].

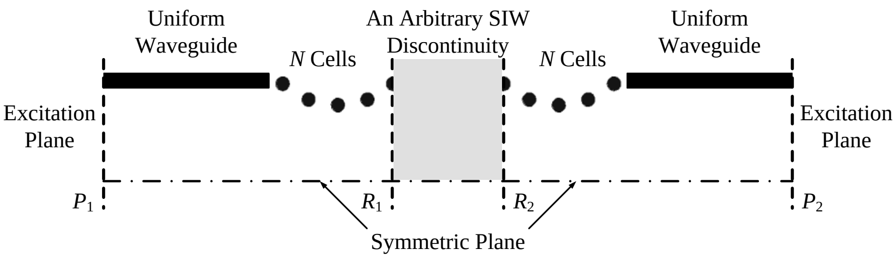

(a)

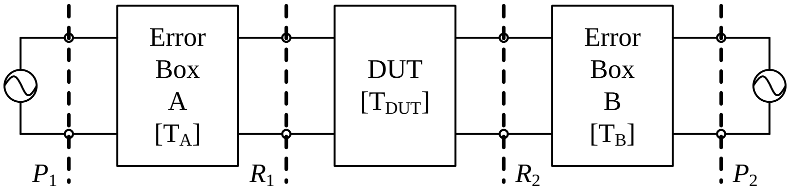

(b) DUT

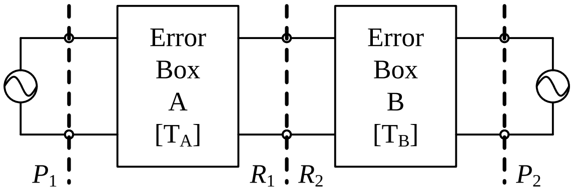

(c) Thru

(d) Reflect

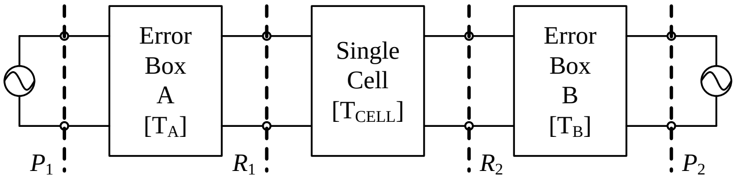

(e) Line

Figure 5.2 Full-wave model of an arbitrary SIW discontinuity (a) and its equivalent circuit topology (b) as well as the numerical TRL calibration kits (c)-(e).

Figure 5.2(a) shows the full-wave model of an arbitrary SIW discontinuity (denoted as DUT in Figure 5.2(b)) and its equivalent circuit topology is given in Figure 5.2(b). Only half of the original coupling slot is considered here since its symmetric plane is a perfect magnetic wall for the even-mode while a perfect electric wall for the odd-mode. Error boxes A and B represent excitation port discontinuities respectively at the left- and right-hand sides and the feeding line between reference planes P_1 and R_1. In our models, the feeding line includes a waveguide-to-SIW transition and N periodic cells. For the purpose of brevity, we only depict one cell as shown in Figure 5.2(a). In addition, a set of numerical TRL calibration kits (Figure 5.2(c)-(e)) is modeled in the full-wave simulator, in which the "Reflect" standard is realized by a short circuit. Note that for the "Line" standard, a single cell of our proposed periodic structure is inserted between reference planes R_1 and R_2. From the simulated transfer matrices of three different calibration standards, we can calibrate out the above-described error boxes A and B and obtain the transfer matrix of the SIW discontinuities through the TRL algorithm. Interestingly, an important by-product of such a TRL calibration technique is that the generated transfer matrix of single cell of the periodic structure enables a direct calculation of the propagation constant of the corresponding mode.

Let us denote the transfer matrices of "Thru" standard and "Line" standard in both cases of even and odd modes as T_{ti} and T_{li} (i = e, o), respectively. Propagation constants β_i can be calculated from eigenvalues of the product of T_{li} and T_{ti}^{-1} as follows,

$$\beta_i = \mathrm{Im}\left(\ln\left(eig\left(T_{li}T_{ti}^{-1}\right)\right)\Big/L_{cs}\right) \tag{5.2}$$

where L_{cs} is the length of a unit cell.

Ideally, the effects of feeding lines should be removed after we apply the TRL algorithm. However, numerical errors would invalidate this assumption. Therefore, the convergence of our extraction results with respect to cell number N should be examined beforehand. The substrate of choice is 0.635 mm-thick RT/duroid® 6010.2LM. In order to design the cut-off frequency at about 6 GHz, the following dimensions are used in our model: R = 3.81 mm, W_{cs} = 7.62 mm, W_s = 0.76 mm, R_{via} = 0.38 mm and the width of uniform SIW is 5.16 mm. Extraction results shown in Figure 5.3 are overlapped when cell number N is larger than 3, which means that at least 3 cells should be used in order to obtain converged extraction results. An interesting observation from Figure 5.3(b) is that there is a stop-band for the odd mode, where the propagating mode becomes evanescent.

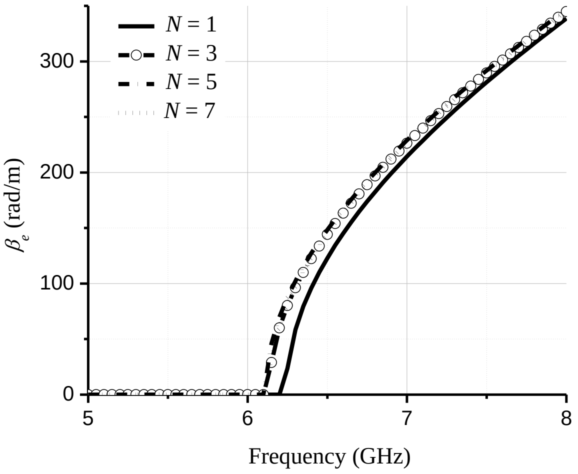

(a) Propagation constant of the even mode.

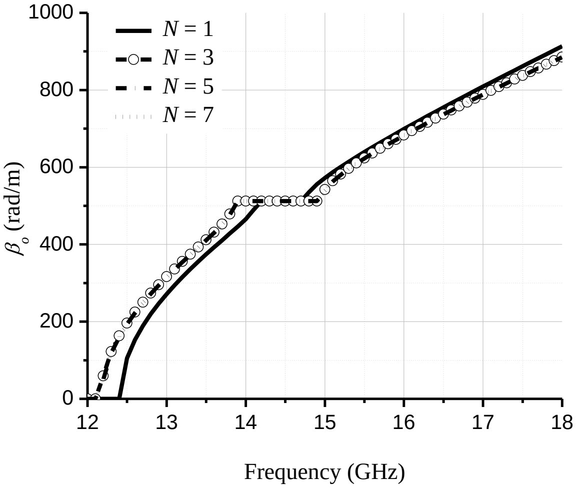

(b) Propagation constant of the odd mode.

Figure 5.3 Extracted frequency-dependent results versus cell number.

5.1.3 Model fitting

The propagation constant of the even mode cannot directly be extracted in the same frequency range as made in Figure 5.3(b) since the odd mode induced by the tapering discontinuities can propagate. Therefore, in order to avoid mode conversion, the extraction of β_e was carried out in the frequency range of single even mode transmission as shown in Figure 5.3(a).

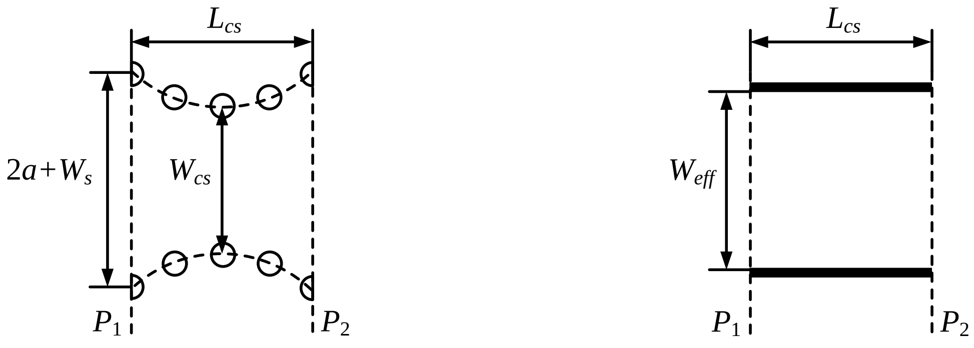

(a) (b)

Figure 5.4 Fitting the tapered coupling section (a) to the model of a uniform rectangular waveguide (b).

From a cross-sectional view of Figure 5.4(a), the width of the tapered section varies from ($2a+W_s$) to W_{cs}. The total phase delay between reference planes P_1 and P_2 can be calculated as an integral of the phase delay of each infinitesimal section of uniform rectangular waveguide. Therefore, it can be concluded from the first mean value theorem for integration that there must exist a uniform rectangular waveguide (Figure 5.4(b)) with a effective width of W_{eff}, whose phase delay between reference planes P_1 and P_2 is the same as that of the tapered coupling section.

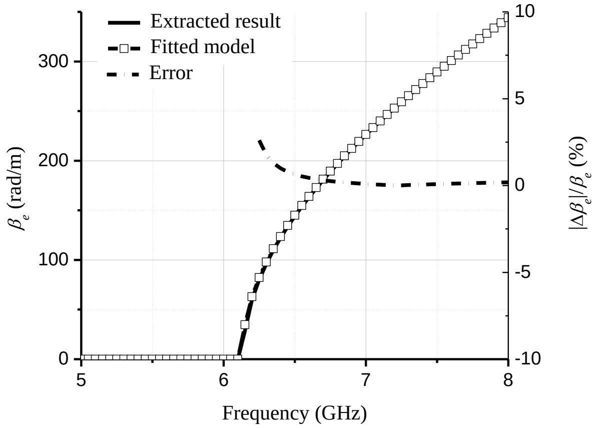

Figure 5.5 Results of model fitting and relative error representations.

Based on the above conclusion, we can fit the extracted β_e to an equivalent waveguide model by the method of least square. The equivalent width of tapering waveguide section W_{eff} in this case is 7.66 mm. The extracted β_e is compared with that calculated from the fitted model in Figure 5.5, and the modeling relative error decreases from 2.6 % near cut-off frequency to 0.2 % at 8 GHz.

5.1.4 Parametric studies of the tapered coupling section

After confirming the accuracy of our fitted model, we carry out a series of parametric studies in order to identify the mapping relationship between physical dimensions and propagation constants of the even and odd modes. Two key parameters are investigated. One is the radius of the circular taper R and the other is the minimum taper width W_{cs}. Figure 5.6 shows the extracted propagation constants for different values of R and W_{cs}.

In Figure 5.6, a group of colored curves is plotted in the case that R varies from 4.06 mm to 5.59 mm while W_{cs} remains to be 8.38 mm. As radius R increases, the cut-off frequency of the even mode is decreasing. The equivalent widths of the fitted waveguide model W_{eff} in the three cases are 8.28 mm, 8.33 mm and 8.38 mm, respectively. Then β_e calculated from the fitted model is plotted together with β_o in Figure 5.6(b). β_e is almost identical for the three cases because their equivalent widths are very close to each other. From Figure 5.6(b), we can also observe that the cut-off frequency for the odd mode also decreases with the increment of R. Moreover, there exist stop-bands for the odd mode, and the bandwidth is increased from 0.6 GHz to 0.8 GHz when R is increased from 4.06 mm to 5.59 mm.

Another group of patterned black curves is plotted in the case that W_{cs} varies from 7.62 mm to 9.14 mm while R remains to be 4.83 mm. It can be observed from Figure 5.6(a) and Figure 5.6(b) that the cut-off frequencies of both even and odd modes shift downward as the width of coupling slot is increasing. The equivalent widths of fitted waveguide model W_{eff} in the three cases are 7.78 mm, 8.33 mm and 8.89 mm, respectively. The stop-band for the odd mode is narrowing down from 1.1 GHz to 0.4 GHz with the increment of the coupling slot width. The explanation is that a narrow coupling slot would introduce a large reactance, which leads to an evanescent mode.

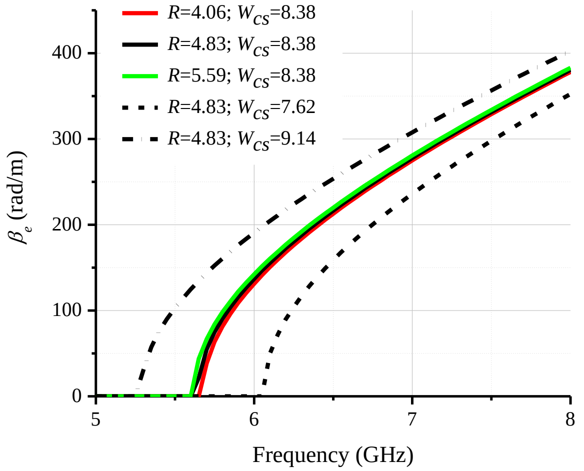

(a) Propagation constant of the even mode.

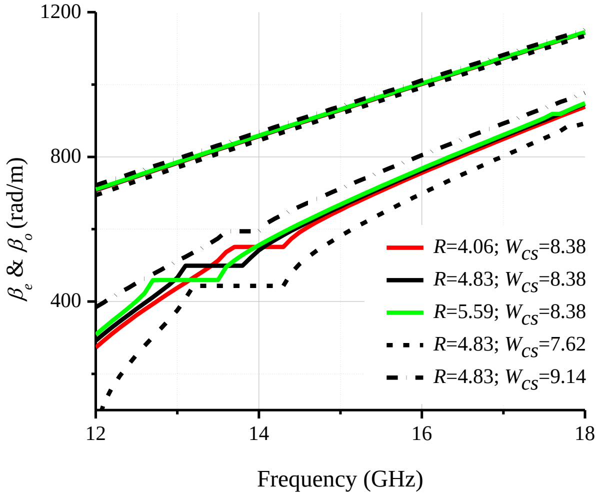

(b) Extracted propagation constant of the odd mode and extrapolated one of the even mode.

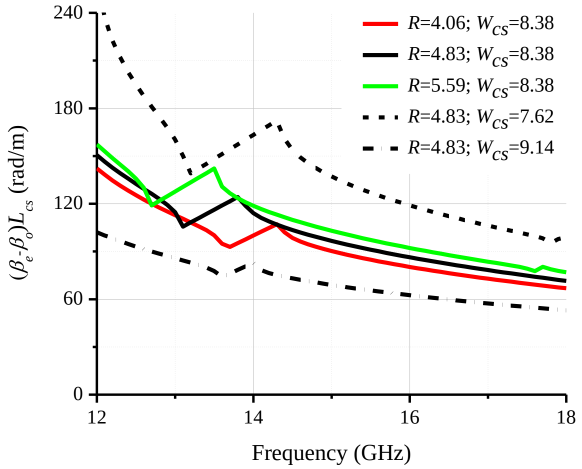

(c) Phase difference between the even and odd modes.

Figure 5.6 Extracted frequency-dependent results versus different cell number.

Finally, the phase difference between the even and odd modes along the tapered section is shown in Figure 5.6(c). The physical length L_{cs} of the directional coupler can be determined when the phase difference is 90°. The sharp transitions in Figure 5.6(c) correspond to the stop band of β_o in Fig. 7(b), which should be avoided in the operational frequency range of the coupler.

5.1.5 Equivalent circuit model of bifurcation effects

If the bifurcation of waveguide has a finite thickness, its effects can no longer be neglected [76]-[78]. In the vicinity of the bifurcation, there exist TE_{m0}-like modes both in the coupling region and in the uniform SIW sections. Since the coupling region is circularly-tapered, all higher-order TE_{m0}-like modes (m >2) are not "accessible" but only "localized" modes [76]. This means that not only they are evanescent modes but also their cut-off frequency is much higher than frequency range of interest.

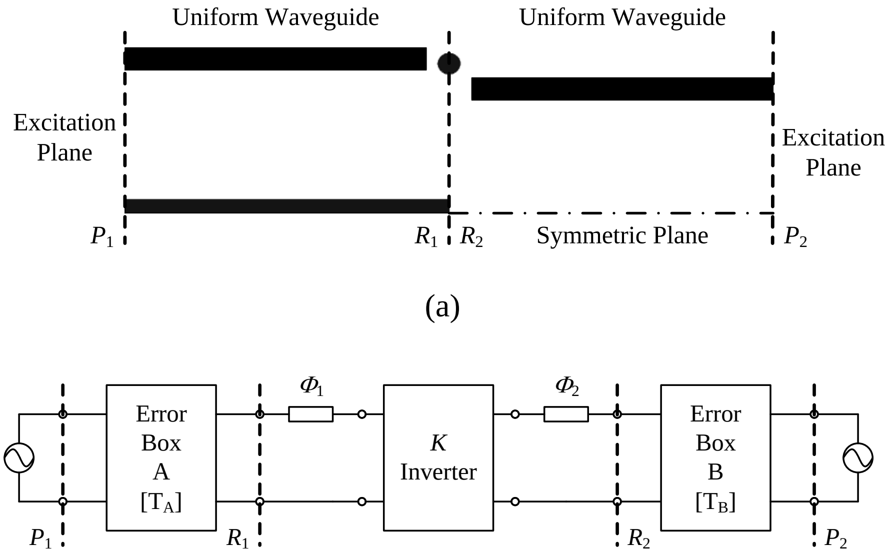

(a)

(b)

Figure 5.7 (a) Simplified model of bifurcation and (b) its equivalent circuit model.

Based on the above statement, we simplify our establishment of equivalent circuit models into the cases of the even and odd modes. Consequently, only half of the original structure should be considered in each case. Symmetric plane can be replaced by a perfect magnetic wall in the case of even mode and a perfect electric wall in the case of odd mode. The bifurcation is reduced to a two-port network as sketched in Figure 5.7(a) and it can be modeled as an impedance inverter together with two sections of equivalent transmission lines on each side shown in Figure 5.7(b).

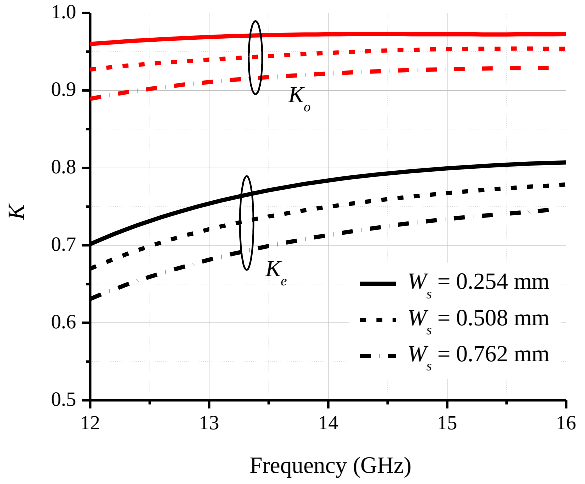

(a) Generalized inverter impedance.

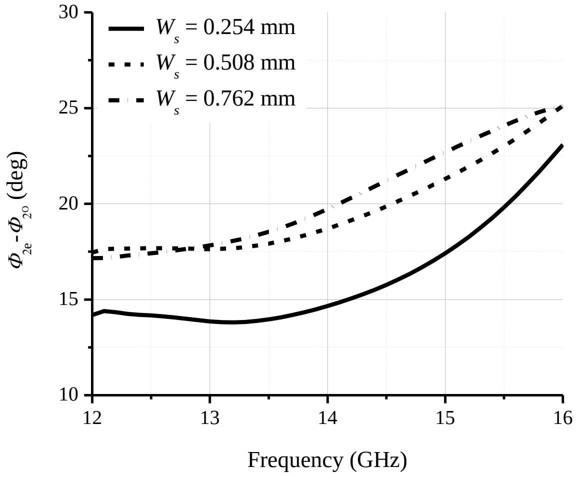

(b) Difference of equivalent electrical lengths.

Figure 5.8 Extracted circuit parameters.

The generalized impedance of the inverter K_i ($i = e, o$) and related electrical lengths Φ_{1i} and Φ_{2i} are extracted for bifurcations of three different thicknesses using the developed numerical TRL calibration technique that was described in Section 5.1.2. Extracted results are plotted in Figure 5.8. From Figure 5.8, we can have the following observations. At first, the bifurcation has little effect on the odd mode but a portion of the even mode would be reflected at the bifurcation since the extracted generalized impedance K_o is almost equal to 1. Second, when the bifurcation is thickening, the junction effects are more pronounced in terms of energy coupling. Third, phase difference between Φ_{2e} and Φ_{2o} is evaluated in Figure 5.8(b). On one hand, the phase difference increases with frequency, which can compensate for the decrease of phase difference between the even and odd modes in the coupling slot. That is why a wideband phase relation can be preserved in this kind of hybrid. On the other hand, the extracted phase difference in Figure 5.8(b) increases in the frequency range from 13 to 16 GHz when the bifurcation has a large discontinuity.

5.1.6 Design examples

5.1.6.1 A 3-dB 90 °SIW coupler at 15 GHz

Based on our analysis, a wideband 3-dB 90 °directional coupler centering at 15 GHz is designed on a substrate of 0.635 mm-thick RT/duroid® 6010.2LM. From our parametric analysis, we found that the phase difference between the even and odd modes are 90 °when R = 4.83 mm and W_{cs} = 8.38 mm. The coupling slot is shortened slightly for compensating the unequal parasitic effects of bifurcation in the cases of even and odd modes, while other parameters remain unchanged. All the physical dimensions are listed in Table 5.1.

The fabricated prototype is measured using four end launchers [79] and a vector network analyzer (VNA, Anritsu 37397C) with a short-open-load-thru (SOLT) calibration. Simulated and measured results of the fabricated prototype are compared in Figure 5.9. Both the simulated return loss and isolation are better than 20 dB while the measured ones are better than 18 dB. The amplitude balance is better than ±0.25 dB and the phase shift is 91.1 °±0.5 ° in our simulations. The measured amplitude balance is within ±0.3 dB and the phase shift varies from 89.2 °to 92.0 °.

Table 5.1 Dimensions of the prototyped 3-dB 90 °SIW coupler.

Symbol	Value (mm)	Symbol	Value (mm)
R	4.83	a	4.98
W_{cs}	8.38	L_{siw}	5.08
L_{cs}	5.26	L_i	3.30
d	0.15	L_b	2.54
W_s	0.76	W_{ms}	0.51
R_{via}	0.38	L_{ms}	5.08
L_{as}	9.65	W_t	1.09
W_{as}	0.51	L_t	2.51

5.1.6.2 A 0-dB SIW coupler at 15 GHz

If the phase difference between the even and odd modes over the coupling slot is 180°, then we can build an SIW 0-dB coupler (crossover) using the same topology. A prototype was fabricated and measured in the same manner. The measured results are compared with the simulated results in Figure 5.10. Good agreement between simulation and measurement is observed. We can see that return loss and isolation are better than 20 dB in simulation and better than 15 dB for the measurement from 14 GHz to 16 GHz. Moreover, the simulated coupling level is around 1.5 dB at 15 GHz with a measured value of 1.9 dB.

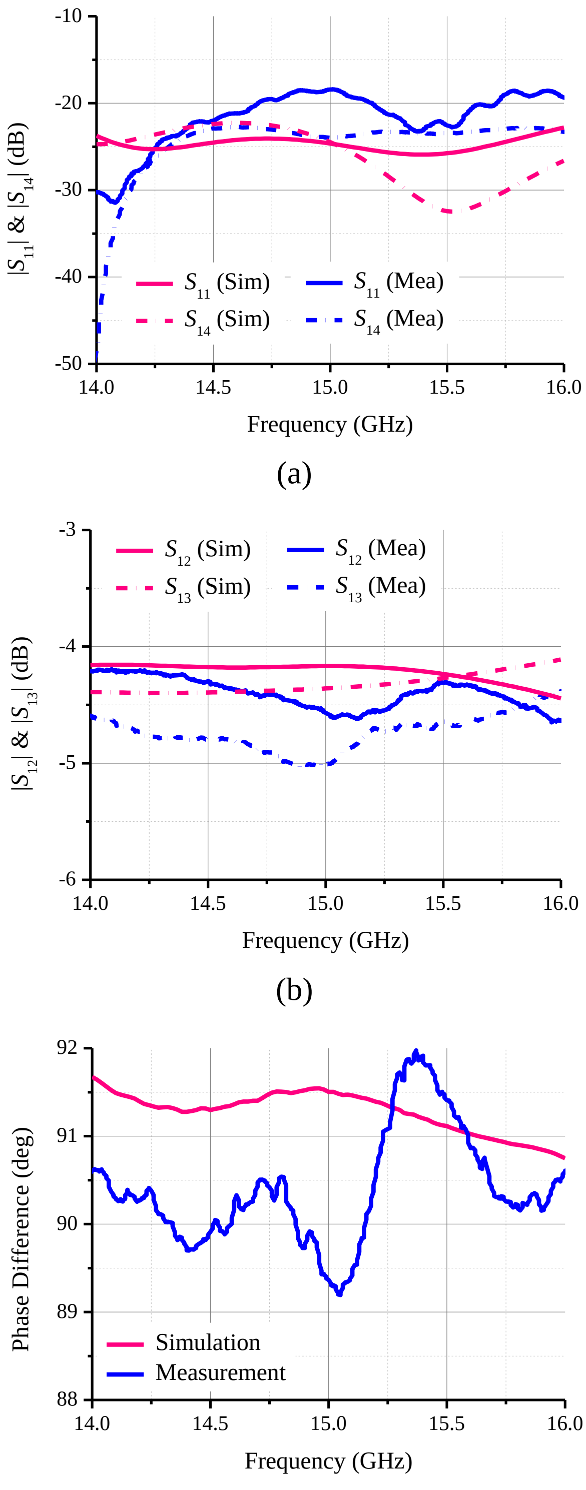

(a)

(b)

(c)

Figure 5.9 Comparison between simulated and measured results of the proposed 3-dB 90 ° SIW coupler.

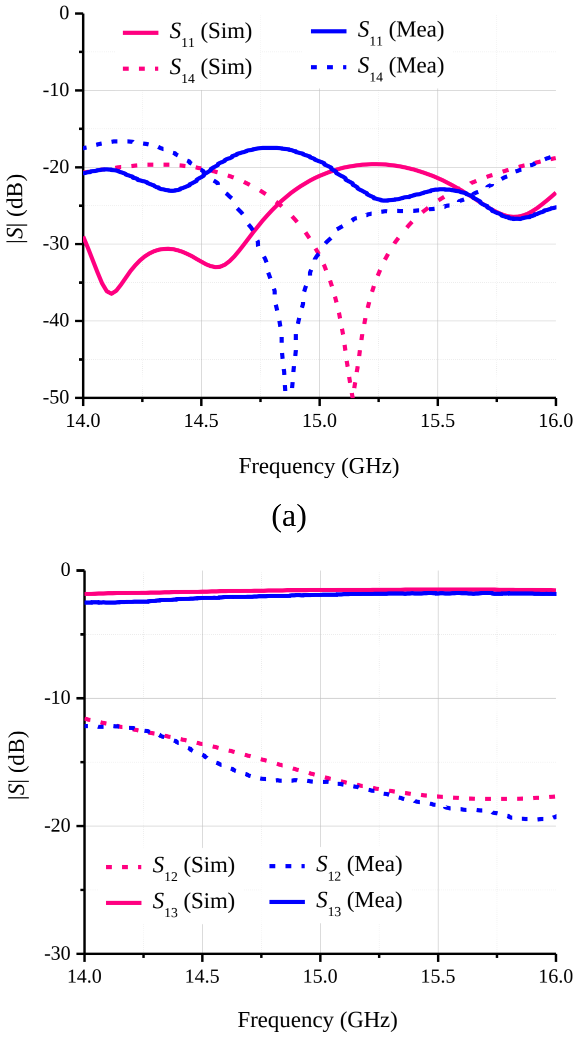

(a)

(b)

Figure 5.10 Comparison between simulated and measured results of an SIW crossover.

5.1.6.3 A 3-dB 90 °SIW coupler at 24 GHz

Our proposed design technique has been verified through experiment at 15 GHz, it is then implemented at 24 GHz with a substrate of 0.5 mm-thick RT/duroid® 6002 that is used for our high-frequency system prototype. Figure 5.11 gives the simulated results, which show very good performance with respect to input return loss, isolation and amplitude and phase balance.

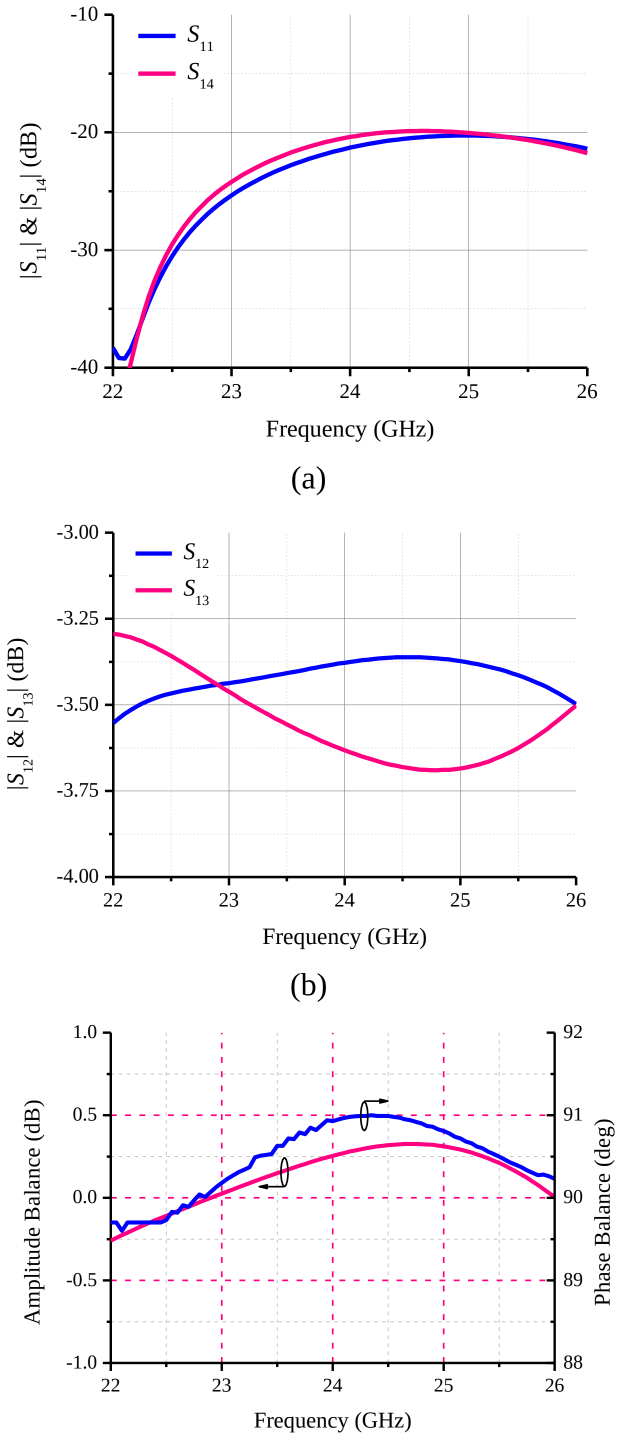

(a)

(b)

(c)

Figure 5.11 Simulated results of 24-GHz 3-dB 90 °SIW coupler.

5.2 Broadband SIW phase shifter

In certain applications, 180 ° phasing is required at two output ports of the directional couplers. For example, singly-balanced mixers based on 180 º-hybrid is more popular than those based on 90 º-hybrid since they have a better isolation between RF and LO and higher low-order spurious response rejection [80].

Intrinsically, phase shift can be realized through modifying signal-guided length [43], or propagation constant [44]-[47], or both [48] of SIW lines as well as introducing some discontinuities [49]. In order to avoid introducing additional phase shift to the following circuits in the system, phase shifters of equal length are usually preferred and in this case the propagation constant can be changed through modifying the width of SIW [44]-[45], periodically loading [46], or replacing part of the substrate by ferrite toroid [47]. However, these realizations suffer from narrow bandwidth operation. In this section, a novel broadband phase shifter using the SIW technology will be presented.

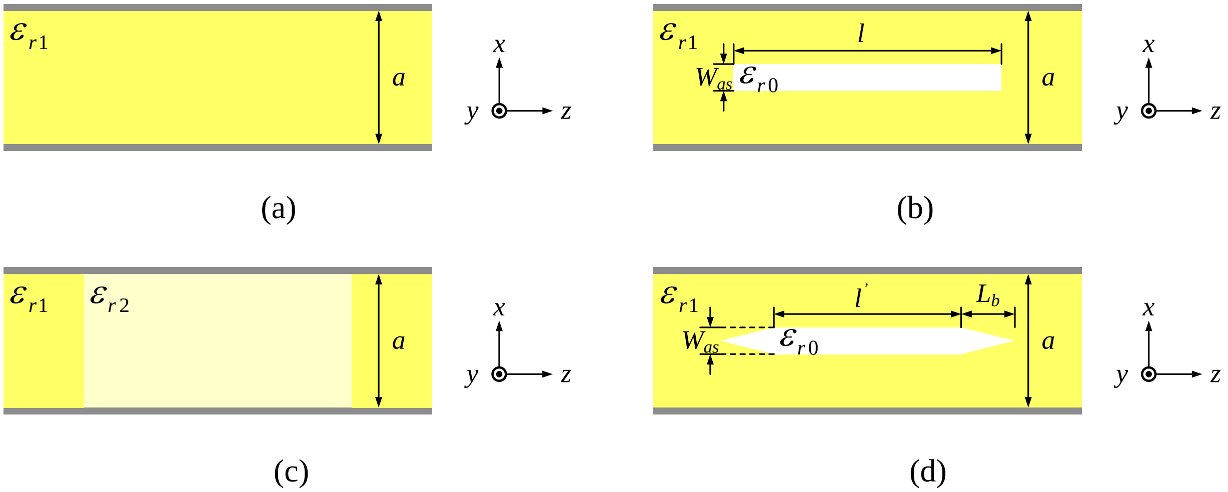

(a) (b)

(c) (d)

Figure 5.12 Illustration of dielectric-filled rectangular waveguide models.

5.2.1 Theoretical analysis

For simplification, we will use dielectric-filled rectangular waveguide models in Figure 5.12 for our mathematical derivation. In Figure 5.12, waveguide 1 is used as reference. If we remove a portion of the substrate along the longitudinal direction (*z*-direction) of waveguide 1 (see Figure

5.12(b)), the effective permittivity inside the slotted waveguide would become lower. This waveguide with the air slot or trench can be equivalent to the original waveguide uniformly filled with a material of lower permittivity ($\varepsilon_{r1} > \varepsilon_{r2}$), which is denoted as waveguide 2 in Figure 5.12(c). We can generalize phase shift $\Delta\varphi$ between two equal-length (l) rectangular waveguide as,

$$\Delta\varphi = l\Delta\beta \tag{5.3}$$

where $\Delta\beta$ is the difference of their propagation constants that can be expressed as,

$$\Delta\beta = \sqrt{k_1^2 - k_c^2} - \sqrt{k_2^2 - k_c^2} \tag{5.4}$$

where $k_i = 2\pi f(\mu_0\varepsilon_0\varepsilon_{ri})^{0.5}$ is the wave number of waveguide i (i = 1, 2) respectively while $k_c = \pi/a$ is the cut-off wave number of the dominant mode in both waveguides. The first-order derivative of $\Delta\beta$ can be derived as

$$\frac{d(\Delta\beta)}{df} = \frac{\left(4\pi^2\mu_0\varepsilon_0\varepsilon_{r1}\right)^2 f(1-x)\left[xf^2 - f_{c1}^2(1+x)\right]}{\sqrt{k_1^2 - k_c^2}\sqrt{k_2^2 - k_c^2}\left(\sqrt{k_2^2 - k_c^2} + x\sqrt{k_1^2 - k_c^2}\right)} \tag{5.5}$$

The expression above has a zero at,

$$f_0 = f_{c1}\sqrt{\frac{1+x}{x}} \tag{5.6}$$

where f_{c1} is the cut-off frequency of waveguide 1 and x is defined as the ratio between ε_{r2} and ε_{r1}. Based on our assumption, x is less than one.

Furthermore, it can be proved that the second-order derivative of $\Delta\beta$ at f_0 is positive.

$$\left.\frac{d^2(\Delta\beta)}{df^2}\right|_{f=f_0} = \left(4\pi^2\mu_0\varepsilon_0\varepsilon_{r1}\right)\frac{(1+x)(1-x)}{\sqrt{x}}k_c^{-1} > 0 \tag{5.7}$$

Therefore, $\Delta\beta$ reaches the minimum at f_0, and $\Delta\beta|_{\min}$ is,

$$\Delta\beta|_{\min} = k_c\frac{1-x}{\sqrt{x}} \tag{5.8}$$

From (5.8), it is easy to see that a smaller value of x leads to a shorter physical length of l if the phase shift is kept unchanged. However, a larger portion of the substrate should be removed in this case and as a result, discontinuities at the interface between the original waveguide and the slotted waveguide would have more pronounced effects. Therefore, there is a trade-off between the impedance-matching performance and the slot length.

On the other hand, it can be found that if $\Delta\beta$ is specified, there are two frequency points that satisfy equation (5.4), and the solutions are denoted as f_1 and f_2, respectively, as follows.

$$\begin{cases} f_1 = f_{c1}\sqrt{\dfrac{r^2}{x} - \dfrac{2r\sqrt{r^2-1}}{\sqrt{x}} + r^2} \\ f_2 = f_{c1}\sqrt{\dfrac{r^2}{x} + \dfrac{2r\sqrt{r^2-1}}{\sqrt{x}} + r^2} \end{cases} \tag{5.9}$$

where r is the ratio between $\Delta\beta$ and $\Delta\beta|_{\min}$. By multiplying a common factor l, it is easy to find that r is also the ratio between $\Delta\varphi$ and $\Delta\varphi|_{\min}$.

Consequently, given the specification of a phase shift as $\varphi_0 \pm \Delta\varphi$ and the frequency range between f_l and f_h, there are two solutions of x after manipulating (5.9), and the results are given below.

$$\begin{cases} x_1 = \left(\dfrac{r}{\sqrt{r^2-1} + \sqrt{\left(f_l/f_{c1}\right)^2 - 1}}\right)^2 \\ x_2 = \left(\dfrac{r}{-\sqrt{r^2-1} + \sqrt{\left(f_h/f_{c1}\right)^2 - 1}}\right)^2 \end{cases} \tag{5.10}$$

However, parameter x in equation (5.9) should be less than one, and this condition leads to the following inequalities, which determines whether the specifications are realizable using our proposed technique.

$$\begin{cases} f_l > f_1|_{\min} = f_{c1}\sqrt{\left(r - \sqrt{r^2-1}\right)^2 + 1} \\ f_h > f_2|_{\min} = f_{c1}\sqrt{\left(r + \sqrt{r^2-1}\right)^2 + 1} \end{cases} \tag{5.11}$$

We conclude our above discussion by summarizing the complete synthesis procedure in the flow chart sketched in Figure 5.13.

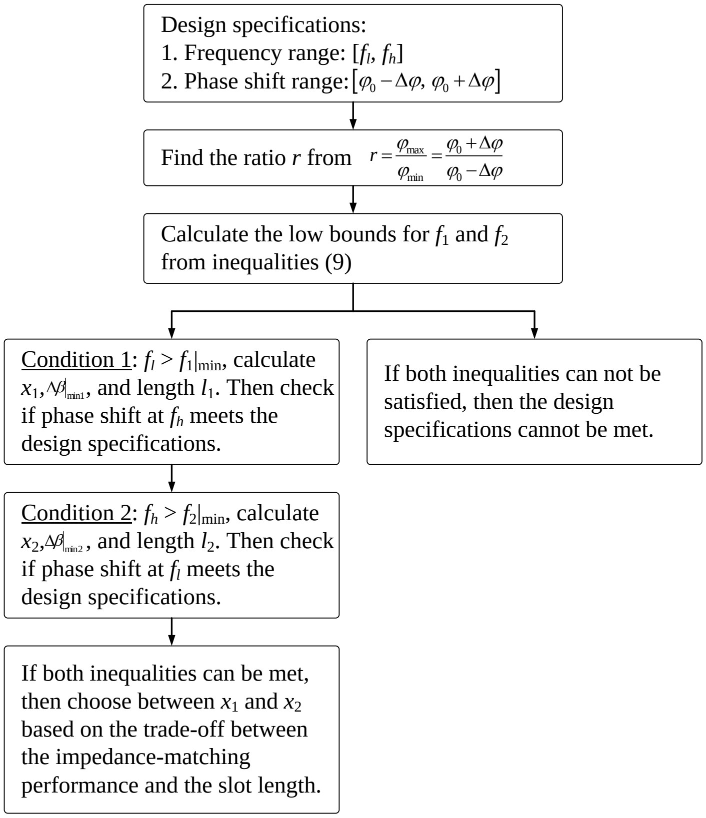

Figure 5.13 Design flow chart of the proposed phase shifter.

5.2.2 Design examples

A design example is showcased to demonstrate the accuracy of our proposed synthesis method. In this example, the phase shift is specified as a variation within 90°±1° from 13.5 to 16.5 GHz. The uniform waveguide has a width of 4.78 mm, a height of 0.635 mm, and it is filled with the dielectric with permittivity of 10.2. After we check the inequalities in (5.11), there exist two solutions for this problem, which are listed in Table 5.2 for reference together with other calculated results. Figure 5.14 compares the synthesized and the full-wave simulation results based on solution 2 since it shows a better impedance matching. The excellent agreement between the analytic solutions and full-wave simulations of solution 2 in Figure 5.14 demonstrates the accuracy of our proposed synthesis method.

Table 5.2 Two solutions of synthesized phase shifter.

Solution	x	f_0 (GHz)	$\Delta\beta\|_{\min}$ (rad/m)	$B=f_2-f_1$ (GHz)	l (mm)
1	0.7840	14.83	160.49	3.15	9.7
2	0.8112	14.69	137.88	3.13	11.3

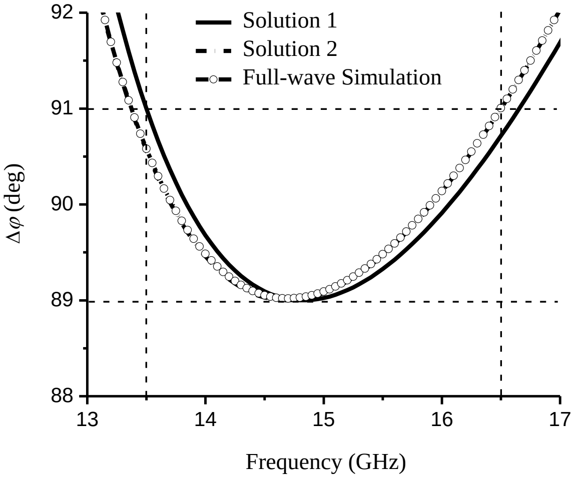

Figure 5.14 Comparison between synthesized and full-wave simulation results.

After obtaining the required parametric value of x from our proposed synthesis method, we can realize the equivalent waveguide 2 with lower permittivity by etching the central part of its substrate. If the slot width is within 10% of the waveguide width, the impedance matching is better than 10 dB for the whole operation band of the dominant mode. We extract the equivalent permittivity of three different kinds of most-commonly-used substrates for SIW technology. They are 0.5 mm-thick RT/duroid® 6002, 0.635 mm-thick RT/duroid® 6010.2LM, and 0.5 mm-thick RT/duroid® 5880 [81]. From the extraction results shown in Figure 5.14, we can observe that the equivalent permittivity is almost linearly decreasing when the width of the air slot is increasing within 10% of the waveguide width.

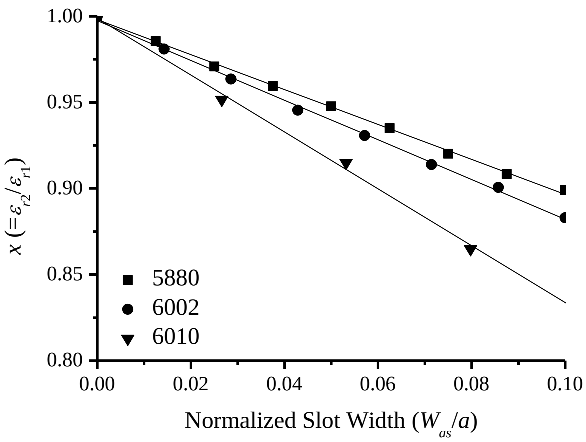

Figure 5.15 Extracted equivalent permittivity of three commonly-used substrates for the SIW technology.

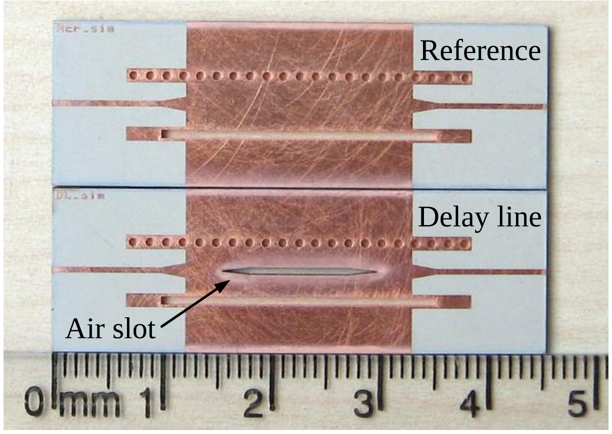

Figure 5.16 Photo of the fabricated samples of SIW phase shifters.

The proposed phase shifter is prototyped on a substrate of 0.635 mm-thick RT/duroid® 6010.2LM with a permittivity of 10.2. In order to improve the impedance matching between the uniform SIW and the etched SIW, the air slot is tapered as shown in Figure 5.12(d). The circuit prototype is measured by a universal test fixture (Wiltron SC5226) with a TRL calibration. Figure 5.16 shows a photo of the fabricated samples and a pair of microstrip-to-SIW transitions is designed as the input and output for measurement purpose. Figure 5.17 compares the simulated and measured magnitudes of *S* parameters. The measured return loss is better than 15 dB for both the reference line and the delay line from 13.5 GHz to 18 GHz. In addition, the measured insertion loss of the reference line is very close to our simulation while the delay line has a higher insertion loss due to the radiation from the air slot.

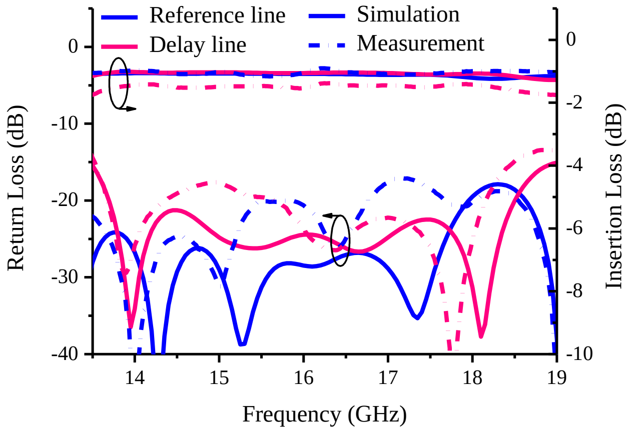

Figure 5.17 Comparison between simulated and measured *S* parameters of the fabricated prototype.

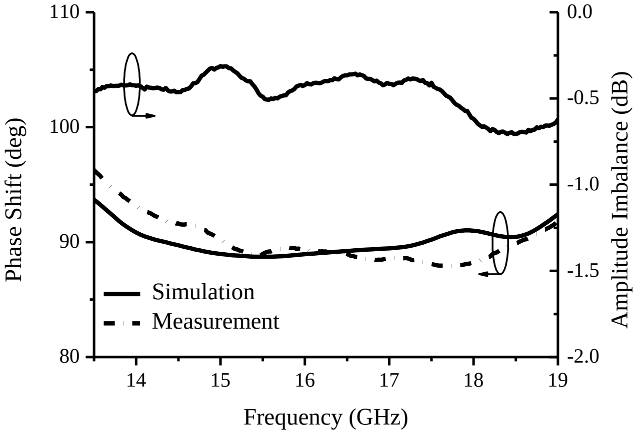

Figure 5.18 Comparison of phase shift and amplitude imbalance.

Simulated and measured phase shifts and amplitude imbalance are compared in Figure 5.18. From Figure 5.18, we can observe that the measured phase shift agrees well with the simulated one. In our simulation, the phase shift varies from 88 ° to 93 ° within the frequency range from 13.5 GHz to 19 GHz while the experimental result varies from 88 ° to 96 °. Moreover, the amplitude imbalance between the reference line and the delay line is 0.5 dB with a small variation of ±0.2 dB.

5.3 Wideband 3-dB 180 °SIW couplers

By integrating our developed 3-dB 90 °coupler in Section 5.1 and 90 °broadband phase shifter in Section 5.2, a 3-dB 180 °directional coupler is designed and fabricated. Four microstrip-to-SIW transitions are designed for measuring the coupler with four end launchers [79]. All the physical dimensions of the coupler are listed in Table 5.3.

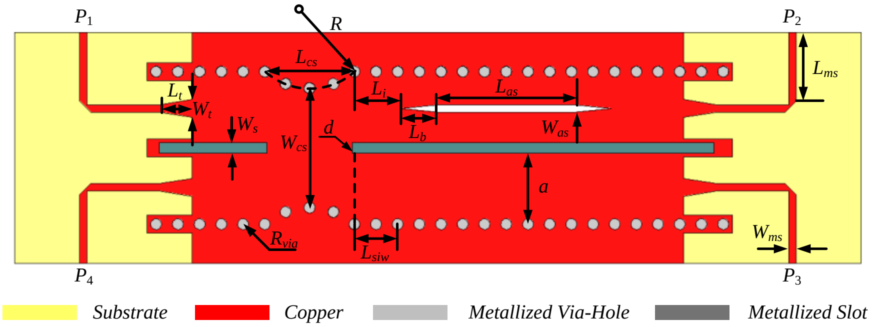

Figure 5.19 Simplified sketch of 3-dB 180 °SIW directional coupler.

Table 5.3 Dimensions of the proposed 3-dB 180 °SIW coupler.

Symbol	Value (mm)	Symbol	Value (mm)
R	4.83	a	4.98
W_{cs}	8.38	L_{siw}	5.08
L_{cs}	5.26	L_i	3.30
d	0.15	L_b	2.54
W_s	0.76	W_{ms}	0.51
R_{via}	0.38	L_{ms}	5.08
L_{as}	9.65	W_t	1.09
W_{as}	0.51	L_t	2.51

A photo of the fabricated prototype is given in Figure 5.20. Our prototype was measured using a VNA (Anritsu 37397C) with a standard SOLT calibration. In Figure 5.21, measured results are compared with simulated ones. The simulated return loss and isolation are better than 20 dB while the measured ones are better than 18 dB from 14 GHz to 16 GHz. The simulated and measured amplitude balances for excitation at port 1 are within 0.5 dB and 0.6 dB, respectively. The phase shift in simulation varies from 179.7 °to 182.3 °, while the measured phase difference at two output ports is 181.7 °±1.5 °. Our measured performance is summarized in Table 5.4 together with one example given in [51] which has a similar working frequency range. From this comparison, we can see that in spite of similar performance of return loss and isolation, our proposed coupler has a wider bandwidth of phase balance, but the insertion loss is 1.5 dB more than that of the example in [51]. Despite a higher dielectric loss, additional loss is brought by the end launchers, which is estimated to be 0.6 dB from our measurement of a back-to-back microstrip-to-SIW transition.

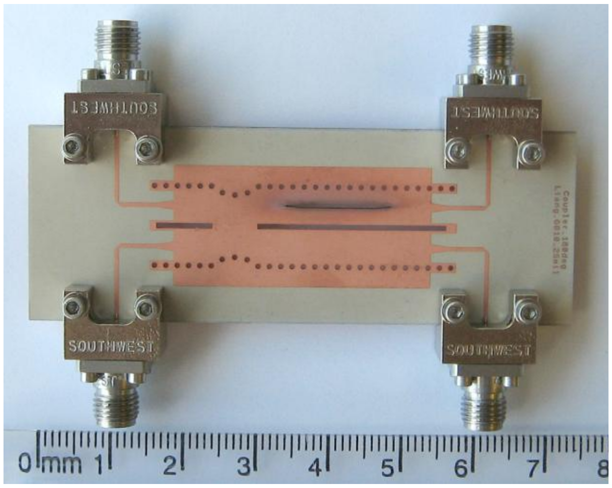

Figure 5.20 Photo of the prototype of the 3-dB 180 °SIW coupler.

Table 5.4 Performance comparison between this work and a reference work.

	Ref. [51]	This work
Return loss	>15.5 dB (14.1–16.1 GHz)	>18 dB (14–16 GHz)
Insertion loss	<0.5 dB (14.2–15.6 GHz)	~2 dB* (14–16 GHz)
Isolation	>20.8 dB (13.1–15.7 GHz)	>23 dB (14–16 GHz)
Amplitude balance	<0.5 dB (14.2–15.6 GHz)	<0.6 dB (14–16 GHz)
Phase balance	180 °±10 °(14.6–16.3 GHz)	181.7 °±1.5 °(14–16 GHz)
Substrate	0.5 mm-thick RT/duroid® 5880	0.635 mm-thick RT/duroid® 6010.2LM

* The insertion loss includes the loss of the transition and the end launchers.

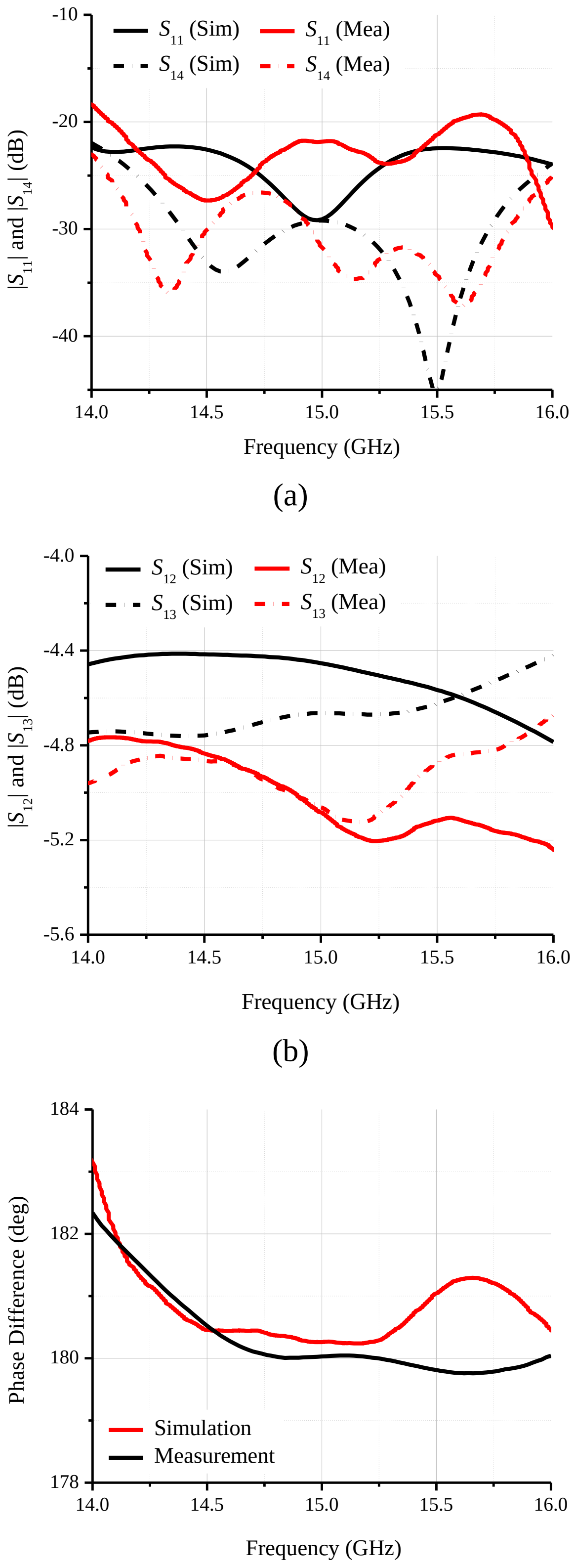

(a)

(b)

(c)

Figure 5.21 Performance comparison of the 3-dB 180 °SIW coupler.

5.4 Highly-selective SIW bandpass filters

In our 24-GHz system shown in Figure 4.1, there are two bandpass filters realized by the SIW technology. One is the RF BPF for removing unwanted mixing products, and the other is Tx/Rx BPF for limiting the spectrum of transmitted and received RF signals.

5.4.1 SIW RF BPF

The specifications of the RF BPF are listed in Table 5.5. It is designed at the center frequency of the 24 GHz ISM-band with a bandwidth of 1 GHz. In order to suppress the feedthrough of the RF LO, there is a transmission zero located at 21.225 GHz.

Table 5.5 Specifications of the RF BPF.

Specifications	Value
Passband	From 23.625 to 24.625 GHz
In-band insertion loss	<2 dB
In-band return loss	>10 dB
Transmission zero	21.225 GHz

This BPF is synthesized with generalized Chebyshev filtering response [65], and the resulting coupling matrix is given below.

$$M = \left[\begin{array}{cccccc} & S & 1 & 2 & 3 & L \\ S & 0 & 0.0449 & 0 & 0 & 0 \\ 1 & 0.0449 & -0.0018 & 0.0423 & -0.0071 & 0 \\ 2 & 0 & 0.0423 & 0.0070 & 0.0423 & 0 \\ 3 & 0 & -0.0071 & 0.0423 & -0.0018 & 0.0449 \\ L & 0 & 0 & 0 & 0.0449 & 0 \end{array}\right] \quad (5.12)$$

Since the transmission zero is located at the low passband of the BPF, our RF BPF is implemented with two TE_{101} SIW cavities and one TE_{102} cavity and it has the same filter topology as the Rx BPF in our low-frequency system demonstrator shown in Figure 3.5(c).

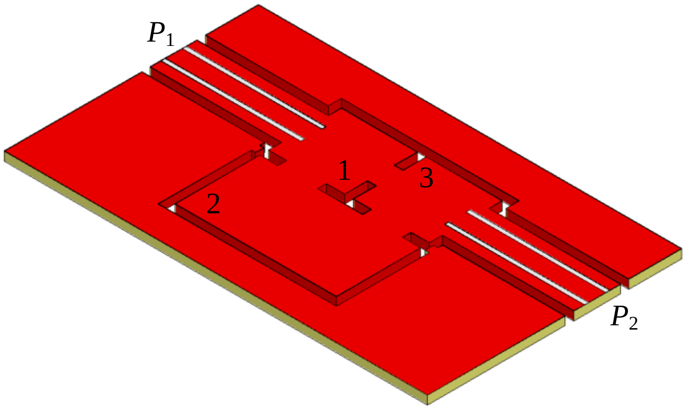

Figure 5.22 Sketch of the 24-GHz RF BPF.

The filter was prototyped with a substrate RT/duroid® 6002 having a permittivity of 2.94 and a thickness of 0.5 mm. Figure 5.23 compares the simulated and measured results of the RF BPF. We can see that simulated results show very good return loss and the insertion loss while measured return loss is better than 10 dB in the passband and the measured insertion loss is about 2.5 dB. In addition, below 22.5 GHz, the attenuation of the RF BPF is higher than 40 dB. Note that the measured results include the effects of test fixture since SOLT calibration is used in the measurement.

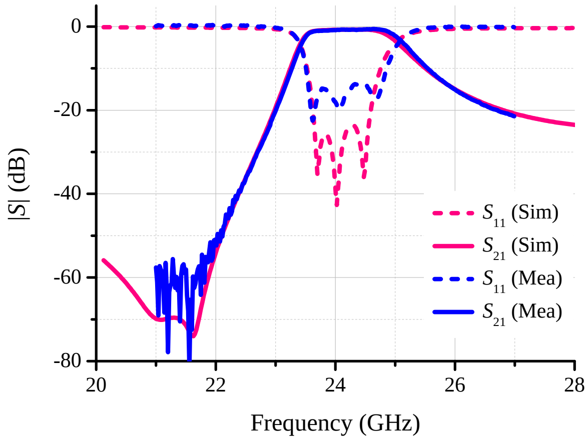

Figure 5.23 Comparison between simulated and measured results of the RF BPF.

5.4.2 SIW Tx/Rx BPF

For the SIW Tx/Rx BPF, our specifications are listed in Table 5.6. It has the same center frequency and bandwidth of the RF BPF, but with two transmission zeros for realizing a very sharp filtering response.

Table 5.6 Specifications of the Tx/Rx BPF.

Specifications	Value
Passband	From 23.625 to 24.625 GHz
In-band insertion loss	<2 dB
In-band return loss	>10 dB
Transmission zero	23.125 GHz & 25.125 GHz

The synthesized coupling matrix is given below.

$$M = \left[\begin{array}{ccccccc} & S & 1 & 2 & 3 & 4 & L \\ S & 0 & 0.0424 & 0 & 0 & 0 & 0 \\ 1 & 0.0424 & 0.0001 & 0.0361 & 0 & -0.0071 & 0 \\ 2 & 0 & 0.0361 & 0.0004 & 0.0318 & 0.0008 & 0 \\ 3 & 0 & 0 & 0.0318 & -0.0011 & 0.0361 & 0 \\ 4 & 0 & -0.0071 & 0.0008 & 0.0361 & 0.0001 & 0.0424 \\ L & 0 & 0 & 0 & 0 & 0.0424 & 0 \end{array}\right] \tag{5.13}$$

Since two transmission zeros have to be generated on both sides of the passband, four cavities are used for implementing this BPF. Figure 5.24 illustrates a sketch of this SIW BPF and its equivalent topology. We can see that in order to keep all the coupling in the same polarity, resonator 2 in Figure 5.24 is implemented with a TE_{102} SIW cavity while other resonators are implemented with TE_{101} cavities.

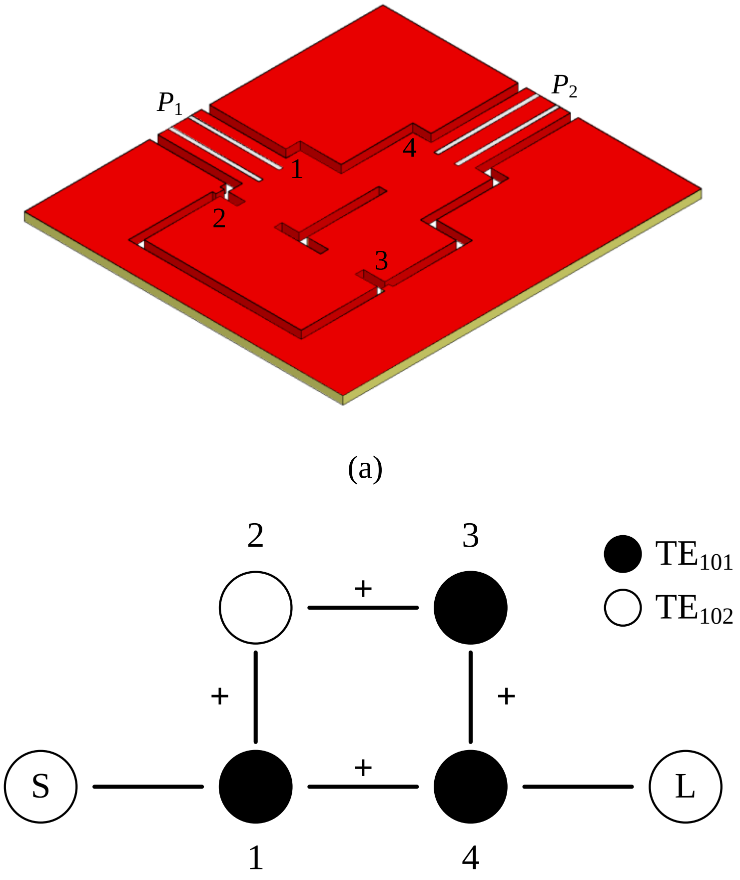

(a)

(b)

Figure 5.24 (a) Sketch of the 24-GHz Tx/Rx BPF and (b) its equivalent filter topology.

The filter was prototyped using the same substrate (0.5 mm-thick RT/duroid® 6002) and measured with a test fixture (Wiltron 3680). Good agreement between simulated and measured results can be found in Figure 5.25. Measured return loss is better than 12 dB and measured insertion loss is less than 3 dB over the passband.

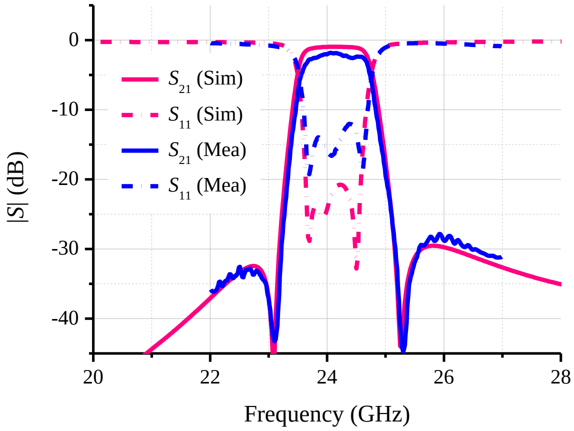

Figure 5.25 Comparison between simulated and measured results of the Tx/Rx BPF.

5.5 Four-line interdigitated coupler

In our 24-GHz transceiver shown in Figure 4.1, a 3-dB coupler is required to split the IF signal into two portions. Considering the fabrication compatibility, monolithic integration technology is selected to implement this coupler. However, the operation bandwidth of microstrip couplers is usually limited for two reasons. On one hand, it is impractical to design 3-dB microstrip backward couplers with parallel strips since the required gap between two strips is much smaller than the fabrication limit of standard PCB process. On the other hand, though 3-dB coupling level can be achieved by branch-line or ring configurations, quadrature phase relationship between two coupler outputs can be only kept within very narrow frequency band.

A viable solution is the interdigitated coupler (or Lange coupler) [82], which has the following distinct advantages. First of all, tight coupling can be achieved with multiple coupled-lines in a single layer circuitry, which enables wideband operation and eliminates strict requirement on the spacing between strips in conventional parallel two-line coupler. Second, it is compatible with the processing techniques of MMICs and miniature hybrid microwave integrated circuits (MHMICs). For the original interdigitated coupler, the use of bonding wires creates parasitic effects on the coupler performance that are difficult to characterize. Therefore, unfolded Lange coupler was proposed in [83] to reduce the number of bonding wires. As a result, the locations of direct and isolated ports are interchanged.

The design method of Lange coupler with arbitrary even number of parallel coupled-lines (Ou's method) was first presented in [84] based on the assumption that velocities of both even and odd modes are equal. Design equations were given in terms of even- and odd-mode impedances of any two adjacent coupled lines in the parallel-strip array because the strip width and the gap between strips are identical. Consequently, previous work on the analysis of conventional two-strip coupled-lines [85] can directly be applied for in this case. However, the velocities of both modes are usually unequal except for pure transverse electromagnetic mode (TEM) transmission lines, and the charge distribution for four-line coupler is completely different from that of two coupled-line scheme. Therefore, a number of studies have been conducted to improve the design accuracy of interdigitated couplers [86]-[89]. On one hand, the limitation of velocity equality in Ou's method was removed and both characteristic impedance and effective dielectric constant for even- and odd-modes are approximately found in [90]. On the other hand, a complete four-strip line analysis procedure was discussed in [91] without resorting to these approximations, and subsequently it was extended to include N-strips, where N can be any integer number larger than 2 [92]. In [93], the physical dimensions of parallel coupled-lines are determined using a synthesis technique [94]-[95] instead of reading the chart of even-odd mode impedances [96].

Parasitic effects such as thickness of line conductors, inductance of bonding wires, and discontinuities of launching pads are usually neglected for simplifying the analysis of interdigitated couplers. In fact, they should finally be included in a full-wave optimization. The conductor thickness can be incorporated as a correction term with respect to either the gap between strips [97]-[98] or the strip width [94],[99]. Bonding wires are usually modeled as lumped inductors [89] or coupled transmission lines [100]. However, previous analysis and measurements show that the effects of bonding wire connections and launching circuits is negligible for frequencies at least up to 12 GHz [87],[89].

There are two aspects of the conventional synthesis and analysis methods that we need to consider further. First, a four-line interdigitated coupler is actually an eight-port network with interdigitating boundary condition. More precisely, four independent TEM or quasi-TEM modes can propagate along the coupled-lines section of coupler. Second, the conventional calculation of mode admittance/impedance through a static field solution of inductance and capacitance matrices is no longer accurate enough at high frequencies. Nevertheless, it has been shown that the self- and mutual-inductance/capacitance extracted through full-wave simulations are independent of frequency within a certain bandwidth [101]-[102]. Therefore, it is still possible to synthesize the interdigitated coupler on the basis of a quasi-static assumption only if the full-wave extracted inductance and capacitance are adopted.

In this section, we will present an accurate and efficient synthesis method of symmetrical four-strip interdigitated coupler because it almost satisfies all practical design applications [103]. After applying the interdigitating boundary condition, the admittance matrix of the resulting coupler is directly calculated from the admittance matrix of four coupled-lines. From the definition of an ideal quadrature coupler, two new mode admittances/impedances are defined for the accurate synthesis of four-line interdigitated coupler. From the prescribed coupler specifications, we can calculate the values of these two admittances/impedances, and physical dimensions are subsequently synthesized by looking up a reference chart. To demonstrate the accuracy and flexibility of our proposed method, a composite microstrip-coplanar waveguide (CPW) coupler that is used in our system will also be showcased in addition to a conventional Lange coupler, of which the effects of bonding wires and launching circuits are accurately modeled.

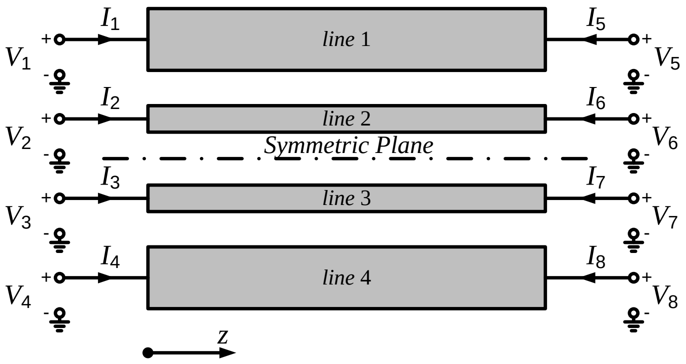

Figure 5.26 Symmetrical four coupled-lines.

5.5.1 Analysis of symmetrical four-line circuits

5.5.1.1 Solution of the telegrapher's equations

Figure 5.26 shows symmetrical four coupled-lines. The matrix-form of the telegrapher's equations in the case of a steady-state sinusoidal excitation can be written as,

$$\frac{d[V]}{dz} = -[Z][I] \tag{5.14}$$

$$\frac{d[I]}{dz} = -[Y][V] \tag{5.15}$$

where [*V*] and [*I*] are column vectors of voltage and current at each port, respectively. $[Z] = [Z_{pq}]$ and $[Y] = [Y_{pq}]$ (p, q = 1, 2, 3, 4) are impedance and admittance matrices of the symmetrical four coupled transmission line, respectively. They are related to inductance matrix [*L*] and capacitance matrix [*C*] of the transmission line through such expressions as $[Z] = j\omega[L]$ and $[Y] = j\omega[C]$.

By differentiating with respect to line position *z* and substituting each first-order equation, two uncoupled second-order ordinary differential equations are obtained,

$$\frac{d^2[V]}{dz} - [Z][Y][V] = 0 \tag{5.16}$$

$$\frac{d^2[I]}{dz} - [Y][Z][I] = 0 \tag{5.17}$$

If we only consider uniformly coupled lines, and the voltage only varies with the propagation direction +z ($V = V_0 e^{-\gamma z}$), we obtain the following eigenvalue problems,

$$\left(\gamma^2 U_0 - [Z][Y]\right)[V] = 0 \tag{5.18}$$

$$\left(\gamma^2 U_0 - [Y][Z]\right)[I] = 0 \tag{5.19}$$

where U_0 is the identity matrix.

From (5.18), we define [*U*] as the product of [*Z*] and [*Y*],

$$[U]=[Z][Y]=\begin{bmatrix} A & B & C & D \\ E & F & G & H \\ H & G & F & E \\ D & C & B & A \end{bmatrix} \tag{5.20}$$

where all its elements are listed below.

$$\begin{cases} A = z_{11}y_{11} + z_{12}y_{12} + z_{13}y_{13} + z_{14}y_{14} \\ B = z_{11}y_{12} + z_{12}y_{22} + z_{13}y_{23} + z_{14}y_{13} \\ C = z_{11}y_{13} + z_{12}y_{23} + z_{13}y_{22} + z_{14}y_{12} \\ D = z_{11}y_{14} + z_{12}y_{13} + z_{13}y_{12} + z_{14}y_{11} \\ E = z_{12}y_{11} + z_{22}y_{12} + z_{23}y_{13} + z_{13}y_{14} \\ F = z_{12}y_{12} + z_{22}y_{22} + z_{23}y_{23} + z_{13}y_{13} \\ G = z_{12}y_{13} + z_{22}y_{23} + z_{23}y_{22} + z_{13}y_{12} \\ H = z_{12}y_{14} + z_{22}y_{13} + z_{23}y_{12} + z_{13}y_{11} \end{cases}$$

Due to the symmetry of this transmission line network, the eigenvalues of products [*Y*][*Z*] and [*Z*][*Y*] are the same as given below,

$$\begin{cases} \gamma_a^2 = \dfrac{A+F-D-G+\sqrt{(A+G-D-F)^2-4(C-B)(E-H)}}{2} \\ \gamma_b^2 = \dfrac{A+F-D-G-\sqrt{(A+G-D-F)^2-4(C-B)(E-H)}}{2} \\ \gamma_c^2 = \dfrac{A+F+D+G+\sqrt{(A+D-F-G)^2+4(C+B)(E+H)}}{2} \\ \gamma_d^2 = \dfrac{A+F+D+G-\sqrt{(A+D-F-G)^2+4(C+B)(E+H)}}{2} \end{cases} \tag{5.21}$$

In the expression above, γ_i ($i = a, b, c, d$) is the propagation constant of each independent mode of the symmetrical four coupled-lines.

Moreover, the corresponding eigenvector matrix of (5.21) is

$$[M_V]=\begin{bmatrix} 1 & 1 & 1 & 1 \\ R_{Va} & R_{Vb} & R_{Vc} & R_{Vd} \\ -R_{Va} & -R_{Vb} & R_{Vc} & R_{Vd} \\ -1 & -1 & 1 & 1 \end{bmatrix} \tag{5.22}$$

with

$$\begin{cases} R_{Va}=\dfrac{A-F-D+G-\sqrt{\left(A+G-D-F\right)^2-4\left(C-B\right)\left(E-H\right)}}{2\left(C-B\right)} \\ R_{Vb}=\dfrac{A-F-D+G+\sqrt{\left(A+G-D-F\right)^2-4\left(C-B\right)\left(E-H\right)}}{2\left(C-B\right)} \\ R_{Vc}=-\dfrac{A-F+D-G-\sqrt{\left(A+D-F-G\right)^2+4\left(C+B\right)\left(E+H\right)}}{2\left(C+B\right)} \\ R_{Vd}=-\dfrac{A-F+D-G+\sqrt{\left(A+D-F-G\right)^2+4\left(C+B\right)\left(E+H\right)}}{2\left(C+B\right)} \end{cases} \tag{5.23}$$

The above matrix presents the voltage distribution of each mode on each line as shown in Figure 5.27.

(a) Mode *a*.

(b) Mode *b*.

(c) Mode *c*.

(d) Mode *d*.

Figure 5.27 Voltage distributions for four normal modes.

From the voltage eigenvector matrix [M_V], we can see that for modes *a* and *b*, the voltage distributions are antisymmetric to the symmetric plane, and therefore, the symmetric plane under these two modes is a perfect electric wall. On the other hand, the voltage distributions are symmetric for modes *c* and *d*. In this case, the symmetric plane is a perfect magnetic wall.

Similarly, the current eigenvector matrix of showing the current distribution of each mode on each line is,

$$M_I = \begin{bmatrix} 1 & 1 & 1 & 1 \\ R_{Ia} & R_{Ib} & R_{Ic} & R_{Id} \\ -R_{Ia} & -R_{Ib} & R_{Ic} & R_{Id} \\ -1 & -1 & 1 & 1 \end{bmatrix} \tag{5.24}$$

with

$$\begin{cases} R_{Ia} = -\dfrac{A-F-D+G-\sqrt{\left(A+G-D-F\right)^2-4\left(C-B\right)\left(E-H\right)}}{2\left(E-H\right)} \\ R_{Ib} = -\dfrac{A-F-D+G+\sqrt{\left(A+G-D-F\right)^2-4\left(C-B\right)\left(E-H\right)}}{2\left(E-H\right)} \\ R_{Ic} = -\dfrac{A-F+D-G-\sqrt{\left(A+D-F-G\right)^2+4\left(C+B\right)\left(E+H\right)}}{2\left(E+H\right)} \\ R_{Id} = -\dfrac{A-F+D-G+\sqrt{\left(A+D-F-G\right)^2+4\left(C+B\right)\left(E+H\right)}}{2\left(E+H\right)} \end{cases} \tag{5.25}$$

5.5.1.2 Solution of mode impedance and admittance

From the voltage and current eigenvector matrices, through a similar procedure in [104], the line admittance matrix $[(Y_C)_{ij}]$ and line impedance matrix $[(Z_C)_{ij}]$ ($i = a, b, c, d$ and $j = 1, 2, 3, 4$) of each strip under the four normal propagation modes can be found, which are given below.

$$\begin{aligned} \left(Y_C\right)_{a1} = \left(Y_C\right)_{a4} &= \frac{y_{11}-y_{14}+R_{Va}\left(y_{12}-y_{13}\right)}{\gamma_a} \\ &= \frac{\gamma_a}{z_{11}-z_{14}+R_{Ia}\left(z_{12}-z_{13}\right)} = \frac{1}{\left(Z_C\right)_{a1}} = \frac{1}{\left(Z_C\right)_{a4}} \end{aligned} \tag{5.26}$$

$$\begin{aligned} \left(Y_C\right)_{a2} = \left(Y_C\right)_{a3} &= \frac{y_{12}-y_{13}+R_{Va}\left(y_{22}-y_{23}\right)}{R_{Va}\gamma_a} \\ &= \frac{R_{Ia}\gamma_a}{z_{12}-z_{13}+R_{Ia}\left(z_{22}-z_{23}\right)} = \frac{1}{\left(Z_C\right)_{a2}} = \frac{1}{\left(Z_C\right)_{a3}} \end{aligned} \tag{5.27}$$

$$\begin{aligned}\left(Y_C\right)_{b1}=\left(Y_C\right)_{b4}&=\frac{y_{11}-y_{14}+R_{Vb}\left(y_{12}-y_{13}\right)}{\gamma_b}\\&=\frac{\gamma_b}{z_{11}-z_{14}+R_{Ib}\left(z_{12}-z_{13}\right)}=\frac{1}{\left(Z_C\right)_{b1}}=\frac{1}{\left(Z_C\right)_{b4}}\end{aligned}\tag{5.28}$$

$$\begin{aligned}\left(Y_C\right)_{b2}=\left(Y_C\right)_{b3}&=\frac{y_{12}-y_{13}+R_{Vb}\left(y_{22}-y_{23}\right)}{R_{Vb}\gamma_b}\\&=\frac{R_{Ib}\gamma_b}{z_{12}-z_{13}+R_{Ib}\left(z_{22}-z_{23}\right)}=\frac{1}{\left(Z_C\right)_{b2}}=\frac{1}{\left(Z_C\right)_{b3}}\end{aligned}\tag{5.29}$$

$$\begin{aligned}\left(Y_C\right)_{c1}=\left(Y_C\right)_{c4}&=\frac{y_{11}+y_{14}+R_{Vc}\left(y_{12}+y_{13}\right)}{\gamma_c}\\&=\frac{\gamma_c}{z_{11}+z_{14}+R_{Ic}\left(z_{12}+z_{13}\right)}=\frac{1}{\left(Z_C\right)_{c1}}=\frac{1}{\left(Z_C\right)_{c4}}\end{aligned}\tag{5.30}$$

$$\begin{aligned}\left(Y_C\right)_{c2}=\left(Y_C\right)_{c3}&=\frac{y_{12}+y_{13}+R_{Vc}\left(y_{22}+y_{23}\right)}{R_{Vc}\gamma_c}\\&=\frac{R_{Ic}\gamma_c}{z_{12}+z_{13}+R_{Ic}\left(z_{22}+z_{23}\right)}=\frac{1}{\left(Z_C\right)_{c2}}=\frac{1}{\left(Z_C\right)_{c3}}\end{aligned}\tag{5.31}$$

$$\begin{aligned}\left(Y_C\right)_{d1}=\left(Y_C\right)_{d4}&=\frac{y_{11}+y_{14}+R_{Vd}\left(y_{12}+y_{13}\right)}{\gamma_d}\\&=\frac{\gamma_d}{z_{11}+z_{14}+R_{Id}\left(z_{12}+z_{13}\right)}=\frac{1}{\left(Z_C\right)_{d1}}=\frac{1}{\left(Z_C\right)_{d4}}\end{aligned}\tag{5.32}$$

$$\begin{aligned}\left(Y_C\right)_{d2}=\left(Y_C\right)_{d3}&=\frac{y_{12}+y_{13}+R_{Vd}\left(y_{22}+y_{23}\right)}{R_{Vd}\gamma_d}\\&=\frac{R_{Id}\gamma_d}{z_{12}+z_{13}+R_{Id}\left(z_{22}+z_{23}\right)}=\frac{1}{\left(Z_C\right)_{d2}}=\frac{1}{\left(Z_C\right)_{d3}}\end{aligned}\tag{5.33}$$

5.5.1.3 Solution of admittance matrix

The impedance and admittance for the four coupled-lines can be obtained by solving for the terminal currents in terms of the voltages. Because of the symmetry and reciprocity, only twelve elements are independent and the results are given below.

$$\left[Y^8\right]=\begin{bmatrix} Y_{11}^8 & Y_{12}^8 & Y_{13}^8 & Y_{14}^8 & Y_{15}^8 & Y_{16}^8 & Y_{17}^8 & Y_{18}^8 \\ Y_{12}^8 & Y_{22}^8 & Y_{23}^8 & Y_{13}^8 & Y_{16}^8 & Y_{26}^8 & Y_{27}^8 & Y_{17}^8 \\ Y_{13}^8 & Y_{23}^8 & Y_{22}^8 & Y_{12}^8 & Y_{17}^8 & Y_{27}^8 & Y_{26}^8 & Y_{16}^8 \\ Y_{14}^8 & Y_{13}^8 & Y_{12}^8 & Y_{11}^8 & Y_{18}^8 & Y_{17}^8 & Y_{16}^8 & Y_{15}^8 \\ Y_{15}^8 & Y_{16}^8 & Y_{17}^8 & Y_{18}^8 & Y_{11}^8 & Y_{12}^8 & Y_{13}^8 & Y_{14}^8 \\ Y_{16}^8 & Y_{26}^8 & Y_{27}^8 & Y_{17} & Y_{12}^8 & Y_{22}^8 & Y_{23}^8 & Y_{13}^8 \\ Y_{17}^8 & Y_{27}^8 & Y_{26}^8 & Y_{16}^8 & Y_{13}^8 & Y_{23}^8 & Y_{22}^8 & Y_{12}^8 \\ Y_{18}^8 & Y_{17}^8 & Y_{16}^8 & Y_{15}^8 & Y_{14}^8 & Y_{13}^8 & Y_{12}^8 & Y_{11}^8 \end{bmatrix} \tag{5.34}$$

and

$$Y_{11}^8=-\frac{R_{Vb}\left(Y_C\right)_{a1}\coth\left(\gamma_a l\right)}{2\left(R_{Va}-R_{Vb}\right)}+\frac{R_{Va}\left(Y_C\right)_{b1}\coth\left(\gamma_b l\right)}{2\left(R_{Va}-R_{Vb}\right)}-\frac{R_{Vd}\left(Y_C\right)_{c1}\coth\left(\gamma_c l\right)}{2\left(R_{Vc}-R_{Vd}\right)}+\frac{R_{Vc}\left(Y_C\right)_{d1}\coth\left(\gamma_d l\right)}{2\left(R_{Vc}-R_{Vd}\right)}$$

$$Y_{12}^8=\frac{\left(Y_C\right)_{a1}\coth\left(\gamma_a l\right)}{2\left(R_{Va}-R_{Vb}\right)}-\frac{\left(Y_C\right)_{b1}\coth\left(\gamma_b l\right)}{2\left(R_{Va}-R_{Vb}\right)}+\frac{\left(Y_C\right)_{c1}\coth\left(\gamma_c l\right)}{2\left(R_{Vc}-R_{Vd}\right)}-\frac{\left(Y_C\right)_{d1}\coth\left(\gamma_d l\right)}{2\left(R_{Vc}-R_{Vd}\right)}$$

$$Y_{13}^8=-\frac{\left(Y_C\right)_{a1}\coth\left(\gamma_a l\right)}{2\left(R_{Va}-R_{Vb}\right)}+\frac{\left(Y_C\right)_{b1}\coth\left(\gamma_b l\right)}{2\left(R_{Va}-R_{Vb}\right)}+\frac{\left(Y_C\right)_{c1}\coth\left(\gamma_c l\right)}{2\left(R_{Vc}-R_{Vd}\right)}-\frac{\left(Y_C\right)_{d1}\coth\left(\gamma_d l\right)}{2\left(R_{Vc}-R_{Vd}\right)}$$

$$Y_{14}^8=\frac{R_{Vb}\left(Y_C\right)_{a1}\coth\left(\gamma_a l\right)}{2\left(R_{Va}-R_{Vb}\right)}-\frac{R_{Va}\left(Y_C\right)_{b1}\coth\left(\gamma_b l\right)}{2\left(R_{Va}-R_{Vb}\right)}-\frac{R_{Vd}\left(Y_C\right)_{c1}\coth\left(\gamma_c l\right)}{2\left(R_{Vc}-R_{Vd}\right)}+\frac{R_{Vc}\left(Y_C\right)_{d1}\coth\left(\gamma_d l\right)}{2\left(R_{Vc}-R_{Vd}\right)}$$

$$Y_{15}^8=\frac{R_{Vb}\left(Y_C\right)_{a1}\operatorname{csch}\left(\gamma_a l\right)}{2\left(R_{Va}-R_{Vb}\right)}-\frac{R_{Va}\left(Y_C\right)_{b1}\operatorname{csch}\left(\gamma_b l\right)}{2\left(R_{Va}-R_{Vb}\right)}+\frac{R_{Vd}\left(Y_C\right)_{c1}\operatorname{csch}\left(\gamma_c l\right)}{2\left(R_{Vc}-R_{Vd}\right)}-\frac{R_{Vc}\left(Y_C\right)_{d1}\operatorname{csch}\left(\gamma_d l\right)}{2\left(R_{Vc}-R_{Vd}\right)}$$

$$Y_{16}^8=-\frac{\left(Y_C\right)_{a1}\operatorname{csch}\left(\gamma_a l\right)}{2\left(R_{Va}-R_{Vb}\right)}+\frac{\left(Y_C\right)_{b1}\operatorname{csch}\left(\gamma_b l\right)}{2\left(R_{Va}-R_{Vb}\right)}-\frac{\left(Y_C\right)_{c1}\operatorname{csch}\left(\gamma_c l\right)}{2\left(R_{Vc}-R_{Vd}\right)}+\frac{\left(Y_C\right)_{d1}\operatorname{csch}\left(\gamma_d l\right)}{2\left(R_{Vc}-R_{Vd}\right)}$$

$$Y_{17}^8=\frac{\left(Y_C\right)_{a1}\operatorname{csch}\left(\gamma_a l\right)}{2\left(R_{Va}-R_{Vb}\right)}-\frac{\left(Y_C\right)_{b1}\operatorname{csch}\left(\gamma_b l\right)}{2\left(R_{Va}-R_{Vb}\right)}-\frac{\left(Y_C\right)_{c1}\operatorname{csch}\left(\gamma_c l\right)}{2\left(R_{Vc}-R_{Vd}\right)}+\frac{\left(Y_C\right)_{d1}\operatorname{csch}\left(\gamma_d l\right)}{2\left(R_{Vc}-R_{Vd}\right)}$$

$$Y_{18}^{8} = -\frac{R_{Vb}\left(Y_C\right)_{a1}\operatorname{csch}\left(\gamma_a l\right)}{2\left(R_{Va}-R_{Vb}\right)} + \frac{R_{Va}\left(Y_C\right)_{b1}\operatorname{csch}\left(\gamma_b l\right)}{2\left(R_{Va}-R_{Vb}\right)} + \frac{R_{Vd}\left(Y_C\right)_{c1}\operatorname{csch}\left(\gamma_c l\right)}{2\left(R_{Vc}-R_{Vd}\right)} - \frac{R_{Vc}\left(Y_C\right)_{d1}\operatorname{csch}\left(\gamma_d l\right)}{2\left(R_{Vc}-R_{Vd}\right)}$$

$$Y_{22}^{8} = -\frac{\left(Y_C\right)_{a1}\coth\left(\gamma_a l\right)}{2R_{Vb}\left(R_{Va}-R_{Vb}\right)} + \frac{\left(Y_C\right)_{b1}\coth\left(\gamma_b l\right)}{2R_{Va}\left(R_{Va}-R_{Vb}\right)} - \frac{\left(Y_C\right)_{c1}\coth\left(\gamma_c l\right)}{2R_{Vd}\left(R_{Vc}-R_{Vd}\right)} + \frac{\left(Y_C\right)_{d1}\coth\left(\gamma_d l\right)}{2R_{Vc}\left(R_{Vc}-R_{Vd}\right)}$$

$$Y_{23}^{8} = \frac{\left(Y_C\right)_{a1}\coth\left(\gamma_a l\right)}{2R_{Vb}\left(R_{Va}-R_{Vb}\right)} - \frac{\left(Y_C\right)_{b1}\coth\left(\gamma_b l\right)}{2R_{Va}\left(R_{Va}-R_{Vb}\right)} - \frac{\left(Y_C\right)_{c1}\coth\left(\gamma_c l\right)}{2R_{Vd}\left(R_{Vc}-R_{Vd}\right)} + \frac{\left(Y_C\right)_{d1}\coth\left(\gamma_d l\right)}{2R_{Vc}\left(R_{Vc}-R_{Vd}\right)}$$

$$Y_{26}^{8} = \frac{\left(Y_C\right)_{a1}\operatorname{csch}\left(\gamma_a l\right)}{2R_{Vb}\left(R_{Va}-R_{Vb}\right)} - \frac{\left(Y_C\right)_{b1}\operatorname{csch}\left(\gamma_b l\right)}{2R_{Va}\left(R_{Va}-R_{Vb}\right)} + \frac{\left(Y_C\right)_{c1}\operatorname{csch}\left(\gamma_c l\right)}{2R_{Vd}\left(R_{Vc}-R_{Vd}\right)} - \frac{\left(Y_C\right)_{d1}\operatorname{csch}\left(\gamma_d l\right)}{2R_{Vc}\left(R_{Vc}-R_{Vd}\right)}$$

$$Y_{27}^{8} = -\frac{\left(Y_C\right)_{a1}\operatorname{csch}\left(\gamma_a l\right)}{2R_{Vb}\left(R_{Va}-R_{Vb}\right)} + \frac{\left(Y_C\right)_{b1}\operatorname{csch}\left(\gamma_b l\right)}{2R_{Va}\left(R_{Va}-R_{Vb}\right)} + \frac{\left(Y_C\right)_{c1}\operatorname{csch}\left(\gamma_c l\right)}{2R_{Vd}\left(R_{Vc}-R_{Vd}\right)} - \frac{\left(Y_C\right)_{d1}\operatorname{csch}\left(\gamma_d l\right)}{2R_{Vc}\left(R_{Vc}-R_{Vd}\right)}$$

5.5.2 Synthesis of interdigitated couplers

A four-line interdigitated coupler can be built up by ideally connecting the eight ports of the four coupled-lines alternatively with infinitesimally short traces as shown in Figure 5.28.

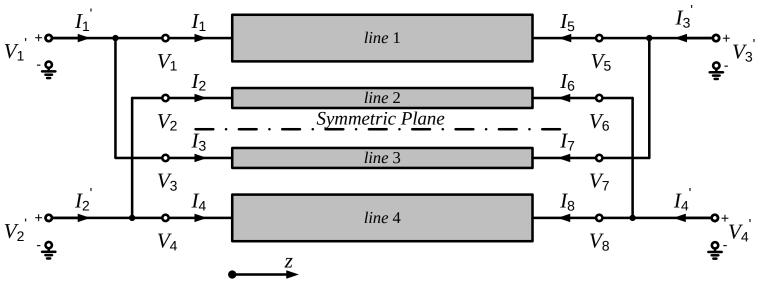

Figure 5.28 Schematic description of a four-line interdigitated coupler.

In this case, the voltages at the connecting ports are forced to be equal and the current of each input port of the coupler is the sum of currents of two connecting ports of the coupled-lines. After some manipulation, the original eight-port admittance matrix reduces to a new four-port admittance matrix [Y_{mn}^{4}] (m, n = 1, 2, 3, 4). The following expressions describe the relationship between the admittance of the proposed coupler Y_{mn}^{4} and the admittance of the original coupled-lines Y_{pq}^{8} (p, q = 1, 2, …, 8).

$$Y_{11}^{4} = Y_{11}^{8} + 2Y_{13}^{8} + Y_{22}^{8} \tag{5.35}$$

$$Y_{12}^{4} = 2Y_{12}^{8} + Y_{14}^{8} + Y_{23}^{8} \tag{5.36}$$

$$Y_{13}^{4} = Y_{15}^{8} + 2Y_{17}^{8} + Y_{26}^{8} \tag{5.37}$$

$$Y_{14}^{4} = 2Y_{16}^{8} + Y_{18}^{8} + Y_{27}^{8} \tag{5.38}$$

For the case of lossless pure TEM homogeneous media and quasi-TEM inhomogeneous media, the propagation constants of four modes are equal ($\gamma = \gamma_a = \gamma_b = \gamma_c = \gamma_d = j\beta$). Therefore, substituting all matrix elements of (5.34) simplify the above expression as,

$$Y_{11}^{4} = -\frac{1}{2}\coth(\gamma l)\left[\begin{array}{l} \dfrac{(Y_C)_{a1}}{R_{Va}-R_{Vb}}\left(\sqrt{R_{Vb}}+\dfrac{1}{\sqrt{R_{Vb}}}\right)^2 - \dfrac{(Y_C)_{b1}}{R_{Va}-R_{Vb}}\left(\sqrt{R_{Va}}+\dfrac{1}{\sqrt{R_{Va}}}\right)^2 \\ +\dfrac{(Y_C)_{c1}}{R_{Vc}-R_{Vd}}\left(\sqrt{R_{Vd}}-\dfrac{1}{\sqrt{R_{Vd}}}\right)^2 - \dfrac{(Y_C)_{d1}}{R_{Vc}-R_{Vd}}\left(\sqrt{R_{Vc}}-\dfrac{1}{\sqrt{R_{Vc}}}\right)^2 \end{array}\right] \tag{5.39}$$

$$Y_{12}^{4} = \frac{1}{2}\coth(\gamma l)\left[\begin{array}{l} \dfrac{(Y_C)_{a1}}{R_{Va}-R_{Vb}}\left(\sqrt{R_{Vb}}+\dfrac{1}{\sqrt{R_{Vb}}}\right)^2 - \dfrac{(Y_C)_{b1}}{R_{Va}-R_{Vb}}\left(\sqrt{R_{Va}}+\dfrac{1}{\sqrt{R_{Va}}}\right)^2 \\ -\dfrac{(Y_C)_{c1}}{R_{Vc}-R_{Vd}}\left(\sqrt{R_{Vd}}-\dfrac{1}{\sqrt{R_{Vd}}}\right)^2 + \dfrac{(Y_C)_{d1}}{R_{Vc}-R_{Vd}}\left(\sqrt{R_{Vc}}-\dfrac{1}{\sqrt{R_{Vc}}}\right)^2 \end{array}\right] \tag{5.40}$$

$$Y_{13}^{4} = -j\frac{1}{2}\csc(\beta l)\left[\begin{array}{l} \dfrac{(Y_C)_{a1}}{R_{Va}-R_{Vb}}\left(\sqrt{R_{Vb}}+\dfrac{1}{\sqrt{R_{Vb}}}\right)^2 - \dfrac{(Y_C)_{b1}}{R_{Va}-R_{Vb}}\left(\sqrt{R_{Va}}+\dfrac{1}{\sqrt{R_{Va}}}\right)^2 \\ +\dfrac{(Y_C)_{c1}}{R_{Vc}-R_{Vd}}\left(\sqrt{R_{Vd}}-\dfrac{1}{\sqrt{R_{Vd}}}\right)^2 - \dfrac{(Y_C)_{d1}}{R_{Vc}-R_{Vd}}\left(\sqrt{R_{Vc}}-\dfrac{1}{\sqrt{R_{Vc}}}\right)^2 \end{array}\right] \tag{5.41}$$

$$Y_{14}^{4} = j\frac{1}{2}\csc(\beta l)\left[\begin{array}{l} \dfrac{(Y_C)_{a1}}{R_{Va}-R_{Vb}}\left(\sqrt{R_{Vb}}+\dfrac{1}{\sqrt{R_{Vb}}}\right)^2 - \dfrac{(Y_C)_{b1}}{R_{Va}-R_{Vb}}\left(\sqrt{R_{Va}}+\dfrac{1}{\sqrt{R_{Va}}}\right)^2 \\ -\dfrac{(Y_C)_{c1}}{R_{Vc}-R_{Vd}}\left(\sqrt{R_{Vd}}-\dfrac{1}{\sqrt{R_{Vd}}}\right)^2 + \dfrac{(Y_C)_{d1}}{R_{Vc}-R_{Vd}}\left(\sqrt{R_{Vc}}-\dfrac{1}{\sqrt{R_{Vc}}}\right)^2 \end{array}\right] \tag{5.42}$$

On the other hand, the scattering matrix for an ideal four-port quadrature coupler is defined as [96],[105],

$$S=\begin{bmatrix} 0 & S_{12} & -j\sqrt{1-S_{12}^2} & 0 \\ S_{12} & 0 & 0 & -j\sqrt{1-S_{12}^2} \\ -j\sqrt{1-S_{12}^2} & 0 & 0 & S_{12} \\ 0 & -j\sqrt{1-S_{12}^2} & S_{12} & 0 \end{bmatrix} \tag{5.43}$$

where S_{12} is the coupling factor of the coupler.

If four ports of the coupler are respectively terminated by admittance Y_0, the corresponding admittance matrix of this coupler is,

$$Y=\frac{jY_0}{\sqrt{1-S_{12}^2}}\begin{bmatrix} 0 & 0 & 1 & -S_{12} \\ 0 & 0 & -S_{12} & 1 \\ 1 & -S_{12} & 0 & 0 \\ -S_{12} & 1 & 0 & 0 \end{bmatrix} \tag{5.44}$$

By matching (5.39) to (5.42) with the matrix elements of (5.44), we can find

$$Y_{13}^4 = jY_0 \Big/ \sqrt{1-S_{12}{}^2} = j\overline{Y}_{13}\csc(\beta l) \tag{5.45}$$

$$Y_{14}^4 = -jY_0S_{12} \Big/ \sqrt{1-S_{12}{}^2} = j\overline{Y}_{14}\csc(\beta l) \tag{5.46}$$

where

$$\overline{Y}_{13}=-\frac{1}{2}\left[\begin{array}{l} \dfrac{(Y_C)_{a1}}{R_{Va}-R_{Vb}}\left(\sqrt{R_{Vb}}+\dfrac{1}{\sqrt{R_{Vb}}}\right)^2-\dfrac{(Y_C)_{b1}}{R_{Va}-R_{Vb}}\left(\sqrt{R_{Va}}+\dfrac{1}{\sqrt{R_{Va}}}\right)^2 \\ +\dfrac{(Y_C)_{c1}}{R_{Vc}-R_{Vd}}\left(\sqrt{R_{Vd}}-\dfrac{1}{\sqrt{R_{Vd}}}\right)^2-\dfrac{(Y_C)_{d1}}{R_{Vc}-R_{Vd}}\left(\sqrt{R_{Vc}}-\dfrac{1}{\sqrt{R_{Vc}}}\right)^2 \end{array}\right] \tag{5.47}$$

$$\overline{Y}_{14}=\frac{1}{2}\left[\begin{array}{l} \dfrac{(Y_C)_{a1}}{R_{Va}-R_{Vb}}\left(\sqrt{R_{Vb}}+\dfrac{1}{\sqrt{R_{Vb}}}\right)^2-\dfrac{(Y_C)_{b1}}{R_{Va}-R_{Vb}}\left(\sqrt{R_{Va}}+\dfrac{1}{\sqrt{R_{Va}}}\right)^2 \\ -\dfrac{(Y_C)_{c1}}{R_{Vc}-R_{Vd}}\left(\sqrt{R_{Vd}}-\dfrac{1}{\sqrt{R_{Vd}}}\right)^2+\dfrac{(Y_C)_{d1}}{R_{Vc}-R_{Vd}}\left(\sqrt{R_{Vc}}-\dfrac{1}{\sqrt{R_{Vc}}}\right)^2 \end{array}\right] \tag{5.48}$$

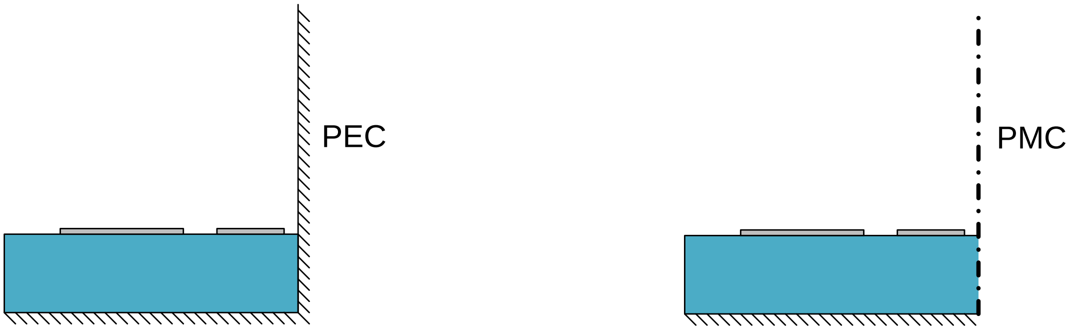

(a) Half structure with PEC.

(b) Half structure with PMC.

Figure 5.29 Simplified solution of the original four-line structure.

We can then define two mode admittances Y_e and Y_m corresponding to the case of perfect electric wall and the case of perfect magnetic wall, respectively.

$$\begin{aligned} Y_e &= \frac{\overline{Y}_{13} - \overline{Y}_{14}}{2} \\ &= \frac{1}{2}\left(\frac{(Y_C)_{b1}}{R_{Va} - R_{Vb}} \left(\sqrt{R_{Va}} + \frac{1}{\sqrt{R_{Va}}} \right)^2 - \frac{(Y_C)_{a1}}{R_{Va} - R_{Vb}} \left(\sqrt{R_{Vb}} + \frac{1}{\sqrt{R_{Vb}}} \right)^2 \right) \end{aligned} \tag{5.49}$$

$$\begin{aligned} Y_m &= \frac{\overline{Y}_{13} + \overline{Y}_{14}}{2} \\ &= \frac{1}{2}\left(\frac{(Y_C)_{d1}}{R_{Vc} - R_{Vd}} \left(\sqrt{R_{Vc}} - \frac{1}{\sqrt{R_{Vc}}} \right)^2 - \frac{(Y_C)_{c1}}{R_{Vc} - R_{Vd}} \left(\sqrt{R_{Vd}} - \frac{1}{\sqrt{R_{Vd}}} \right)^2 \right) \end{aligned} \tag{5.50}$$

From these expressions of Y_e and Y_m, we can have the following observations. First, admittance Y_e is only related to modes *a* and *b*. Since the symmetrical plane is a perfect electric wall for modes *a* and *b*, we only need to solve half of the original four coupled-lines with the symmetrical plane set as a perfect electric conductor boundary (Figure 5.29(a)). Similarly, admittance Y_m is only related to modes *c* and *d*. We only need to solve half of the original four coupled lines with the symmetrical plane set as a perfect magnetic conductor boundary because the symmetrical plane is a perfect magnetic wall for modes *c* and *d* (Figure 5.29(b)). Second, both admittances Y_e and Y_m are calculated from the admittances and the propagation constants of *c*- and *π*-modes of two parallel coupled-lines in the presence of perfect electric wall or perfect magnetic wall. Third, if we impose conditions $R_{va} = -R_{vb} = -1$ and $R_{vc} = -R_{vd} = -1$, the expressions for Y_e and Y_m will then degenerate to the conventional odd- and even-mode admittances of two identical parallel coupled-lines, which have widely been used in the conventional design. However, the imposed condition means that modes *a* and *b* or modes *c* and *d* must be a pair of even- and odd-modes, which is not possible even for identical strips due to the presence of perfect electric wall or perfect magnetic wall. Therefore, the conventional design technique is no longer accurate in this sense. Finally, as what have been done in the conventional synthesis method [90],[91],[96], a reference chart should be plotted in order to find out the physical dimensions of the coupled lines from the calculated mode impedances Z_e ($1/Y_e$) and Z_m ($1/Y_m$).

There are two ways to generate such a reference chart. In the first way, the capacitance matrix $[C]$ of the four-line network in Figure 5.26 can be obtained by using any two-dimensional (2-D) field solvers based on finite difference method or finite element method. At the same time, the inductance matrix $[L]$ can be calculated from the capacitance matrix $[C_0]$ while the substrate material is replaced by vacuum. Then, the capacitance and inductance matrices can be used for calculating Y_e and Y_m through the expressions given in Section 5.5.1. On the other hand, the inductance matrix $[L]$ and the capacitance matrix $[C]$ can also be extracted from full-wave simulations [101]-[102]. Compared with the 2-D field solution, the full-wave solution is advantageous in the two aspects. First, the full-wave simulation is more flexible in terms of frequency sweep and boundary setting while commercial 2-D field solver is restricted to static field only. Second, the full-wave solution is generally more accurate than 2-D field solution due to its capability of solving frequency-dependent wave propagation and dispersion problems only on an electrically-small section of uniform coupled-lines. Therefore, the computational complexity is comparable to that of 2-D field solution.

In summary, the complete synthesis procedure of the four-line interdigitated quadrature coupler is described as follows:

1) From the prescribed coupler performance (usually, the coupling factor S_{12}) and termination admittance Y_0, we can calculate the required Y_e and Y_m using (5.49) and (5.50);
2) The physical dimension of the four coupled lines can be found by looking up the reference chart.

5.5.3 Design examples

Two examples will be given to demonstrate the accuracy and versatility of our proposed synthesis method.

5.5.3.1 A 3-dB unfolded Lange coupler

In the beginning, two coupled microstrip lines with certain boundary conditions shown in Figure 5.29 are analyzed in a commercial method-of-moments (MoM) package [106]. We choose an alumina substrate Superstrate® 996 with a dielectric constant of 9.9 and a thickness of 0.254 mm. In our simulation, the widths of the four strips are set identical for facilitating our simulation as well as comparing with conventional results. As described in Section 5.5.2, mode impedances Z_e and Z_m are calculated from the line impedances and propagation constants of *c*- and π-modes. The calculated results are plotted as a reference chart in Figure 5.30.

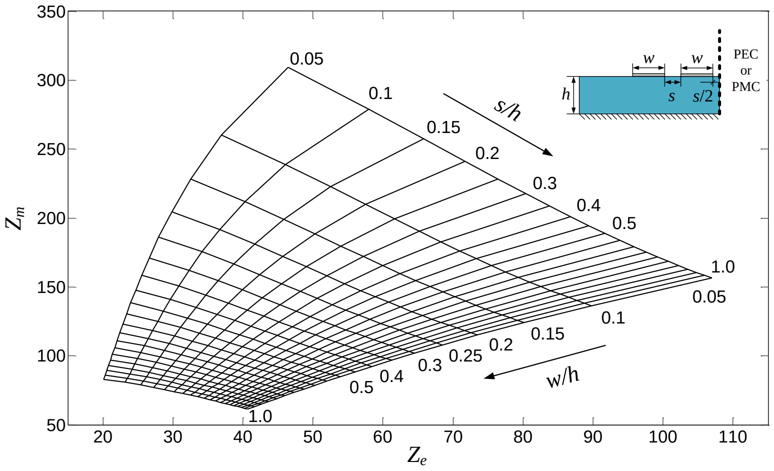

Figure 5.30 Reference chart for the four-line interdigitated coupler on the specified substrate.

Interdigitated coupler is often used when a strong coupling is required. Therefore, we will show the design procedure of a 3-dB unfolded Lange coupler for *X*-band applications. From the given specification, the coupling factor S_{12} equals to 0.7079. Mode impedances Z_e and Z_m are calculated to be 41.35 Ω and 241.83 Ω, respectively. Therefore, we can read out the physical dimensions of four coupled-lines from Figure 5.30 as w/h = 0.104 and s/h = 0.079. For the purpose of comparison, the corresponding values of *w*/*h* and *s*/*h* in the conventional design are 0.081 and 0.080, respectively.

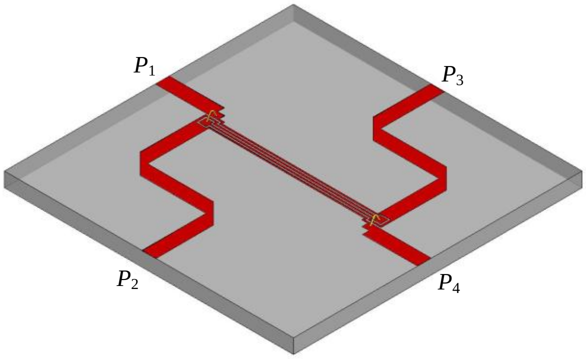

(a) Perspective view.

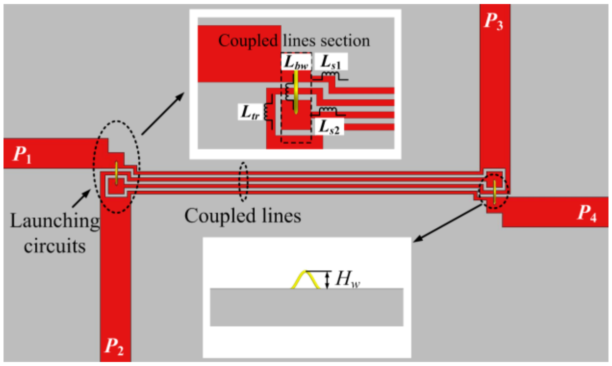

(b) Top view.

Figure 5.31 Sketch of an unfolded four-line Lange coupler.

Then, launching circuits and gold bonding wires are incorporated with four coupled-lines in a commercial FEM-based package [66], which is depicted in Figure 5.31. The 50 ohm feeding lines are extended for easy measurement with coaxial adapters. The profile of the bonding wires is assumed to conform to a cosine function (see the vignette of Figure 5.31(b)). The dimension of two pads is 0.127×0.127 mm^2 for wire bonding, and the length of the coupled lines is 2.75 mm, which equals to 90 °at 10 GHz.

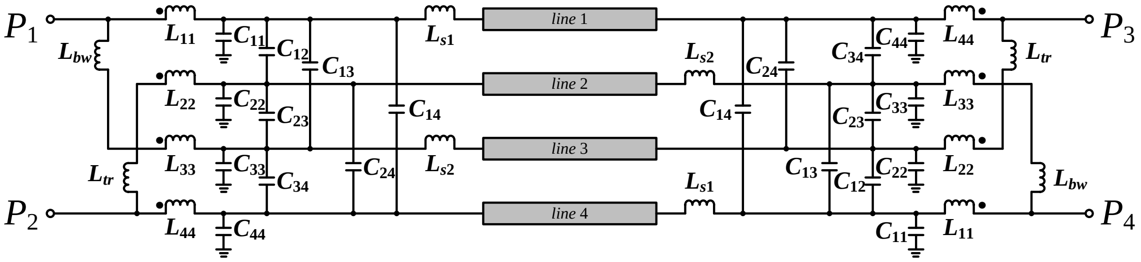

Figure 5.32 Equivalent circuit model of the Lange coupler in Figure 5.31.

Since we have already established the equivalent circuit model of coupled lines, we can carry out our simulations in circuit simulator in order to save both time and resources if the equivalent circuit model of launching circuit is available. Figure 5.32 presents the equivalent circuit model corresponding to the Lange coupler shown in Figure 5.31.

In Figure 5.32, the bonding wire is modeled as an inductor (L_{bw}), while the bonding pads and interconnecting lines are modeled as a short section of four-coupled lines with unequal line width, of which two are connected by a small section of transmission line (L_{tr}) as shown in Figure 5.31. The inductance of bonding wire is extracted through the use of a numerical TRL calibration technique [75]. The height of bonding wire is increased from 25 um to 100 um in order to find the variation of inductance L_{bw} (Figure 5.33). We can conclude that the bonding wire inductance is increased with the increment of the wire length.

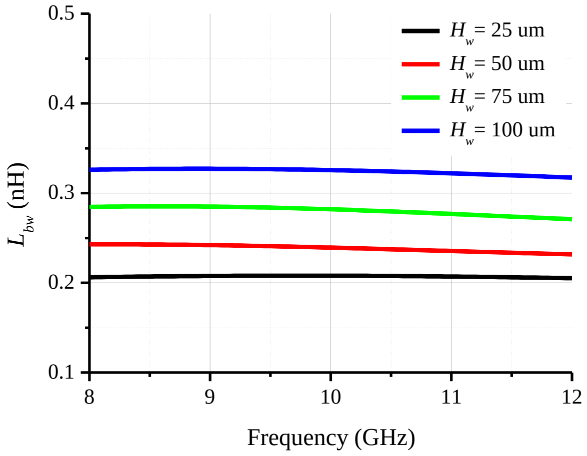

Figure 5.33 Extracted inductances of bonding wires with different heights.

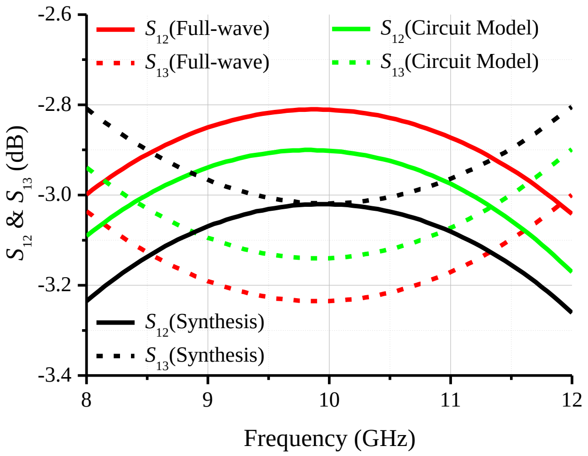

(a) Magnitude of S_{12} and S_{13} in dB.

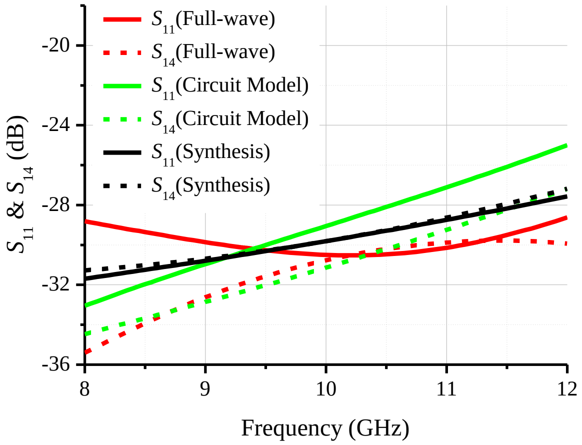

(b) Magnitude of S_{11} and S_{14} in dB.

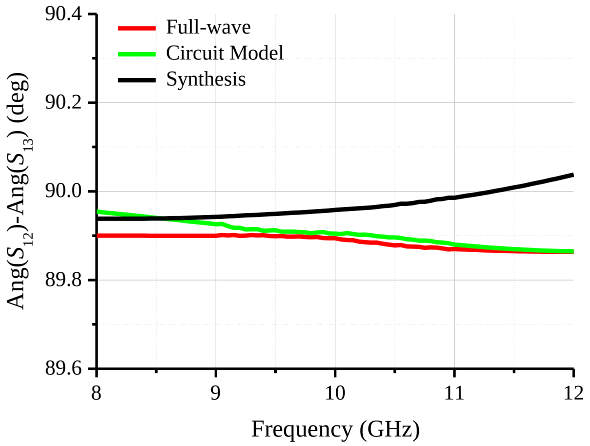

(c) Phase difference between the coupled port and the direct port.

Figure 5.34 Comparison among circuit simulation and full-wave simulation results as well as synthesized results.

Table 5.7 Extracted parametric values of equivalent circuit model in Figure 5.32.

Symbol	Value	Symbol	Value
L_{11}	0.069 (nH)	C_{11}	0.0112 (pF)
L_{22}	0.097 (nH)	C_{22}	0.0022 (pF)
L_{33}	0.069 (nH)	C_{33}	0.0083 (pF)
L_{44}	0.103 (nH)	C_{44}	0.0052 (pF)
L_{12}	0.044 (nH)	C_{12}	0.0073 (pF)
L_{13}	0.029 (nH)	C_{13}	0.0028 (pF)
L_{14}	0.022 (nH)	C_{14}	0.0002 (pF)
L_{23}	0.044 (nH)	C_{23}	0.0072 (pF)
L_{24}	0.031 (nH)	C_{24}	0.0001 (pF)
L_{34}	0.046 (nH)	C_{34}	0.0082 (pF)
L_{bw}	0.261 (nH)	L_{s1}	0.055 (nH)
L_{tr}	0.167 (nH)	L_{s2}	0.045 (nH)

In the lossless case, circuit simulation results and full-wave simulation results [66] are compared together with the synthesized results in Figure 5.34. From Figure 5.34, we have the following observations. First, in the ideal case, Figure 5.30 is very accurate for synthesizing a four-line interdigitated coupler. The coupling factor is 3 ± 0.25 dB over the X-band while the return loss and the isolation are found to be better than 28 dB. Moreover, the phase difference between the coupled port (P_2) and the direct port (P_3) is less than 90 ± 0.06 °in the entire frequency band. Second, the full-wave simulation results are different from our synthesized results due to the input/output launching circuits and two bonding wires. There are two aspects of their influence. On one hand, the coupling level is increased by 0.2 dB in the presence of bonding wire. On the other hand, the phase difference between P_2 and P_3 is also affected. However, the circuit simulation based on our extracted and established circuit model is quite close to the full-wave simulation except for a maximum 0.08 dB difference in S_{12} and a maximum 0.05 ° difference in phase difference. Therefore, the full-wave simulation can well be predicted through the circuit simulation. The extracted values of all circuit parameters in Figure 5.32 are listed in Table 5.7 for reference.

After slight optimization for introducing all losses and compensating the parasitic effects of the launching circuits and bonding wires, a quite good performance is obtained as plotted in Figure 5.35. In the simulated frequency band, the coupling factor varies from −3.6 dB to −3.28 dB, and the return loss is better than 23.5 dB while the isolation is better than 27.7 dB. The phase difference between the coupled and the direct ports is 89.8 ± 0.2 °.

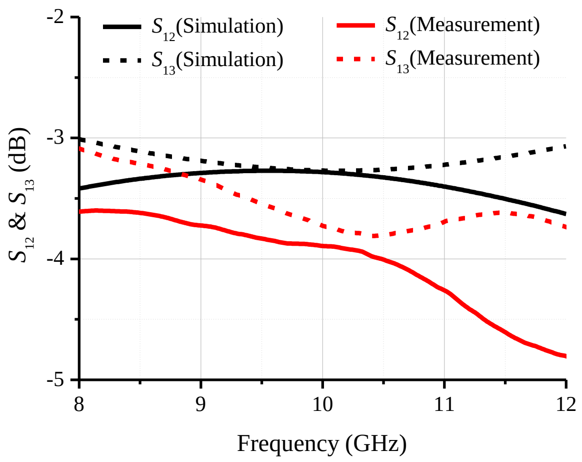

(a) Magnitude of S_{12} and S_{13} in dB.

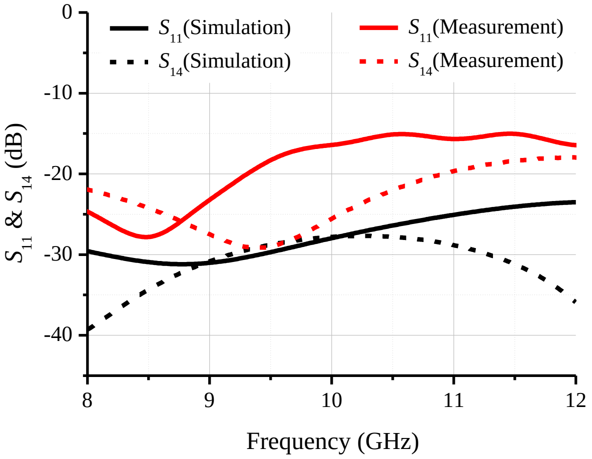

(b) Magnitude of S_{11} and S_{14} in dB.

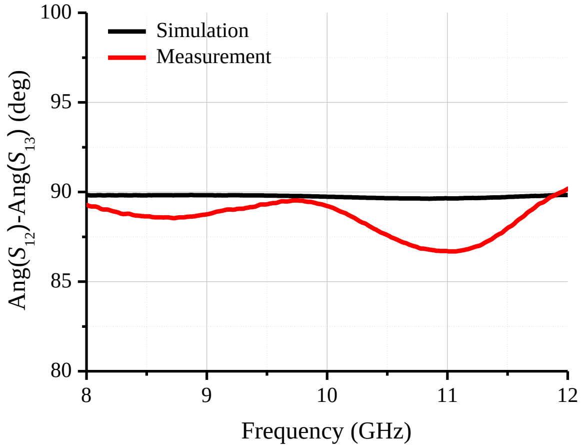

(c) Phase difference between the coupled port and the direct port.

Figure 5.35 Comparison between simulated and measured performance.

This Lange coupler is processed using a single layer liftoff process, and Figure 5.36 shows a scanning electron microscope (SEM) photograph of the fabricated sample. After the assembly of wire bonding, the Lange coupler is mounted on a brass base, and then measured with four subminiature version A (SMA) connectors. The photograph of the entire test fixture is shown in Figure 5.37. Total circuit size is 4.3×4.3 cm^2.

Figure 5.36 An SEM photo of the fabricated Lange coupler before bonding wires assembly.

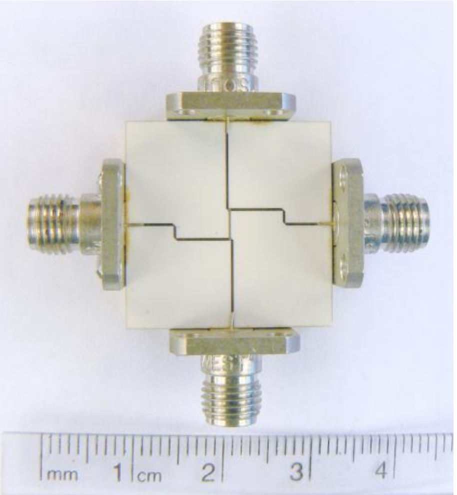

Figure 5.37 Test fixture with Lange coupler mounted.

The measured results are compared with the simulated results in Figure 5.35. There is an additional loss of 0.6 dB at 10 GHz, which could be partly brought in by the SMA connectors and partly by the inadequate estimation of the dielectric loss of substrate as well as the metallic losses.

The measured return loss is better than 15 dB while the measured isolation is better than 18 dB. Moreover, the measured phase difference varies within ±2°. In our experiment, the SOLT calibration method is used. After calibration, the reference planes are set at the input of the SMA connectors, and the parasitic effects (both the insertion loss and the inserted phase response) of the SMA connectors are embedded in the measurement results. Therefore, the discrepancy between these measurement results and simulation results, especially for the return loss and the isolation (Figure 5.35(b)), is much dependent on the quality of the SMA connectors.

It is worthwhile to mention that by making use of the strong coupling between interdigitated lines, a novel kind of packaged ultra-wideband bandpass filters has been successfully developed based on the stub-loaded resonator [107]-[108]. In addition, the technique we developed for modeling bonding wires have also been used to analyze the performance of wire-bonding interconnection between PCB and commercial leaded package. As a result, a miniaturized packaged microstrip diplexer has been designed [109].

5.5.3.2 A composite microstrip-CPW coupler

As a second example, our proposed synthesis method is used to design a kind of interdigitated couplers that can be implemented through a standard PCB fabrication process [110]-[111]. In this kind of interdigitated couplers, CPW is selected as the coupled transmission line and the bonding wires are realized by a connecting route of vias and strips underneath the central CPW conductors (see Figure 5.38). The substrate selected is 0.5 mm-thick RT/duroid® 6002 with a permittivity of 2.94.

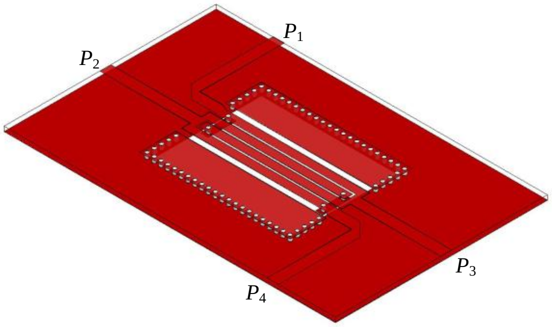

(a) Perspective view.

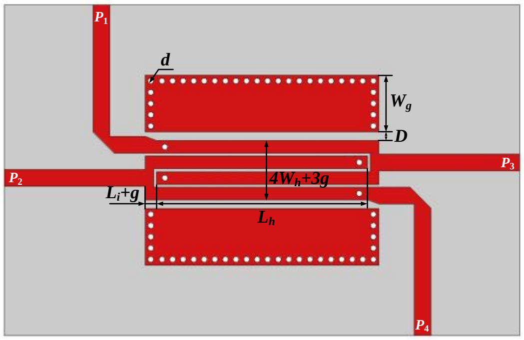

(b) Top view.

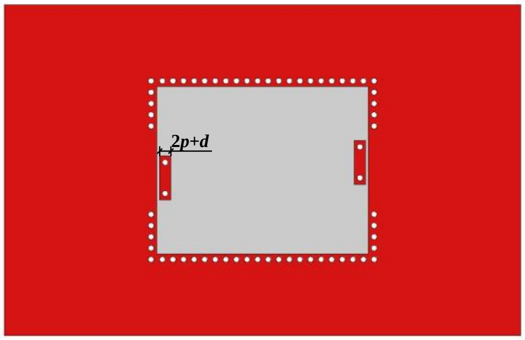

(c) Bottom view.

Figure 5.38 Sketch of a composite microstrip-CPW coupler.

In the case of using the CPW technology, the coupling between interdigitated strips can be adjusted through changing strips width W_h, gaps g between four central strips, and gap D between the outmost strip and the CPW ground on the same plane. Therefore, we set the value of D as 0.762 mm to build up the reference chart (Figure 5.39) for the edge-coupled CPW as already showcased in the last section.

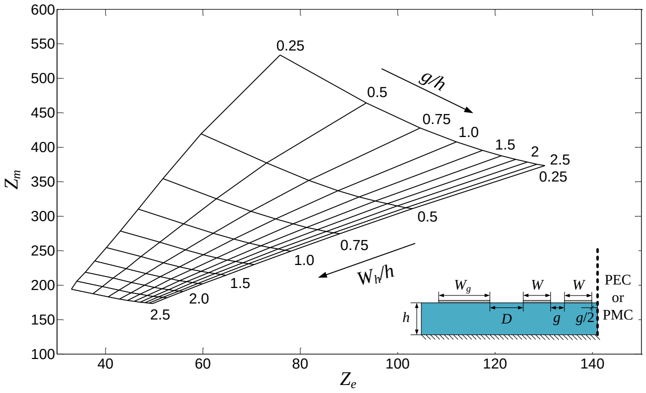

Figure 5.39 Reference chart for designing the composite microstrip-CPW coupler.

Again, we synthesize a 3-dB coupler in this case, and Z_e and Z_m are therefore the same as in the former example. Ratios W_h/h and g/h are read out from Figure 5.39 as 1.8 and 0.4, respectively. The width of interconnecting line L_i is 0.6 mm. The ground width of edge coupled CPW section W_g is 4 mm, and length L_h is 17.78 mm corresponding to center frequency at 2.9 GHz. All the vias have a diameter d of 0.4 mm and marginal distance p is 0.2 mm. Simulated responses plotted in Figure 5.40 show good performance, which verifies the great utility of this kind of coupler in the our proposed 24-GHz systems. The return loss is better than 23.5 dB and the isolation is better than 18 dB from 1 to 5 GHz, while the phase difference between the coupled port and the direct port is increased from 90 ^{o}to 92 ^{o}.

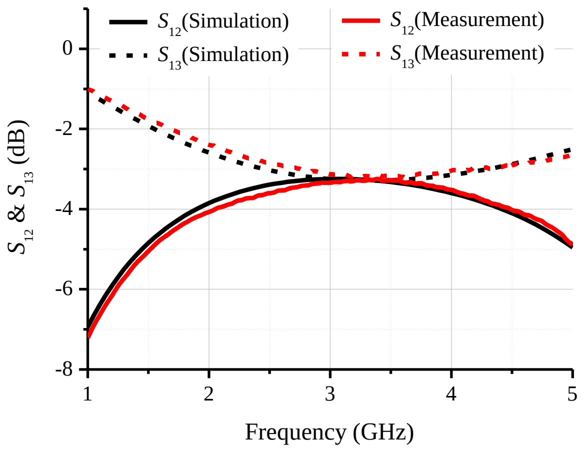

(a) Magnitude of S_{12} and S_{13} in dB.

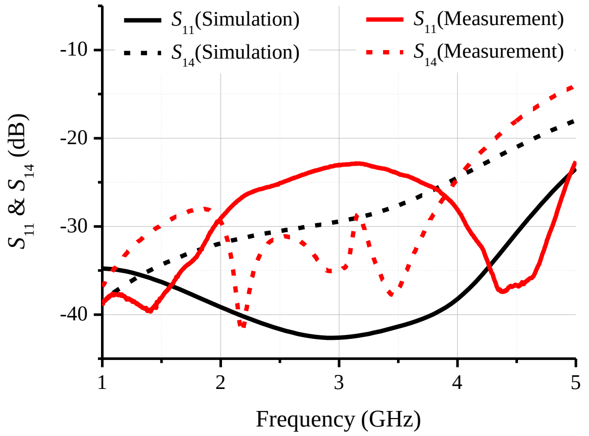

(b) Magnitude of S_{11} and S_{14} in dB.

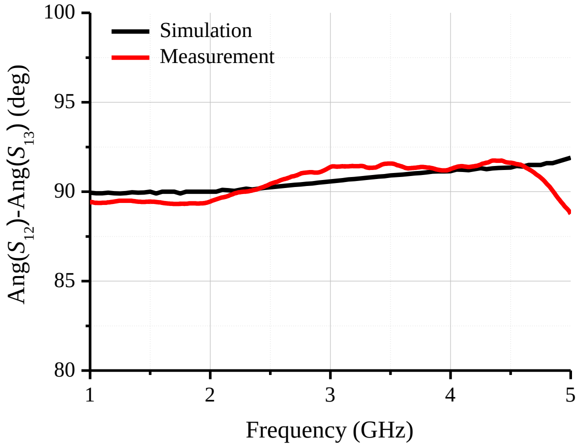

(c) Phase difference between the coupled port and the direct port.

Figure 5.40 Comparison between simulation and measurement.

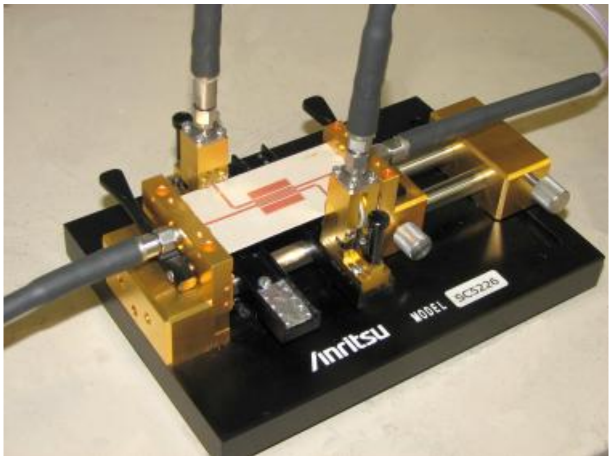

Figure 5.41 Measurement setup using a four-port VNA.

A prototype is fabricated using a standard PCB fabrication process, and then it is fixed on a universal test fixture (Wiltron SC5226) together with two right angles (Wiltron 36801K) and measured using a four-port VNA (Anritsu 37369D). The measurement setup is pictured in Figure 5.41. The measurement procedure is briefly described here. The VNA is firstly calibrated using four-port SOLT method and then the four test ports of VNA are connected to two ports of the fixture and two right angles. Pretty good measurement results (Figure 5.40) are obtained which verify our proposed synthesis method. As we described in the last subsection, the return loss and the isolation measurement (Figure 5.40(b)) are easily affected by the inserted responses of coaxial adapters after calibration.

5.6 Conclusion

In this chapter, detail synthesis design of a number of passive components including wideband 3-dB SIW couplers, broadband SIW phase shifter, highly-selective SIW bandpass filters and four-line interdigitated couplers, are discussed in detailed. Measured performance of the fabricated samples agrees well with our simulation and they are quite satisfactory for our 24-GHz system.

CHAPTER 6 MODELING OF MUTUAL COUPLING AND DESIGN OF 24-GHZ ARRAY ANTENNA

Microstrip antenna is regarded as a very good candidate for 24-GHz vehicular applications due to its low profile, light weight and easy fabrication as well as low cost of mass production. In addition to high gain, low sidelobe level is also required for microstrip array antenna in order to suppress the interference and reducing the clutter. Therefore, in our 24-GHz system, we design a microstrip array antenna on a single thin substrate with high gain and low sidelobe level. In our design, the parasitic mutual coupling is modeled through a circuit approach, which is able to model arbitrary-order mutual coupling that exists in any large-scale EM structures and high-density ICs. In this chapter, this fundamental modeling strategy will be firstly introduced, and then a multitude of application examples will be showcased to prove the efficiency and accuracy of the proposed method. Finally, a complete design procedure of the 24-GHz microstrip array will be presented with measurement results.

6.1 Research background

Microwave and millimeter-wave circuits and antennas become more and more complex and electrically large in topology due to their increased functionality, higher-frequency operation, and reduced component size. Conventional design and optimization approaches based on direct full-wave simulations may be no longer practical or even impossible with commonly available computational resources. This is particularly true when dealing with a large-scale array of mutually coupled elements or synthetic finite periodic or non-periodic waveguiding structures such as electromagnetic bandgap (EBG) structures and SICs. An efficient and flexible design approach is to segment the entire complex structure into a number of geometrically simple and electrically small discontinuities or building blocks together with uniform transmission line sections that are physically expressive, and then characterize and establish equivalent circuit models of these discontinuities and transmission line sections. In this way, the circuit models can easily be regenerated with certain modifications to the original model. This method thus leads to a direct synthesis and optimization procedure that can be carried out in a circuit simulator. However, in this case, electromagnetic parasitic effects due to element-to-element mutual coupling are ignored, which could significantly affect the circuit design accuracy and performance prediction when couplings are no longer negligible. Therefore, it can be anticipated that this segmentation and optimization procedure is capable of yielding more accurate results if the accurate equivalent circuit model of principal or dominant mutual couplings can be formulated and incorporated into the circuit simulator.

The mutual coupling, whether it is adjacent or crosstalk, is ubiquitous. This can be found between any circuit elements of any size in proximity. Let us consider the following two examples. Parasitic mutual coupling between any pair of resonators in a filter would create an influence on the entire filtering response no matter what kind of classic synthesis procedures are adopted. The other is the mutual coupling between parallel transmission lines for high-speed signal propagation in connection with its impact on digital signal integrity and synchronization performance.

Equivalent source method has been used for calculating the mutual coupling between discontinuities in planar circuits [112]-[114]. When it comes to a large but finite-extent antenna array, there are two main methods for modeling mutual coupling, namely the spatial domain (element-by-element) method and the spectral domain (periodic cell) method [115]-[116]. The spatial domain method is more suitable for modeling small and medium-sized arrays because it needs to calculate the mutual impedance or mutual admittance of each pair of elements. Various numerical techniques such as MoM [117]-[118] and mixed potential integral equation (MPIE) technique [119]-[120] have been developed for this purpose. However, when a large array is analyzed, it could consume a large amount of computational resources and time. On the other hand, the spectral domain method has been considered to be more efficient in this case. To include all the mutual coupling effects, periodic boundary conditions are imposed on a single element, which implies that the excitations of a phased array are the same for all elements except for a progressive exponential multiplier. Therefore, this technique ignores edge or border effects as well as non-uniform current distributions. This is because any large but finite array has a limited boundary so that the periodic array theorem (Floquet’s theorem) is no longer valid, particularly for elements close to the array edges. Moreover, there are a number of alternative algorithms, which were developed for reducing the computational requirements by combining these two methods [121]-[123].

In [112], the mutual coupling of higher than first-order is neglected, assuming that any higher-order mutual coupling is not strong enough or has no influence on system performance. A method for evaluating the mutual coupling of microstrip dipoles in an array environment was reported and discussed in [124], which only considered a small array of five elements. However, it cannot be applied to a large array since the high-order mutual coupling is no longer explicitly formulated.

Equivalent circuit models have widely been used to establish the relationship between physical phenomena and electrical properties of electromagnetic structures. In the equivalent circuit models, electromagnetic field interactions or coupling between circuit elements or building blocks are usually represented by a certain form of impedance/admittance networks. This opens up the possibility of using equivalent circuit models to describe both low- and high-order coupling for multiple-coupled circuits and elements since any coupling is related to electric and/or magnetic fields. As a result, the segmentation method would become more complete and consistent by incorporating equivalent circuit models of mutual couplings.

A method of modeling mutual coupling of any-order was proposed in [125], which is on the basis of parameter extraction and formulation of its equivalent circuit through field-theoretical electromagnetic modeling technique. In this case, the mutual coupling of arbitrary-order is explicitly modeled and characterized in the form of an equivalent circuit. The equivalent-circuit description for low-order mutual coupling (adjacent coupling) allows the successive extraction of the circuit model of a high-order coupling (crosstalk coupling). This modeling strategy has been successfully applied to the comprehensive analysis and accurate design of different types of electromagnetic structures including linear and planar array antenna, finite periodic structures and low-pass filters [125]-[127].

In the modeling strategy, the kth-order mutual coupling is defined as the coupling between two elements in the presence of $(k-1)$ other elements. If we assume that mutual coupling of $(k+1)$th-order does not affect lower-order mutual coupling, then the equivalent circuit models of the $(k+1)$th-order mutual coupling can be obtained from the difference between the equivalent circuit network including $(k+1)$th-order and that excluding it.

6.2 Description of coupling decomposition

To begin with, the concept of coupling decomposition is introduced. Let us consider an N-port microwave network consisting of N mutually coupled elements shown in Figure 6.1. These elements are considered generally dissimilar; however, they can be identical, such as the elements of a finite periodic structure [128].

Assume that element i (i = 1, 2, …, N) in Figure 6.1 is excited by a current I_i, the resulting voltage vector V is related to the excitation current vector I through the following expression.

$$I = YV \tag{6.1}$$

where $Y = [Y_{mn}]_{N\times N}$ is the admittance matrix of this N-port network.

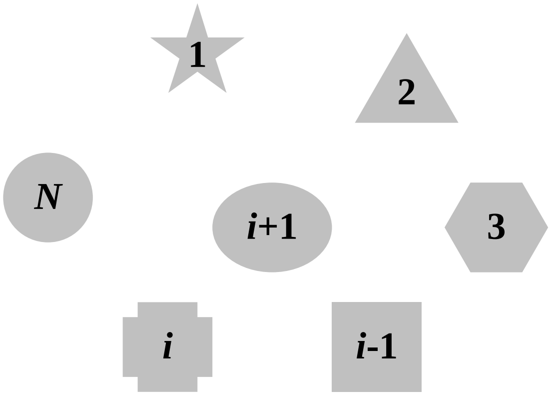

Figure 6.1 Mutually coupled elements numerated from 1 to N.

We introduce a matrix $Y^{iso} = [Y^{iso}_{mn}]_{N\times N}$ whose diagonal elements are the input admittance of isolated element i as Y^{iso}_{i},

$$Y^{iso}_{mn} = \begin{cases} Y^{iso}_{i} & (m = n) \\ 0 & (m \neq n) \end{cases} \tag{6.2}$$

Then, the admittance matrix could be found as a sum of Y^{iso} and M, which reflects such mutual coupling between the elements as,

$$M=\begin{bmatrix} Y_{11}-Y_1^{iso} & Y_{12} & \cdots & Y_{1N} \\ Y_{21} & Y_{22}-Y_2^{iso} & \cdots & Y_{2N} \\ \cdots & \cdots & \cdots & \cdots \\ Y_{N1} & Y_{N2} & \cdots & Y_{NN}-Y_N^{iso} \end{bmatrix} \tag{6.3}$$

Consequently, (6.1) can be rewritten as,

$$V=ZI=\left(Y^{iso}+M\right)^{-1}I \tag{6.4}$$

In (6.4), matrix Z is the impedance matrix of the N-port network, and it can be expanded as in [129],

$$Z=\left(Y^{iso}+M\right)^{-1}=\sum_{k=0}^{\infty}\left[-\left(Y^{iso}\right)^{-1}M\right]^{k}\left(Y^{iso}\right)^{-1} \tag{6.5}$$

Studies have already shown that the mutual impedance between elements is in most cases much smaller than the input impedance of an isolated element in case that the wavelength-normalized distances between elements are larger than half-wavelength [125],[130]. Therefore, matrix M can be seen as a small perturbation of the isolated admittance matrix Y^{iso}, and the sum series is convergent. Moreover, (6.5) suggests the possibility of a coupling decomposition, which allows extracting the mutual coupling of arbitrary-order in a successive manner.

In our implementation, equivalent circuit networks are built up in order to model mutual coupling of arbitrary-order. It is assumed that the equivalent circuit networks of low-order mutual coupling do not change when they are used for extracting equivalent circuit networks of high-order mutual coupling. In the following sections, this modeling technique will be elaborated.

6.3 Modeling of mutual coupling in one-dimensional structures

6.3.1 Design of a single radiating element

In our demonstration, a microstrip inset-fed patch antenna resonating at 10 GHz is chosen as an element, of which the dimensions are given in Table 6.1. This antenna is designed on the substrate RO3003® with a permittivity of 3 and a thickness of 0.5 mm. Simulated return loss from 8 GHz to 12 GHz is shown in Figure 6.2, which indicates very good matching at 10 GHz.

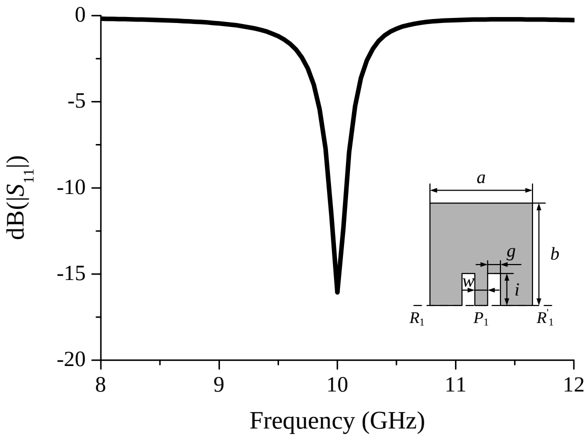

Figure 6.2 Return loss of a single microstrip inset-fed patch antenna.

Table 6.1 Dimensions of the inset-fed microstrip antenna.

Symbol	Value (mm)
a	11.94
b	8.48
g	1.27
i	2.16
w	1.27

6.3.2 Modeling of first-order mutual coupling

Figure 6.3 depicts two adjacent coupled circuit elements that are separated by a distance of *s*. Two excitation ports are designated as P_1 and P_2, respectively, with their reference planes marked as R_1-R_1' and R_2-R_2'.

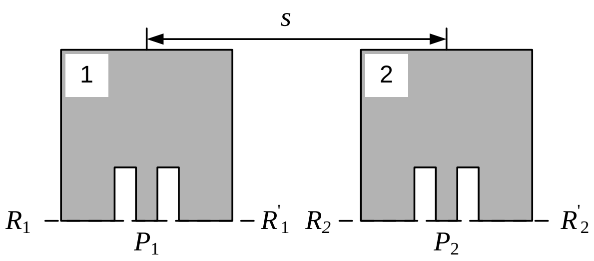

Figure 6.3 Two adjacent coupled circuit elements.

In fact, the elements can be resonators, antennas, or even small discontinuities. It is well-known that a two-port network can be represented by its impedance matrix (*Z*-matrix), or admittance matrix (*Y*-matrix). We will use the *Y*-matrix representation in the following discussions. Note that a *Z*-matrix description is also applicable to a different circuit topology.

We assume that the admittance matrix of the two coupled circuit elements is expressed by,

$$Y^{(1)} = \begin{bmatrix} Y_{11}^{(1)} & Y_{12}^{(1)} \\ Y_{12}^{(1)} & Y_{22}^{(1)} \end{bmatrix} \tag{6.6}$$

where the superscript stands for the order of mutual coupling. $Y_{11}^{(1)}$ is the self admittance of element 1 and $Y_{22}^{(1)}$ is the self admittance of element 2. In our case, those elements are identical so that $Y_{11}^{(1)}$ is equal to $Y_{22}^{(1)}$. $Y_{12}^{(1)}$ is the mutual admittance reflecting the strength of first-order mutual coupling between the two elements.

The well-known equivalent circuit representation of the above *Y*-matrix is shown in Figure 6.4(a). If we segment the shunt admittances of the π-type network further (Figure 6.4(b)), the relationship or mapping between each element of the *Y*-matrix and the element in the equivalent circuit representation is easily understood. In Figure 6.4(b), the centered π-type network stands for the first-order mutual coupling between two circuit elements, while the two remaining shunt admittances represent the self admittance of each element, respectively.

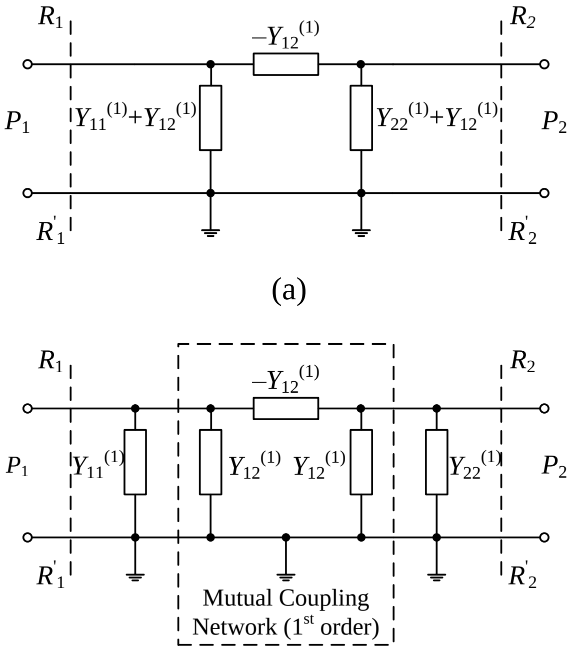

(a)

(b)

Figure 6.4 Modeling of first-order mutual coupling.

Our equivalent circuit model is extracted and developed with the help of a commercial MoM package [106]. It has been demonstrated that the direct MoM algorithms using impressed voltage excitation cannot generate accurate equivalent circuit models, especially for electrically small structures, because the impressed fields are theoretically impossible to excite an ideal dominant mode [131]. In other words, the impressed voltage excitation is used to approximately simulate the electrical field of the dominant mode in a way of lumped-element over an interface of reference. This creates an artificial “port discontinuity” with respect to the real dominant modal field at that particular location. To completely remove these parasitic “port discontinuity” effects and other potential errors in the direct or deterministic MoM algorithm, a short-open calibration (SOC) technique was proposed and implemented for obtaining much more accurate results [132]-[133]. It makes use of two standards, namely short and open standards. Through the calculation of two standards, the error boxes in the model could be removed through network theorem, which leaves the accurate calibrated network of device-under-test (DUT).

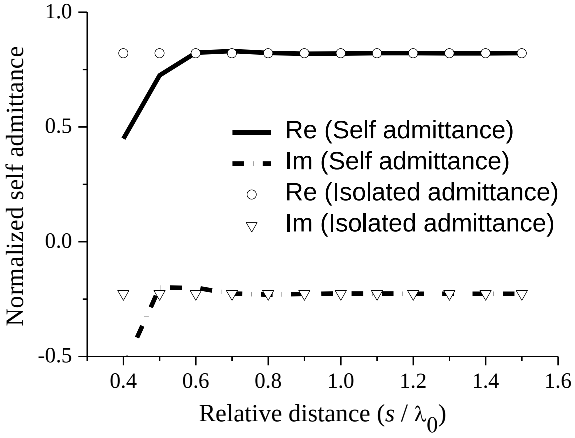

(a) Extracted normalized self admittance of first-order mutual coupling versus wavelength-normalized distance (s/λ_0).

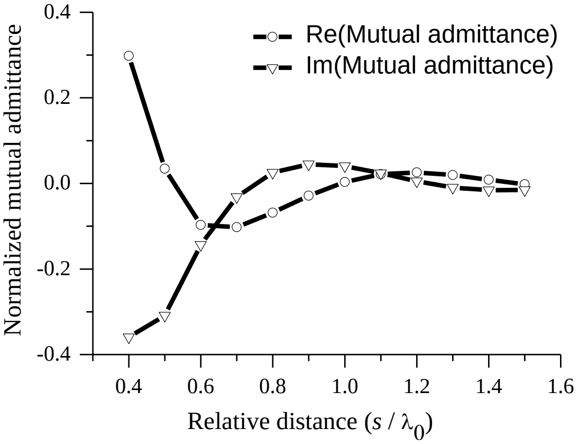

(b) Extracted normalized mutual admittance of first-order mutual coupling versus wavelength-normalized distance (s/λ_0).

Figure 6.5 Extracted results of first-order mutual coupling.

The extracted self and mutual admittances are given in Figure 6.5. From Figure 6.5, we can observe that when the distance between the two elements s is enlarged from 0.4 λ_0 to 1.5 λ_0, the self admittance of both elements converges to the input admittance of an isolated element, and the mutual admittance approaches zero. This result indicates that if the two elements are separated far away from each other, their mutual coupling is weak enough so that we can treat each of these elements as an isolated element.

6.3.3 Modeling of second-order mutual coupling

In the case of three coupled elements (Figure 6.6), if we add two external ports to P_1 and P_2 and terminate P_3 with a matched load Z_0 (50 ohm in our case), we will consider two kinds of mutual coupling. One is the first-order mutual coupling between elements 1 and 3 and between elements 2 and 3. The other is the second-order mutual coupling between elements 1 and 2 in the presence of element 3.

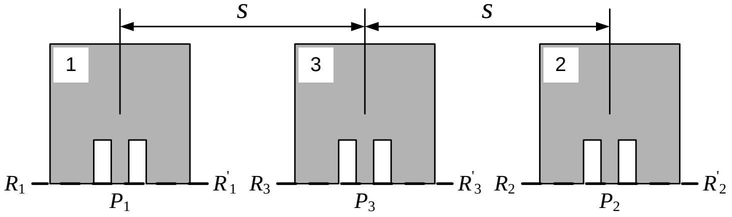

Figure 6.6 Three coupled elements.

The equivalent circuit topology of such a configuration of three mutually coupled elements is described in Figure 6.7(a). The admittance matrix of this two port network is designated as $Y^{(2)}$. For extracting the equivalent circuit model of a second-order mutual coupling, we build up a cascaded equivalent circuit network with self-admittances of three elements and two first-order mutual coupling networks on the basis of the previous extraction results. This configuration can be seen in Figure 6.7(b). Since P_3 in Figure 6.7(b) is terminated with Z_0, we could obtain another two-port Y-matrix which is designated as $Y'^{(2)}$. Based on our assumption, the parametric values in Figure 6.7(a) are the same as those in Figure 6.7(b) except for the unknown terms of the second-order mutual coupling. Since Figure 6.7(b) does not include the effect of second-order mutual coupling, the equivalent circuit network of the second-order mutual coupling can simply be calculated from the difference of $Y^{(2)}$ and $Y'^{(2)}$ through the standard network theorem.

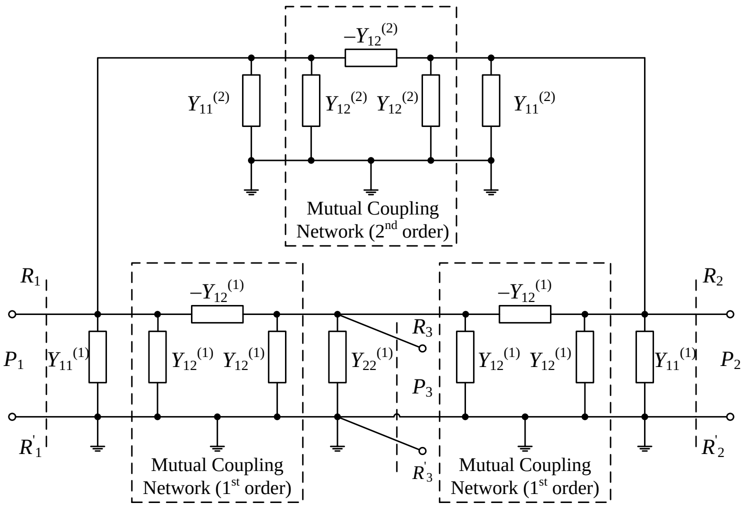

(a) Equivalent circuit including second-order mutual coupling.

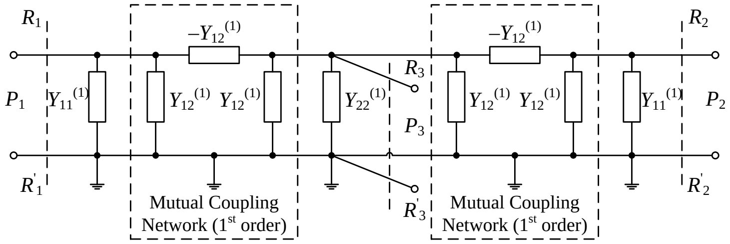

(b) Equivalent circuit excluding second-order mutual coupling.

Figure 6.7 Modeling of second-order mutual coupling.

The self admittance of second-order mutual coupling indicates the second-order mutual coupling effect on the self admittance of each element. It can be observed from Figure 6.8(a) that when s is larger than $0.6\lambda_0$ in this particular example, the self admittance is nearly equal to zero and therefore independent of second-order mutual coupling. This suggests that under the given condition, the second-order mutual coupling has no effect on the self admittance of each element.

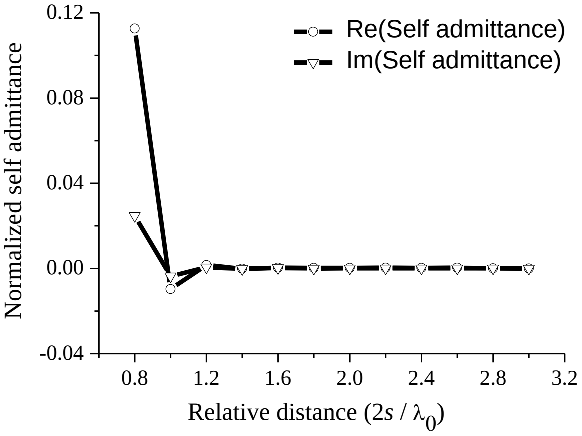

(a) Extracted normalized self admittance of second-order mutual coupling versus relative distance ($2s/\lambda_0$).

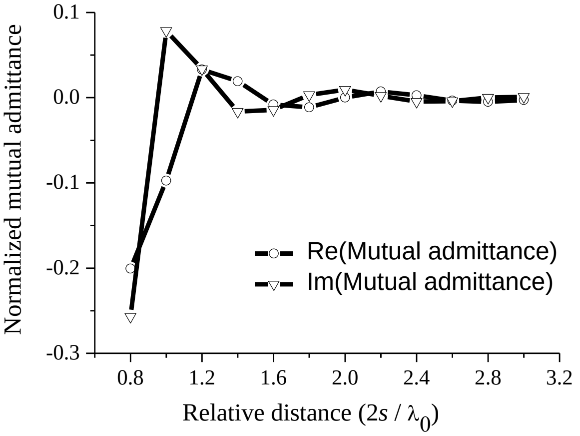

(b) Extracted normalized mutual admittance of second-order mutual coupling versus relative distance ($2s/\lambda_0$).

Figure 6.8 Extracted results of second-order mutual coupling.

The second-order mutual admittance also has a similar tendency of converging to zero as the distance between elements 1 and 2 is enlarged (Figure 6.8(b)). The first- and second-order mutual admittances are compared in Figure 6.9. It is shown that the second-order mutual coupling is larger than the first-order, which is to say that the coupling level between elements 1 and 2 is larger in the presence of element 3. The reason behind this phenomenon is that the current of element 2 is more easily induced by the current of element 3 induced from element 1 rather than directly by element 1.

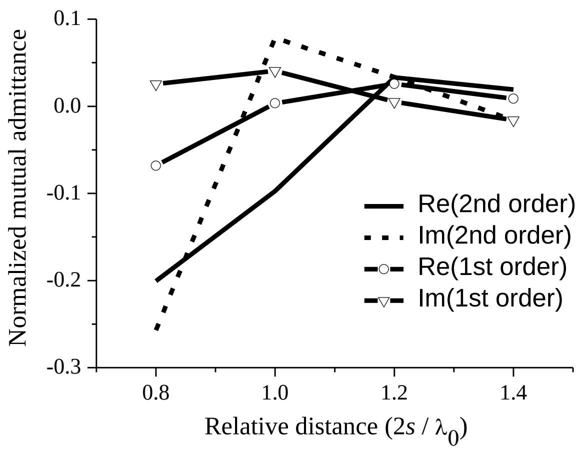

Figure 6.9 Comparison of extracted first-order and second-order mutual admittances.

6.3.4 Modeling of higher-order mutual coupling

Following the same procedure, we can successively model the mutual coupling of arbitrary-order. Scattering coefficients S_{21} of the mutual coupling networks (see Figure 6.4(b)) from the first- to the fourth-order are plotted in Figure 6.10. It can be seen that, if only the mutual coupling network is considered, there is still a moderate coupling between two edge or border elements even for the fourth-order mutual coupling due to the presence of the intermediate elements.

The entire extraction procedure can be summarized in a flowchart illustrated in Figure 6.11. The *n*th-order mutual coupling ($Y_{mc}^{(n)}$) between two coupled elements is obtained by the difference of calibrated simulation results ($Y_c^{(n+1)}$) including the *n*th-order mutual coupling and calculated results ($Y'^{(n+1)}$) based on the cascaded equivalent circuit models of lower-orders mutual coupling which excludes the mutual coupling of the *n*th-order. Based on our experiences, it is better to choose strong mutual coupling as low-order for reducing the modeling error. Additionally, a criterion needs to be used for setting the highest order of mutual coupling that should be taken into account according to the specified performance modeling and the required design accuracy.

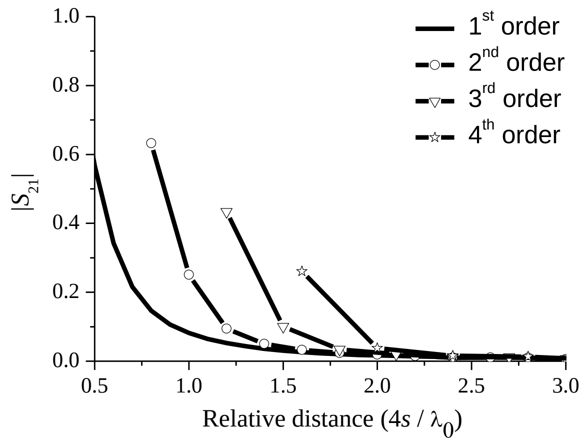

Figure 6.10 Comparison of mutual coupling of different orders.

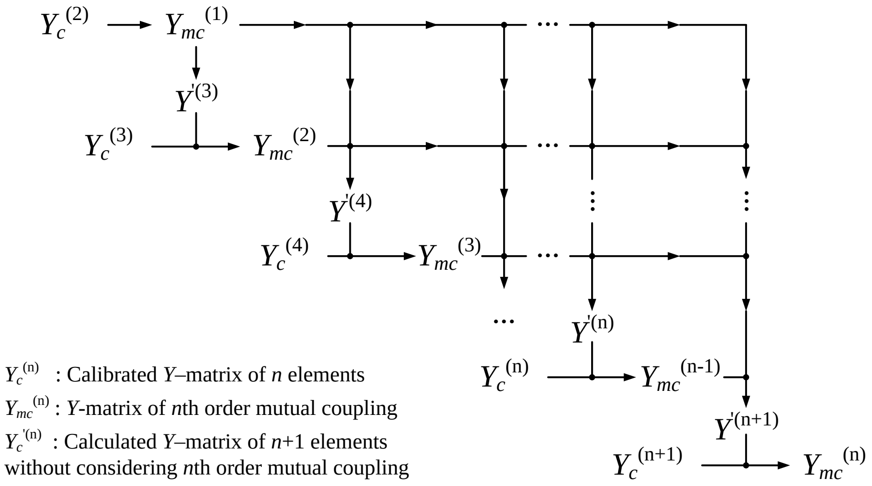

Figure 6.11 Flowchart of successive modeling of arbitrary-order mutual coupling.

6.3.5 Application examples

The following practical applications are used to examine the influences of mutual coupling of arbitrary-order with focus on higher-order mutual coupling effects. Both theoretical and experimental results will be explored to validate the proposed strategy and its usefulness.

6.3.5.1 Analysis of linear phased array antenna

First of all, a linear phased array antenna composed of 19 half-wavelength-spaced elements with a beam direction of $\theta = -30^{\circ}$ will be modeled with the help of the proposed method to demonstrate its accuracy and efficiency (Figure 6.12). This array antenna is placed along the *x*-axis in the *xoy*-plane.

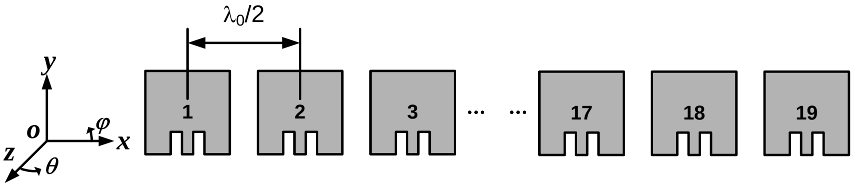

Figure 6.12 A linear phased array antenna composed of 19 half-wavelength-spaced elements.

To begin with, the equivalent circuit models of mutual coupling from the first-order to the third-order are extracted and the fourth-order mutual coupling is found to be too weak to be considered in this case. In Figure 6.13, the normalized self admittances of different elements (elements 1-5) in the array are plotted during the process of establishing the equivalent circuit network of mutual coupling.

From Figure 6.13, we can make the following observations. First, the influence of neighbouring elements on the host element is shown. When there is no neighbouring element present, the self admittance is equal to the input impedance of an isolated element. If we consider for example the leftmost element (element 1) with three neighbouring elements (elements 2-4, $N = 3$), there is no influence of the next neighbouring element (element 5) on it, and this can be seen from the convergence of its admittance. This observation concludes that we only need to consider the mutual coupling of up to the third-order. Second, Figure 6.13 also shows the "edge effect". The edge elements (elements 1 and 2) behave differently in the array environment from the inner elements (i.e., elements 3-5) in terms of the number of neighbouring elements and the order of mutual coupling which should be considered. It is also interesting to find out that the normalized input conductance (Figure 6.13(a)) of elements 2 and 3-5 are almost equal, while the susceptance (Figure 6.13(b)) are different. As a result, the return losses for these elements are still different. Therefore, in the final array design, elements 1 and 2 as well as their symmetrical counterparts (elements 19 and 18, respectively) should be treated differently from the interior or inner elements (elements 3-17).

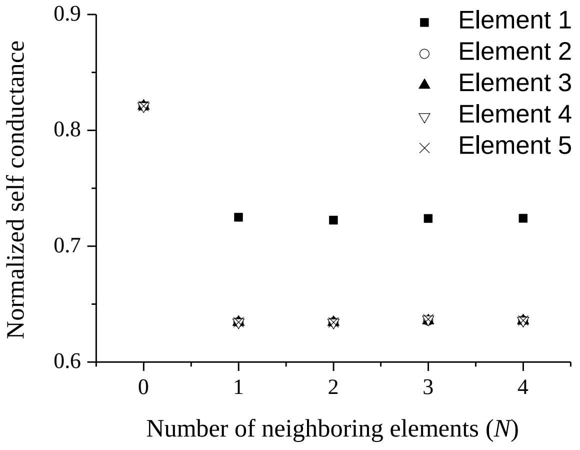

(a)

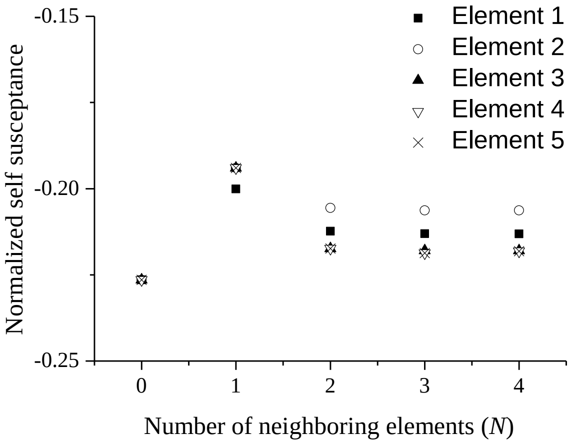

(b)

Figure 6.13 Influences of neighbouring elements on the host element.

Then, the scattering matrix of this 1×19 array is obtained by cascading and simulating the equivalent circuit networks of the patches themselves and their mutual couplings in a commercial circuit simulator [63].

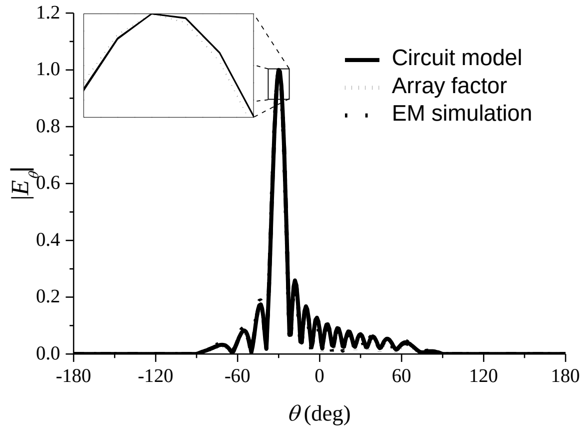

(a) Radiation pattern for the 1x19 array (*xoz*-plane).

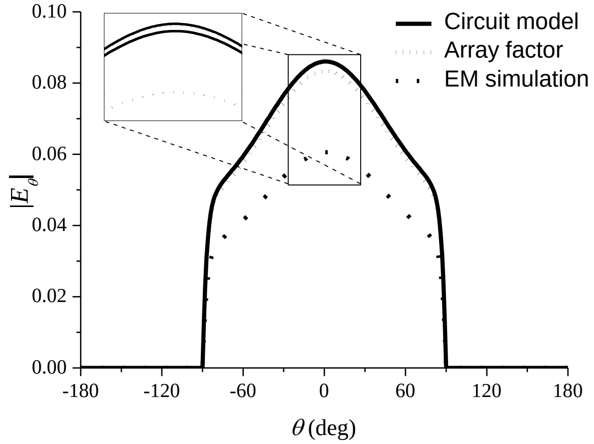

(b) Radiation pattern for the 1x19 array (*yoz*-plane).

Figure 6.14 Array patterns comparison.

Finally, we can calculate the array pattern from the simulation results of scattering matrix of the antenna array as it is known that the pattern of a phased array can be expressed by the product of the active element pattern ("scan element pattern" in [115]-[116]) and the array factor [134]-[135]. The array patterns are calculated by three different methods in our investigation for the purpose of comparison (Figure 6.14). The first method (Circuit model) calculates the active element pattern with the help of the proposed circuit modeling technique and multiplies it by the array factor, whereas the second method (Array factor), the array pattern is obtained from the product of a single element pattern and the array factor. The third method (EM simulation) uses a direct full-wave simulation in a commercial MoM package [106].

From this systematic comparison among the results of these three methods in Figure 6.14, we can conclude that: for the *xoz*-plane pattern, the calculated results from the proposed circuit model and the direct EM simulation are almost the same. However, we can find that there is a deviation among these results and the array pattern obtained from the product of a single element pattern and the array factor. The reason for this behaviour is that in the latter calculation, the mutual coupling between elements is not included. On the other hand, for the *yoz*-plane, the array pattern calculated by means of the proposed circuit model has little difference from the direct EM simulation. It should also be mentioned that a good agreement of the array gains is achieved with these three methods, which are listed in Table 6.2.

Table 6.2 Comparison of array gains calculated by three different methods.

Method	Array Gain
Circuit model	16.6001
Array factor	16.6142
Direct EM simulation	16.6770

6.3.5.2 Analysis of periodic structures

This example is showcased to present a design method for finite periodic structures, which takes the mutual coupling effect into account and compares the results with those obtained from conventional design methods.

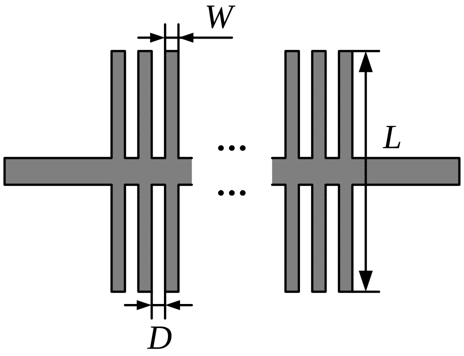

Figure 6.15 A periodic structure of finite size consisting of *N* microstrip stubs.

Figure 6.15 shows a microstrip periodic structure consisting of *N* stubs with a width of *W* and a spacing of *D*. In our investigation, we choose a RT/duroid® 6010.2LM substrate with a thickness of 1.27 mm. The stub length *L* is kept constant as 10 mm in this example.

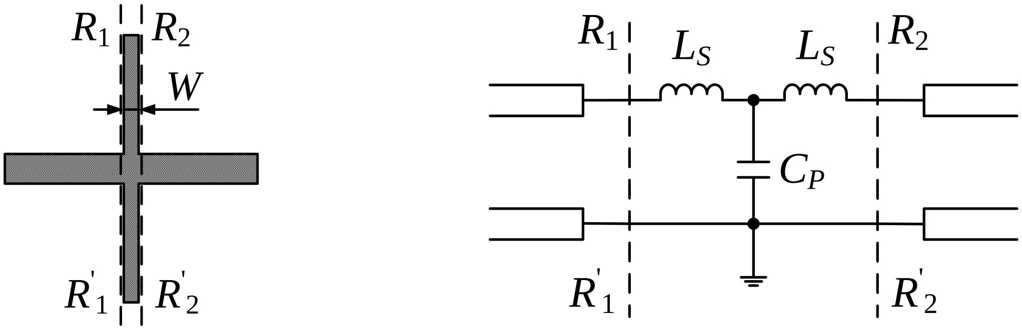

(a) (b)

Figure 6.16 (a) A microstrip stub and (b) its equivalent circuit model.

The microstrip stub discontinuity and its equivalent circuit model are plotted in Figure 6.16(a) and (b), respectively. First, inductance L_S and capacitance C_P in Figure 6.16(b) for a set of stub widths *W* are extracted by means of a numerical TRL calibration method [75], and the extracted results are shown in Figure 6.17. From Figure 6.17, we can see that both extracted inductance and capacitance show a nearly frequency-independent behaviour for frequencies up to 5 GHz and they increase due to the incremental change in the stub width *W*.

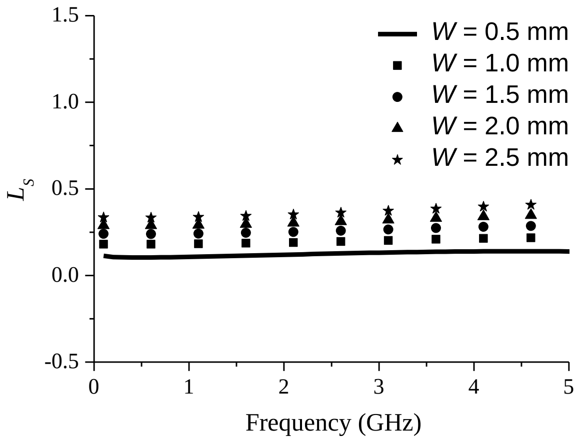

(a) Series inductance L_S (nH).

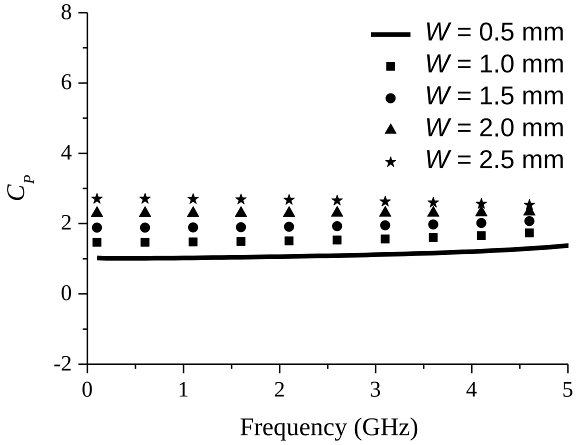

(b) Shunt capacitance C_P (pF).

Figure 6.17 Extracted parameters of the equivalent circuit model shown in Figure 6.16(b).

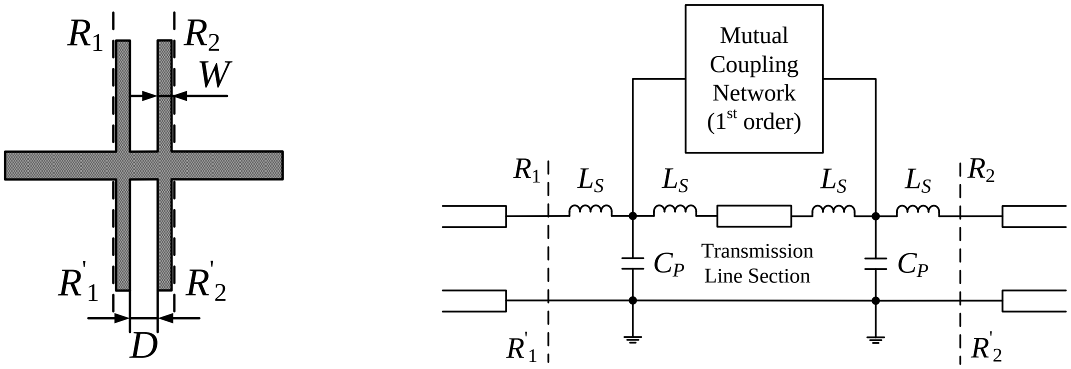

(a)

(b)

Figure 6.18 (a) Two mutually coupled microstrip stubs and (b) its equivalent circuit topology.

Then, the first-order mutual coupling between such two stubs of the same width *W* and spacing *D* is modeled as shown in Figure 6.18. The variations of scattering coefficients with respect to the physical dimensions at 1 GHz are investigated and the results are given in Figure 6.19. It is observed that the coupling between the two stubs decreases as both stub width *W* and distance *D* increase. This is because, in the case of two short stubs closely positioned, coupling between them occurs more easily through the magnetic fields. Therefore, we need to decrease the distance *D* as well as the stub width *W* to achieve a strong coupling between such two stubs.

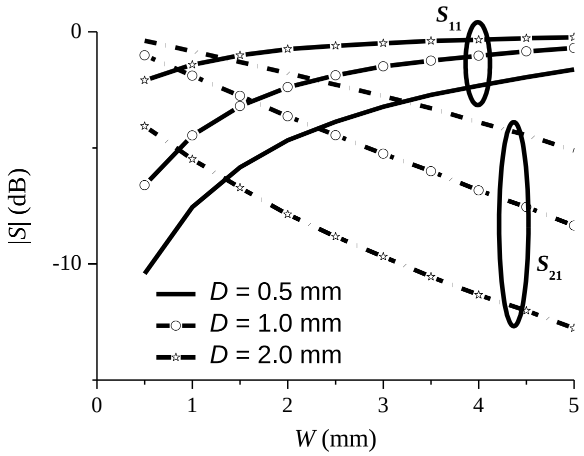

(a) Magnitude.

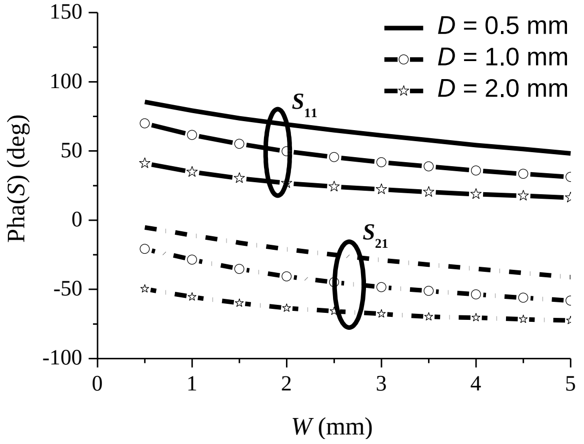

(b) Phase.

Figure 6.19 Scattering coefficients S_{11} (solid line) and S_{12} (dash dot line) of the mutual coupling network versus the physical dimension.

For verification, the presented microstrip periodic structure of finite size is designed with a fixed width *W* = 0.5 mm and two different values of spacing *D* in order to show the effects of mutual coupling. The scattering parameters of both a strong coupling case (*D* = 0.5 mm) and a weak coupling case (*D* = 5.0 mm) are compared in Figure 6.20. From Figure 6.20(a), we can observe that the simulation results obtained from our equivalent circuit model technique agree well with those obtained from full-wave simulations [66] as well as measured results. The small discrepancy is possibly caused by a small increment of the extracted inductance and capacitance in Figure 6.17 as well as fabrication tolerances. However, it is clearly observed that if the mutual coupling is neglected, the circuit simulation results are significantly different from other simulation results as well as measurements. On the other hand, for the case of a distance *D* of 5.0 mm, the coupling between the stubs is much lower than that in the previous case. In this case, we observe only a minor difference whether to include mutual coupling effects or not (Figure 6.20(b)). From this comparison, we can conclude that if the mutual coupling effect is neglected in circuits containing strongly coupled components, a good prediction cannot be provided by circuit simulations.

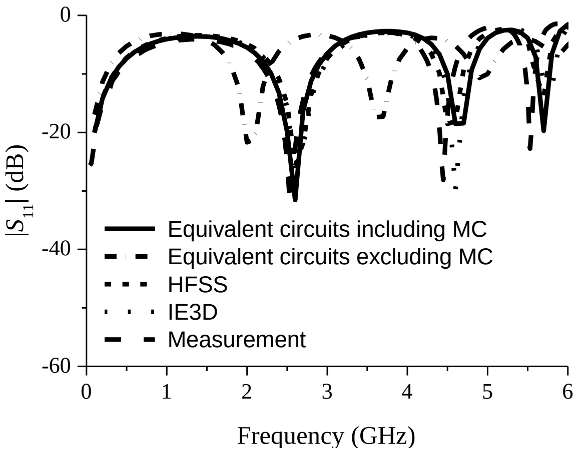

(a) Strong coupling case (D = 0.5 mm).

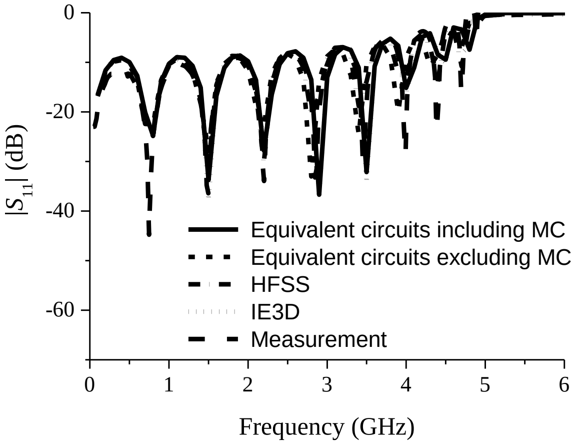

(b) Weak coupling case (D = 5.0 mm).

Figure 6.20 Simulated and measured return losses of two microstrip periodic structures with different spacing D between the stubs when the stub width W is fixed at 0.5 mm.

6.3.5.3 Design of low-pass filters

In the design of a microstrip low-pass filter, the length of a semi-lumped inductor is usually chosen as short as possible for obtaining a good stop-band performance [136]. Under this scenario, conventional synthesis method is no more valid because the mutual coupling becomes noticeable.

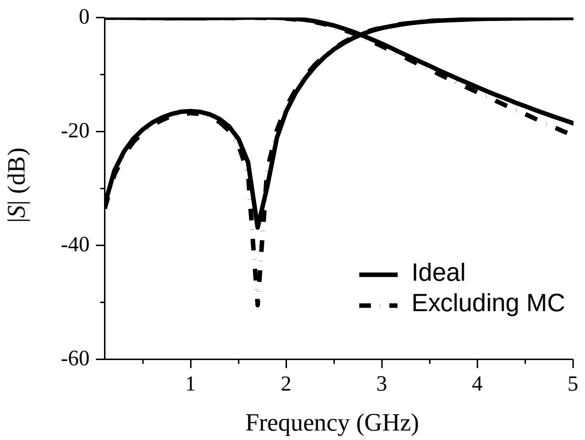

Figure 6.21 Ideal *S*-parameters response and equivalent circuit network modeling results excluding mutual coupling (MC denotes mutual coupling).

In this example, we consider a Chebyshev low-pass filter with a passband ripple of 0.1 dB and a cut-off frequency of 2 GHz yielding prototype parameters as follows: $C_1 = C_3 = 1.6420$ pF and $L_2 = 4.5654$ nH. We choose the same substrate (1.27 mm-thick RT/duroid® 6010.2LM) for its experimental implementation. With the help of the numerical TRL calibration technique that was used in the above case study, the capacitors and the inductor are realized by low-impedance microstrip lines and a short section of high-impedance microstrip line, respectively. The filtering characteristic obtained from the cascaded equivalent circuit network is plotted in Figure 6.21 together with the ideal response. It is found that without considering the effect of a mutual coupling between the two microstrip stubs, the simulation results of the cascaded equivalent circuit network agree very well with the ideal filter response, which asserts that the extracted value for both capacitors and inductor are very close to the desired lumped element values.

However, when the filter with the same physical dimensions of low- and high-impedance microstrip lines is entirely simulated by using a full-wave simulator [66], the simulation results are different from those of the circuit simulation (Figure 6.22). Indeed, this phenomenon occurs very often in microwave circuits design using the segmentation method. Since our extracted inductance and capacitance are accurate enough in terms of circuit simulation, we conclude that the difference between the circuit simulation and full-wave simulation should be attributed to neglecting the effect of mutual coupling in the circuit simulation. Once the equivalent model is refined with the mutual coupling, the filtering response is optimized with the help of several iterations in the circuit simulator, and the final response is shown in Figure 6.23. Compared with the full-wave simulation result as well as measurement result, an excellent agreement is observed.

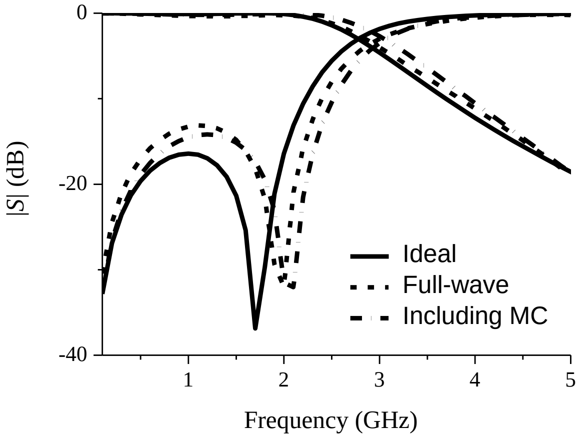

Figure 6.22 Ideal response, full-wave simulation, and equivalent circuit network modeling results including mutual coupling effect.

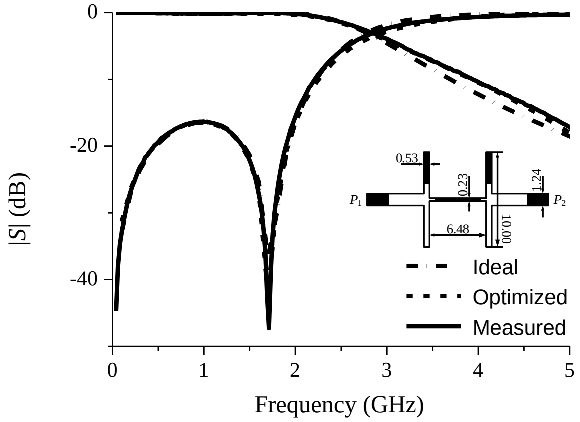

Figure 6.23 Comparison between the ideal, the optimized, and the measured responses. (The unit of all physical dimensions is mm.)

6.4 Modeling of mutual coupling in two-dimensional structures

Our proposed strategy can also be applied to model mutual coupling in two-dimensional structures [126],[137]. In this section, detailed modeling procedure will be discussed, and two design examples will be showcased including a planar phased array antenna and a 24-GHz planar array for our multifunctional system.

6.4.1 Modeling of first-order mutual coupling

In order to extract the first-order mutual coupling (immediate adjacent), two coupled microstrip inset-fed patch antennas are placed with an orientation angle of ψ and a distance of r, as shown in Figure 6.24. We will model the first-order mutual coupling between two patches for the following three cases: broadside ($\psi = 0°$), echelon ($\psi = 45°$), and collinear ($\psi = 90°$).

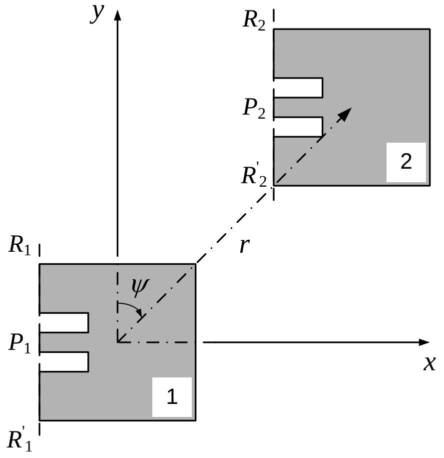

Figure 6.24 Two coupled microstrip patch antennas.

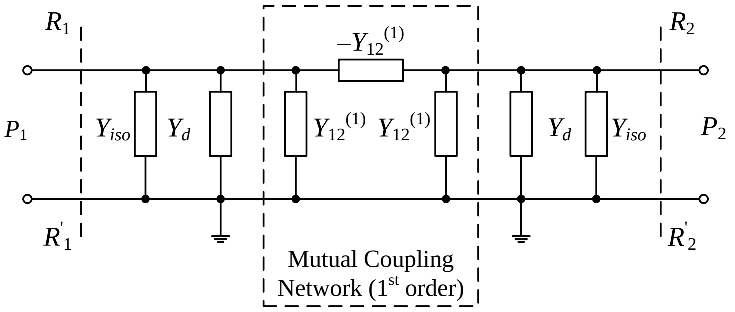

Figure 6.25 Equivalent circuit topology of two adjacent coupled elements.

As described for the one-dimensional (1-D) case, Figure 6.4(b) is the equivalent circuit network of the Y-matrix of two coupled elements and it can also be sketched as shown in Figure 6.25, in which Y_{iso} is the normalized input admittance of an isolated patch and Y_d is defined as the difference between $Y_{11}^{(1)}$ and Y_{iso} in order to manifest the effect of element 2 on the self-admittance of element 1 through the first-order mutual coupling.

$$Y_d = Y_{11}^{(1)} - Y_{iso} \tag{6.7}$$

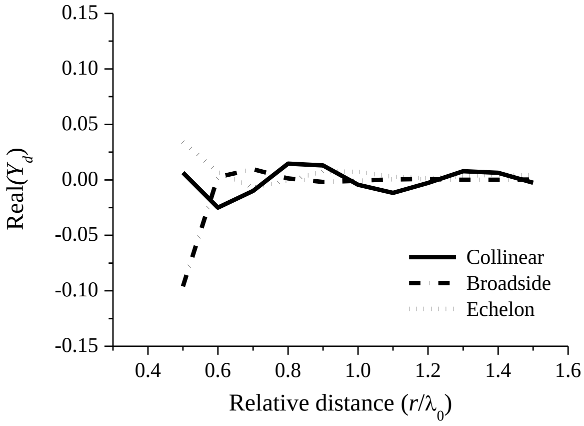

(a) Real part.

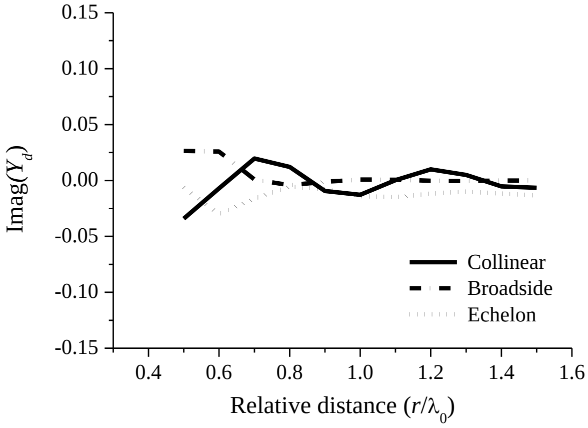

(b) Imaginary part.

Figure 6.26 Extracted Y_d.

Figure 6.26 and Figure 6.27 respectively plot the variation of extracted Y_d and the variation of mutual admittance $Y_{12}^{(1)}$ with respect to the distance between two elements in case of three different orientations. Through Figure 6.26, we can have the following observations. Firstly, it can be observed in Figure 6.26(a) that element 2 has an influence not only on the radiation characteristic of element 1 which is related to self conductance, but also on its energy storage capability which is related to self susceptance. Secondly, the variations of Y_d in all three cases are different which verify the geometrical dependence of mutual coupling. Thirdly, both of the real and the imaginary parts of Y_d and $Y_{12}^{(1)}$ converge to zero in all three cases when the distance between two elements increases. This tallies with the fact that if element 2 is put far away from element 1, element 1 can be treated as an isolated element, and vice versa. Fourthly, from the relative magnitude of Y_d (and $Y_{12}^{(1)}$ as well), it reveals that in the case of broadside and echelon, they converge much faster than collinear orientation, for which the explanation is the presence of a strong coupling between the two collinear elements through the TM_0 surface wave [130].

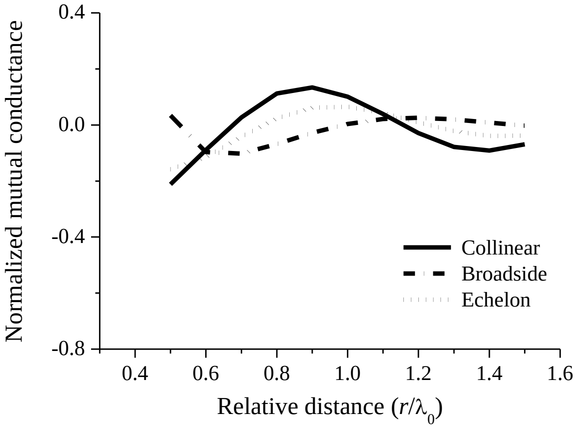

(a) Real part.

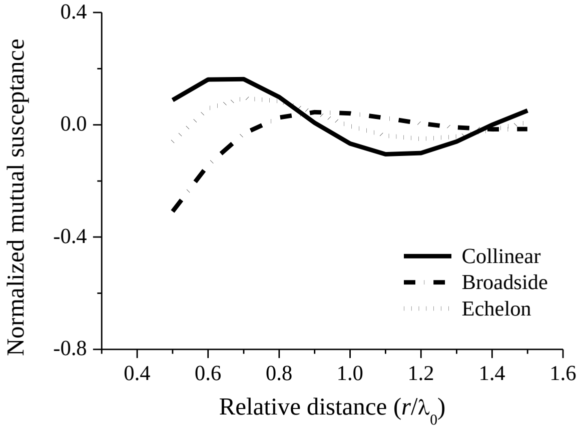

(b) Imaginary part.

Figure 6.27 Extracted $Y_{12}^{(1)}$.

6.4.2 Modeling of second-order mutual coupling

Three coupled elements are used for extracting the equivalent circuit model of second-order mutual coupling. Figure 6.28 shows three coupled elements in a planar configuration and the corresponding equivalent network topology is depicted in Figure 6.29.

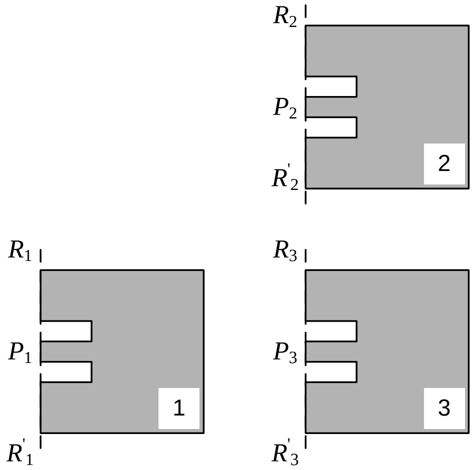

Figure 6.28 Three coupled elements in a planar configuration.

$Y_{d,c}$ and $Y_{d,b}$ correspond to the admittance Y_d in Figure 6.25 for collinear coupling and broadside coupling, respectively. Y_{iso} is the input admittance of an isolated element. Based on equivalent circuit models of both collinear and broadside first-order mutual couplings, we can obtain an equivalent network topology without the effect of second-order mutual coupling. Therefore, with the calibrated results of these three coupled elements, the equivalent circuit network of the second-order mutual coupling can be calculated through standard network theorem.

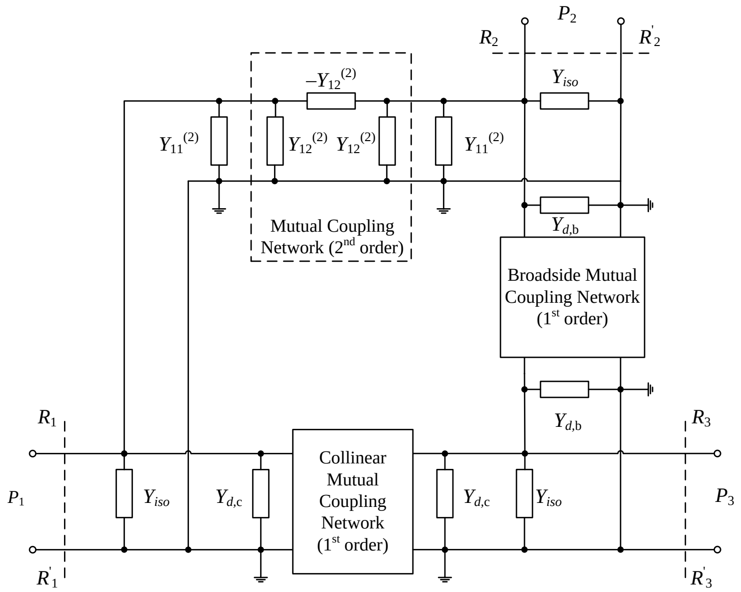

Figure 6.29 Equivalent network topology for extracting second-order mutual coupling.

From the extracted results of three configurations which are plotted through Figure 6.30 to Figure 6.32, we can see that the extracted admittances nearly have the same variation tendency as the first-order mutual coupling such as the convergence towards zero, and a slower decay in the collinear case.

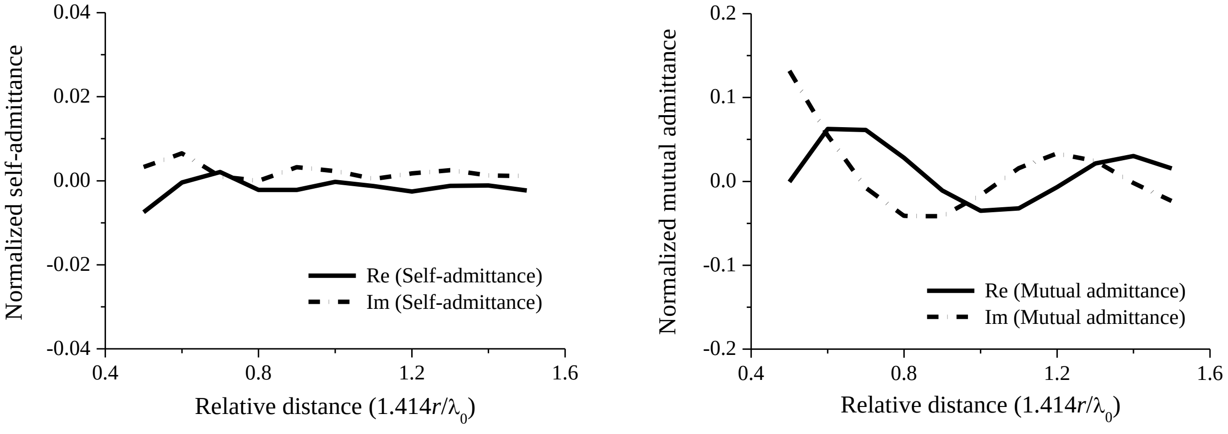

(a) (b)

Figure 6.30 Extracted equivalent circuit parameters of second-order mutual coupling in an echelon configuration.

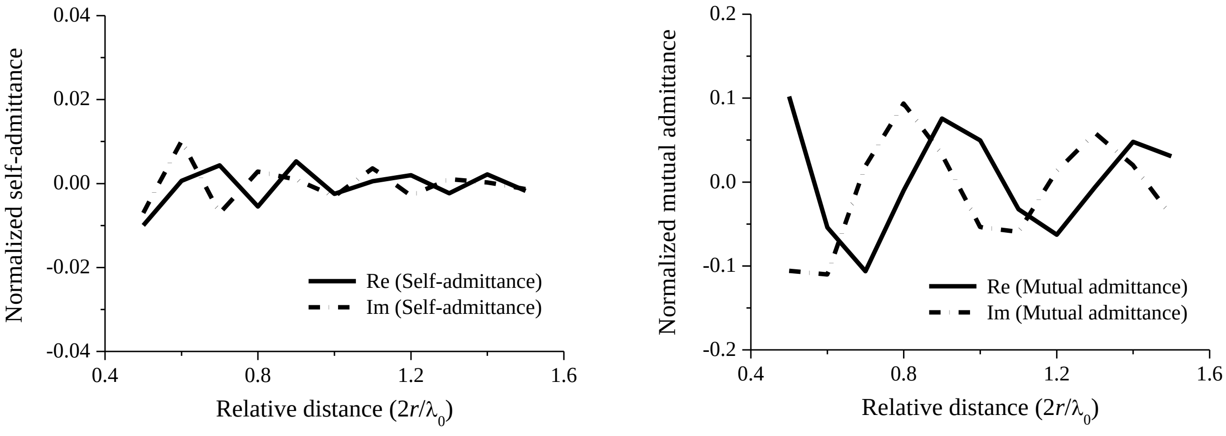

(a) (b)

Figure 6.31 Extracted equivalent circuit parameters of second-order mutual coupling in a collinear configuration.

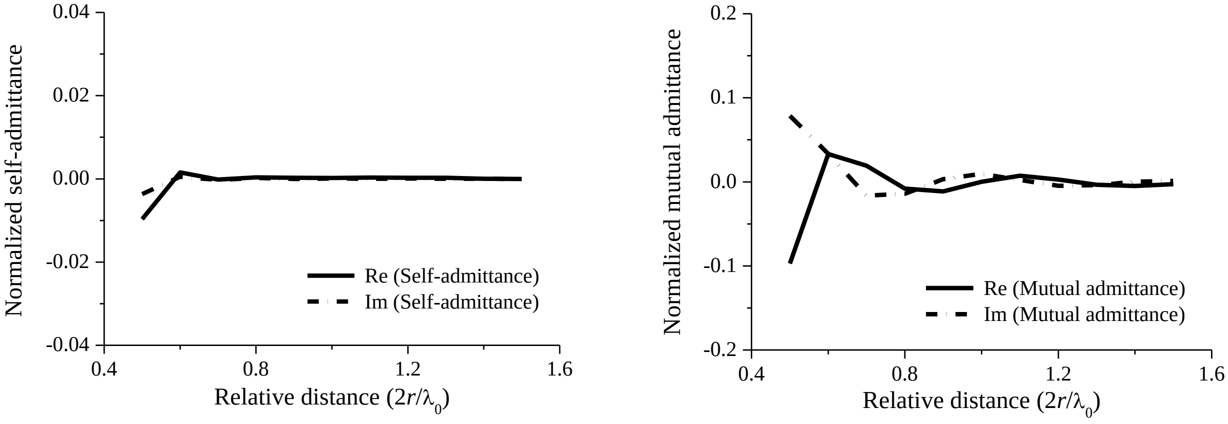

(a) (b)

Figure 6.32 Extracted equivalent circuit parameters of second-order mutual coupling in a broadside configuration.

Through this successive modeling procedure, higher-order mutual coupling can be extracted from previous lower-order mutual coupling representation. We only extract the mutual coupling up to the third-order in case of the four coupled elements in a planar configuration. The extracted results are no longer shown here.

6.4.3 Application examples

6.4.3.1 Analysis of planar phased array antenna

The analysis of a microstrip phased array antenna will be performed as an application example of our modeling strategy to show its usage and accuracy. In Figure 6.33, the elements are half-wavelength spaced on a square lattice ($d_x = d_y = \lambda_0/2$) with 3 elements along the *x*-axis and 3 elements along the *y*-axis.

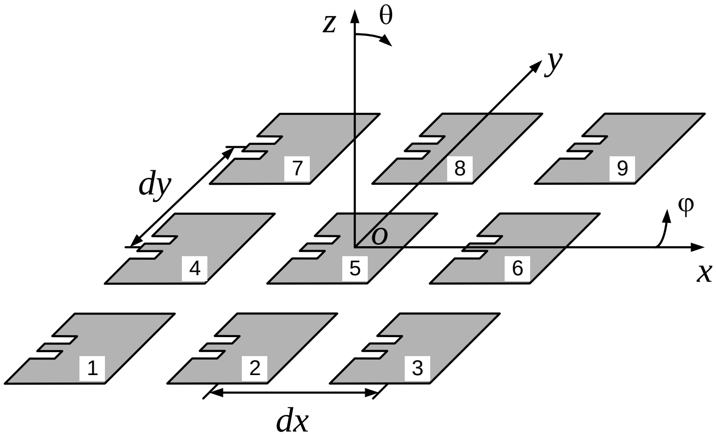

Figure 6.33 Illustration of a 3×3 microstrip phased array antenna.

Based on the extracted equivalent circuit model of the elements and those of mutual couplings up to third-order, a circuit simulation can be performed to analyze this planar array. The simulated *S*-matrix is then used to calculate the active element pattern of each element. After [134], the active element pattern of the *m*th element of the planar array is given by,

$$E_m^e\left(r,\theta,\varphi\right) = F\left(\theta,\varphi\right)\frac{e^{-jkr}}{r}V_0\left[e^{j\left[(i_m-1)u+(j_m-1)v\right]} + \sum_{n=1}^{K} S_{nm} e^{j\left[(i_n-1)u+(j_n-1)v\right]}\right] \quad m = 1,2,3...K \tag{6.8}$$

with

$$\begin{cases} u = kdx\sin\left(\theta\right)\cos\left(\varphi\right) \\ v = kdy\sin\left(\theta\right)\sin\left(\varphi\right) \end{cases} \tag{6.9}$$

where V_0 is the terminal voltage, $F(\theta,\varphi)$ represents the dominant polarization of the element pattern and S_{nm} is the *S*-parameter of elements *n* and *m*. i_m is the *x* index of element *m* and j_m is the *y* index of element *m*.

The calculation results are drawn for comparison in Figure 6.34 at two different planes.

1) *xoz*-Plane ($\varphi = 0^\circ$)

In this case, $u = kdxsin(\theta)$ and $v = 0$. The active element pattern of the *m*th element is simplified as

$$E_m^e(r,\theta,0) = F(\theta,0)\frac{e^{-jkr}}{r}V_0\left[e^{j(i_m-1)u} + \sum_{n=1}^{K} S_{nm}e^{j(i_n-1)u}\right] \quad m=1,2,3...K \tag{6.10}$$

From the above expression, we can see that elements having the same i_m and *S*-parameters such as elements 1 and 3, 4 and 6 as well as 7 and 9 have the same active element patterns. Therefore, the calculated active element patterns of elements 3, 6 and 9 are omitted in Figure 6.34. On the other hand, elements which are placed symmetrically about the $\varphi = 0^\circ$ plane such as elements 1 and 7, and 2 and 8, will have symmetrical active element pattern. This conclusion can be verified by our calculation results in Figure 6.34(a).

2) *yoz*-Plane ($\varphi = 90^\circ$)

In this case, $u = 0$ and $v = kdysin(\theta)$. The active element pattern of the *m*th element is simplified as

$$E_m^e(r,\theta,90) = F(\theta,90)\frac{e^{-jkr}}{r}V_0\left[e^{j(j_m-1)v} + \sum_{n=1}^{K} S_{nm}e^{j(j_n-1)v}\right] \quad m=1,2,3...K \tag{6.11}$$

We can come up with the following conclusion in this case. Elements having the same j_m and *S*-parameters such as elements 1 and 7, 2 and 8, as well as 3 and 9 have the same active element patterns while elements symmetrically placed about the $\varphi = 90^\circ$ plane such as elements 1 and 3, and 4 and 6, should have symmetrical active element pattern. Figure 6.34(b) verifies this concluding remark.

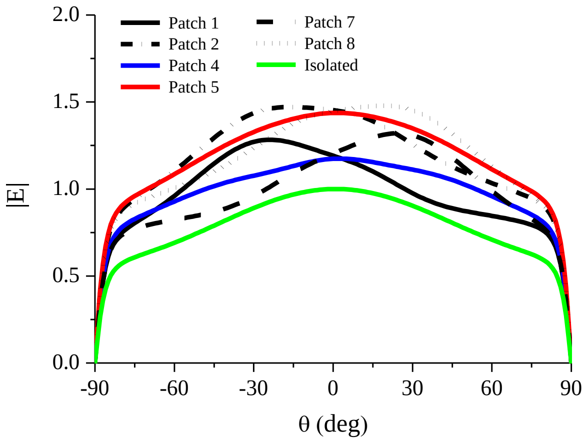

(a) *xoz*-plane.

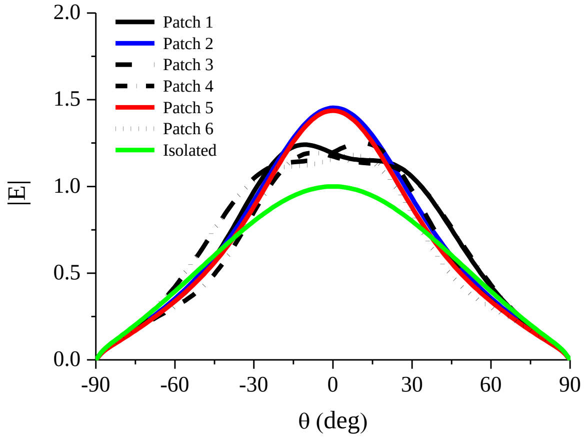

(b) *yoz*-plane.

Figure 6.34 Calculated active element patterns of different elements at (a) *xoz*-plane and (b) *yoz*-plane.

The array pattern can be obtained by the summation of active element patterns of all array elements. The calculated results shown in Figure 6.35 agree well with the direct full-wave simulation [106] as well as array factor.

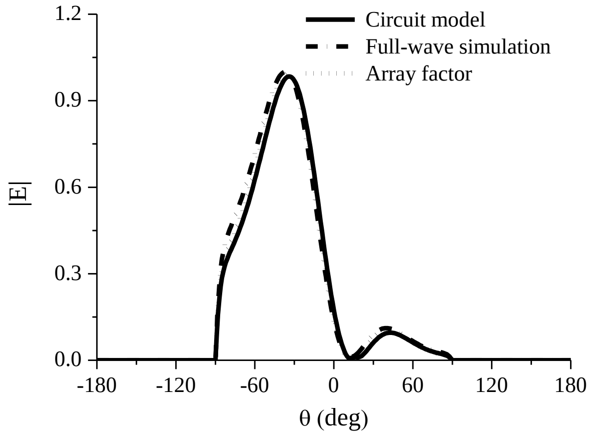

(a) φ = 37°.

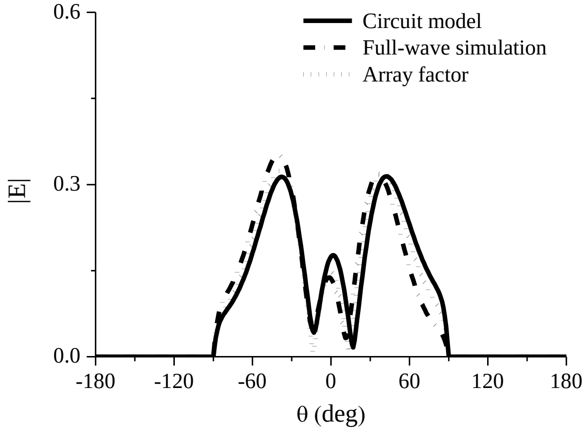

(b) φ = 127°.

Figure 6.35 Calculated array pattern.

6.4.3.2 Design of 24-GHz planar array antenna

A pair of microstrip planar array is designed for our 24-GHz system prototype, which is also taken as an example for the application of our proposed modeling technique. Here, we choose a thin layer substrate for the array antenna since there are two problems associated with electrically thick substrate. One is the high spurious radiation of feeding networks and the other is the unwanted surface wave propagation, which leads to the reduction of radiation efficiency and degradation of radiation pattern [138]. Our specified frequency band is centered at 24.125 GHz with an absolute bandwidth of 1 GHz. However, due to the substrate thickness ($0.02\lambda_0$), this frequency specification is quite stringent and difficult to achieve using conventional techniques.

Different techniques have been reported to enhance the impedance bandwidth of microstrip antennas, such as cascading impedance matching network, adding additional lossy mechanism and introducing multiple resonances [138]. In our design, in addition to a transmission line impedance transformer, two parasitic straight slots are etched close to and parallel with the non-radiating edges of a conventional microstrip rectangular patch to enhance the impedance bandwidth. This technique is advantageous since the fabrication process is simplified compared to the stacked configuration and therefore manufacturing cost and time is greatly reduced. Our proposed antenna is depicted in Figure 6.36 and the substrate selected is RT/duroid® 5880 having a permittivity of 2.2 and a thickness of 0.25 mm.

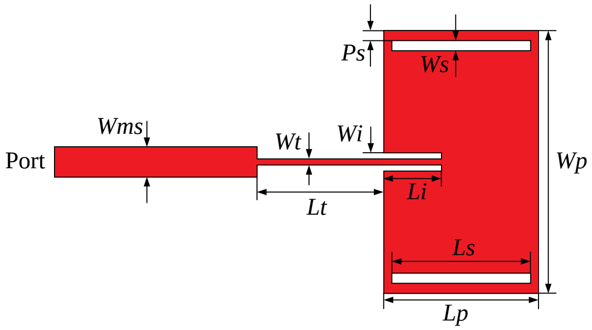

Figure 6.36 Inset-fed microstrip rectangular patch loaded with two straight slots.

Figure 6.37 plots the current distributions of the slotted patch and a conventional patch, which are obtained from a method-of-moments-based simulation package [106]. As can be seen from Figure 6.37, the current distribution of the original patch is only affected near the non-radiating edges. We can have two observations with respect to the effects of slots loading. On one hand, compared to the current distribution of an original patch shown in Figure 6.37(b), currents of the slotted patch shown in Figure 6.37(a) are more induced around the slots. Therefore, by changing the position and sizes of the slots, it becomes more flexible to control the input impedance of the patch that is highly related to the patch width [139]. In our case, the loaded slots actually create an effective width for the patch that is determined by the perturbation of the current distribution. On the other hand, the currents induced around the slots are in the same direction as those in the center region of the patch except for a very trivial portion near the radiating slots. Therefore, the radiation performance of the original patch is well preserved.

(a) Slotted patch.

(b) Conventional patch.

Figure 6.37 Current distributions of the fundamental mode for (a) slotted patch and (b) conventional patch.

In order to provide design guidance, parameter studies were performed to investigate the effects of loaded slots. Three critical parameters related to the straight slots are studied, including slot width W_S, slot length L_S and slot position P_S. The same commercial simulation package is used. All the analysis results are plotted in three Smith charts in Figure 6.38, which are normalized to a reference impedance of 50 ohm. Other physical parameters are: L_p = 3.87 mm, W_p = 6.60 mm, L_t = 3.18 mm, W_t = 0.15 mm, L_i = 1.45 mm, W_i = 0.15 mm, W_{ms} = 0.76 mm.

Figure 6.38(a) shows the variation of return loss with the increment of slot width W_S from 0 mm (no slots) to 0.38 mm. From Figure 6.38(a), we can observe that when the slot width is increased from 0 mm (no slots) to 0.25 mm, input impedance changes a lot. However, it nearly remains the same when the slot width is larger than 0.51 mm. The optimum slot width is 0.25 mm for the best impedance matching to the reference impedance. The effect of the slot length is also studied. In this case, the slot length is limited by patch length L_P. In Figure 6.38(b), return losses in the case of different slot lengths are plotted and it is easy to find an optimum slot length from the movement trajectory. The optimum slot length is found to be 0.42 mm shorter than L_P due to the parasitic open-end capacitances of the slots. Finally, return losses for different slot positions are plotted in Figure 6.38(c). It is concluded that the slots have to be etched at least 0.25 mm from the edges; otherwise the current distribution of the microstrip patch would be greatly deformed. However, when slot position P_S is larger than 0.38 mm, return loss is almost unchanged until P_S equals to 1.27 mm.

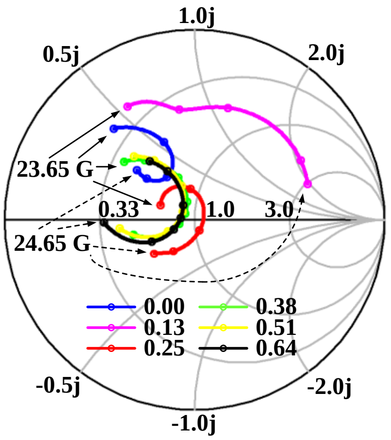

(a) S_{11} vs. slot width W_S. (L_S = 3.48, P_S = 0.25).

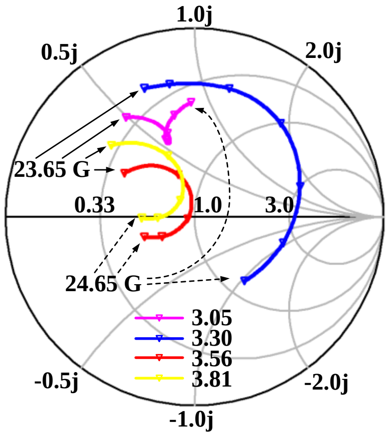

(b) S_{11} vs. slot length L_S. (W_S = 0.25, P_S = 0.25).

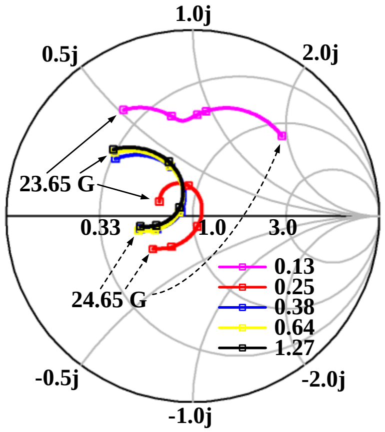

(c) S_{11} vs. slot position P_S. (L_S = 3.48, W_S = 0.25).

Figure 6.38 Results of parametric study.

Based on the above discussion, the optimum physical dimensions are determined through a global optimization and the optimum physical dimensions are listed in the Table 6.3 for reference. Figure 6.39 compares the return loss of our proposed radiating element with that of a conventional patch. From the comparison, we can observe that the slotted patch has much better impedance matching, and the input VSWR is less than 1.5 over the entire frequency band of interest.

Table 6.3 Optimum physical dimensions of the 24-GHz patch.

Symbol	Value (mm)	Symbol	Value (mm)
Lp	3.87	*Lt*	3.18
Wp	6.60	*Wt*	0.15
Ls	3.45	*Li*	1.45
Ws	0.25	*Wi*	0.15
Ps	0.25	*Wms*	0.76

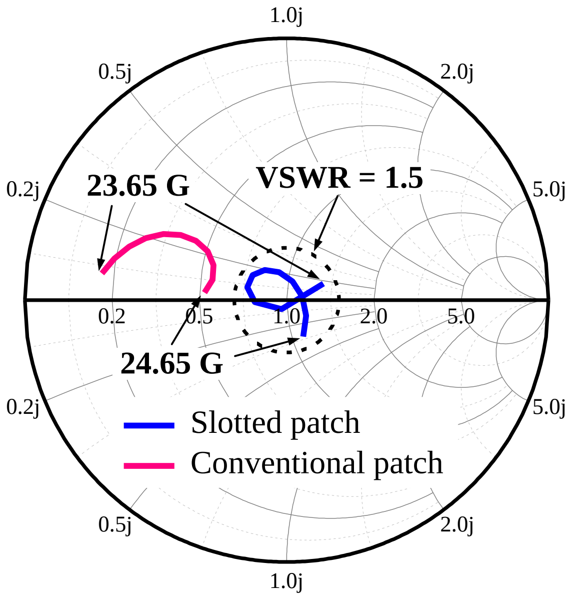

Figure 6.39 Comparison of return losses of a slotted patch and a conventional patch.

Based on the proposed radiating element, a high-gain planar array composed of 8×8 elements is developed at 24 GHz, of which the layout is sketched in Figure 6.40. For radar applications, it is sometimes preferred to have low sidelobe level (for example, 20 dB) in order to suppress the interference and reduce the clutter. Considering the design and implementation error, a sidelobe level of 25 dB in both *E*-plane and *H*-plane is specified with a design margin of 5 dB. The distance between patches in both directions is selected as $0.8\lambda_0$ for maximizing the array gain.

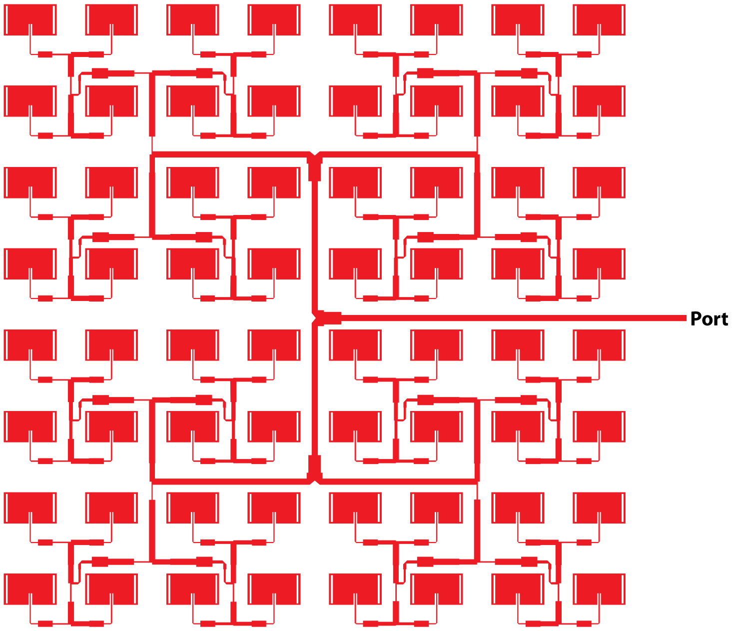

Figure 6.40 Sketch of an 8×8 corporate-fed planar array.

The design procedure of this planar array is described as follows. First of all, from the specified sidelobe level, the Taylor one parameter method [140] was used to synthesize the excitation distribution for both *E*-plane and *H*-plane. The synthesized radiation pattern and amplitude distribution for a discrete source is plotted in Figure 6.41(a) and Figure 6.41(b), respectively. In Figure 6.41(a), the blue solid line represents the synthesized pattern for a continuous source while the blue dashed line shows that for a discrete source. It can be observed that the sidelobe level of the radiation pattern for a discrete source is satisfactory except at the end-fire direction due to the large spacing between elements. Then, according to the synthesized amplitude distribution, a corporate feeding network is designed using a number of unequal power dividers [96]. Finally, an array is built by combining the radiating elements and the feeding network.

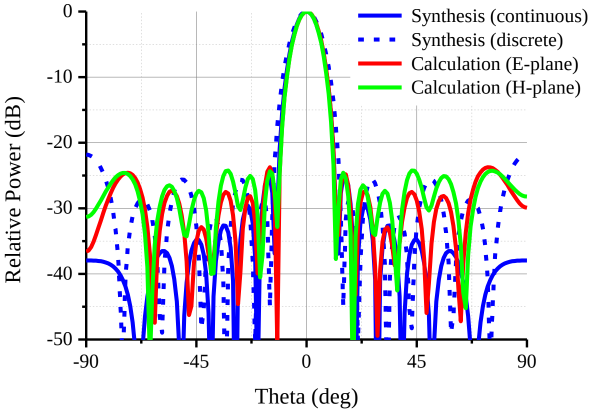

(a) Radiation pattern.

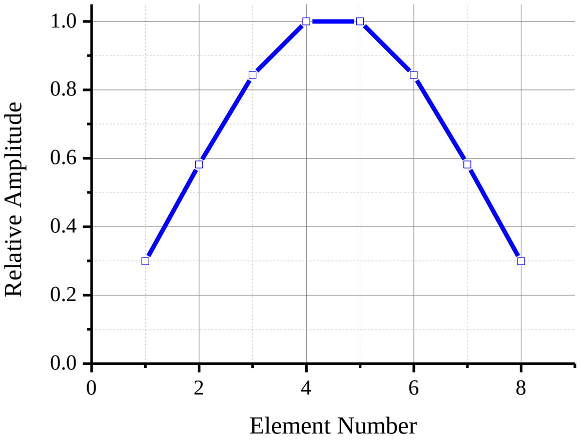

(b) Current distribution.

Figure 6.41 Synthesized results.

If a direct EM-simulation is performed for the entire array, there would be a huge amount of unknowns, which requires unbearable computational resources. Therefore, after modeling each patch and the mutual coupling between patches, we build up an equivalent circuit network by combining the equivalent circuit model of the patch and that of the feeding network. Subsequently, the input return loss of the array can be easily obtained from the circuit simulation in [63]. Furthermore, the radiation performance of the entire array is evaluated by the array factor, which is calculated from the scattering parameters of our equivalent circuit network. The calculation results for both *E*-plane and *H*-plane are compared with the synthesized patterns in Figure 6.41(a). From Figure 6.41(a), we can see that both *E*-plane and *H*-plane patterns are very close to the synthesized results. The sidelobe level of calculated patterns is better than 24 dB for both *E*-plane and *H*-plane.

The array prototype was fabricated using standard PCB process and a photo of the fabricated sample mounted with a *K* connector is shown in Figure 6.42. The total area is about 10 mm by 10 mm. Return loss of the prototype was measured using a VNA (Anritsu 37397C) with a standard SOLT calibration. The comparison between the modeled and measured return losses for our specified frequency range shows close similarity in Figure 6.43. Moreover, a wideband measurement result plotted in the vignette of Figure 6.43 shows that the frequency band for VSWR less than 2 is from 23.2 GHz to 25 GHz, which is 1.8 times of the specified frequency range because the radiation loss is not included in the circuit simulation and conductor loss may be insufficiently evaluated.

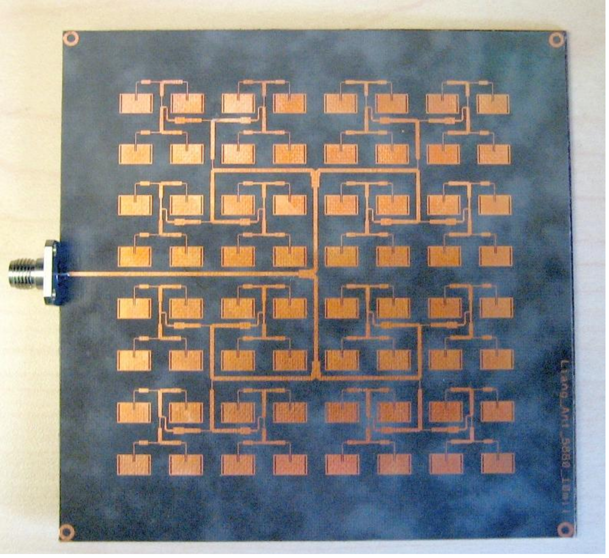

Figure 6.42 Photo of the fabricated prototype of the 24-GHz planar array.

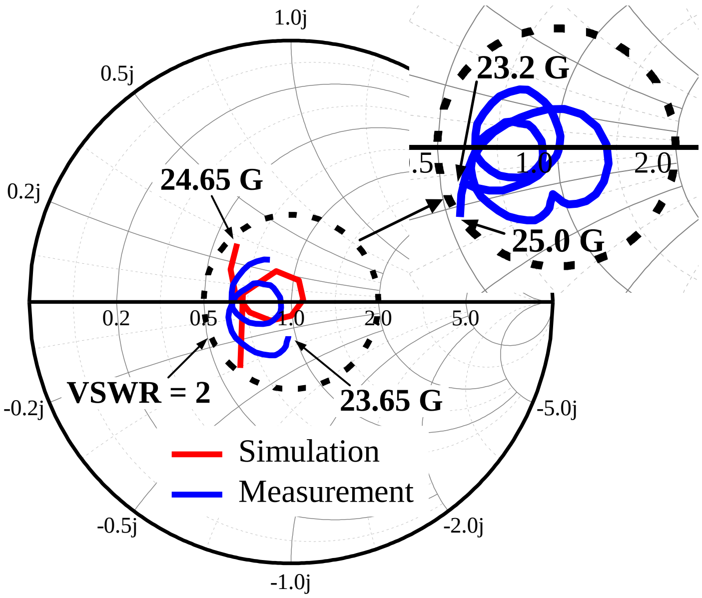

Figure 6.43 Comparison between simulated and measured return loss of the planar array.

As shown in Figure 6.44, measured gain is higher than 21 dBi over the frequency band from 23.65 GHz to 24.65 GHz with a value of 22.5 dBi at the center frequency. Measured radiation pattern in both *E*-plane and *H*-plane at different frequencies are plotted in Figure 6.45. It can be observed that measured sidelobe level in the *E*-plane (Figure 6.45(a)) is better than 20 dB while it is better than 18 dB in the *H*-plane (Figure 6.45(b)). The minor difference between calculation and measurement can be ascribed to the mutual coupling among patches themselves and between feeding network and patches, which is hard to avoid in the case a single-layer substrate. Finally, the measured beamwidth is about 8 ° in both *E*-plane and *H*-plane.

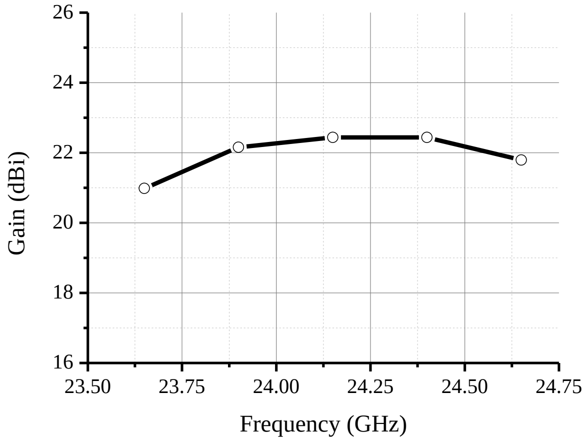

Figure 6.44 Measured gain of the 24-GHz planar array over frequencies.

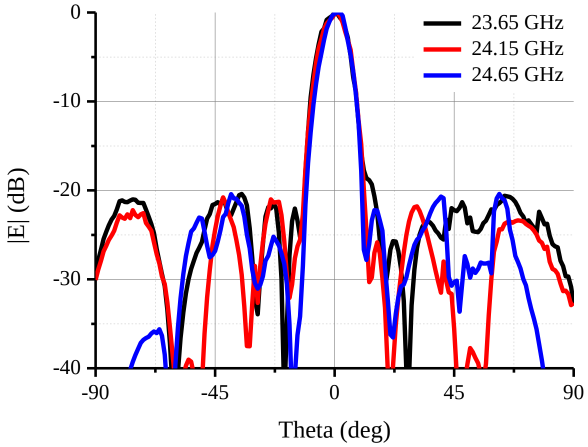

(a) *E*-plane.

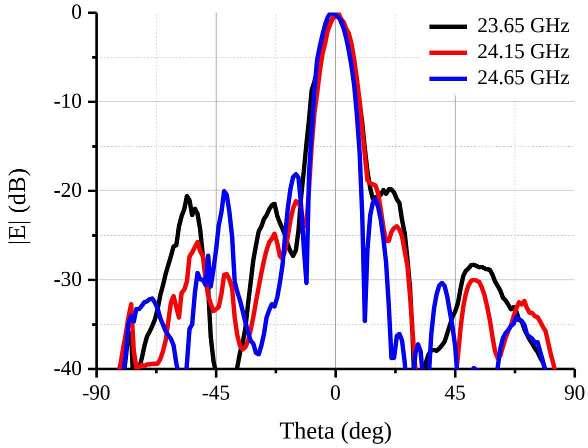

(b) *H*-plane.

Figure 6.45 Measured radiation pattern of the array.

6.5 Conclusion

A fundamental scheme has been proposed in this chapter for modeling arbitrary-order mutual coupling. Its accuracy and effectiveness have been proved by different electromagnetic circuits including array antennas, finite periodic electromagnetic structures and low-pass filters. Moreover, it has also been successfully applied to the development of an 8×8 planar array for our 24-GHz system.

CHAPTER 7 A 24 GHZ SYSTEM PROTOTYPE: INTEGRATION AND MEASUREMENT

The SIW technology provides a unique solution for monolithic integration of high-*Q* waveguide structures and active devices through planar transmission lines. Based on this technology, we have designed a number of SIW passive circuits including filters, phase shifters, and couplers. By integrating these SIW passive circuits with commercial off-the-shelf active devices, our 24-GHz system is prototyped and then measured with a pair of our designed microstrip array. In this chapter, we will present system prototyping and measurement results.

7.1 System prototyping

After being fabricated on two individual substrates, the transmitter and the receiver in our 24-GHz system are assembled into two housings shown in Figure 7.1 for EMC and EMI considerations. The final transmitted and receiver prototypes are pictured in Figure 7.2.

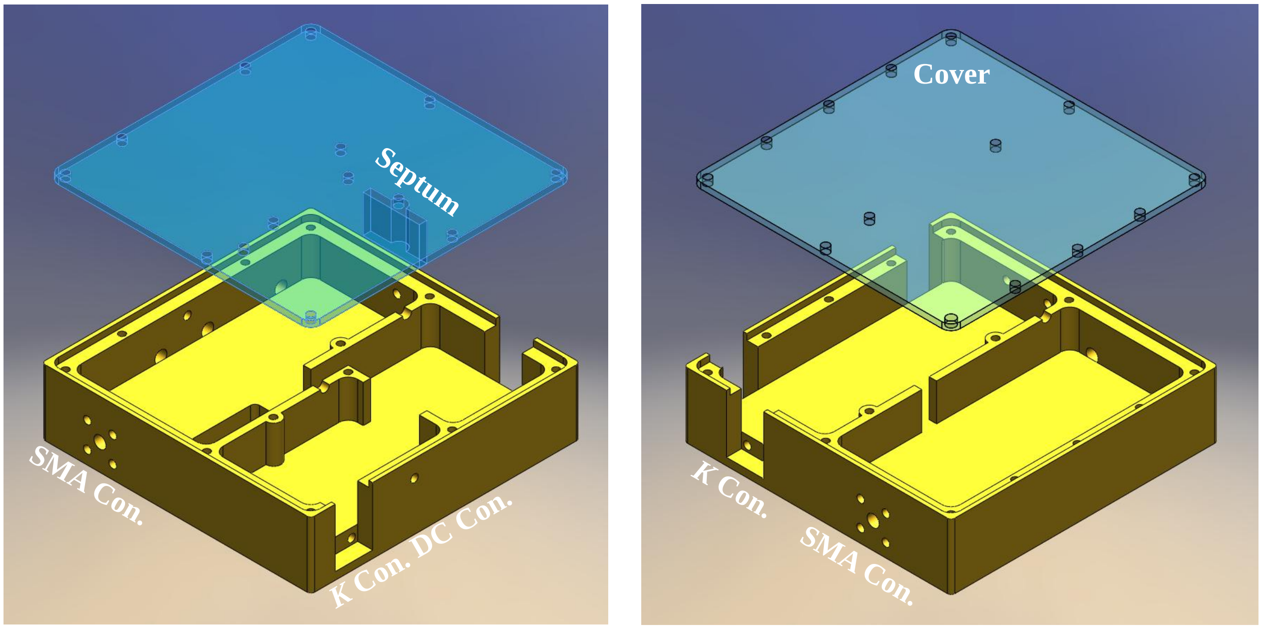

(a) Transmitter.

(b) Receiver.

Figure 7.1 3D sketch of the housings for 24-GHz system prototype.

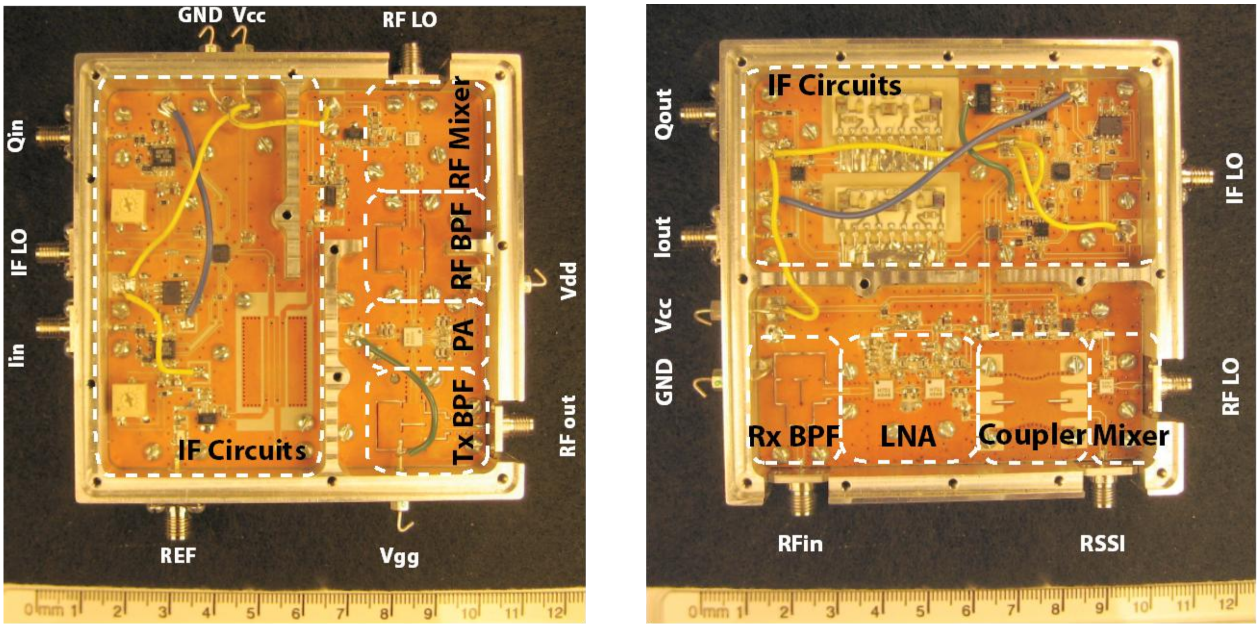

(a) Transmitter prototype.

(b) Receiver prototype.

Figure 7.2 Photos of the fabricated transmitter and receiver prototype.

7.2 Experimental results

7.2.1 Radio mode

7.2.1.1 Measurement for an AWGN channel

System performance of data communication is measured using the test setup in Figure 7.3. A vector signal generator (Agilent E4438C) sends the modulated I&Q signal into our transmitter, which generates the transmitted signal at RF frequency. Then, the transmitted signal is fed into our receiver, and the demodulated I&Q signals are compared with the referenced I&Q signal in an oscilloscope (Agilent DSO81204B). In this setup, two other signal generators (Anritsu MG3694A and Rohde & Schwarz SMR 40) are used as RF LO and IF LO, respectively. Note that the input power of the receiver is controlled by inserting additional attenuators between the transmitter and the receiver.

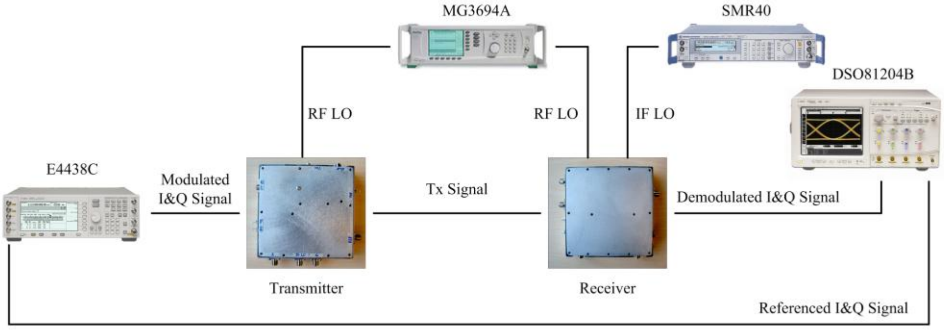

Figure 7.3 Measurement setup for evaluating system performance of the radio mode.

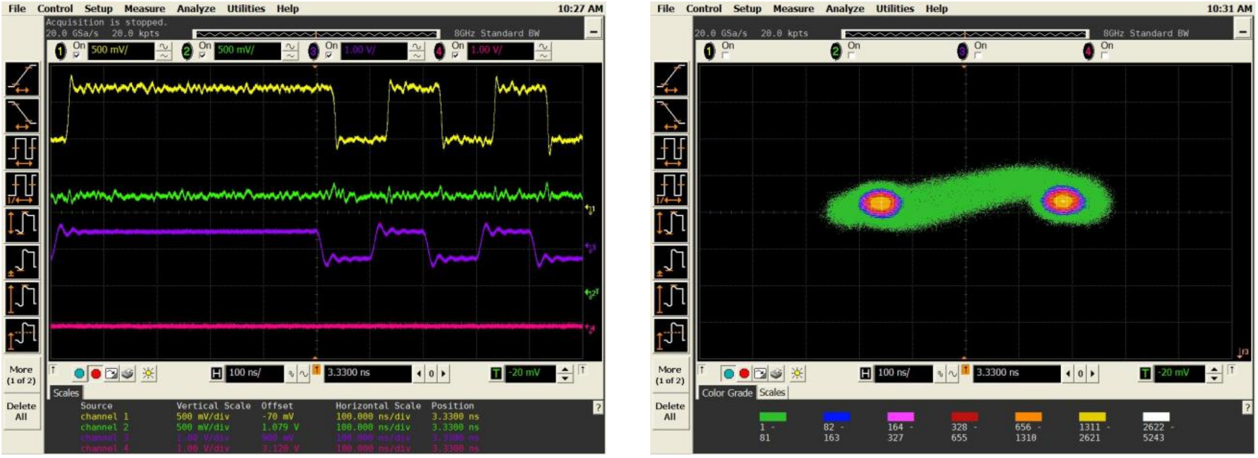

Source	Vertical Scale	Offset	Horizontal Scale	Position
channel 1	500 mV/div	-70 mV	100.000 ns/div	3.3300 ns
channel 2	500 mV/div	1.079 V	100.000 ns/div	3.3300 ns
channel 3	1.00 V/div	900 mV	100.000 ns/div	3.3300 ns
channel 4	1.00 V/div	3.120 V	100.000 ns/div	3.3300 ns

(a) Waveform of 10-Mbps BPSK signal. (b) Constellation of 10-Mbps BPSK signal.

Source	Vertical Scale	Offset	Horizontal Scale	Position
channel 1	500 mV/div	-70 mV	100.000 ns/div	3.3300 ns
channel 2	500 mV/div	1.079 V	100.000 ns/div	3.3300 ns
channel 3	1.00 V/div	900 mV	100.000 ns/div	3.3300 ns
channel 4	1.00 V/div	3.120 V	100.000 ns/div	3.3300 ns

(c) Waveform of 50-Mbps BPSK signal. (d) Constellation of 50-Mbps BPSK signal.

🟩 1.55%	🟦 1.55%	🟪 3.1%	🟥 6.3%	🟧 12.5%	🟨 25.0%	⬜ 50.0%

(e) Enlarged color bar.

Figure 7.4 Measured results for BPSK signals with an input power of −60 dBm.

Figure 7.4 and Figure 7.5 present the measured results for BPSK and QPSK signals with an input power of −60 dBm. In these two figures, the yellow and green waveforms are respectively the demodulated I and Q signals from our receiver while the purple and pink waveforms are respectively the referenced I and Q signals generated by the signal generator. From the comparison between these waveforms, we can see that the referenced signals are transmitted and received with a very small distortion, which proves very good system performance of data transmission.

Source	Vertical Scale	Offset	Horizontal Scale	Position
channel 1	500 mV/div	-70 mV	100.000 ns/div	3.3300 ns
channel 2	500 mV/div	1.079 V	100.000 ns/div	3.3300 ns
channel 3	1.00 V/div	900 mV	100.000 ns/div	3.3300 ns
channel 4	1.00 V/div	3.120 V	100.000 ns/div	3.3300 ns

🟩	🟦	🟪	🟥	🟧	🟨	⬜
1 - 25	26 - 50	51 - 101	102 - 202	203 - 405	406 - 810	811 - 1620

(a) Waveform of 10-Mbps QPSK signal. (b) Constellation of 10-Mbps QPSK signal.

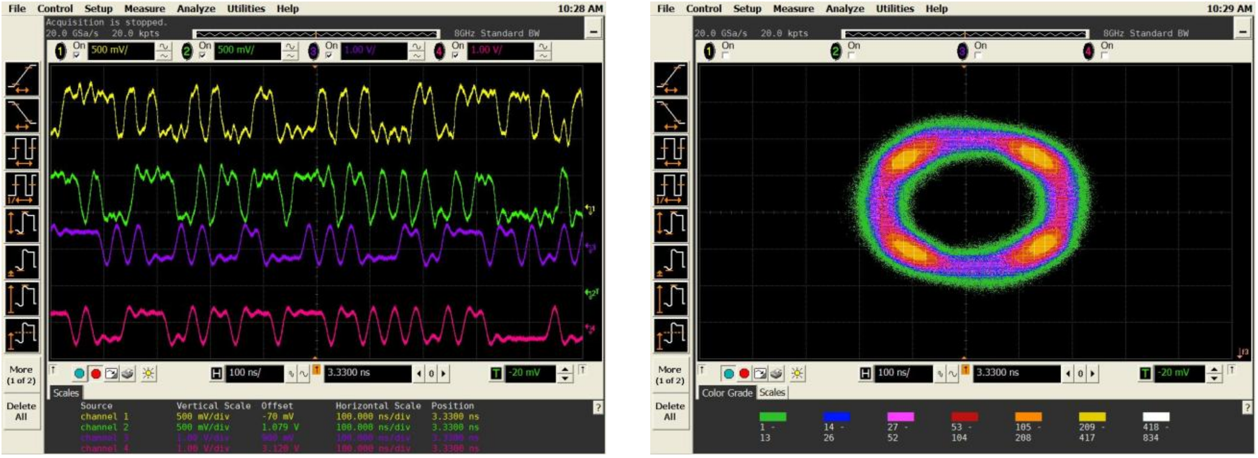

Source	Vertical Scale	Offset	Horizontal Scale	Position
channel 1	500 mV/div	-70 mV	100.000 ns/div	3.3300 ns
channel 2	500 mV/div	1.079 V	100.000 ns/div	3.3300 ns
channel 3	1.00 V/div	900 mV	100.000 ns/div	3.3300 ns
channel 4	1.00 V/div	3.120 V	100.000 ns/div	3.3300 ns

🟩	🟦	🟪	🟥	🟧	🟨	⬜
1 - 13	14 - 26	27 - 52	53 - 104	105 - 208	209 - 417	418 - 834

(c) Waveform of 50-Mbps QPSK signal. (d) Constellation of 50-Mbps QPSK signal.

🟩	🟦	🟪	🟥	🟧	🟨	⬜
1.55%	1.55%	3.1%	6.3%	12.5%	25.0%	50.0%

(e) Enlarged color bar.

Figure 7.5 Measured results for QPSK signals with an input power of −60 dBm.

7.2.1.2 Measurement with a reflector

In order to evaluate system performance more practically, our system is measured with the transmitting and receiving antennas as depicted in Figure 7.6. A reflector is used to bounce back the transmitted wave in order to realize a monostatic configuration. Actually, the same measurement setup will be used for radar mode, which will be outlined in the following sections.

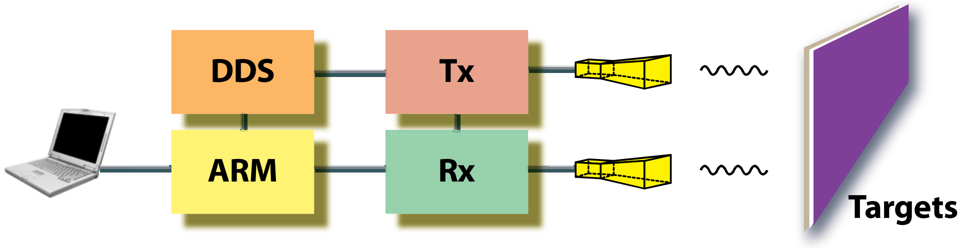

Figure 7.6 Measurement setup with antennas.

Measurement results are given in Figure 7.7 and Figure 7.8. The distance of the reflector is calibrated for achieving the same input power of −60 dBm as the previous experiment. It should be noted that in these two figures, the yellow and green waveforms respectively present the referenced I and Q signals while the purple and pink waveforms are respectively the demodulated I and Q signals from our receiver. From the comparison between these waveforms, we can see that the demodulated waveforms are more distorted than those in the case of a direct connection between the transmitter and the receiver. The distortion maybe ascribed to the multipath fading in the laboratory. However, in spite of the distortion and noise, the constellations in Figure 7.7 and Figure 7.8 manifest good performance of our system for such a more practical measurement setup compared to the previous experiment.

12:00 PM

Acquisition is stopped.
20.0 GSa/s 20.0 kpts

1 On 1.00 V/ 2 On 1.00 V/ 3 On 1.00 V/ 4 On 1.00 V/

100 ns/ 3.3300 ns 0 -20 mV

Source	Vertical Scale	Offset	Horizontal Scale	Position
channel 1	1.00 V/div	-3.030 V	100.000 ns/div	3.3300 ns
channel 2	1.00 V/div	-1.320 V	100.000 ns/div	3.3300 ns
channel 3	1.00 V/div	[illegible]	100.000 ns/div	3.3300 ns
channel 4	1.00 V/div	4.000 V	100.000 ns/div	3.3300 ns

11:44 AM

Acquisition is stopped.
20.0 GSa/s 20.0 kpts

1 On 2 On 3 On 4 On

100 ns/ 3.3300 ns 0 -20 mV

1 - 48 | 49 - 97 | 98 - 195 | 196 - 391 | 392 - 782 | 783 - 1565 | 1566 - 3130

(a) Waveform of 10-Mbps BPSK signal. (b) Constellation of 10-Mbps BPSK signal.

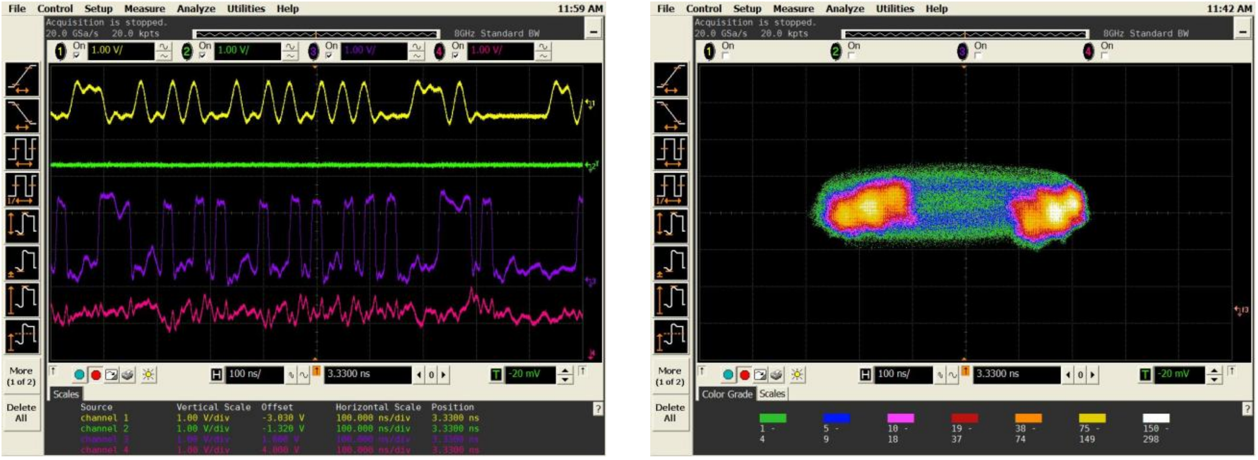

11:59 AM

Acquisition is stopped.
20.0 GSa/s 20.0 kpts

1 On 1.00 V/ 2 On 1.00 V/ 3 On 1.00 V/ 4 On 1.00 V/

100 ns/ 3.3300 ns 0 -20 mV

Source	Vertical Scale	Offset	Horizontal Scale	Position
channel 1	1.00 V/div	-3.030 V	100.000 ns/div	3.3300 ns
channel 2	1.00 V/div	-1.320 V	100.000 ns/div	3.3300 ns
channel 3	1.00 V/div	[illegible]	100.000 ns/div	3.3300 ns
channel 4	1.00 V/div	4.000 V	100.000 ns/div	3.3300 ns

11:42 AM

Acquisition is stopped.
20.0 GSa/s 20.0 kpts

1 On 2 On 3 On 4 On

100 ns/ 3.3300 ns 0 -20 mV

1 - 4 | 5 - 9 | 10 - 18 | 19 - 37 | 38 - 74 | 75 - 149 | 150 - 298

(c) Waveform of 50-Mbps BPSK signal. (d) Constellation of 50-Mbps BPSK signal.

1.55%	1.55%	3.1%	6.3%	12.5%	25.0%	50.0%

(e) Enlarged color bar.

Figure 7.7 Measured results for BPSK signals with an input power of −60 dBm.

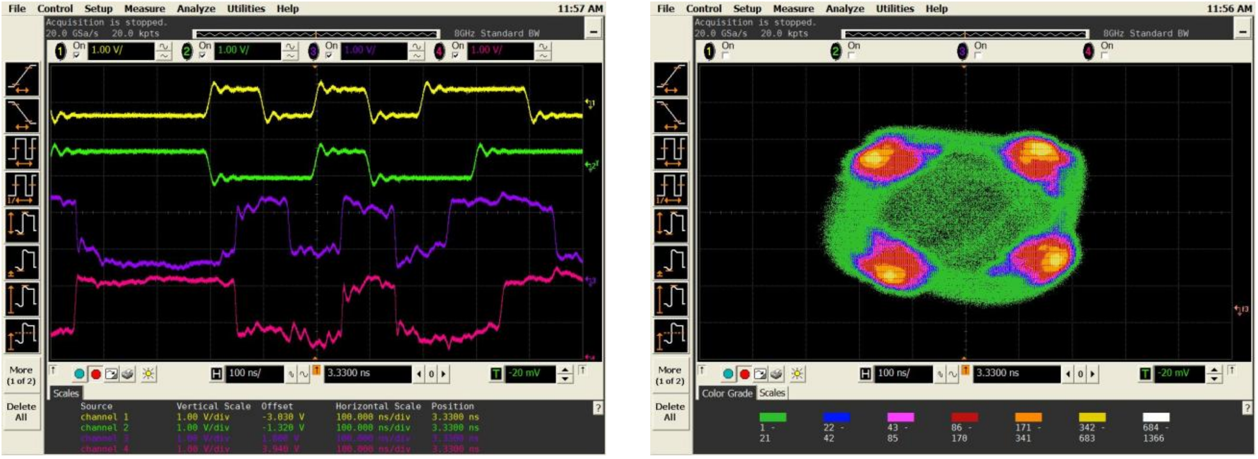

```
Source       Vertical Scale  Offset     Horizontal Scale  Position
channel 1    1.00 V/div      -3.030 V   100.000 ns/div    3.3300 ns
channel 2    1.00 V/div      -1.320 V   100.000 ns/div    3.3300 ns
channel 3    1.00 V/div      1.080 V    100.000 ns/div    3.3300 ns
channel 4    1.00 V/div      3.940 V    100.000 ns/div    3.3300 ns
```

(a) Waveform of 10-Mbps QPSK signal. (b) Constellation of 10-Mbps QPSK signal.

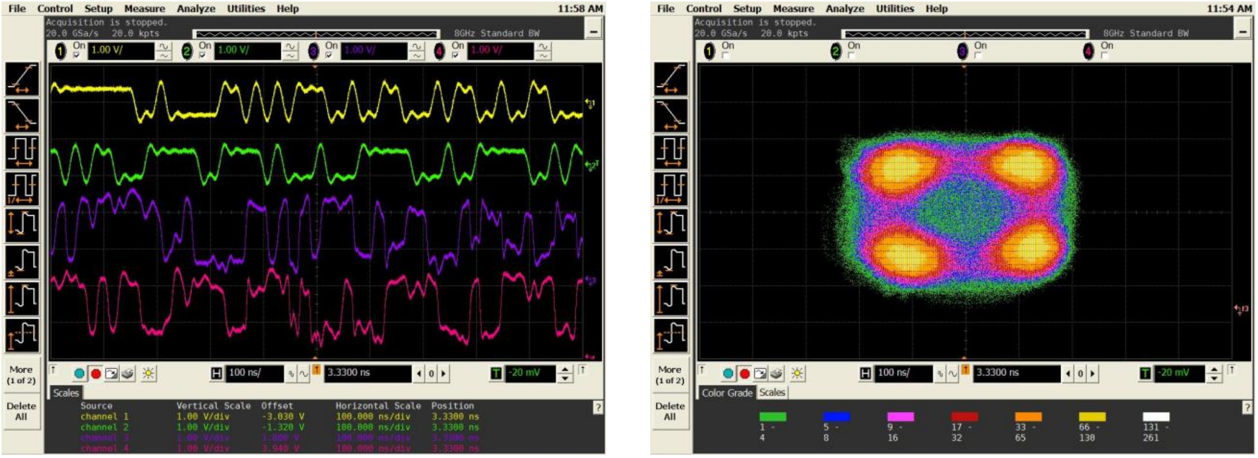

```
Source       Vertical Scale  Offset     Horizontal Scale  Position
channel 1    1.00 V/div      -3.030 V   100.000 ns/div    3.3300 ns
channel 2    1.00 V/div      -1.320 V   100.000 ns/div    3.3300 ns
channel 3    1.00 V/div      1.080 V    100.000 ns/div    3.3300 ns
channel 4    1.00 V/div      3.940 V    100.000 ns/div    3.3300 ns
```

(c) Waveform of 50-Mbps QPSK signal. (d) Constellation of 50-Mbps QPSK signal.

(e) Enlarged color bar.

Figure 7.8 Measured results for QPSK signals with an input power of −60 dBm.

7.2.2 Radar mode

7.2.2.1 Measurement in the Lab

The same measurement setup in Figure 7.6 is constructed to validate our system performance in the radar mode. Figure 7.9 gives a photo of the real measurement setup. Four targets including three chairs and one VNA are deliberately arranged and the distance between Target 2 and Target 3 is set less than our range resolution of 1.5 m on purpose. Our measurement results in Figure

7.10 show the range profile for six targets and two more targets other than our designated four targets are detected by our system. One is the door to another room and the other is the closet in that room.

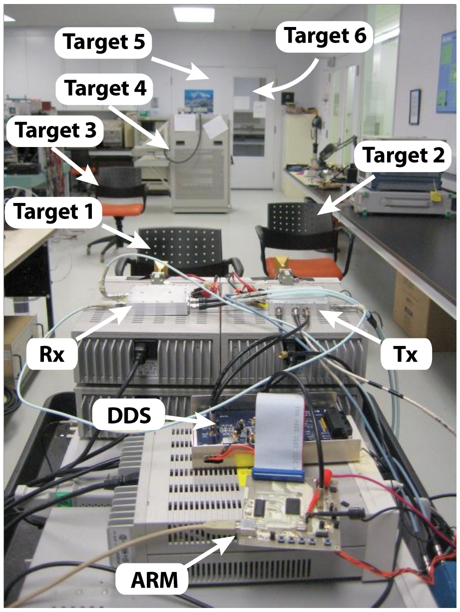

Figure 7.9 Measurement setup of the radar mode in the lab.

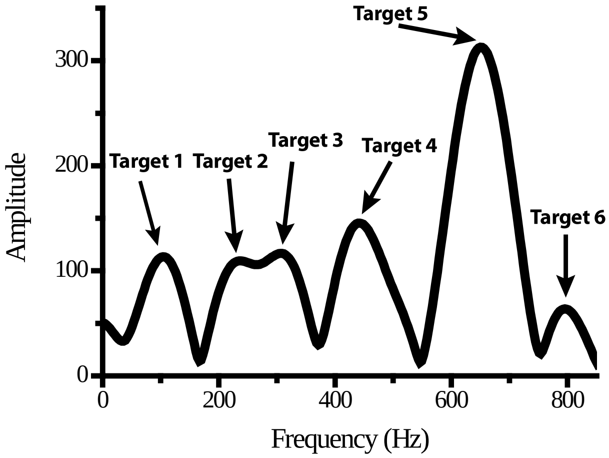

Figure 7.10 Range profile of six targets.

According to Figure 7.10, an example will be given to calculate the distance of Target 5 from the estimated beat frequency. The estimated beat frequency of Target 5 is around 650 Hz, and therefore the time delay can be calculated from (1.21). It should be mentioned that in our practical system implementation, the time duration of one period in the radar mode is 10.5 ms, and therefore the calculated round-trip time delay is 68.25 ns. Finally, the distance of Target 5 can be obtained as 10.24 m.

Moreover, the distance of Target 4 is varied from 1 m to 8 m and measured results plotted in Figure 7.11 demonstrate an excellent range detection capability of our system.

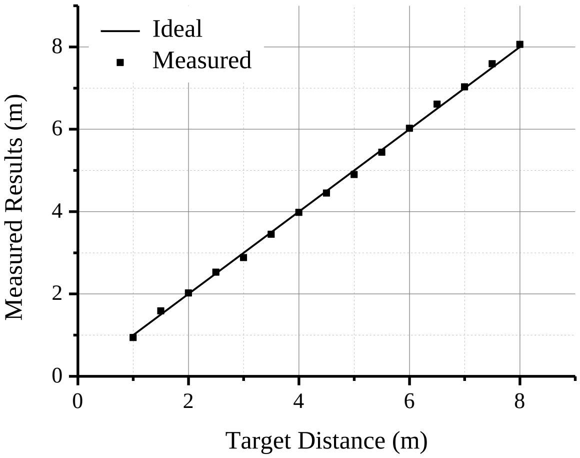

Figure 7.11 Measured range profile of Target 4.

7.2.2.2 Measurement in the garage

An *in-situ* experiment is very difficult to perform since both power supplies and signal generators are indispensable in our measurement setup. In lieu of *in-situ* experiments, a number of experiments were carried out in an indoor garage. Figure 7.12 presents a photo of this measurement scenario. In the following paragraphs, we will describe five measurement scenarios.

Figure 7.12 Photo of the measurement setup in an indoor garage.

Scenario 1: Static cars

The estimated range profile of multiple static objects is plotted in Figure 7.13, which proves that in the case of static objects, the upchirp and downchirp generate the same beat frequencies.

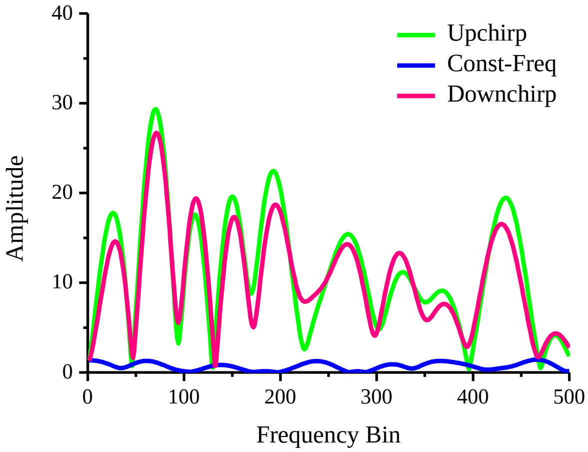

Figure 7.13 Beat frequencies of multiple static cars.

Scenario 2: A close and slowly-moving car

Figure 7.14 gives the beat frequencies of a close car moving slowly towards the radar. From the estimated beat frequencies, we can calculate the range and velocity of the car is 4.1 m and 2.6 km/h, respectively.

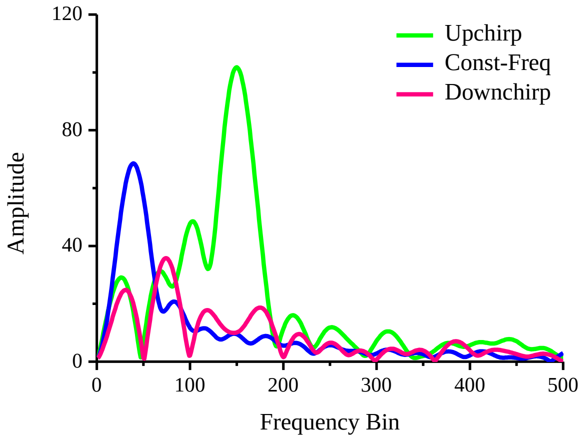

Figure 7.14 Beat frequencies of a close and slowly-moving car.

Scenario 3: A car with medium distance and speed

Figure 7.15 presents the measured beat frequencies of a car with medium distance and speed. From the estimated beat frequencies, we can justify that the car is 7.5 m away from our system and it is coming with a speed of 5.4 km/h.

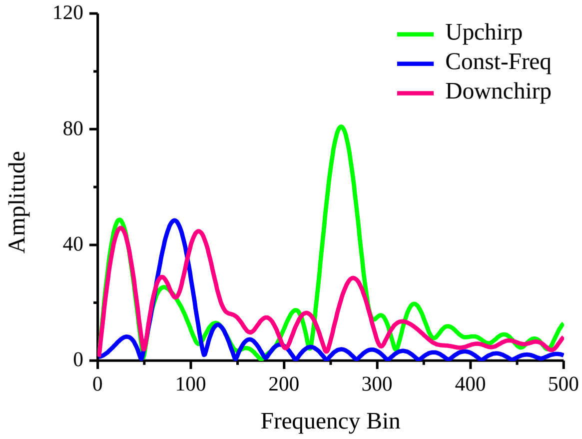

Figure 7.15 Beat frequencies of a car with medium distance and speed.

Scenario 4: An object with medium distance moving away from the system

In the case of an outgoing car, the beat frequency of the downchirp is higher than that of the upchirp, and measured results in this scenario is depicted in Figure 7.16. The calculated range and velocity of the car is 8.9 m and 5.4 km/h, respectively.

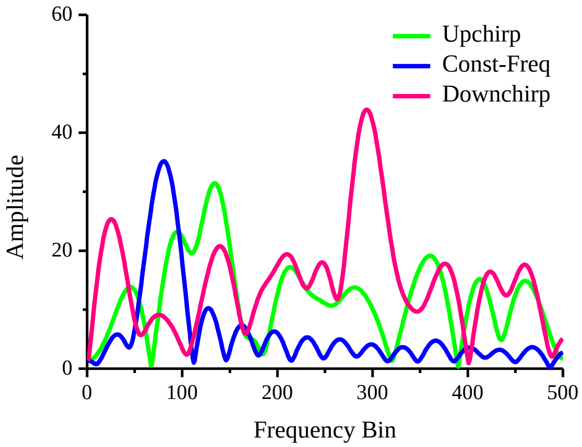

Figure 7.16 Beat frequencies of an incoming car with medium distance and speed.

Scenario 5: A distant object moving away from the system with high speed

Finally, a distant car is leaving from the system is detected, and Figure 7.17 gives the measured results, from which the range and velocity of the car are calculated to be 10.9 m and 10.3 km/h, respectively.

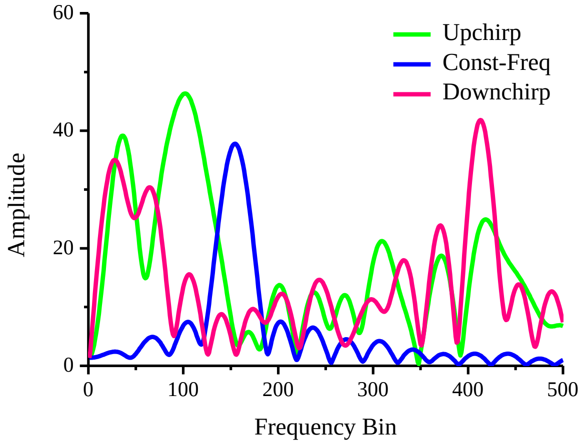

Figure 7.17 Beat frequencies of an incoming car with large distance and high speed.

7.3 Conclusion

This chapter covers the prototyping and experiments of our 24-GHz system. Our 24-GHz system is developed by integrating all the passive components designed in Chapter 5 and active components. Extensive experiments are performed both in the lab and in the garage. Experimental results show very promising system performance, which finally concludes this PhD project.

CONCLUSION AND FUTURE WORK

1. Conclusion

This PhD thesis has presented the comprehensive and systematic development of iCars for future ITSs. Starting from an extensive literature research, the entire project is carried out in a top-down approach, from system-level to component-level. In the beginning, a novel kind of modulation waveform was proposed, in which wireless communication and radar sensing functions are specially allocated in sequential time slots in order to minimize their interference. In addition to this functional integration, this modulation scheme has other attractive features such as functional reconfiguration (time-agile operation) and functional fusion (joint operation), and enhancement of network capacity (TDMA and FDMA). In the meanwhile, conventional radio transceiver architecture is studied and adapted to the proposed modulation scheme. A low-frequency system demonstrator for 5.9-GHz U.S. FCC's DSRC applications has been analyzed through system and circuit simulations and then prototyped with commercial off-the-shelf components. Experimental results have verified system functionality and manifested excellent system performance. In order to improve system performance in connection with communication data rate and radar range resolution, another system prototype has been developed in the 24-GHz ISM-band with a bandwidth up to 250 MHz. This high-frequency system prototype was designed and implemented with the help of a new circuit integration concept called SIW. A number of innovative passive SIW components such as wideband coupler, broadband phase shifter and highly-selective bandpass filters are proposed together with novel synthesis and analysis method by dint of numerical calibration technique. Moreover, a novel equivalent-circuit-model-based modeling method has been proposed to characterize mutual coupling from low-orders to high-orders in a successive manner and it was applied to the design of a 24-GHz microstrip array. By integrating all the developed passive SIW components with commercial off-the-shelf active devices, a 24-GHz system has been synthesized on a single substrate and promising measurement results obtained both in the laboratory and in an indoor garage have validated our system performance.

So far, this PhD project has generated fruitful research outcomes including 1invited book chapter, 6 journal publications and 8 conference papers as well as 2 U.S. patent applications. The principle scientific contributions of this thesis are the following:

1) A novel modulation scheme that integrates both wireless communication and radar sensing functions was proposed and analyzed for the first time, which possesses decisive advantages concerning minimized mutual interference, versatile and time-agile functionality, possibility of functional fusion and increased network capacity.

2) The modulated waveform is generated through a DDS in a software-defined platform.

3) Conventional heterodyne transceiver architecture is adapted regarding the proposed modulation scheme.

4) A low-frequency system has been demonstrated at 5.9 GHz for DSRC applications. In this context, system specifications were proposed, and then link budget analysis was performed for both radar and radio (communication) modes in order to unlock their major differences. System performance was analyzed and optimized using a novel approach, by which both RF front-ends and baseband back-ends can be co-simulated. Excellent agreement between experimental results of the fabricated system prototype and simulation results has proved our system concept and validated our analysis method.

5) A wideband SIW coupler is proposed. By circularly tapering the coupling slot of conventional SIW Riblet hybrid, the operation bandwidth can be increased. In order to find out the phase difference between even and odd modes along the coupling slots, numerical TRL calibration technique is used to extract the propagation constants of even and odd modes and also the equivalent circuit model of bifurcation effects. Three design examples including a 15-GHz 3-dB 90° SIW coupler, a 15-GHz 0-dB SIW coupler and a 24-GHz 3-dB 90° SIW coupler are given to demonstrate the efficiency and accuracy of our proposed structure and analysis method.

6) A broadband SIW phase shifter is developed by removing a portion of the substrate. Through rigorous theoretical analysis, a complete synthesis method was proposed to provide direct design guideline. By combining the wide-band SIW coupler and broadband SIW phase shifter, a wideband 3-dB 180° coupler is designed and prototyped with very good experimental results.

7) SIW bandpass filters with high selectivity were also investigated and prototyped. Different filter topologies were studied and measured results of the filter prototypes show very

promising results, which are very beneficial to enhance system performance at 24 GHz compared to conventional planar filters.

8) An original idea was developed for accurately synthesizing four-line interdigitated couplers. With the derivation of four coupled transmission lines and the use of interconnecting condition, only half of the original coupled-line structures should be considered with its symmetric plane replaced by a perfect electric wall and/or perfect magnetic wall. Subsequently, two new mode admittances are respectively calculated from the propagation constants and the line impedances of *c*- and π-modes, which are extracted from full-wave simulations. In this way, a reference chart is generated and it describes the relationship between the two mode admittances and physical dimensions of the coupled lines. With any prescribed performance, the physical dimensions of a four-line interdigitated coupler can effectively be synthesized by looking up the reference chart. To demonstrate the accuracy and flexibility of the propose scheme, two examples are given including a conventional Lange coupler and a composite microstrip-CPW coupler that is taken as an IF coupler in our 24-GHz system.

9) A novel fundamental strategy for accurately modeling the mutual coupling of arbitrary order in any electromagnetic structures and antenna arrays are proposed. Starting from the first-order mutual coupling, the proposed method consists of two steps. In the beginning, an equivalent circuit model describing low-order mutual coupling (adjacent coupling) is characterized and established, of which each parametric value is accurately extracted by making use of a numerical calibration technique. Then, the circuit model for high-order mutual coupling (crossover or crosstalk coupling) is generated from the low order models and it can be further used for the modeling of mutual coupling of any high orders. The accuracy and efficiency of the proposed method are demonstrated by three different kinds of electromagnetic structures including linear and planar phased array antenna, periodic structures, and low-pass filters. In the 24-GHz system, a pair of high-gain and low-sidelobe microstrip arrays composed of 8×8 elements are also developed by means of this modeling technique.

10) A high-frequency system has been prototyped at 24 GHz on a single substrate by integrating developed SIW passive components together with commercial active devices

through a monolithic integration approach. This 24-GHz system prototype outperforms the 5.9-GHz system demonstrator judging from good performance with respect to high-rate data communication and high-accuracy target detection.

2. Future work

The research contributions presented in this thesis may be extended in the following ways.

1) For practical applications, it is necessary to design two oscillators with good spectral purity and high frequency stability for the IF LO and the RF LO that are generated by two signal generators in the present system measurement setup.

2) The radar mode of present system is able to detect target range and velocity. Its capability can be extended with multiple receiving channels to detect target direction. Smart antenna technologies including multi-beam antenna, phased array antenna and adaptive array antenna with extension to multiple-input and multiple-output (MIMO) system, can be integrated into the present system for estimating directional of arrival (DOA), forming radiation patterns and improving communication performance.

3) In our software defined platform, multi-target detection is possible by varying the chirp rate in a consecutive operation cycles through software programming of DDS. In addition, according to usage situations, time-agility or a flexible functional reconfiguration can also be achieved by adaptively adjusting the durations of each period that could be determined by a certain kind of cognitive signal processing algorithms.

4) Joint operation of communication and radar modes can be analyzed with respect to performance improvement and then verified through experiments.

5) The operation frequency of this multifunctional system can be up-scaled to such high-frequency band as *E*-band, which has two advantages. One is a large amount of frequency resources available at *E*-band, and the other is low atmospheric attenuation of radio wave. In this frequency range, the complete system will be realized by a hybrid integration of different SICs including SIW, SINRD and SIIG.

BIBLIOGRAPHIE

[1] *Global status report on road safety: time for action*. Geneva, World Health Organization, 2009 (www.who.int/violence_injury_prevention/ road_safety_status/2009).

[2] http://www.ccmta.ca/remember_souvenez-vous/home.php.

[3] R. Bishop, *Intelligent Vehicle Technology and Trends*. Norwood, MA: Artech House, 2005.

[4] R. H. Rasshofer and K. Gresser, “Automotive radar and lidar systems for next generation driver assistance functions,” *Advances in Radio Science*, vol. 3, pp. 205–209, 2005.

[5] P. Barrenechea, F. Elferink, and J. Janssen, “FMCW radar with broadband communication capability,” in *Proceedings of 4th European Radar Conference*, Munich, Germany, Oct. 2007, pp. 130–133.

[6] V. Winkler and J. Detlefsen, “Automotive 24GHz pulse radar extended by a DQPSK communication channel,” in *Proceedings of 4th European Radar Conference*, Munich, Germany, Oct. 2007, pp. 138–141.

[7] S. Lindenmeier, K. Boehm, and J. F. Luy, “A wireless data link for mobile applications,” *IEEE Microwave and Wireless Components Letters*, vol. 13, no. 8, pp. 326–328, 2003.

[8] X. Yin, *et al*. “Embedded ranging system in ISM band,” *IET Eletronics Letters*, vol. 44, no. 17, pp. 1043–1045, Aug. 2008.

[9] S. J. Xu, Y. Chen, and P. Zhang, “Integrated radar and communication based on DS-UWB,” in *Proceedings of International Conference on Ultrawideband and Ultrashort Impulse Signals*, Sevastopol, Ukraine, Sept. 2006, pp. 142–144.

[10] Z. Lin and P. Wei, “Pulse amplitude modulation direct sequence ultra wideband sharing signal for communication and radar systems,” in *Proceedings of International Symposium on Antennas, Propagation and EM Theory*, Guilin, China, Oct. 2006.

[11] M. Jamil, H.-J. Zepernick, and M. I. Pettersson, “On integrated radar and communication systems using oppermann sequences,” in *Proceedings of IEEE Military Communications Conference*, San Diego, CA, Nov. 2008.

[12] K. Mizui, M. Uchida, and M. Nakagawa, “Vehicle-to-vehicle communications and ranging system using spread spectrum techniques,” in *Proceedings of IEEE Vehicular Technology Conference*, Secaucus, NJ, May 1993, pp.335-338.

[13] Z. Lin and P. Wei, “Pulse position modulation time hopping ultra wideband sharing signal for radar and communication system,” in *Proceedings of International Conference on Radar,* Shanghai, China, Oct. 2006.

[14] G. N. Saddik, R. S. Singh, and E. R. Brown, “Ultra-wideband multifunctional communications/radar system,” *IEEE Transactions on Microwave Theory and Techniques*, vol. 55, no. 7, pp. 1431–1437, July 2007.

[15] N. Levanon, “Multifrequency complementary phase-coded radar signal,” *IEE Proceedings − Radar Sonar and Navigation*, vol. 147, no. 6, pp. 276–284, Dec. 2000.

[16] G. E. A. Franken, H. Nikookar, and P. van Genderen, “Doppler tolerance of OFDM-coded radar signals,” in *Proceedings of 3rd European Radar Conference*, Manchester, UK, 2006, pp. 108−111.

[17] C. Sturm, E. Pancera, T. Zwick, and W. Wiesbeck, “A novel approach to OFDM radar processing,” in *Proceedings of IEEE Radar Conference 2009*, Pasadena, CA, May 2009.

[18] B. Donnet and I. Longstaff, “Combining MIMO radar with OFDM communications,” in *Proceedings of 3rd European Radar Conference*, Manchester, UK, Sept. 2006, pp. 37−40.

[19] D. Garmatyuk, et al, “Feasibility study of a multi-carrier dual-use imaging radar and communication system,” in *Proceedings of 4th European Radar Conference*, Munich, Germany, Oct. 2007, pp. 194−197.

[20] G. Lellouch and H. Nikookar, “On the capability of a radar network to support communications,” in *Proceedings of 14th IEEE Symposium on Communications and Vehicular Technology*, Benelux, Nov. 2007.

[21] R. Fens, M. Ruggiano, and G. Leus, “Channel characterization using radar for transmission of communication signals,” in *Proceedings of 1st European Wireless Technology Conference*, Amsterdam, The Netherlands, Oct. 2008, pp. 127−130.

[22] M. Braun, C. Sturm, A. Niethammer, and F. Jondral, “Parametrization of joint OFDM-based radar and communication systems for vehicular applications,” in *Proceedings of IEEE 20th International Symposium on Personal, Indoor and Mobile Radio Communications*, Tokyo, Japan, Sept. 2009, pp. 3020−3024.

[23] D. Garmatyuk and K. Kauffman, “Radar and data communication fusion with UWB-OFDM software-defined system,” in *Proceedings of IEEE International Conference on Ultra-Wideband*, Vancouver, Canada, 2009, pp.454−458.

[24] M. Braun, Y. Koch, C. Sturm, and F. Jondral, “Signal design and coding for high-bandwidth OFDM in car-to-car communication,” in *Proceedings of IEEE 72nd Vehicular Technology Conference (VTC-Fall)*, Ottawa, Canada, Sept. 2010.

[25] K. Konno and S. Koshikawa, “Millimeter-wave dual mode radar for headway control in IVHS,” in *International Microwave Symposium Digest IEEE-MTT-S 1997*, Denver, CO, June 1997, pp. 1261−1264.

[26] A. Stelzer, M. Jahn, and S. Scheiblhofer, “Precise distance measurement with cooperative FMCW radar units,” in *Proceedings of IEEE Radio Wireless Conference*, Orlando, FL, Jan. 2008, pp. 771−774.

[27] H. Zhang, L. Li, and K. Wu, “24GHz software-defined radar system for automotive applications,” in *Proceedings of 10th European Wireless Technology Conference*, Munich, Germany, Oct. 2007, pp. 138−141.

[28] L. Han and K. Wu, “Radio and Radar Data Fusion Platform for Future Intelligent Transportation Systems”, in *Proceedings of 7th European Radar Conference*, Paris, France, 2010, pp. 65−68.

[29] Federal Communications Commission (FCC), “Amendment of Parts 2 and 90 of the Commission’s Rules to Allocate the 5.850-5.925 GHz Band to the Mobile Service for Dedicated Short Range Communications of Intelligent Transportation Services,” ET Docket no. 98−95 RM−9096, Feb. 2004.

[30] Electronic Communications Committee, “ECC Decision of 15 March 2002 on the frequency bands to be designated for the coordinated introduction of Road Transport and Traffic Telematic Systems,” ECC/DEC/(02)01, 2002.

[31] Association of Radio Industries and Business (ARIB), “Dedicated short-range communication system,” ARIB standard no. STD−T75, Dec. 2007.

[32] General Administration of of Quality Supervision, Inspection and Quarantine (AQSIQ) and the Standardization Administration of China (SAC), “Electronic toll collection − dedicated short range communication”, GB/T 20851.1−2007, 2007.

[33] K. Wu, D. Deslandes, and Y. Cassivi, “The substrate integrated circuits − A new concept for high-frequency electronics and optoelectronics,” in *Proceedings of the 6th International Conference on Telecommunication, Modern Satellite, Cable, Broadcasting Service (TELSIKS 2003)*, Nis, Serbia and Montenegro, vol. 1, 2003, pp. P-III–P-X.

[34] X.-P. Chen and K. Wu, “Substrate integrated waveguide cross-coupled filter with negative coupling structure,” *IEEE Transactions on Microwave Theory and Techniques*, vol. 56, no. 1, pp. 142−149, Jan. 2008.

[35] Z. Li and K. Wu, “24-GHz frequency-modulated continuous-wave radar front-end system-on-substrate” *IEEE Transactions on Microwave Theory and Techniques*, vol. 56, no. 2, pp. 278−285, Feb. 2008.

[36] Z. C. Hao, W. Hong, J. X. Chen, H. X. Zhou, and K. Wu, “Single-layer substrate integrated waveguide directional couplers,” *IEE Proceedings − Microwaves, Antennas and Propagation*, vol. 153, no. 5, pp. 426−431, Oct. 2006.

[37] J. X. Chen, W. Hong, Z. C. Hao, H. Li, and K. Wu, “Development of a low cost microwave mixer using a broadband substrate integrated waveguide coupler,” *IEEE Microwave and Wireless Components Letters*, vol. 16, no. 2, pp. 84−86, 2006.

[38] P. Chen, *et al*, “A multibeam antenna based on substrate integrated waveguide technology for MIMO wireless communications,” *IEEE Transactions on Antennas and Propagation*, vol. 57, no. 6, pp. 1813−1821, June 2009.

[39] W. Hong, “Development of antennas, components and subsystems based on SIW technology,” in *Proceedings of IEEE International Symposium on Microwave, Antenna, Propagation and EMC Technologies for Wireless Communications 2005*, Beijing, China, 2005, pp. 14−17.

[40] S. Yamamoto, J. Hirokawa, and M. Ando, “Length reduction of short slot directional coupler in a single layer dielectric substrate waveguide by removing dielectric near the side walls,” in *IEEE Antennas and Propagation Symposium 2004*, Monterey, CA, vol. 3, 2004, pp. 2353−2356.

[41] L. Han, K. Wu, X.-P. Chen, and F. He, “Accurate analysis of finite periodic substrate integrated waveguide structures and its applications,” in *International Microwave Symposium Digest IEEE-MTT-S 2010*, Anaheim, CA, May 2010, pp. 864−867.

[42] X.-P. Chen and K. Wu, “Accurate and efficient design approach of substrate integrated waveguide filter using numerical TRL calibration technique,” in *International Microwave Symposium Digest IEEE-MTT-S 2008*, Atlanta, GA, June 2008, pp.1231−1234.

[43] X. Xu, R. G. Bosisio, and K. Wu, “A new six-port junction based on substrate integrated waveguide technology,” *IEEE Transactions on Microwave Theory and Techniques*, vol. 53, no. 7, pp. 2267−2273, Jul. 2004.

[44] Y. J. Cheng, W. Hong, and K. Wu, “Novel substrate integrated waveguide fixed phase shifter for 180-degree directional coupler,” in *International Microwave Symposium Digest IEEE-MTT-S 2007*, Honolulu, HI, 2007, pp.189−192.

[45] E. Sbarra, L. Marcaccioli, R. V. Gatti, and R. Sorrentino, “A Novel Rotman Lens in SIW Technology,” in *Proceedings of 37th European Microwave Conference*, Munich, Germany, Oct. 2007, pp. 1515−1518.

[46] B. Liu, W. Hong, Z. C. Hao, and K. Wu, “Substrate integrated waveguide 180-degree narrow-wall directional coupler,” in *Proceedings of Asia-Pacific Microwave Conference 2005*, Suzhou, China, 2005.

[47] W. Che, E. K. N. Yung, K. Wu, and X.-D. Nie, “Design investigation on millimeter-wave ferrite phase shifter in substrate integrated waveguide,” *Progress In Electromagnetics Research*, PIER 45, pp. 263−275, 2007.

[48] Y. J. Cheng, K. Wu, and W. Hong, “Substrate integrated waveguide (SIW) broadband compensating phase shifter,” in *International Microwave Symposium Digest IEEE-MTT-S 2008*, Atlanta, GA, 2008, pp.845−848.

[49] K. Sellal, L. Talbi, T. A. Denidni, and J. Lebel, “Design and implementation of a substrate integrated waveguide phase shifter,” *IET Microwaves, Antennas & Propagation*, vol. 2, no. 2, pp. 194−199, Mar. 2008.

[50] L. Han, K. Wu, X.-P. Chen, and F. He, “Broadband compact substrate integrated waveguide phase shifter,” *IEEE Microwave and Wireless Components Letters*, submitted.

[51] B. Liu, *et al*, “Half mode substrate integrated waveguide 180º 3-dB directional couplers,” *IEEE Transactions on Microwave Theory and Techniques*, vol. 55, no. 12, pp. 2586−2592, Dec. 2007.

[52] L. Han, K. Wu, and S. Winkler, “Singly balanced mixer using substrate integrated waveguide magic-T structure,” in *Proceedings of 11th European Wireless Technology Conference*, Amsterdam, The Netherlands, Oct. 2008, pp. 9–12.

[53] F. He, K. Wu, L. Han, X.-P. Chen, and W. Hong, “A modified planar magic-T using substrate integrated circuits concept,” *IEEE Transactions on Microwave Theory and Techniques*, vol. 59, no. 1, pp. 72–79, Jan. 2011.

[54] F. He, K. Wu, W. Hong, L. Han, and X.-P. Chen, “A low phase noise VCO using a novel tunable substrate integrated waveguide resonator,” *IEEE Transactions on Microwave Theory and Techniques*, vol. 58, no. 12, pp. 3452–3458, Dec. 2010.

[55] X.-P. Chen, K. Wu, L. Han, and F. He, “Low-cost planar antenna with high gain for 60-GHz band wireless applications,” *IEEE Transactions on Antennas and Propagation*, vol. 58, No. 6, pp. 2126–2129, June 2010.

[56] F. He, K. Wu, X.-P. Chen, L. Han, and W. Hong, “A planar magic-T structure using substrate integrated circuits concept,” in *International Microwave Symposium Digest IEEE-MTT-S 2010*, Anaheim, CA, May 2010, pp. 720–723.

[57] B. Sklar, *Digital Communications − Fundamentals and Applications*. Englewood Cliffs: Prentice-Hall, 1988.

[58] L. Han and K. Wu, “Multifunctional transceiver for future intelligent transportation systems,” *IEEE Transactions on Microwave Theory and Techniques*, vol. 59, no.7, pp. 1879–1892, July 2011.

[59] M. I. Skolnik, *Introduction to Radar Systems*, 3rd ed., New York: McGraw-Hill, 2000.

[60] M. Mitsumoto, N. Uehara, S. Inatsune, and T. Kirimoto, “Target distance and velocity measurement algorithm to reduce false target in FMCW automotive radar”, *IEICE Transactions on Communications*, vol. E83-B, no. 9, pp. 1983−1989, Sept. 2000.

[61] H. Rohling and E Lissel, “77 GHz radar sensor for car application,” in *Proceedings of IEEE International Radar Conference*, Alexandria, VA, May 1995, pp.373−379.

[62] L. Cheng, B. E. Henty, D. D. Stancil, F. Bai, and P. Mudalige. “Mobile vehicle-to-vehicle narrow-band channel measurement and characterization of the 5.9 GHz dedicated short range communication (DSRC) frequency band,” *IEEE Journal on Selected Areas in Communications*, vol. 25, no. 8, pp. 1501−1516, Oct. 2007.

[63] Advanced Design System (ADS) 2009. Agilent Technology, Santa Clara, CA, 2009.

[64] J. G. Proakis, *Digital Communications*, 4th ed., New York: McGraw-Hill, 2000.

[65] R. J. Cameron, “Advanced coupling matrix synthesis techniques for microwave filters,” *IEEE Transactions on Microwave Theory and Techniques*, vol. 51, no. 1, pp. 1−10, Jan. 2003.

[66] High Frequency Structure Simulator (HFSS) v12, Ansoft Corporation, Pittsburgh, PA, 2010.

[67] F. M. Gardner, “A BPSK/QPSK timing-error detector for sampled receivers,” *IEEE Transactions on Communications*, vol. 34, no. 5, pp. 423−429, May 1986.

[68] F. M. Gardner, “Interpolation in digital modems – part I: fundamentals”, *IEEE Transactions on Communications*, vol. 41, no. 3, pp. 501−507, Mar. 1993.

[69] L. Erup, F. M. Gardner, and R. A. Harris, “Interpolation in digital modems – part II: implementation and performance”, *IEEE Transactions on Communications*, vol. 41, no. 6, pp. 998−1008, June 1993.

[70] L. Han and K. Wu, “24-GHz joint radar and radio system capable of time-agile wireless sensing and communication,” in *International Microwave Symposium Digest IEEE-MTT-S 2011*, Baltimore, MD, 2011.

[71] H. J. Riblet, “The short-slot hybrid junction,” *Proceedings of the IRE*, vol. 40, pp. 180−184, Feb. 1952.

[72] L. T. Hildebrand, “Results for a simple compact narrow-wall directional coupler,” *IEEE Microwave and Guided Wave Letters*, vol. 10, no.6, pp. 231−232, June 2000.

[73] I. Ohta, A. Hino, T. Kawai, and Y. Kokubo, “Broad-band simple H-plane directional couplers,” in *Proceedings of Asia-Pacific Microwave Conference 2001*, Taiwan, China, 2001, pp.41−44.

[74] R. Levy, “Directional couplers,” in *Advances in Microwaves*, L. Young, Ed. New York: Academic, 1966, vol. 1, pp. 115−209.

[75] L. Li, K. Wu, and L. Zhu, “Numerical TRL calibration technique for parameter extraction of planar integrated discontinuities in a deterministic MoM algorithm,” *IEEE Microwave and Wireless Components Letters*, vol. 12, pp. 485−487, Dec. 2002.

[76] T. E. Rozzi and W. F. G. Mecklenbrauker, “Wide-band network modeling of interacting inductive irises and steps,” *IEEE Transactions on Microwave Theory and Techniques*, vol. 23, no. 2, pp. 235−245, Feb. 1975.

[77] H. Schmiedel and F. Arndt, “Field theory design of rectangular waveguide multiple-slot narrow-wall couplers,” *IEEE Transactions on Microwave Theory and Techniques*, vol. 34, no. 7, pp. 791−798, July 1986.

[78] R. Levy, “Determination of simple equivalent circuits of interacting discontinuities in waveguides or transmission lines,” *IEEE Transactions on Microwave Theory and Techniques*, vol. 48, no.10, pp. 1712−1716, Oct. 2000.

[79] Southwest Microwave, End launcher connector series [Online]. Available: http://mpd.southwestmicrowave.com/pdf/series_endlaunch.pdf.

[80] S. A. Maas, *Microwave Mixers*, 2nd ed. Norwood, MA: Artech House, 1993.

[81] Rogers Corporation. *High Frequency Circuit Materials Product Selector Guide* [Online]. Available: http://www.rogerscorp.com /documents/776/acm/High-Frequency-Laminates---Product-Selector-Guide.aspx.

[82] J. Lange, “Interdigitated stripline quadrature hybrid,” *IEEE Transactions on Microwave Theory and Techniques*, vol. 17, no. 12, pp. 1150−1151, Dec. 1969.

[83] R. Waugh and D. LaCombe, “Unfolding the Lange coupler,” *IEEE Transactions on Microwave Theory and Techniques*, vol. 20, no. 11, pp. 777−779, Nov. 1972.

[84] W. P. Ou, “Design equations for an interdigitated directional coupler,” *IEEE Transactions on Microwave Theory and Techniques*, vol. 23, no. 2, pp. 253−255, Feb. 1975.

[85] T. G. Bryant and J. A. Weiss, “Parameters of microstrip transmission lines and of coupled pairs of microstrip lines,” *IEEE Transactions on Microwave Theory and Techniques*, vol. 16, no. 12, pp. 1021−1027, Dec. 1968.

[86] V. Rizzoli, “Stripline interdigitated couplers: Analysis and design considerations,” *IET Electronics Letters*, vol. 11, no. 16, pp. 392−393, Aug. 1975.

[87] S. J. Hewitt and R. S. Pengelly, “Design data for interdigital directional couplers,” *IET Electronics Letters*, vol. 12, no.3, pp. 86−87, Feb. 1976.

[88] J. A. G. Malherbe, “Interdigital directional couplers with an odd or even number of lines and unequal characteristic impedances,” *IET Electronics Letters*, vol. 12, no. 18, pp. 464−465, Sept. 1976.

[89] V. Rizzoli and A. Lipparini, “The design of interdigitated couplers for MIC applications,” *IEEE Transactions on Microwave Theory and Techniques*, vol. 26, no. 1, pp. 7−15, Jan. 1978.

[90] D. Kajfez, Z. Paunovic, and S. Pavlin, “Simplified design of Lange coupler,” *IEEE Transactions on Microwave Theory and Techniques*, vol. 26, no. 10, pp. 806−808, Oct. 1978.

[91] D. D. Paolino, “Design more accurate interdigitated couplers,” *Microwaves*, pp. 34−38, May 1976.

[92] Y. Tajima and S. Kamishashi, “Multiconductor couplers,” *IEEE Transactions on Microwave Theory and Techniques*, vol. 26, no. 10, pp. 795−801, Oct. 1978.

[93] R. M. Osmani, “Synthesis of Lange couplers,” *IEEE Transactions on Microwave Theory and Techniques*, vol. 29, no. 2, pp. 168−170, Feb. 1981.

[94] S. Akhtarzad, T. Rowbotham, and P. Johns, "The design of coupled microstrip lines," *IEEE Transactions on Microwave Theory and Techniques*, vol. 23, no. 6, pp. 486−492, Jun. 1975.

[95] R. M. Osmani, "Correction to 'The design of coupled microstrip lines'," *IEEE Transactions on Microwave Theory and Techniques*, vol. 28, no. 6, pp. 672−673, Jun. 1980.

[96] D. M. Pozar, *Microwave Engineering*, 2nd ed. New York: Wiley, 1998.

[97] A. Presser, "Interdigitated microstrip coupler design," *IEEE Transactions on Microwave Theory and Techniques*, vol. 26, no. 10, pp. 801−805, Oct. 1978.

[98] H. A. Wheeler, "Transmission line properties of parallel strips separated by a dielectric sheet," *IEEE Transactions on Microwave Theory and Techniques*, vol. 13, pp. 172−185, Mar. 1965.

[99] H. A. Wheeler, "Transmission line properties of a strip on a dielectric sheet on a plane." *IEEE Transactions on Microwave Theory and Techniques*, vol. 25, no. 8, pp. 631−647; Aug. 1977.

[100] G. G. Gentili, G. B. Stracca, G. Macchiarella, M. Politi, and G. Gatti, "Accurate modeling of Lange couplers for CAD applications," in *Proceedings of 21st European Microwave Conference*, Stuttgart, Germany, Oct. 1991, vol. 2, pp. 1556−1561.

[101] Y. Kim, *et al*, "Extraction of multiple coupled line parameters using FDTD simulation," *IEE Proceedings − Microwaves, Antennas and Propagation*, vol. 146, no.6, pp. 443-446, Dec. 1999.

[102] J. Nickel, D. Trainor, and J. Schutt-Ainé, "Frequency-domain-coupled microstrip-line normal-mode parameter extraction from *S*-parameters," *IEEE Transactions on Electromagnetic Compatibility*, vol. 43, no. 4, pp. 495−503, Nov. 2001.

[103] L. Han, K. Wu, and X.-P. Chen, "Accurate synthesis of four-line interdigitated coupler," *IEEE Transactions on Microwave Theory and Techniques*, vol. 57, No.10, pp. 2444−2455, Oct. 2009.

[104] V. K. Tripathi, “Asymmetric coupled transmission lines in an inhomogeneous medium,” *IEEE Transactions on Microwave Theory and Techniques*, vol. 23, no. 9, pp. 734−739, Sept. 1975.

[105] R. Mongia, I. Bahl, and P. Bhartia, *RF and Microwave Coupled-Line Circuits*, Norwood: Artech House, 1999.

[106] IE3D (Zeland Package), Zeland Software Inc., Fremont, CA, 2009.

[107] L. Han, K. Wu, and X.-P. Chen, “Compact ultra-wideband bandpass filter using stub-loaded resonator,” *IET Electronics Letters*, vol.45, pp. 504−506, May 2009.

[108] L. Han, K. Wu, and X.-P. Zhang, “Development of packaged ultra-wideband bandpass filters,” *IEEE Transactions on Microwave Theory and Techniques*, vol. 58, No.1, pp. 220−228, Jan. 2010.

[109] L. Han, K. Wu, X.-P. Chen, and F. He, “Packaged microstrip line diplexer,” To appear in *Microwave Journal*.

[110] J.-C. Chiu, J.-M. Lin, M.-P. Houng, and Y.-H. Wang, “A PCB-compatible 3-dB coupler using microstrip-to-CPW via-hole transitions,” *IEEE Microwave and Wireless Components Letters*, vol. 16, no. 6, pp. 369−371, Jun. 2006.

[111] J.-C. Chiu, C.-M. Lin, and Y.-H. Wang, “A 3-dB Quadrature Coupler Suitable for PCB Circuit Design,” *IEEE Transactions on Microwave Theory and Techniques*, vol. 54, no. 9, pp. 3521−3525, Sept. 2006.

[112] B. Van Thielen and G. A. E. Vandenbosch, “Method for the calculation of mutual coupling between discontinuities in planar circuits,” *IEEE Transactions on Microwave Theory and Techniques*, vol. 50, no. 1, pp. 155−164, Jan. 2002.

[113] B. Van Thielen and G. A. E. Vandenbosch, “Fast method for calculation of mutual coupling in planar microwave circuits on general multilayer substrates,” *International Journal of RF and Microwave Computer-Aided Engineering*, vol. 13, no. 5, pp. 378−388, Aug. 2003.

[114] A. Benalla and K. C. Gupta, “Multiport network approach for modeling the mutual coupling effects in microstrip patch antennas and arrays,” *IEEE Transactions on Antennas and Propagation*, vol. 37, no. 2 , pp. 148−152, 1989.

[115] R. C. Hansen, *Phased Array Antennas*. New York: John Wiley & Sons, 1998.

[116] R. J. Mailloux, *Phased Array Antenna Handbook*. Norwood: Artech House, 1994.

[117] D. M. Pozar, “Input impedance and mutual coupling of rectangular microstrip antennas,” *IEEE Transactions on Antennas and Propagation*, vol. 30, no. 11, pp. 1191−1196, Nov. 1982.

[118] D. M. Pozar, “Finite phased arrays of rectangular microstrip patches,” *IEEE Transactions on Antennas and Propagation*, vol. 34, no. 5, pp. 658−665, May 1986.

[119] F. J. Demuynck, G. A. E. Vandenbosch, and A. R. Van de Capelle, “The expansion wave concept − Part I: Efficient calculation of spatial Green’s functions in a stratified dielectric medium,” *IEEE Transactions on Antennas and Propagation*, vol. 46, no. 3, pp. 397−406, Mar. 1998.

[120] G. A. E. Vandenbosch, and F. J. Demuynck, “The expansion wave concept − Part II: A new way to model mutual coupling in microstrip arrays,” *IEEE Transactions on Antennas and Propagation*, vol. 46, no. 3, pp. 407−413, Mar. 1998.

[121] A. Ishimaru, R. Coe, G. Miller, and W. Geren, “Finite periodic structure approach to large scanning array problems,” *IEEE Transactions on Antennas and Propagation*, vol. 33, no. 11, pp. 1213−1220, Nov. 1985.

[122] A. Skrivervik and J. Mosig, “Analysis of finite phase arrays of microstrip patches,” *IEEE Transactions on Antennas and Propagation*, vol. 41, no. 8, pp. 1105−1114, Aug. 1993.

[123] D. Kelley and W. Stutzman, “Array antenna pattern modeling methods that include mutual coupling effects,” *IEEE Transactions on Antennas and Propagation*, vol. 41, no. 12, pp. 1625−1632, Dec. 1993.

[124] P. Katehi, “Mutual coupling between microstrip dipoles in multielement arrays,” *IEEE Transactions on Antennas and Propagation*, vol. 37, no. 3, pp. 275−280, Mar. 1989.

[125] L. Han and K. Wu, “Modeling of arbitrary-order mutual coupling,” in *International Microwave Symposium Digest IEEE-MTT-S 2008*, Atlanta, GA, 2008, pp. 1389−1392.

[126] L. Han and K. Wu, “Circuit representation and performance analysis of planar phased array antenna including mutual coupling effects,” in *Proceedings of IEEE MTT-S International Mini-Symposium on Electromagnetic Network Theory and their Microwave Technology Applications*, Munich, Germany, 2008.

[127] L. Han and K. Wu, “Modeling of mutual coupling of arbitrary order in coupled circuits and array antennas,” *International Journal of RF and Microwave Computer-Aided Engineering*, vol. 21, no. 1, pp. 5−16, Jan. 2011.

[128] K.-C. Lee and T.-H. Chu, “A circuit model for mutual coupling analysis of a finite antenna array,” *IEEE Transactions on Electromagnetic Compatibility*, vol. 38, no. 3, pp. 483−489, Aug. 1996.

[129] C. D. Meyer, *Matrix Analysis and Applied Linear Algebra*. Philadelphia: SIAM, 2000.

[130] P. B. Katehi, “A generalized method for evaluation of mutual coupling in microstrip arrays,” *IEEE Transactions on Antennas and Propagation*, vol. 35, no. 2, pp. 125−133, Feb. 1987.

[131] L. Zhu and K. Wu, “Unified equivalent-circuit model of planar discontinuities suitable for field theory-based CAD and optimization of M(H)MIC’s,” *IEEE Transactions on Microwave Theory and Techniques*, vol. 47, no. 9, pp. 1589−1602, Sept. 1999.

[132] L. Zhu and K. Wu, “Short-open calibration technique for field theory-based parameter extraction of lumped elements of planar integrated circuits,” *IEEE Transactions on Microwave Theory and Techniques*, vol. 50, no. 8, pp. 1861−1869, Aug. 2002.

[133] L. Han, K. Wu, W. Hong, L. Li, and X.-P. Chen, “Embedding of short-open calibration technique in commercial MoM simulators for parameter extraction of planar integrated circuits,” in *Proceedings of Asia-Pacific Microwave Conference 2006*, Yokohama, Japan, 2006, pp. 1956−1959.

[134] D. M. Pozar, “A relation between the active input impedance and the active element pattern of a phased array,” *IEEE Transactions on Antennas and Propagation*, vol. 51, no. 9, pp. 2486−2489, Sept. 2003.

[135] D. M. Pozar, “The active element pattern,” *IEEE Transactions on Antennas and Propagation*, vol. 42, no. 8, 1176−1178, Aug. 1994.

[136] J.-S. Hong and M. J. Lancaster, *Microstrip Filters for RF/Microwave Applications*. New York: John Wiley & Sons, Inc., 2001.

[137] L. Han and K. Wu, “24-GHz bandwidth-enhanced microstrip array printed on single-layer electrically-thin substrate for automotive applications,” *IEEE Transactions on Antennas and Propagation*, submitted.

[138] D. M. Pozar, “A review of bandwidth enhancement techniques for microstrip antennas,” *Microstrip Antennas: The Analysis and Design of Microstrip Antennas*, D. M. Pozar and D. H. Schaubert, Eds. New York: IEEE Press, 1995, pp. 157−166.

[139] R. Garg, P. Bhartia, I. Bahl, and A. Ittipiboon, *Microstrip Antenna Design Handbook*. Norwood, MA: Artech House, 2001.

[140] C. A. Balanis, *Antenna Theory: Analysis and Design*. 2nd ed., New York: John Wiley & Sons, 1997.

APPENDIX 1 – LIST OF PUBLICATIONS & AWARDS

1. Invited book chapter

[B1] **L. Han** and K. Wu, “Circuit representation and performance analysis of phased array antennas including mutual coupling effects,” in ***Electromagnetics and Network Theory and Their Microwave Technology Applications***, S. Lindenmeier and R. Weigel, Eds. Berlin: Springer−Verlag Berlin Heidelberg, 2011, pp. 35–49.

2. Peer-reviewed journal publications

2.1 Published papers

[J1] **L. Han**, K. Wu, X.-P. Chen, and F. He, “Packaged microstrip line diplexer,” To appear in ***Microwave Journal***.

[J2] **L. Han** and K. Wu, “Multifunctional transceiver for future intelligent transportation systems,” ***IEEE Trans. Microwave Theory and Techniques***, vol. 59, no. 7, pp. 1879–1892, July 2011.

[J3] **L. Han** and K. Wu, “Modeling of mutual coupling of arbitrary-order in coupled circuits and array antennas,” ***International Journal of RF and Microwave Computer−Aided Engineering***, vol. 21, no. 1, pp. 5–16, Jan. 2011.

[J4] **L. Han**, K. Wu, and X.-P. Zhang, “Development of packaged ultra-wideband bandpass filters,” ***IEEE Trans. Microwave Theory and Techniques***, vol. 58, no. 1, pp. 220–228, Jan. 2010.

[J5] **L. Han**, K. Wu, and X.-P. Chen, “Accurate synthesis of four-line interdigitated coupler,” ***IEEE Trans. Microwave Theory and Techniques***, vol. 57, no. 10, pp. 2444–2455, Oct. 2009.

[J6] **L. Han**, K. Wu, and X.-P. Chen, “Compact ultra-wideband bandpass filter using stub-loaded resonator,” ***IET Electronics Letters***, vol.45, pp. 504–506, May 2009.

[J7] L. Yang, P. Cheong, **L. Han**, W.-W. Choi, K.-W. Tam, and K. Wu, “Miniaturized parallel coupled-line filter-antenna with spurious response suppression,” To appear in ***IEEE Antennas and Wireless Propagation Letters.***

[J8] F. He, K. Wu, **L. Han**, X.-P. Chen, and W. Hong, “A modified planar magic-T using substrate integrated circuits concept,” ***IEEE Trans. Microwave Theory and Techniques***, vol. 59, no. 1, pp. 72–79, Jan. 2011.

[J9] F. He, K. Wu, W. Hong, **L. Han**, and X.-P. Chen, “A low phase noise VCO using a novel tunable substrate integrated waveguide resonator,” ***IEEE Trans. Microwave Theory and Techniques***, vol. 58, no. 12, pp. 3452–3458, Dec. 2010.

[J10] X.-P. Chen, K. Wu, **L. Han**,and F. He, “Low-cost planar antenna with high gain for 60-GHz band wireless applications,” ***IEEE Trans. Antennas and Propagation***, vol. 58, no. 6, pp. 2126–2129, June 2010.

2.2 Submitted papers

[J11] **L. Han** and K. Wu, “24-GHz integrated radio and radar system capable of time-agile wireless communication and sensing,” ***IEEE Trans. Microwave Theory and Techniques*** (under review).

[J12] **L. Han** and K. Wu, “24-GHz bandwidth-enhanced microstrip array printed on single-layer electrically-thin substrate for automotive applications,” ***IEEE Trans. Antennas and Propagation*** (under review).

[J13] **L. Han**, K. Wu, X.-P. Chen, and F. He, “Accurate and efficient design technique for wideband substrate integrated waveguide directional couplers,” ***International Journal of RF and Microwave Computer-Aided Engineering*** (under review).

[J14] F. He, K. Wu, W. Hong, **L. Han**, and X.-P. Chen, “Low-cost 60 GHz smart antenna receiver sub-system based on substrate integrated waveguide technology,” ***IEEE Trans. Microwave Theory and Techniques*** (under review).

3. Conference papers

[C1] **L. Han** and K. Wu, “24-GHz joint radar and radio system capable of time-agile wireless sensing and communication,” in ***IEEE MTT-S Int. Microw. Symp. Dig.***, Baltimore, MD, June 2011, pp. 1–4.

[C2] **L. Han** and K. Wu, “Radio and radar data fusion platform for intelligent transportation systems,” in ***Proc. European Radar Conference (EuRAD)***, Paris, France, Oct. 2010, pp. 65–68.

[C3] **L. Han**, K. Wu, X.-P. Chen, and F. He, “Accurate analysis of finite periodic substrate integrated waveguide structures and its applications,” in ***IEEE MTT-S Int. Microw. Symp. Dig.***, Anaheim, USA, May 2010, pp. 864–867.

[C4] **L. Han**, K. Wu, and S. Winkler, “Singly balanced mixer using substrate integrated waveguide magic-T structure,” in ***Proc. European Wireless Technology Conference (EuWiT)***, Amsterdam, The Netherlands, Oct. 2008, pp. 9–12.

[C5] **L. Han**, K. Wu, W. Hong, and X.-P. Chen, “Compact and broadband transition of microstrip line to finite-ground coplanar waveguide,” in ***Proc. European Microwave Conference (EuMC)***, Amsterdam, The Netherlands, Oct. 2008, pp. 480–483.

[C6] **L. Han** and K. Wu, “Circuit representation and performance analysis of planar phased array antenna including mutual coupling effects,” in ***IEEE MTT-S International Mini-Symposium on EMNT***, Munich, Germany, Oct. 2008, pp. 1–4.

[C7] **L. Han** and K. Wu, “Modeling of arbitrary-order mutual coupling,” in ***IEEE MTT-S Int. Microw. Symp. Dig.***, Atlanta, USA, June 2008, pp. 1389–1392.

[C8] **L. Han**, K. Wu, and W. Hong, “Design considerations of ultra-broadband finite-ground CPW filters using multipole generation technique,” in ***Proc. International Symposium on Signals, Systems, and Electronics***, Montreal, Canada, July 2007, pp. 436–439.

[C9] F. He, K. Wu, X.-P. Chen, **L. Han**, and W. Hong, “A planar magic-T structure using substrate integrated circuits concept,” in ***IEEE MTT-S Int. Microw. Symp. Dig.***, Anaheim, USA, May 2010, pp. 720–723.

[C10] S. A. Winkler, **L. Han**, K. Wu, and A. Stelzer, “A novel multiple-element phased high-order subharmonic self-oscillating mixer for millimeter-wave receivers,” in ***Proc.***

European Microwave Conference (EuMC), Amsterdam, The Netherlands, Oct. 2008, pp. 163–166.

[C11] S. A. Winkler, **L. Han**, K. Wu, and A. Stelzer, "A novel technique for millimeter-wave receivers using multiple-element high-order subharmonic self-oscillating mixers," in ***Proc. Global Symposium on Millimeter Waves***, Nanjing, P. R. China, Apr. 2008, pp. 104–107.

[C12] X.-P. Chen, **L. Han**, and K. Wu, "Synthesis and design of substrate integrated waveguide filter using predistortion technique," in ***Proc. Asia–Pacific Microwave Conference (APMC)***, Bangkok, Thailand, Dec. 2007, pp. 843–846.

4. Patents

[P1] **L. Han** and K. Wu, "Radar system with integrated communication functionality," ***U.S. Patent Application***, 61/384,697, Sept. 2010.

[P2] **L. Han** and K. Wu, "Stub-loaded resonator filter," ***U.S. Patent Application***, 61/285,230, Dec. 2009.

5. Awards

[A1] **MTT-S Graduate Fellowship** from the IEEE Microwave Theory and Techniques Society.

[A2] **EuRAD Young Engineer Prize** for the best paper presented at the 7th European Radar Conference within the framework of European Microwave Week 2010.

[A3] **Second prize** in the student paper competition of CREER General Assembly 2010.

[A4] **Third Prize** in the student design competition of a packaged diplexer at the IEEE MTT-S International Microwave Symposium 2010, Anaheim, CA, May 2010.

[A5] **Chinese Government Award for Outstanding Self-Financed Students Abroad** from the Chinese Government.

[A6] **Second Prize** in the student design competition of a packaged UWB filter at the IEEE MTT-S International Microwave Symposium 2009, Boston, MA, June 2009.